SINGLE-ELECTRON RESOLUTION PHONON-MEDIATED DETECTORS: PROGRESS AND APPLICATIONS

A Dissertation

by

FEDJA KADRIBASIC

Submitted to the Office of Graduate and Professional Studies of
Texas A&M University
in partial fulfillment of the requirements for the degree of

DOCTOR OF PHILOSOPHY

Chair of Committee,	Nader Mirabolfathi
Committee Members,	Glenn Agnolet
	Tahir Cagin
	Bhaskar Dutta
	Harlan Rusty Harris
	Robert Webb
Head of Department,	Grigory Rogachev

May 2020

Major Subject: Physics

ABSTRACT

Many astrophysical observations indicate that nonbaryonic dark matter makes up around 85% of the total mass content of the Universe. The SuperCDMS experiment represents one of many concerted efforts around the world to better understand dark matter by attempting to measure it directly and setting limits on its properties, such as mass and interaction cross section. As SuperCDMS and experiments like it get closer to the neutrino floor, which is the level of cross section sensitivity when the dominant background comes from neutrino interactions, new methods will be required to probe to lower cross section parameter space. Additionally, a paradigm shift to include dark matter models with masses lower than about 1 GeV/c^2means that dark matter detectors need ever-better resolution to investigate ever-lower-mass dark matter models.

To address these scientific questions, I propose using defect creation to help discriminate potential dark matter signal from backgrounds. Molecular dynamics simulations based on more computationally-intensive time-dependent density functional theory calculations suggest that the anisotropy in defect creation energy threshold in solid-state materials could be used to make directionally-sensitive dark matter detectors. Additionally, defect creation energy loss could be used as a separate handle to discriminate possible signal from electron-recoil backgrounds, which is difficult to do at nuclear recoil energies approaching the threshold displacement energy. Finally, this computational work is in tandem with improvements in low-energy threshold, high-mass semiconductor detectors that could enable dark matter experiments to take advantage of defect creation effects. I present the world's first 100-gram-scale detector with single-electron resolution, which is the first step towards utilizing defect creation effects for dark matter searches.

DEDICATION

To my family.

ACKNOWLEDGMENTS

I would like to take this opportunity to thank all those who have offered help and support over the past six years.

First and foremost, I would like to thank my family: my mother, father, sister, and grandma for all their help and support, especially when the going was toughest. Without their words of encouragement and support, this dissertation would not have been possible. I would also like to thank my cousin, Faruk Avdić, and my parents for instilling in me a love of science that has unceasingly persisted to this very day.

Next, I would like to thank all my friends, especially Dr. Robert Moffatt for staying in touch throughout the years and all my California friends for sticking around, offering support, and cheering me up when things seemed at their worst, especially Mr. Tony Tzeng for arranging most of our get-togethers. Special mention goes to all the friends I made in Texas, especially Dr. Mike Smitka, Dr. Sean Wu, Mr. Curtis Hunt, Mr. Joshua Winchell, Dr. Minjie Lu, Ms. Leo Alcorn, and Mr. Andrew Quick, for spreading cheers in difficult times.

I would like to thank my research advisor, Professor Mirabolfathi, for guiding and supporting my work, even through difficult times. I would also like to thank my committee for approving my dissertation. Special thanks go to Professor Webb for his help, support, patience, and understanding and Professor Agnolet for sharing with me a lot of wonderful anecdotes and for his sage advice.

I would also like to thank Professor Nordlund, Professor Djurabekova, Dr. Holmström, and Dr. Sand for providing the datasets required to see how defect creation could have an effect on a possible dark matter signal. The papers on defect creation written by Dr. Holmström, Professor Nordlund, and Professor Kuronen that I have found have led to an amazing collaboration culminating in our mutual Physical Review Letters publication.

I would like to thank Professor Mirabolfathi, Professor Agnolet, Dr. Charles Hays, Mr. Mark Platt, Mr. Shahriar Esmaeili, Mr. Joel Larakers, Mr. Lazar Kish, Mr. Lorenzo Delcroix, Mr. Genesis Hearne, Mr. Braden Eller, Dr. Andy Kubik, Dr. Andrew Jastram, Dr. Jonathan Wilson, Mr. Minjie Lu, and Mr. Hao Chen for helping build the detector research and development facility that made data collection possible with detector S17B, among other prior projects. A special thanks goes to Mr. Mark Platt for all that he has taught me about making SuperCDMS detectors and for his advice about working in industry.

I would like to thank all of the machinists in the Physics and Astronomy Machine Shop, especially Mr. Garrick Garza, for making parts, providing the facility and equipment to make parts, and for general machining advice whenever it was needed.

I would like to thank the entire Freshman Lab Development Team, especially Professor Eusebi and Professor Christian for allowing me to be a part of an exceptional team. I am very glad to have contributed to such a productive and successful collaboration.

I would like to thank all of the Physics and Astronomy Department staff for providing help and support whenever it was needed, especially Ms. Sherree Kessler, Ms. Veronica Rodriguez, and Ms. RaéChel Superville. I would also like to thank the Office of Graduate and Professional Studies at Texas A&M University for providing extremely helpful advice about the dissertation process in a professional and timely manner.

I would like to thank all the teachers and professors who taught me over the years, especially my high school biology teacher Ms. Kane More for guiding me in my scientific pursuits as her student. A distinguished place among my former teachers and professors belongs to my friend and undergraduate research advisor, Professor Blas Cabrera, for all his help and support over the years. Another thanks goes to Professor Betty Young for all her friendly advice.

Finally, I would like to thank the entire Physics and Astronomy Department for providing a supportive working environment. Special thanks goes to Professor Rogachev for his understanding of my situation and Professor Ford for allowing me to get a last-minute teaching position when I needed it. I would also like to thank Professor Jennifer Marshall for helping me become a better teacher. Last but not least, I would like to thank Professor Naugle and his team for allowing us to borrow the indium press and Professor Ross for allowing us to use his hydrogen for the exchange gas and for providing the unused mu-metal for the mu-metal shield.

CONTRIBUTORS AND FUNDING SOURCES

Contributors

This work was supported by a dissertation committee consisting of Professor Mirabolfathi, Professor Agnolet, Professor Dutta, Professor Harris, and Professor Rogachev of the Department of Physics and Astronomy and Professor Cagin of the Department of Materials Science and Engineering and Professor Harris of the Department of Electrical and Computer Engineering.

The data analyzed for Section 3 and Section 4 was provided by Professor Nordlund of the Department of Physics and Dean of Science at the University of Helsinki.

All other work conducted for the dissertation was completed by the student independently.

Funding Sources

Graduate study was supported by the Department of Physics and Astronomy, Professor Mirabolfathi of the Department of Physics and Astronomy, and the Freshman Lab Development program at the Department of Physics and Astronomy. Under Professor Nader Mirabolfathi, experimental setup and data collection was supported by the DOE office of science grants DE-SC0014036 and DE-SC0017859 and also by the Mitchell Institute for Fundamental Physics and Astronomy.

NOMENCLATURE

TAMU	Texas A&M University
CDMS	Cryogenic Dark Matter Search
SuperCDMS	Super Cryogenic Dark Matter Search
TES	Transition Edge Sensor
QET	Quasi-Electrothermal Feedback Transition Edge Sensor
MD	Molecular Dynamics
DFT	Density Functional Theory
TDDFT	Time-Dependent Density Functional Theory
Si	Silicon
Ge	Germanium
C	Carbon
SQUID	Superconducting Quantum Interference Device
RMS	Root-Mean Squared
MC	Monte Carlo, as in Monte Carlo Simulation
PSD	Power Spectral Density
FWHM	Full Width at Half-Maximum
Ntuple	Data structure for storing relevant information for each particle event during a data-taking run with a SuperCDMS-style detector; literally translates to a tuple of size n
Digitizer	Device for saving analog electronic output as a digital signal for later data analysis; in the context of this work, saves particle interaction event data from detector

Trace	Single analog representation of signal output from digitizer, oscilloscope, or similar device
Trigger Level	Level above which digitizer, oscilloscope, or similar device saves and/or displays a trace, depending on the desired output
Channel	A separate path through which signal can flow; in the context of SuperCDMS-style detectors, it refers to one out of a number of separate signal outputs
Subtrace	Portion of a trace
Warm Electronics	Power supplies and amplifiers at room temperature for reading out SuperCDMS-style detectors
Cold Electronics	Amplifiers at cryogenic temperatures for reading out SuperCDMS-style detectors
RT-Loom	Room-temperature wiring in vacuum for carrying signal from cold electronics to warm electronics
Cryoloom ®	Cryogenic-temperature wiring in vacuum for carrying signal from cold electronics to warm electronics
Python	Programming language used for data analysis and simulations in this work
NumPy	Numerical Python; collection of Python modules for fast numerical calculations used frequently throughout this work
SciPy	Scientific Python; collection of Python modules for scientific calculations used throughout this work
FFT	Fast Fourier Transform; numerical algorithm for performing Fourier Transform of discrete data
RA	Right Ascension
dec	Declination
alt	Altitude
az	Azimuth

JD	Julian Day
WIMP	Weakly Interacting Massive Particle
Threshold Displacement Energy	Minimum energy required to displace a nucleus in an atomic lattice to produce a defect. Varies with material and direction in a given material.
MCNP	Monte Carlo N-Particle Transport Code
MOG	Modified Gravity
MoND	Modified Newtonian Dynamics
TeVeS	Tensor-Vector-Scalar Gravity
MaCHO	Massive Compact Halo Object
Macro	Macroscopic Dark Matter
CMB	Cosmic Microwave Background
FSL	Free Streaming Length
ATLAS	A Toroidal LHC ApparatuS
CMS	Compact Muon Solenoid
LHC	Large Hadron Collider
NTL	Neganov-Trofimov-Luke, usually referring to Neganov-Trofimov-Luke gain, Neganov-Trofimov-Luke phonons, or Neganov-Trofimov-Luke effect. Sometimes referred to as Luke-Neganov or Neganov-Luke.
DCRC	Detector Control and Readout Card
Stripline	CDMS cable connecting warm electronics inputs to cold electronics outputs in a cryogenic vacuum environment

TABLE OF CONTENTS

Page

LIST OF FIGURES

LIST OF TABLES

TABLE Page

1. DARK MATTER INTRODUCTION

Strong astrophysical evidence indicates that baryonic matter, the atoms we are familiar with, makes up only about 15% of all matter and that matter composes only about 30% of the total mass-energy content of the Universe [1]. However, the vast majority of the mass and energy, which are referred to as dark matter and dark energy, respectively, remains unknown. Between these two open scientific questions, dark matter seems more straightforward to study since an experiment could observe it directly in principle. However, dark matter is so elusive that no experiment has conclusively observed it yet. In this dissertation, I discuss detectors designed to measure the signal when dark matter occasionally does interact with baryonic matter in the context of large-scale experiments searching for it. I focus on recent progress towards phonon-mediated large-mass single-electron-resolution detectors and the science applications possible with such detectors.

1.1 Cosmological and Astronomical Evidence

If dark matter is so difficult to observe, it begs the question why scientists know it exists in the first place. It turns out that dark matter, despite not emitting any electromagnetic radiation, does possess gravitational mass, which means that it affects visible matter that emits electromagnetic radiation. Studies thereof have provided strong evidence for the existence of dark matter, which I discuss in the next several subsections.

1.1.1 Spiral Galaxy Rotation Curves

The average velocity of stars as a function of distance from the center of a spiral galaxy scales with the galaxy's radial mass density distribution. Because a spiral galaxy has spiral arms that surround a central bulge, and the highest concentration of stars is in the central bulge and drops off with distance from the center, one expects stellar velocities to also drop as a function of distance from the center. On the contrary, stellar velocities stay flat, which indicates that the local mass density does not follow the concentration of stars or visible matter. Instead, this velocity profile implies that there is a lot more mass than expected near the outskirts of spiral galaxies, which a dark matter halo surrounding the galaxy could explain.

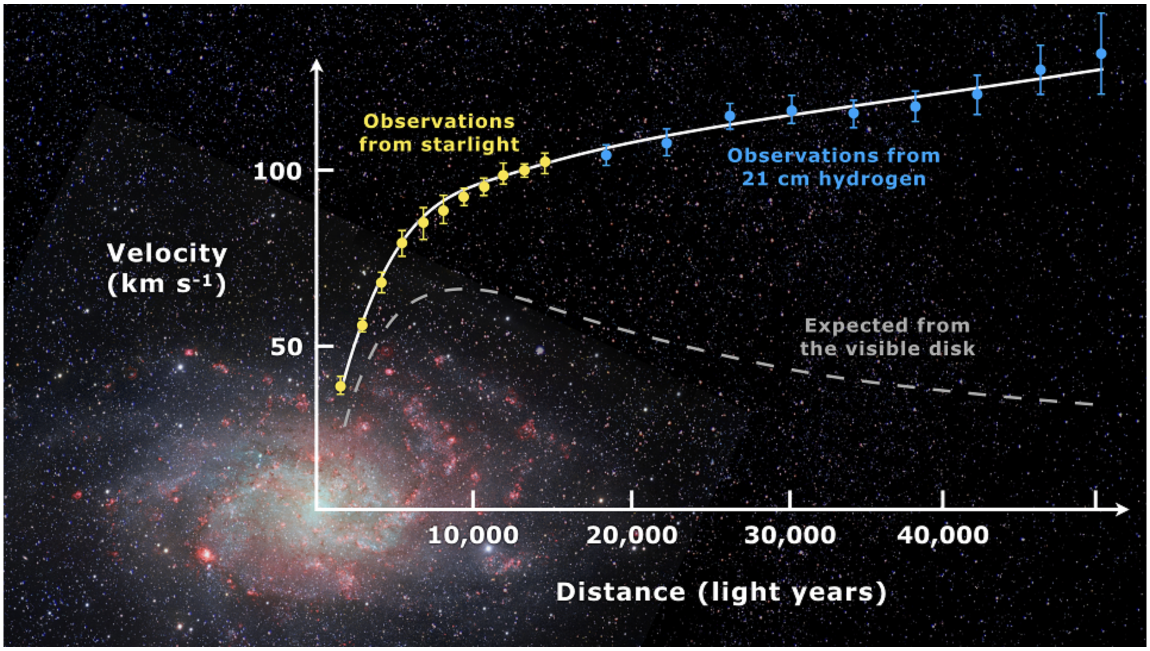

Figure 1.1: Plot showing the rotation curve of the galaxy Messier 33 (M33) atop an optical image of the galaxy. The large deviation in the baryonic matter velocity distribution relative to that expected from the visible disk implies excess mass near the edges of the galaxy. This provides evidence for the existence of nonbaryonic dark matter. Figure reprinted from the public domain from [2].

The nearby spiral galaxy Messier 33 (M33), often referred to as the Triangulum galaxy because of its location near the constellation Triangulum, provides a great example of this effect. Fig. 1.1 shows an optical image of M33 with its radial velocity profile overlaid [3]. The rotation curve shown by the dotted line assumes that a large fraction of the total mass of the spiral galaxy is concentrated in its central bulge. The solid curve, on the other hand, is the rotation curve measured using stellar observations (yellow points) and spectral shifts in interstellar hydrogen (blue points). The measured data deviates from the expected trend significantly since the velocity tends to plateau at large distances rather than dropping. This implies that, rather than being concentrated in the center, a majority of the mass of this spiral galaxy seems to surround it in a halo-like shape. Given that this trend applies for the majority of spiral galaxies [4], the rotational curves of spiral galaxies provide evidence for the existence of dark matter.

1.1.2 Velocity Dispersions of Elliptical Galaxies and Globular Clusters

The velocity dispersion of stars in an elliptical galaxy, which can be calculated from the stars' radial velocities, can be used to estimate the mass of the entire galaxy via the virial theorem. Consequently, a mass deviation from an expected model without dark matter, just like in the case for stellar velocities, corresponds to unobservable mass in the form of dark matter. Fig. 1.2 shows how the velocity dispersion of stellar-mass objects in a lenticular galaxy, which is a type of galaxy between an elliptical and spiral galaxy, changes as a function of distance from the center. Since there is a large deviation between the velocity dispersion data and the velocity dispersion model without dark matter, it is very likely that dark matter plays a significant role in the galaxy's dynamical behavior.

Additionally, because of the virial theorem, velocity dispersions can be used for measuring the properties of any gravitationally-bound system, not just galaxies. Hence, globular clusters in orbit around galaxies, like our own Milky Way, can be used to find the mass of the galaxies [5, 6, 7]. Both the elliptical galaxy and globular cluster results show that there is likely an excess of invisible mass without which one cannot explain the high velocity dispersion, which could be due to dark matter.

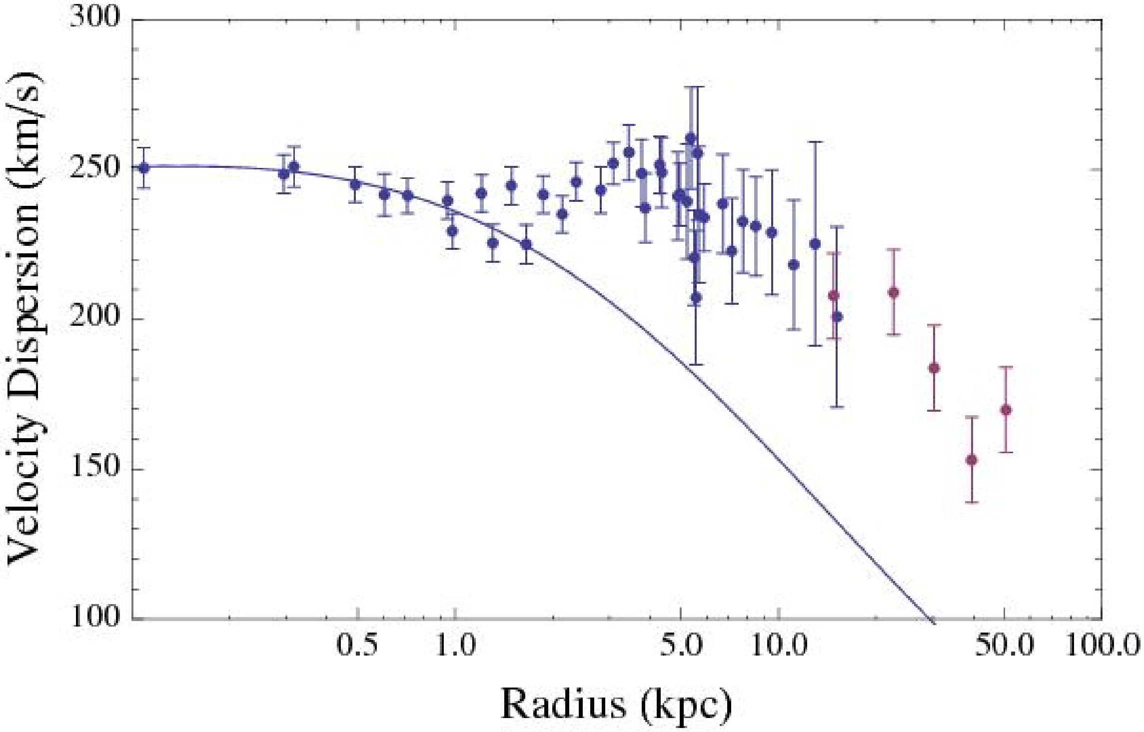

Figure 1.2: Plot showing the velocity dispersion of NGC 1316, a lenticular galaxy, as a function of distance from its center. The large deviation between the model without dark matter, the solid line, and the actual data underscores how large of an effect dark matter can have on the velocity dispersion of stellar-mass objects in a galaxy. Reprinted with permission from [8].

1.1.3 Galaxy Clusters

Galaxy clusters can contain many galaxies and have a very high mass, which makes them ideal for testing whether there is a nonluminous component to their masses. Several mutually exclusive methods can be used to measure their masses and any discrepancies can be accounted for. Overall, galaxy cluster mass estimates, regardless of method, tend to agree with each other and indicate that there is an excess nonluminous mass component in galaxy clusters.

As discussed in the previous subsection, radial velocity dispersions can be used to estimate the total mass of a gravitationally-bound system. The same procedure can be used with the galaxies that make up a galaxy cluster. These measurements show that galaxies orbit around the center at speeds much greater than expected given the visible mass in the cluster.

Another possibility is to balance the pressure exerted by hot intergalactic gas pushing a cluster apart with gravitational pressure holding it together. The total gas and its temperature profile can be measured via x-rays. The result is that the pressure is too high for the mass from solely the intergalactic gas and galaxies to keep the gas gravitationally bound. An example of this result is shown in Fig. 1.3, which shows how the cluster mass, based on simulations and real data, scales with the total x-ray luminosity. A more detailed explanation of the current status of the field, as well as the models and data used in Fig. 1.3, is given in Ref. [9].

Gravitational lensing can also be used to determine the mass of a galaxy cluster. Gravitational lensing occurs when a massive object bends the light from an object behind it relative to an observer, which causes the light of the background object to appear both brighter and deformed. The larger the foreground object's mass and the more the two objects are aligned with respect to the viewer, the more the background object looks like a ring. Consequently, the degree of distortion and brightening of the background object can be used to precisely measure the mass of the foreground object. This is an especially useful measurement for galaxy clusters since they are such massive objects. As with the other two methods discussed previously, the total mass of the cluster inferred via gravitational lensing exceeds the amount predicted by the visible matter alone, which provides further support for the existence of dark matter.

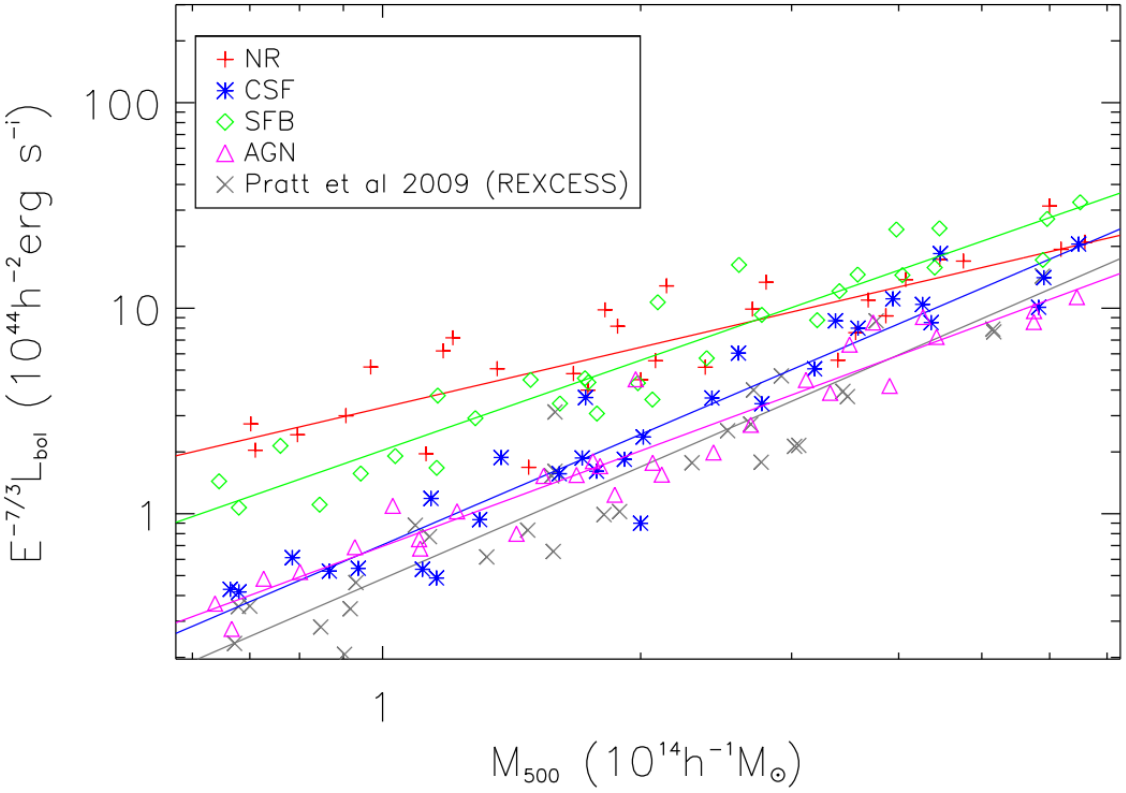

Figure 1.3: Plot showing the x-ray luminosity as a function of cluster mass. The different symbols and colors represent different gas physics models in the computations: red crosses for the non-radiative model, blue stars for the cooling and star formation model, green diamonds for the supernova feedback model, and magenta triangles for active galactic nuclei model. Gray diamonds are data from Ref. [10]. Reprinted with permission from [9].

1.1.3.1 Bullet Cluster

The Bullet Cluster is one of the best, if not the best, examples of how multiple independent measurements can be used to understand the true nature of dark matter. Additionally, it provides some of the strongest evidence supporting the claim that dark matter is actual matter rather than an illusion caused by physical laws that behave differently at large distance scales. The reason for this is that the Bullet Cluster shows how the regions with high

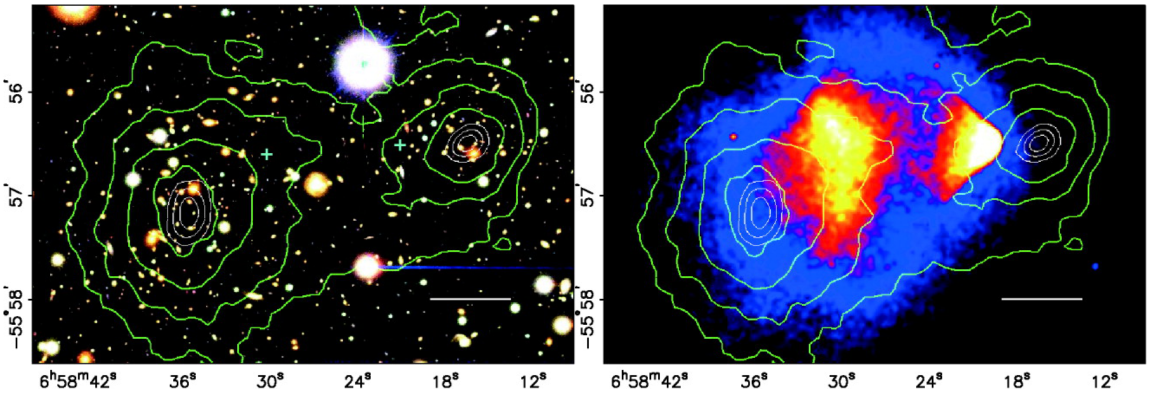

Figure 1.4: Images of the Bullet Cluster, which is the small cluster at right in both images that passed through the larger cluster at left about 150 million years ago. The mass distribution measured by gravitational lensing (green contours in both) and intergalactic gas distribution (blue to white distribution in right image) is superimposed over an optical image of the two clusters. The image shows how the mass distribution is distinct from the extragalactic gas, the location of most of the baryonic mass. © AAS reproduced with permission. Figure reprinted with permission from [11].

baryonic mass have separated from the areas with the highest overall mass [12, 13].

Fig. 1.4 shows the mass distribution in blue and intergalactic gas in red superimposed over an optical image of the two colliding clusters - the smaller Bullet Cluster at right and its larger companion at left. The mass distribution was mapped using gravitational lensing, and the intergalactic gas distribution was measured via the x-ray signal from the clusters. As shown in the Figure, the mass distribution tends to follow the location of the galaxies and not the location of the intergalactic gas, which is where most of the baryonic mass actually is.

The baryonic mass, mostly composed of intergalactic, x-ray-luminous gas, slows down during the collision due to self-interaction. However, most of the overall mass passes straight through essentially unaffected. The overall mass follows the galaxies, which also interact with each other very little. However, there is much more baryonic mass in the intergalactic gas than the galaxies themselves. Consequently, the Bullet Cluster strongly supports the fact that most of the mass is in a form that cannot be detected since it interacts very little with itself or ordinary matter. Studies since then using other galaxy clusters further support the Bullet Cluster observations [14, 15].

1.1.4 Relics of the Big Bang

To understand the next several pieces of evidence, one needs to wind the clock back to when time and space themselves began - the Big Bang. At some point very soon after the initial inferno, the Universe quickly expanded, which smoothed out a large portion of initial anisotropies immediately after its creation. Almost immediately afterwards, the first atomic nuclei were created. The young Universe then continued expanding and cooling in the process. At some point, the temperature became low enough for free electrons to combine with the atomic nuclei, and the Universe became transparent. This storyline of the Universe's formation leads to three pieces of evidence that strongly support the existence of invisible dark matter that makes up the majority of the Universe's mass: the existence of large-scale structures such as galaxies and galaxy clusters, anisotropies in the cosmic microwave backround (CMB), and the size of baryon acoustic oscillations.

1.1.4.1 Structure Formation

Without dark matter, galactic-scale structures could not exist in our Universe to begin with. Powerful supercomputers can model the evolution of the Universe after electrons combined with nuclei, the epoch of recombination. Essentially regardless of model, if there is only baryonic matter that is strongly coupled to radiation, there is not enough time between recombination and the birth of the first stars for matter to accrete into galaxies and galaxy clusters from the primordial overdensities in the early Universe. Additionally, once the stars are born, their radiation pressure pushes all of the remaining uncoalesced baryonic matter away, making it much more difficult for galaxies and galaxy clusters to form [16]. Not even neutrinos, despite making up a large portion of the Universe's total mass, can help since they travel at relativistic speeds [17].

On the other hand, if there is some type of dark matter that makes up a large portion of the Universe's mass but does not interact with electromagnetic radiation, then the problem of structure formation is solved. At some point before recombination, the temperature of the Universe was so high that dark matter was popping in and out of existence by annihilating with itself. As the temperature dropped, the process tended to shift away from equilibrium and towards creating dark matter that does not annihilate with itself. At some point, the number density reached a constant, a process referred to as dark matter relic density freeze-out. However, this would have happened much earlier than recombination because of the dark matter's low cross-section, despite there being much more dark matter in total than radiation and baryonic matter combined. This means that local overdensities in mass would have had time to form *before* recombination, thereby solving the structure formation problem [17, 16].

What is even more amazing is that the regions of over- and under-density from the early Universe persist to this day and can be observed by carefully measuring the anisotropies in the CMB. I go over how these anisotropies support the existence of dark matter next.

1.1.4.2 Cosmic Microwave Background

Given the importance of the discovery of the CMB not only to physics, but to all of science, it is only natural to devote some time to explaining the CMB and its importance to cosmology in general. I will then focus on how the anisotropies in it relate to dark matter.

The relevance of the CMB to our modern understanding of the Universe can be summed up with the simple question - why is the night sky dark? This paradox, also known as Olber's paradox, refers to the fact that if the Universe were infinite, homogenous, and static, the entire night sky would actually be as bright as the surface of the Sun. For any point in the sky, there would be a star at that location at a far enough distance away, which would

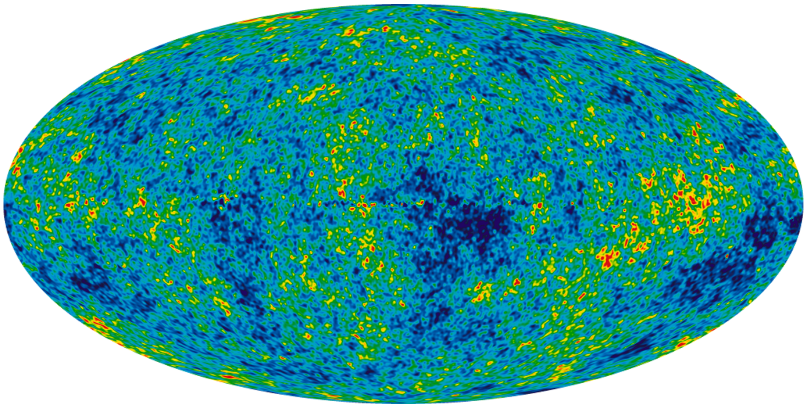

Figure 1.5: All-sky map showing the fluctuations in the cosmic microwave background (CMB). The fluctuations are on the order of one part in one hundred thousand after removing the dipole distribution from the relative motion of the Solar System with respect to the CMB. Image reproduced from public domain from [18].

mean that the entire sky would glow like a giant blackbody of a few thousand kelvin temperature.

The fact that the night sky has not completely fried our planet, and humankind with it, is proof that at least one of the three assumptions required for Olber's paradox are not met. It turns out that even a finitely-sized Universe that is not entirely homogenous would still make the sky glow about as bright as the surface of a star. Consequently, the only way the paradox is resolved is if the Universe is finitely old, as opposed to infinitely old.

A Universe that is finitely old, on the other hand, must have had a beginning. On average, all galactic-scale structures in the Universe move away from each other at speeds that increase with distance, which means that the Universe as a whole is expanding. Winding back the clock thus implies that objects in the early Universe were much closer to each other than they are today, which means that the Universe was much hotter as well. Going back all the way to the beginning of the Universe leads to the Big Bang theory, which also implies that there was a time after the Big Bang when the Universe actually was as hot as the surface of a star and all matter was ionized. This means that the radiation from this hot beginning should still be travelling throughout space, in line with Olber's paradox.

Since the Universe has been expanding since the Big Bang and still is, the radiation from immediately after recombination has been stretched due to the expansion of space itself. Consequently, the radiation will have redshifted in the more than 13 billion years since then to a much cooler $\sim$2.7 K. Hence, the radiation would only be visible in the radio spectrum rather than in the visible spectrum like Olber's Paradox naïvely implies. This radiation was finally observed by Arno Penzias and Robert Woodrow Wilson in 1964, who won the Nobel Prize for their discovery in 1978. In conclusion, the CMB both resolves Olber's Paradox and provides very strong proof that the Universe began with the Big Bang.

Now that the context for CMB observations has been presented, the relevance of how the CMB relates to our understanding of dark matter can be fully appreciated. The CMB is composed of electromagnetic waves that have been travelling the Universe since recombination about 400,000 years after the Big Bang. The signal reaches an observer from all directions, and the relative signal strength varies depending on the position in the sky.

If the dark matter number density must have frozen out before recombination, then dark matter would have started to clump together before recombination as well. Because the slightly overdense dark matter regions would have attracted the primordial plasma before recombination, there would have been anisotropies in the CMB as well. Once the Universe became transparent, those slight fluctuations would have remained until the present day, and they would be observable. The length scale of the fluctuations, then and now, corresponds to the cosmological density parameter Ω for all of its constituents, such as baryons, radiation, neutrinos, dark matter, and dark energy. Hence, the key to understanding dark matter on a cosmological scale during recombination lies in understanding the measurable CMB fluctuations today.

The cosmological parameters can be determined using a mathematical construct sim-

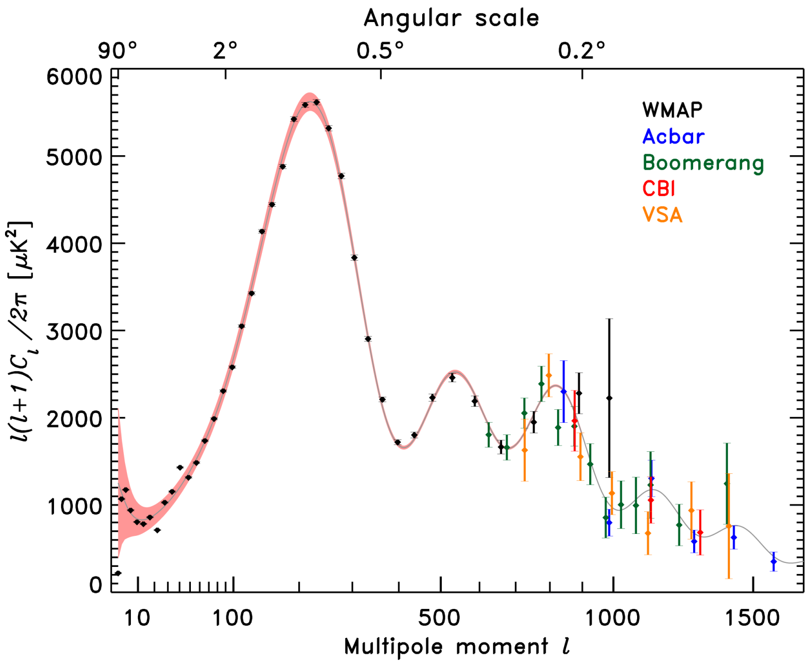

Figure 1.6: CMB power spectrum generated from observed anisotropies in the CMB measured by WMAP and several other experiments. This plot can be conceptualized as the decomposition of the CMB anisotropy distribution into its spherical harmonics and plotting the relative strength of the contribution as a function of the multipole moment l. A Fourier series decomposition is the one-dimensional analog of this process. Each peak corresponds to a different angular scale of anisotropy features on the sky, as indicated by the scale along the top of the plot. The best fit to the data is shown by the grey curve. The relative positions and heights of the first three peaks indicate how much of the total mass-energy of the Universe is composed of dark matter relative to the radiation contribution, which can be inferred from the overall strength of the CMB itself. Plot reproduced from public domain from [19].

ilar to a Fourier transform applied to an angular distribution on the surface of a sphere. [*] The signal is decomposed into spherical harmonics and the contribution to each multipole moment is properly weighted. The relative strengths and positions of the peaks in such a plot, in conjunction with similar measurements of the overall anisotropy, determine the cosmological parameters to within a few percent precision [23, 24, 25]. Fig. 1.5 shows the

---

[*] This explanation assumes one ignores higher-order effects that can also be measured in the CMB, such as polarization and anomalous over- or under-dense regions such as the CMB Cold Spot [20, 21, 22].

anisotropies in the CMB after data reduction and processing. This processing includes removing the dipole contribution from the relative motion of the Solar System with respect to the CMB, which includes the Milky Way Galaxy's motion towards the Great Attractor, among other motions, and removing the contribution of the Milky Way itself [26, 27]. The shape of this curve strongly supports the existence of dark matter.

Thus, measuring the anisotropy of the CMB can constrain cosmological parameters, which can help scientists better understand dark matter. Additionally, because the CMB is a phenomenon that originated, to first order, from every point in the early Universe, it is next to impossible to attribute the contribution from dark matter to localized effects. Since the effect of dark matter is visible in the anisotropies to begin with also indicates that dark matter has been around at least long enough to help create the anisotropies. Combined with the high precision of the cosmological parameter results, the CMB offers one of the strongest pieces of evidence supporting the existence of dark matter.

1.1.4.3 Large-Scale Galactic Structures

A related effect to the anisotropies observed in the CMB that supports the existence of dark matter is the distribution of galaxies observable in the relatively nearby Universe. All-sky surveys such as the Sloan Digital Sky Survey (SDSS) have measured the positions of thousands of galaxies out to several hundred megaparsecs from the Milky Way Galaxy, as shown in Fig. 1.7. Doing so has allowed scientists to determine that, at a very slight but statistically significant level, galaxies tend to space themselves about 150 megaparsecs apart, in agreement with other cosmological measurements. This spacing comes from baryon acoustic oscillations (BAOs), which are sound waves caused by the interaction of matter, dark matter, and radiation in the early Universe. The fact that this scale agrees with the cosmological parameters measured from the CMB further supports the current model of the Universe and, in so doing, provides more evidence for the existence of dark matter.

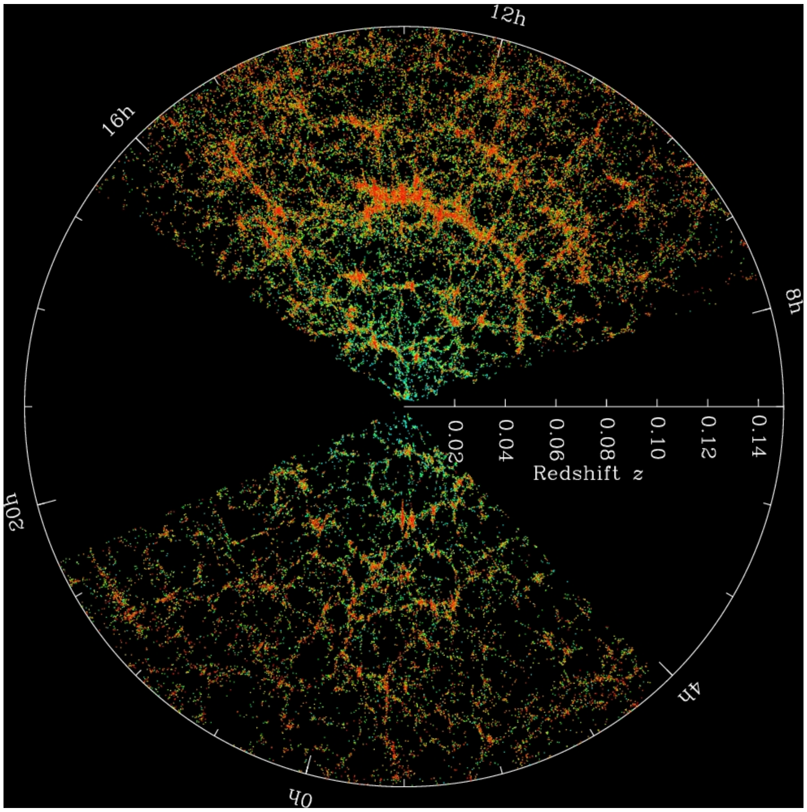

Figure 1.7: Map of the visible universe produced by the SDSS collaboration. Each dot represents a single galaxy, and redder regions indicate regions indicate relative overdensities whereas bluer and black regions represent underdensities. Figure reprinted from the public domain from the SDSS collaboration [28].

1.1.5 Possible Galaxies Without Dark Matter

If confirmed true, one of the strongest pieces of evidence supporting the existence of dark matter could be the existence of galaxies without any dark matter [29, 30, 31, 32]. Although the process of how a galaxy might form without dark matter is not yet fully understood, it could happen only if the gravitational effect we perceive is due to a physical substance. Consequently, this discovery, if verified, could rule out many models that propose other ways to explain dark matter observations.

1.2 Candidates and Models

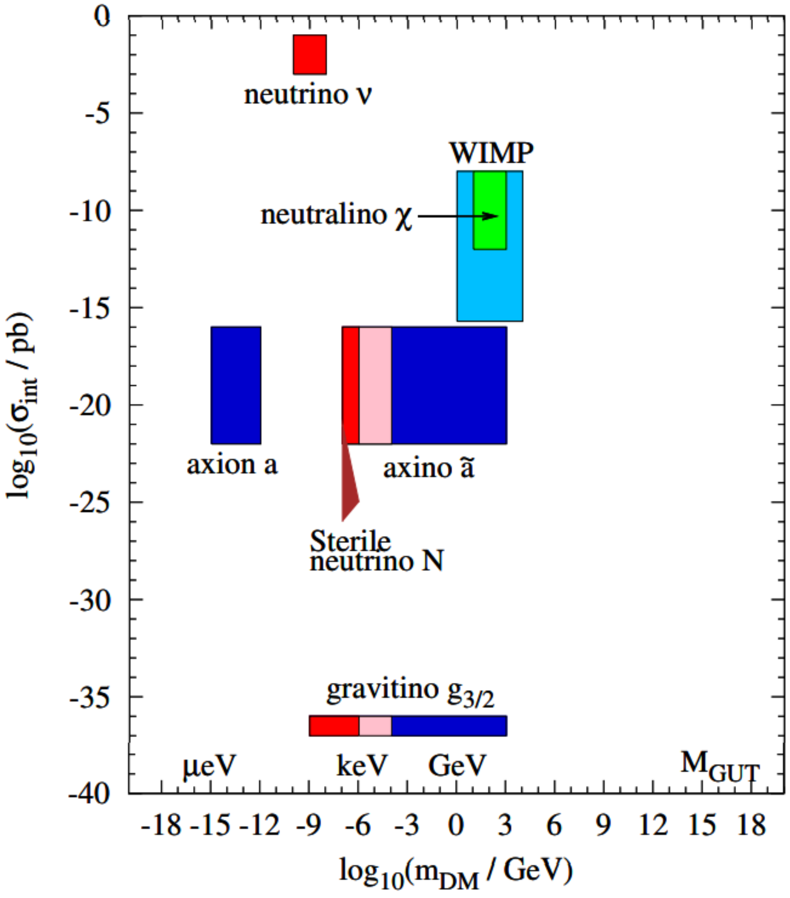

Figure 1.8: Plot indicating several well-motivated dark matter particle models, shown as log of cross section as a function of log of mass. Hot dark matter is in red, warm dark matter is in pink, and cold dark matter is in blue. Of particular note is the range of cross sections and masses, which spans dozens of orders of magnitude. Diagram reprinted with permission from [33].

It is possible that the effect of dark matter could be due to physical laws that work differently at very large length scales than those we are used to dealing with on Earth, as explained by theories such as modified Newtonian gravity (MoND), tensor-vector-scalar

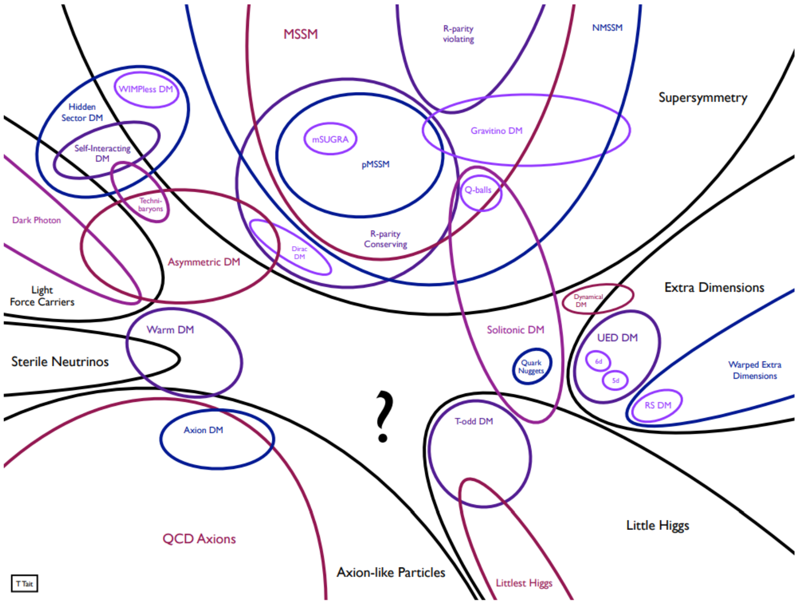

Figure 1.9: Plot indicating many dark matter particle models and how they relate one to another, which shows the wide range of theories and the types of models they predict that could be dark matter candidates. Diagram reprinted with permission from [34].

gravity (TeVeS), and entropic gravity. It is also possible that dark matter could be due to macroscopic baryonic, or possibly non-baryonic, objects such as primordial black holes, massive compact halo objects (MaCHOs), and Macroscopic dark matter (Macros). However, the observations presented in the previous section, especially of the anisotropies of the CMB, combined with strong exclusion limits from microlensing studies [35, 36, 37, 38], indicate that as-yet undiscovered nonbaryonic particles that rarely interact with normal matter are the most likely explanation.

This argument can be further elaborated by including the effect of dark energy, an energy density that drives the expansion of the Universe. Understanding this phenomenon has become the focus of many astrophysical efforts ever since observations of Type Ia supernovae indicated that the expansion of the Universe is accelerating [39]. This information, combined with measurements from BAOs and the CMB, leads to the contours in density parameter space shown in Fig. 1.10. All three contours meet on the line for a spatially flat universe, which has important repercussions for how the Universe might end in the far future.

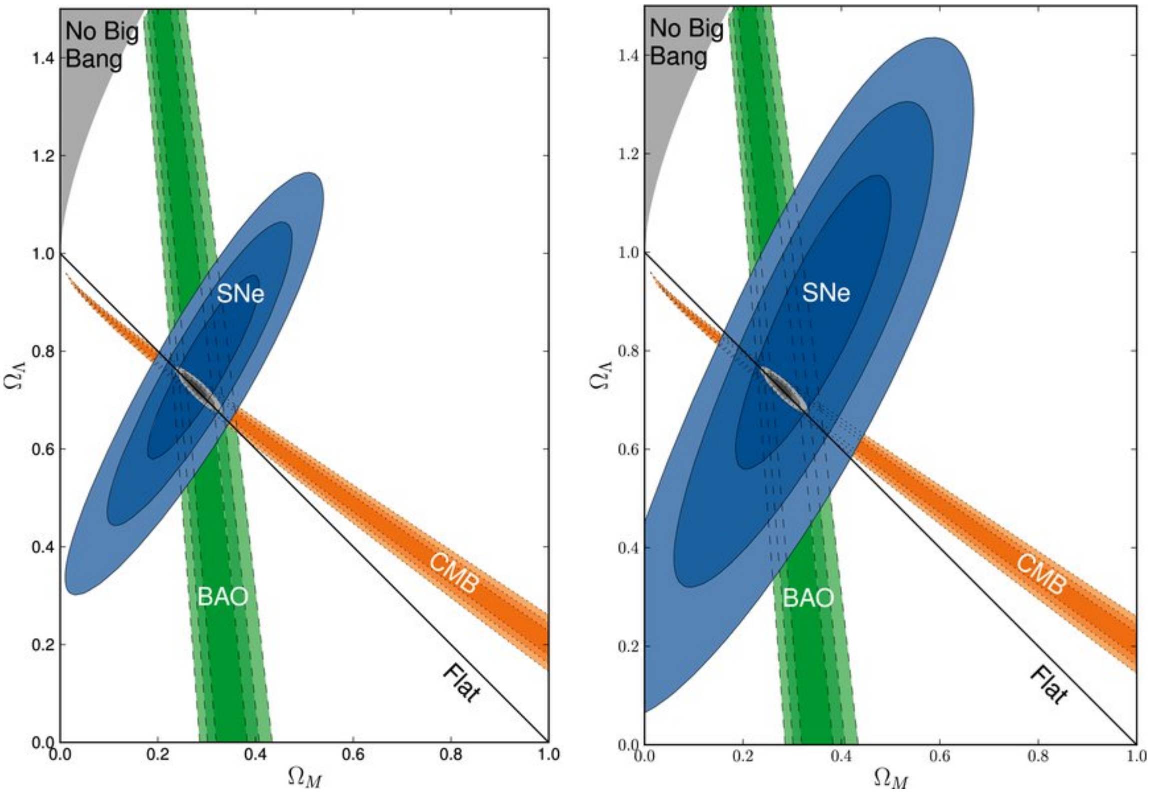

Figure 1.10: Plots showing best-fit contours for measurements of the dark energy density parameter, Ω_Λ, as a function of the mass energy density parameter, Ω_M. Regions of the same color represent, from inner to outer, 1-σ, 2-σ, and 3-σ confidence regions. Blue regions show supernova (SNe) measurements, orange regions show cosmic microwave background (CMB) measurements, and green regions show baryon acoustic oscillation (BAO) measurements. The black line shows what density parameters to expect for a flat universe, and the gray region is excluded since it can only occur if there is no Big Bang. The left plot is without systematic error bars included, and the rightmost plot includes them. © AAS reproduced with permission. Figure reprinted with permission from [40].

Despite all of this major progress in recent years, there still remains the problem of which particles actually constitute dark matter. What Fig. 1.10 does not show is that $\sim$85% of the Universe's matter is nonbaryonic, as per measurements by the Planck collaboration [1]. Additionally, the primordial elemental abundances, especially the ratio of deuterium to protonic hydrogen, can be used to calculate the range of possible energy density parameters for baryonic matter if one assumes that the lithium discrepancy is due to measurement systematics [41, 42]. This is because the deuterium created during Big Bang nucleosynthesis can only be used up in stars [43], and, as shown in Fig. 1.11, the amount of deuterium left over from nucleosynthesis strongly depends on the nucleon density during that epoch [42, 44]. Lower nucleon densities correspond to more of the deuterium not combining to form He-4 [44], hence the deuterium abundance. According to Ref. [42], performing the calculation yields $0.021 \leq \Omega_b h^2 \leq 0.024$ for the baryonic density parameter, which is much lower than the $\sim$0.3 for the total mass density parameter Ω_M. Consequently, a large fraction of matter in the Universe must be non-nucleonic.

Following this reasoning, dark matter models can be roughly divided based on their temperature at freeze-out into three categories: hot dark matter (HDM), warm dark matter (WDM), and cold dark matter (CDM). Alternatively, the free-streaming-length (FSL) for each model type can be related to the size of proto-galaxies since the temperature of the dark matter particles corresponds to how far they travel in the Universe before interacting with something. Thus, HDM corresponds to dark matter whose FSL is much larger than proto-galaxies, WDM corresponds to an FSL comparable to the size of proto-galaxies, and CDM to an FSL much smaller than proto-galaxies. CMB observations, structure formation, and simulations have excluded HDM as a possible contender, which also excludes all known particles as candidates for dark matter [17].

Nonetheless, these arguments do not clearly indicate what kind of particle the dark matter could be. Knowing this fact could tell scientists much more about the evolution of the Universe and how dark matter could contribute to what we observe in it today. Fig. 1.8

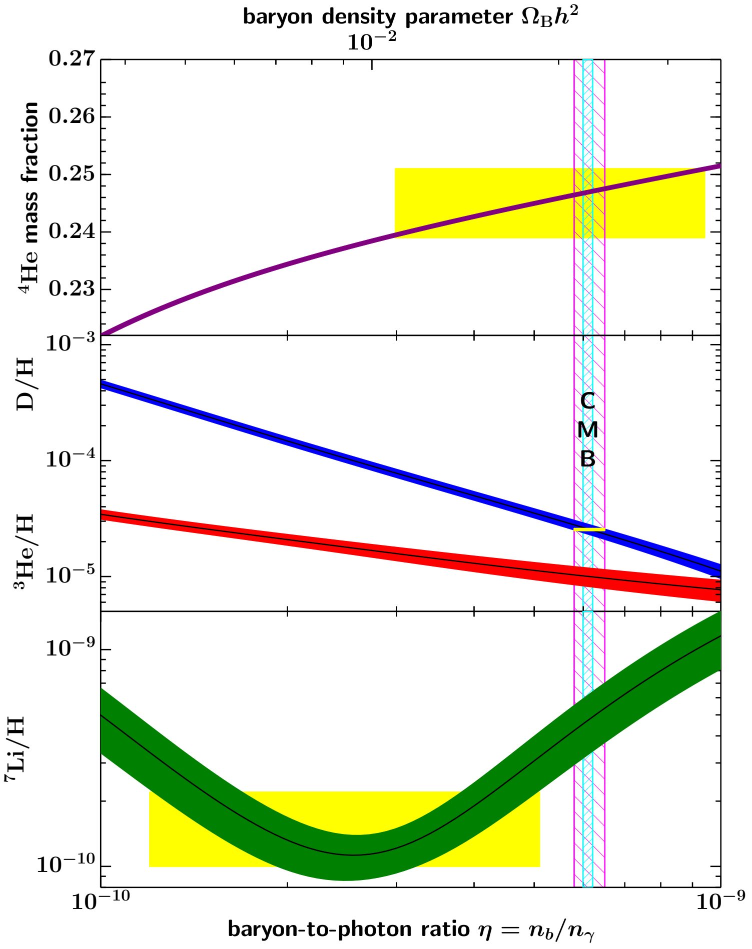

Figure 1.11: Plot showing the primordial elemental abundances as a function of baryon-to-photon ratio. The colored bands show elemental abundances based on the standard model of Big Bang nucleosynthesis. The yellow bands are the observed elemental abundances, and the wide magenta vertical band shows the deuterium to ^{4}He concordance range. The blue vertical band is the cosmic baryon density obtained from CMB observations. All bands are at the 95% confidence level limit. Figure reprinted with permission from [42].

shows the masses and cross sections of several well-motivated particle models and how they relate to the three categories described; HDM is in red, WDM is in pink, and CDM is in blue. As shown in Fig. 1.9, there are many other interrelated possible dark matter particle models. Experiments can attempt to exclude dark matter models based on their cross sections and masses to understand more clearly which models can and cannot be good candidates. This is a challenging task given the large number of models in Fig. 1.9 and the low expected cross sections in Fig. 1.8.

Additionally, many of the models in Fig. 1.9 do not correspond to the old Weakly Interacting Massive Particle (WIMP) paradigm. In this model, one expects dark matter, if it interacts with baryonic matter at all, to interact via the weak nuclear force, which means that it would interact much more readily with nucleons. By that paradigm, any experiment looking for WIMP or WIMP-like dark matter would need to exclude for electron-recoil particle interaction backgrounds. On the other hand, as per Ref. [45], models such as WIMPless dark matter [46], "MeV" dark matter [47, 48, 49, 50, 51, 52], asymmetric dark matter [53, 54, 55, 56], bosonic super-WIMP dark matter [57], axino dark matter [58, 59, 60], gravitino dark matter [61], and sterile neutrino dark matter [62] are expected to deposit much higher energies when interacting with electrons, which means, in that case, radioactive and nuclear-interaction processes become backgrounds.

Axions are also dark matter candidates that do not follow the WIMP paradigm, and it arises as a natural solution to the strong charge-parity (CP) problem [63, 64]. Despite the fact that the SuperCDMS experiment is not sensitive to the classic axion particle [65], certain string theories do give rise to axion-like particles (ALPs) [66, 67]. These particles would couple to standard model photons [67, 68] and to electrons [69]. By treating electron recoil events rather than nuclear recoil events as the signal, the SuperCDMS experiment is sensitve to ALPs and particles with similar couplings such as dark photons [65].

Thus, there are many types of candidate particles that could make up dark matter. Different dark matter models call for different types of dark matter paradigms. Nonetheless, the process of elimination is being pursued on multiple fronts to narrow down the possibilities, as further explained in § 1.4.

1.3 Dark Matter Rate Calculations

A standard scattering experiment might accelerate particles to collide them with a target and measure the energy of the scattered incoming particles with a detector. Perhaps this single detector may actually be composed of a dome of many smaller detectors so both the particle recoil energy and recoil angle can be determined. However, in the case of dark matter or similar low-cross-section particles, it is highly unlikely that the particle of interest will interact with both the experimental substrate and the detector since the chance of the particle interacting with the substrate is extremely small to begin with. For this reason, the differential rate for low-scattering-cross-section particles, such as dark matter or neutrinos, is actually calculated for a stand-alone detector. In other words, looking for dark matter or neutrinos is like combining the particle detector and substrate from the thought experiment earlier into a single detector. In this subsection, I derive the expected differential rate for dark matter assuming a perfect detector, and I assume that the dark matter particle interacts with normal matter as though a Weakly Interacting Massive Particle (WIMP) might. I treat the corrections resulting from defect creation in later sections.

1.3.1 Dark Matter Scattering From Nucleus Energy Transfer

Consider two particles, m_1 and m_2 that collide elastically. If particle m_2 is initially at rest, and particle m_1 initially moves with speed v, the particles move at speeds v_1' and v_2' and are deflected at angles θ_1 and θ_2 in the lab frame. In the center-of-mass frame, the deflection is given by θ. Hence, the final speeds and deflections of the two particles are given by

$$v_1' = \frac{\sqrt{m_1^2 + m_2^2 + 2m_1 m_2 \cos\theta}}{m_1 + m_2}, \tag{1.1}$$

$$\tan\theta_1 = \frac{m_2 \sin\theta}{m_1 + m_2 \cos\theta}, \tag{1.2}$$

$$\theta_2 = \frac{\pi - \theta}{2}. \tag{1.3}$$

and

$$\begin{aligned} v_2' &= \frac{2m_1 v}{m_1 + m_2} \sin\frac{\theta}{2} \\ &= \pm\frac{2m_1 v}{m_1 m_2}\sqrt{\frac{1-\cos\theta}{2}}. \end{aligned} \tag{1.4}$$

Since a detector for a dark matter search experiment usually measures the energy of the recoiling nucleus in one way or another, one desires the energy as a function of the initial kinetic energy of the dark matter particle. Thus, using Eq. 1.4 to find the recoil energy E_r given the initial dark matter particle energy E_i yields

$$E_r = E_i r \frac{1-\cos\theta}{2} \tag{1.5}$$

where

$$r \equiv \frac{4m_\chi m_A}{(m_\chi + m_A)^2} = \frac{4\mu}{m_\chi + m_A}, \tag{1.6}$$

$$\mu = \frac{m_\chi m_A}{m_\chi + m_A}, \tag{1.7}$$

and

$$E_i = \frac{1}{2} m_\chi v^2, \tag{1.8}$$

which agrees with the dark matter literature [70]. In Eq. 1.5, I made the substitutions $m_\chi \equiv m_1$ and $m_A \equiv m_2$ to more closely resemble the result in Ref. [70].

1.3.2 Full Lab Velocity Calculation

To find the energy of the recoiling nucleus using the above equations, one first needs to know what energy the incoming dark matter particles are expected to have. One assumes that there is a velocity distribution of dark matter particles in our galaxy that is close to a

Maxwell-Boltzmann distribution and that our Solar System moves through this distribution as it revolves around the center of the galaxy. We are interested in the motion of the lab relative to the dark matter distribution, so there are several higher-order terms to take into account. Following the calculations in the appendix of Ref. [71], if one assumes that the detector is oriented in the same coordinate system as the lab, the three components of the lab velocity $\boldsymbol{v}_{lab}$ are given by

$$\begin{aligned} v_{\text{lab},x} &= [-\cos(\text{LST})A(t) + \sin(\text{LST})B(t)]\sin(\lambda_{\text{lab}}) + C(t)\cos(\lambda_{\text{lab}}), \\ v_{\text{lab},y} &= \sin(\text{LST})A(t) + \cos(\text{LST})B(t) - 0.465\sin(\lambda_{\text{lab}}), \\ v_{\text{lab},z} &= [\cos(\text{LST})A(t) - \sin(\text{LST})B(t)]\cos(\lambda_{\text{lab}}) + C(t)\sin(\lambda_{\text{lab}}), \end{aligned} \tag{1.9}$$

so that

$$\begin{aligned} \hat{\boldsymbol{q}} \cdot \boldsymbol{v}_{\text{lab}} = {} & [-\cos(\text{LST})A(t) + \sin(\text{LST})B(t)]\sin(\lambda_{\text{lab}}) + C(t)\cos(\lambda_{\text{lab}}) \\ & + \sin(\text{LST})A(t) + \cos(\text{LST})B(t) - 0.465\sin(\lambda_{\text{lab}}) \\ & + [\cos(\text{LST})A(t) - \sin(\text{LST})B(t)]\cos(\lambda_{\text{lab}}) + C(t)\sin(\lambda_{\text{lab}}). \end{aligned} \tag{1.10}$$

The terms that make up $\hat{\boldsymbol{q}} \cdot \boldsymbol{v}_{\text{lab}}$ are given by

$$\begin{aligned} A(t) &= 0.4927\, v_{\text{GalRot}} - 1.066\text{km/s} + v_{\oplus}(\lambda(t))\mathscr{A}(t), \\ B(t) &= 0.4503\, v_{\text{GalRot}} + 16.56\text{km/s} - v_{\oplus}(\lambda(t))\mathscr{B}(t), \\ C(t) &= 0.7445\, v_{\text{GalRot}} + 7.077\text{km/s} + v_{\oplus}(\lambda(t))\mathscr{C}(t). \end{aligned} \tag{1.11}$$

where

$$\begin{aligned}
\mathscr{A}(t) &= -0.06699\cos\beta_x \sin(\lambda(t)-\lambda_x) + 0.4927\cos\beta_y \sin(\lambda(t)-\lambda_y) \\
&\quad - 0.8676\cos\beta_z \sin(\lambda(t)-\lambda_z), \\
\mathscr{B}(t) &= -0.8728\cos\beta_x \sin(\lambda(t)-\lambda_x) + 0.4503\cos\beta_y \sin(\lambda(t)-\lambda_y) \\
&\quad - 0.1883\cos\beta_z \sin(\lambda(t)-\lambda_z), \\
\mathscr{C}(t) &= -0.4835\cos\beta_x \sin(\lambda(t)-\lambda_x) + 0.7446\cos\beta_y \sin(\lambda(t)-\lambda_y) \\
&\quad + 0.4602\cos\beta_z \sin(\lambda(t)-\lambda_z).
\end{aligned} \tag{1.12}$$

In the final result Eq. 1.10, λ_{lab} is the latitude of the lab on the surface of the Earth. The LST, or local sidereal time, is given by

$$\text{LST} = 101.0308 + 36000.770\,T_0 + 15.04107\ \text{UT} + l_{\text{lab}} \tag{1.13}$$

where

$$T_0 = \frac{\text{MJD} - 55197.5}{36525.0}, \tag{1.14}$$

MJD is the modified Julian date, UT is the universal time in hours, and l_{lab} is the longitude of the lab on the surface of the Earth. The Sun's ecliptic longitude $\lambda(t)$ is given by

$$\lambda(t) = L + (1.915^\circ - 0.0048^\circ\,T_0)\sin g + 0.020^\circ \sin 2g \tag{1.15}$$

where

$$L = 281.0298^\circ + 36000.77^\circ\,T_0 + 0.04107\ \text{UT}. \tag{1.16}$$

The term $v_\oplus(\lambda(t))$ is given by

$$v_\oplus(\lambda(t)) = v_\oplus[1 - e\sin(\lambda(t) - \lambda_0)] \tag{1.17}$$

where $e = 0.016722$, and $\lambda_0 = 14°$. The remaining constants, which represent the ecliptic latitudes and longitudes, respectively, are given by

$$\begin{aligned} \beta_i &= (-5.5303°, 59.575°, 29.812°) \\ \lambda_i &= (266.141°, -13.3485°, 179.3212°). \end{aligned} \tag{1.18}$$

1.3.3 Dark Matter Differential Rate

Calculating the total signal rate to see the modulation and the expected recoil energy spectrum to find the effect of the energy loss requires performing integrals over the dark matter differential rate per unit steradian per unit recoil energy for a given dark matter mass and detector material. Ref. [72] gives this differential rate as

$$\frac{\partial^2 R}{\partial E_r \partial \Omega_r} = \frac{\rho_0 \sigma_{\chi-n} A^2}{4\pi m_\chi \mu_{\chi n}^2} \times F^2(E_r) \hat{f}_{\text{lab}}(v_{\text{min}}, \hat{\boldsymbol{q}}_{\boldsymbol{r}}; t) \tag{1.19}$$

where m_χ is the WIMP mass, $\mu_{\chi n}$ is the WIMP-nucleus reduced mass, $\rho_0 = 0.3$ GeV cm^{-3} is the local dark matter density, A is the mass number of the nucleus, $\sigma_{\chi-n}$ is a particular WIMP-nucleon cross section, $v_{\text{min}} = \sqrt{2m_N E_r}/2\mu_{\chi n}$ is the minimum WIMP speed required to produce a nuclear recoil of energy E_r for a given nuclear mass m_N, and $F^2(E_r)$ is the Helm nuclear form factor [73]. According to Ref. [74], with a slight change in variable conventions, this form factor is given by

$$F^2(p) = \left(\frac{3j_1(pR_1)}{pR_1}\right)^2 e^{-E_r^2 s^2} \tag{1.20}$$

where

$$p = \sqrt{2mE_r}. \tag{1.21}$$

The function $j_1(x)$ is the spherical Bessel function of the first kind given by

$$j_1(x) = \frac{\sin x}{x^2} - \frac{\cos x}{x} \tag{1.22}$$

and the parameters in the form factor are given by Ref. [73] as

$$R_1 = \sqrt{c^2 + \frac{7}{3}\pi^2 a^2 - 5s^2},\ c \simeq 1.23A^{1/3} - 0.60\ \text{fm} \tag{1.23}$$

$s \simeq 0.9$ fm, and $a \simeq 0.52$ fm.

The Radon transform of the WIMP velocity distribution $f_{\text{lab}}(\boldsymbol{v})$ is given by Ref. [72] as

$$\hat{f}_{\text{lab}}(v_{\text{min}}, \hat{\boldsymbol{q}}; t) = \frac{1}{N_{\text{esc}}\sqrt{2\pi\sigma_\nu^2}} \left\{ \exp\left[-\frac{|v_{\text{min}} + \hat{\boldsymbol{q}} \cdot \boldsymbol{v}_{\text{lab}}|^2}{2\sigma_\nu^2} \right] - \exp\left[-\frac{v_{\text{esc}}^2}{2\sigma_\nu^2} \right] \right\} \tag{1.24}$$

where $\hat{\boldsymbol{q}}$ is the recoil direction in detector coordinates given by

$$\hat{\boldsymbol{q}} = \sin\theta\cos\phi\hat{\boldsymbol{x}} + \sin\theta\sin\phi\hat{\boldsymbol{\phi}} + \cos\theta\hat{\boldsymbol{z}}, \tag{1.25}$$

$\boldsymbol{v}_{\text{lab}}$ is the velocity of the laboratory relative to a stationary observer, v_{esc} is the circular escape velocity at the Solar System's distance from the Milky Way's center, $\sigma_v = v_0/\sqrt{2}$ is the dark matter velocity dispersion, and N_{esc} is a normalization factor given by

$$N_{\text{esc}} = \text{erf}\left[\frac{v_{\text{esc}}}{\sqrt{2}\sigma_\nu} \right] - \sqrt{\frac{2}{\pi}} \frac{v_{\text{esc}}}{\sigma_\nu} \exp\left[-\frac{v_{\text{esc}}^2}{2\sigma_\nu^2} \right]. \tag{1.26}$$

I use $v_0 = 220$ km s^{-1} for the circular speed and $v_{\text{esc}} = 544$ km s^{-1} [72] and Appendix B of Ref. [71] to find the total lab velocity using the galactic rotation, solar motion, Earth's revolution, and Earth's rotation contributions, as discussed in § 1.3.2. The detector is situated at SNOLAB for these calculations, since that is where the SuperCDMS experiment is located $(46.4719° N, 81.1868° W)$, and the differential rate is calculated on September 6, 2015 to coincide with Ref. [72]. Below I describe in more detail how one arrives at the expected differential rate given dark matter particles scattering off nuclei, following the derivations in Ref. [75] and Ref. [76].

1.3.4 Dark Matter Differential Rate Derivation

I start off with a few simple results that will be useful later on. Imagine that there is a particle of mass m_1 with speed v recoiling off a mass m_2. Particle 1 deflects at angle θ_1 with respect to its initial trajectory, and particle 2 deflects at angle θ_2. The particles have velocities $\boldsymbol{v_1'}$ and $\boldsymbol{v_2'}$, respectively, after the collision, following the convention in § 1.3.1.

Equation 1.4 can be used to find the maximum possible recoil momentum, and hence the maximum possible recoil energy, via

$$\begin{aligned} p_2 = m_2 v_2' &= \frac{2 m_1 m_2 v}{m_1 + m_2} \sin \frac{\theta}{2} \\ &= 2\mu v \sin \frac{\theta}{2} \end{aligned} \tag{1.27}$$

where μ is the reduced mass of the particle system and θ is the deflection in the rest frame. Noting that the maximum value of $\sin \frac{\theta}{2}$ is 1 yields

$$p_{\text{max}} = 2\mu v. \tag{1.28}$$

Additionally, combining 1.27 with 1.3 gives

$$\begin{aligned} p_2 &= 2\mu v \sin \frac{\pi - 2\theta_2}{2} \\ &= 2\mu v \sin \left(\frac{\pi}{2} - \theta_2 \right) \\ &= 2\mu v \cos \theta_2, \end{aligned} \tag{1.29}$$

or

$$p = 2\mu v \cos\theta \tag{1.30}$$

where I have made the substitution $p_2 \rightarrow p$ and $\theta_2 \rightarrow \theta$, which I use for the rest of the derivation to be more consistent with Ref. [75].

As per Ref. [75], the most straightforward way to derive a differential rate that takes into account directionality is to calculate the differential cross section so that it takes directionality into account. This result can then be combined with the portion that contains the dark matter distribution. First, one notes that the differential cross section per unit momentum squared can be written as

$$\frac{\partial\sigma}{\partial p^2} = \frac{\sigma_0}{p_{\text{max}}^2} F^2\left(p\right) \tag{1.31}$$

where $F^2\left(p\right)$ is the nuclear form factor, which is given by Eq. 1.20 for this work. To find the differential cross section per unit squared momentum and steradian, one uses the fact that, by symmetry,

$$d\Omega_r = 2\pi d\left(\cos\theta\right). \tag{1.32}$$

Additionally, one needs a delta function of the form

$$\delta\left(\cos\theta - \frac{p}{2\mu v}\right), \tag{1.33}$$

which is based on Eq. 1.30, to preserve the directionality when integrating over all solid angles. Thus, the differential cross section per unit squared momentum per unit recoil solid angle is given by

$$\begin{aligned}\frac{\partial^2\sigma}{\partial p^2\partial\Omega_r} &= \frac{\partial\sigma}{\partial p^2}\frac{1}{2\pi}\delta\left(\cos\theta-\frac{p}{2\mu v}\right)\\ &= \frac{\sigma_0}{p^2_{\text{max}}}\frac{F^2\left(p\right)}{2\pi}\delta\left(\cos\theta-\frac{p}{2\mu v}\right)\\ &= \frac{\sigma_0}{4\mu^2v^2}\frac{F^2\left(p\right)}{2\pi}\delta\left(\cos\theta-\frac{p}{2\mu v}\right)\\ &= \frac{\sigma_0}{8\pi\mu^2v^2}F^2\left(p\right)\delta\left(\cos\theta-\frac{p}{2\mu v}\right),\end{aligned} \tag{1.34}$$

or

$$\frac{\partial^2\sigma}{\partial p^2\partial\Omega_r} = \frac{\sigma_0}{8\pi\mu^2 v}F^2\left(p\right)\delta\left(v\cos\theta-\frac{p}{2\mu}\right), \tag{1.35}$$

which agrees with Ref. [75]. Since we know that $E_r = \dfrac{p^2}{2m_N}$, where m_N is the mass of the interacting nucleus, changing coordinates yields

$$\frac{\partial^2\sigma}{\partial E_r\partial\Omega_r} = \frac{m_N\sigma_0}{4\pi\mu^2 v}F^2\left(p\right)\delta\left(v\cos\theta-\frac{p}{2\mu}\right), \tag{1.36}$$

According to Eq. 7 in Ref. [72], the differential rate is found by multiplying the differential cross section by the differential flux and integrating over all input energies. In this case, the integral is over all velocities, and the differential flux element in a differential phase space volume element $\mathrm{d}v^3$ is given by

$$\mathrm{d}\Phi = nvf\left(\boldsymbol{v}\right)\mathrm{d}v^3 \tag{1.37}$$

according to Ref. [75]. $n = \dfrac{\rho}{m_\chi}$ is the local number density of dark matter particles, expressed as the ratio of the local dark matter mass density ρ and the mass of a dark matter particle m_χ. $f\left(\boldsymbol{v}\right)$ is the local dark matter velocity distribution normalized to one. Thus, multiplying the differential cross section given by Eq. 1.36 with the differential flux given by Eq. 1.37, and scaling this result by the total number of particles in the detector N divided by the detector mass $m_N N$ yields

$$\begin{aligned}\frac{\partial^2 R}{\partial E_r \partial \Omega_r} &= \frac{N}{m_N N} \int \frac{\partial^2 \sigma}{\partial E_r \partial \Omega_r} \mathrm{d}\Phi \\ &= \frac{1}{m_N} \int \frac{m_N \sigma_0}{4\pi\mu^2 v} F^2(p)\, \delta\left(v \cos\theta - \frac{p}{2\mu}\right) n v f(\boldsymbol{v})\, \mathrm{d}v^3 \\ &= \frac{n\sigma_0 F^2(p)}{4\pi\mu^2} \int \delta\left(v\cos\theta - \frac{p}{2\mu}\right) f(\boldsymbol{v})\, \mathrm{d}v^3.\end{aligned} \tag{1.38}$$

The differential rate Eq. 1.38 can be rewritten as

$$\frac{\partial^2 R}{\partial E_r \partial \Omega_r} = \frac{n\sigma_0 F^2(p)}{4\pi\mu^2} \widehat{f}\left(v_{\text{min}}, \widehat{\boldsymbol{q}}_{\boldsymbol{r}}\right) \tag{1.39}$$

where

$$v_{\text{min}} = \frac{p}{2\mu} = \sqrt{\frac{m_N E_r}{2\mu^2}} \tag{1.40}$$

is the minimum velocity required to deposit an energy E_r and $\widehat{f}$ is the Radon transform

$$\widehat{f}(w, \widehat{\boldsymbol{q}}) = \int \delta\left(\boldsymbol{v} \cdot \widehat{\boldsymbol{q}} - w\right) f(\boldsymbol{v})\, \mathrm{d}^3 v. \tag{1.41}$$

When the velocity distribution is isotropic, as is expected for dark matter at a particular location relative to the center of the Milky Way galaxy, $f(\boldsymbol{v}) = f(v)$. This implies that the recoil spectrum is also isotropic, or $\widehat{f}(w, \widehat{\boldsymbol{q}}_{\boldsymbol{r}}) = \widehat{f}(w)$. Since recoil directions can only cover one half of the unit sphere, Ref. [75] gives the Radon transform in this case as

$$\widehat{f}(w) = 2\pi \int_w^\infty f(v)\, v\, \mathrm{d}v. \tag{1.42}$$

Thus, a Maxwellian velocity distribution

$$f\left(v\right)=\frac{1}{\left(2\pi\sigma_v^2\right)^{3/2}}\exp\left[-\frac{v^2}{2\sigma_v^2}\right] \tag{1.43}$$

has Radon transform

$$\widehat{f}\left(w\right)=\frac{1}{\left(2\pi\sigma_v^2\right)^{1/2}}\exp\left[-\frac{w^2}{2\sigma_v^2}\right]. \tag{1.44}$$

Using the result Eq. 1.54 in § 1.3.4.1 in conjunction with Eq. 1.44 yields the Radon transform of the dark matter distribution shifted by the lab velocity with respect to the dark matter halo, whose full form for the calculations in this chapter are presented in § 1.3.2. Thus, the Radon transform of the shifted velocity distribution is

$$\widehat{f}\left(w,\widehat{\boldsymbol{q}}_{\boldsymbol{r}}\right)=\frac{1}{\left(2\pi\sigma_v^2\right)^{1/2}}\exp\left[-\frac{\left(w+\widehat{\boldsymbol{q}}_{\boldsymbol{r}}\cdot\boldsymbol{v}_{\text{lab}}\right)^2}{2\sigma_v^2}\right]. \tag{1.45}$$

The change in sign in the dot product in Eq. 1.45 comes from the fact that, the way one normally defines the recoil direction and lab velocity, the recoil direction points in the opposite direction from the lab velocity. In other words, one shifts the dark matter velocity distribution by $-\boldsymbol{v}_{\text{lab}}$ as opposed to by $\boldsymbol{v}_{\text{lab}}$.

Since the system of the Milky Way galaxy and dark matter distribution is gravitationally bound, one expects particles that have velocity higher than the escape velocity to escape from the overall distribution. Thus, many dark matter models use a velocity distribution that is truncated at the escape velocity. For a Maxwellian velocity distribution,

$$f\left(v\right)=\begin{cases}\dfrac{1}{N_{\text{esc}}\left(2\pi\sigma_v^2\right)^{3/2}}\exp\left[-\dfrac{v^2}{2\sigma_v^2}\right], & v<v_{\text{esc}}\\ 0, & v\geq v_{\text{esc}}\end{cases} \tag{1.46}$$

where

$$N_{\text{esc}} = \text{erf}\left[\frac{v_{\text{esc}}}{\sqrt{2}\sigma_v}\right] - \sqrt{\frac{2}{\pi}}\frac{v_{\text{esc}}}{\sigma_v}\exp\left[\frac{v_{\text{esc}}^2}{2\sigma_v^2}\right] \tag{1.47}$$

to make sure that the velocity distribution is normalized to one. Thus, integrating to find the Radon transform using Eq. 1.42 yields

$$\widehat{f}\left(w\right) = \frac{1}{N_{\text{esc}}\left(2\pi\sigma_v^2\right)^{1/2}}\left\{\exp\left[-\frac{w^2}{2\sigma_v^2}\right] - \exp\left[-\frac{v_{\text{esc}}^2}{2\sigma_v^2}\right]\right\}. \tag{1.48}$$

To take into account the velocity shift due to the motion of the laboratory, one combines Eq. 1.48 with Eq. 1.54 to yield, with an appropriate change of variables and explicit time-dependence,

$$\widehat{f}_{\text{lab}}(v_{\text{min}}, \hat{\boldsymbol{q}}; t) = \frac{1}{N_{\text{esc}}\sqrt{2\pi\sigma_\nu^2}}\left\{\exp\left[-\frac{\left|v_{\text{min}} + \hat{\boldsymbol{q}}\cdot\boldsymbol{v}_{\text{lab}}\right|^2}{2\sigma_\nu^2}\right] - \exp\left[-\frac{v_{\text{esc}}^2}{2\sigma_\nu^2}\right]\right\} \tag{1.49}$$

as expected. Plugging Eq. 1.49 into Eq. 1.39 yields the expected differential rate assuming isotropic dark matter with a truncated Maxwellian velocity distribution and a detector on the Earth's surface.

1.3.4.1 Radon Transform Change of Coordinates

Below, I show how to find the Radon transform given a change of coordinates. This derivation follows, and expands slightly on, the derivation in Appendix B of Ref. [75].

Given the Radon transform Eq. 1.41, one desires the Radon transform after a change of coordinates $\boldsymbol{v} \mapsto \boldsymbol{v'} = A\boldsymbol{v} + \boldsymbol{b}$ where A is an invertible matrix, and $\boldsymbol{v}$ and $\boldsymbol{b}$ are vectors. One knows that the phase space volume element scaled by the velocity distribution is a constant irrespective of the coordinate system, which can be rewritten as

$$f'\left(\boldsymbol{v'}\right)\mathrm{d}^3\boldsymbol{v'} = f\left(\boldsymbol{v}\right)\mathrm{d}^3\boldsymbol{v}. \tag{1.50}$$

This result implies that

$$\begin{aligned}
f'\left(\boldsymbol{v'}\right) &= f\left(\boldsymbol{v}\right)\frac{\mathrm{d}^3\boldsymbol{v'}}{\mathrm{d}^3\boldsymbol{v}} \\
&= f\left(\boldsymbol{v}\right)\left(\frac{\mathrm{d}^3\boldsymbol{v}}{\mathrm{d}^3\boldsymbol{v'}}\right)^{-1} \\
&= \frac{f\left(\boldsymbol{v}\right)}{\left|\det A\right|}.
\end{aligned} \tag{1.51}$$

Hence,

$$\begin{aligned}
\widehat{f'}\left(w', \widehat{\boldsymbol{q}}\right) &= \int \delta\left(\boldsymbol{v'}\cdot\widehat{\boldsymbol{q}}' - w'\right) f\left(\boldsymbol{v'}\right)\mathrm{d}^3v' \\
&= \int \delta\left(\left(A\boldsymbol{v}+\boldsymbol{b}\right)\cdot\widehat{\boldsymbol{q}}' - w'\right) f\left(\boldsymbol{v'}\right)\mathrm{d}^3v' \\
&= \int \delta\left(\left(A\boldsymbol{v}\right)\cdot\widehat{\boldsymbol{q}}' + \boldsymbol{b}\cdot\widehat{\boldsymbol{q}}' - w'\right) f\left(\boldsymbol{v'}\right)\mathrm{d}^3v' \\
&= \int \delta\left(\left(A\boldsymbol{v}\right)\cdot\widehat{\boldsymbol{q}}' + \boldsymbol{b}\cdot\widehat{\boldsymbol{q}}' - w'\right) \frac{f\left(\boldsymbol{v}\right)}{\left|\det A\right|}\mathrm{d}^3v' \\
&= \int \delta\left(\left(A\boldsymbol{v}\right)\cdot\widehat{\boldsymbol{q}}' + \boldsymbol{b}\cdot\widehat{\boldsymbol{q}}' - w'\right) f\left(\boldsymbol{v}\right)\mathrm{d}^3v \\
&= \int \delta\left(\boldsymbol{v}\cdot\left(A^T\widehat{\boldsymbol{q}}'\right) - \left(w' - \boldsymbol{b}\cdot\widehat{\boldsymbol{q}}'\right)\right) f\left(\boldsymbol{v}\right)\mathrm{d}^3v,
\end{aligned} \tag{1.52}$$

which implies

$$\widehat{f'}\left(w', \widehat{\boldsymbol{q}}\right) = \widehat{f}\left(w' - \boldsymbol{b}\cdot\widehat{\boldsymbol{q}}', A^T\widehat{\boldsymbol{q}}'\right). \tag{1.53}$$

When there is only a translation of coordinates, as is the case for the dark matter velocity distribution when the detector is on the Earth's surface, Eq. 1.53 simplifies to

$$\widehat{f'}\left(w', \widehat{\boldsymbol{q}}\right) = \widehat{f}\left(w' - \boldsymbol{b}\cdot\widehat{\boldsymbol{q}}', \widehat{\boldsymbol{q}}'\right). \tag{1.54}$$

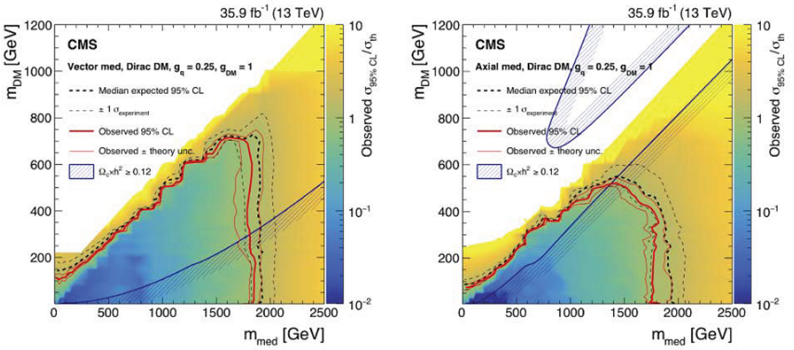

(**a**) CMS

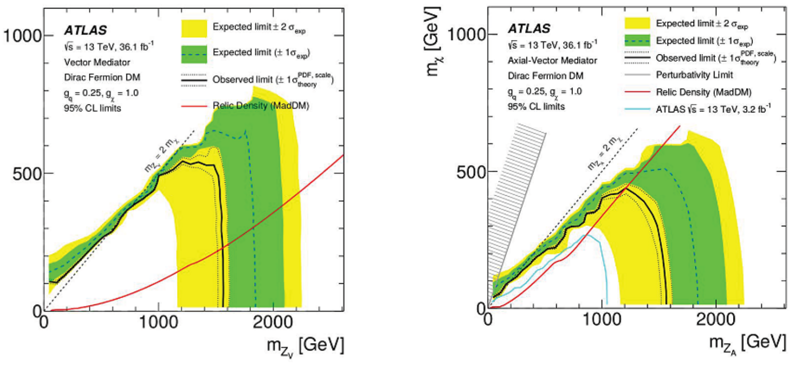

(**b**) ATLAS

Figure 1.12: Exclusion limits for the CMS and ATLAS experiments at the Large Hadron Collider for two possible dark matter production processes. The plots for the CMS experiment are at the top, and the plots for the ATLAS experiment are at the bottom. More plots similar to these can be found in Ref. [77]. Figure reprinted with permission from [77].

1.4 Detection Methods: Direct, Indirect, and Collider

1.4.1 Collider Searches

Given the large range of theoretical models that could explain dark matter, certain models must be excluded based on observational or experimental evidence so that researchers can come closer to understanding the true nature of dark matter. One way to do this is by smashing particles together at very high energies in particle accelerators and by carefully measuring the products. If there is a small fraction of events for which there is some unaccounted-for energy, then the processes that caused those events could also be responsible for dark matter. An example of limits set by the ATLAS (A Toroidal LHC ApparatuS) experiment and the CMS (Compact Muon Solenoid) experiment at the Large Hadron Collider (LHC) by two possible creation channels is shown in Fig. 1.12. More such limits can be found in [77].

1.4.2 Indirect Searches

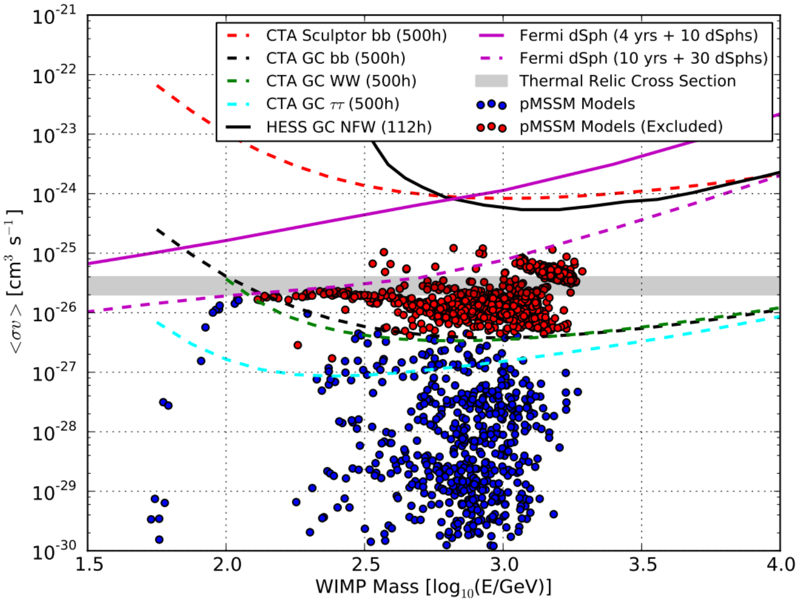

Figure 1.13: Exclusion limits for dark matter annihilation gamma ray searches as a funciton of WIMP mass. Solid curves show current limits, and dashed curves show future expected limits. Blue and red points show different model predictions. Models in red would be excluded with a 95% upper confidence limit by observing the Galactic Center for 500 hours using the Cherenkov Telescope Array (CTA). Figure reprinted with permission from [78].

Even if the LHC were to create events with an unmeasurable energy excess, there is no way to tell whether the particle(s) created could be responsible for dark matter or simply particles that are not accounted for in the Standard Model of Particle Physics. For this reason, one needs astrophysical evidence to put limits on possible dark matter models. One way to set those limits is by searching for the very rare interactions dark matter might have with itself or other particles. For example, if dark matter does sometimes interact with itself and annihilates with itself in the process, there should be a faint gamma ray background that is strongest towards the centers of gravitational potentials. In other words, the center of the Milky Way Galaxy and the centers of nearby satellite galaxies should weakly emit gamma rays that astrophysics experiments can measure. A compendium of limits set by such observations is shown in Fig. 1.13. Given more observations, the expected 95% confidence upper limits are also shown in addition to the models that those future results could exclude.

1.4.3 Direct Searches

A third approach, a specific example of which is the focus of this dissertation, is to directly measure the rare particle interactions between dark matter and normal matter, thereby limiting theoretical models based on the cross section for dark matter interacting with normal matter. A limit plot for several such direct-detection dark matter experiments is shown in Fig. 1.14. This plot shows which regions of dark matter parameter space have been excluded by which experiments, so it summarizes the status of the dark matter direct-detection field. These experiments detect the particle interactions in one or several high-mass particle detectors and limit the known particle backgrounds via special shielding, event differentiation techniques, or both. The experiments look for events that satisfy dark matter signal requirements and, based on the total exposure time, exclude the regions of parameter space above the curves in Fig. 1.14.

The yellow region in Fig. 1.14 represents a lower limit for standard direct-detection dark matter experiments and comes from the elastic neutrino scattering background present

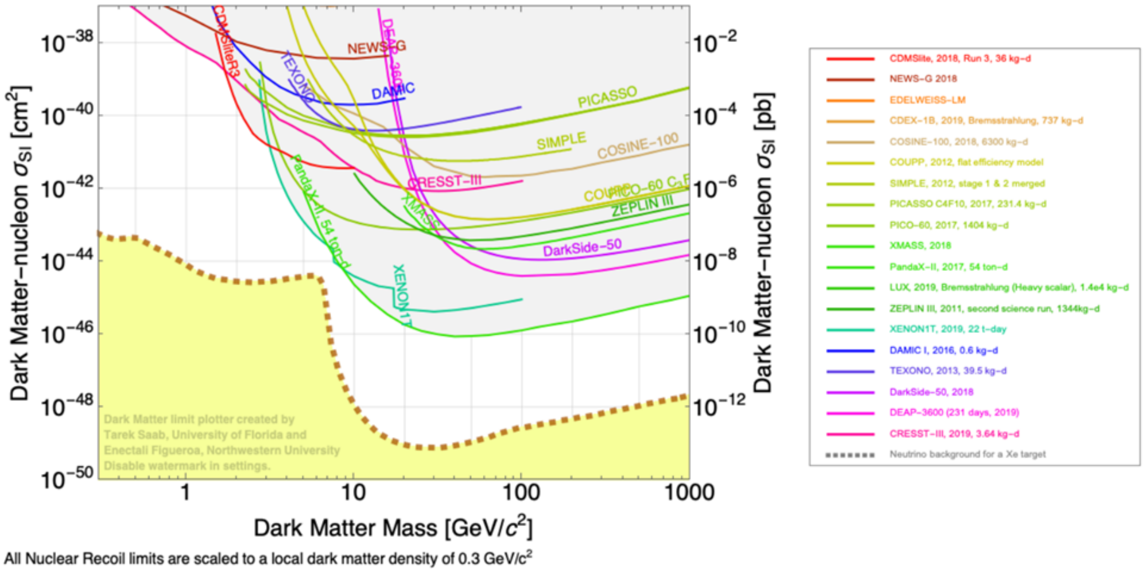

Figure 1.14: 90% confidence limit exclusion curves for several direct-detection dark matter experiments. All of the curves are for spin-independent interactions. The orange region represents the neutrino floor, the lowest possible cross-section region that can be probed by most direct-detection dark matter experiments. Plot reprinted with permission from [79].

for all such experiments. These neutrinos come predominantly from the Sun, Earth's atmosphere, and the diffuse supernova neutrino background (DSNB) [72]. The neutrino floor also provides a way to subdivide direct-detection dark matter search experiments into those more sensitive to dark matter below ∼10 GeV/c^2mass and those more sensitive to dark matter above it.

Assuming weak-force-like coupling to detector nuclei, experiments whose atoms have a large number of nucleons tend to be more useful for searching for high-mass dark matter particles because the differential dark matter rate scales with the mass number squared, as discussed later in this dissertation. For this reason, experiments such as Xenon1T and LZ try to maximize the detector exposure. On the other hand, experiments looking for low-mass dark matter tend to be limited more by the minimum energy threshold the detector can measure, which explains the large increase in the limit curves in Fig. 1.14 at low dark matter masses. Consequently, these experiments seek to reduce the detector energy threshold as much as possible. Since the SuperCDMS experiment falls into the latter category, I will focus most of my attention on low-mass dark matter types and searches thereof.

1.5 Why Low Mass

There are several reasons why dark matter experiments might look for dark matter at masses below $\sim$10 GeV/c^2 [80, 81, 82]. These include the fact that there has not been a conclusive dark matter signal measured yet in the supersymmetric WIMP parameter space, the fact that CRESST, CDMS II Si, CoGeNT, and DAMA may have measured a dark matter signal, and the fact that there are many well-motivated dark matter models. According to [82], these models include “Real scalar dark matter coupled to nucleons through a hadrophilic scalar,” “real scalar dark matter coupled to an leptophilic scalar mediator,” and “Dirac fermion dark matter, coupled to a kinetically mixed dark photon or a B-L gauge boson.”

Novel dark matter paradigms include searching for electron-recoil dark matter in addition nuclear-recoil dark matter. For nuclear-recoil dark matter, electron recoil events are the background experiments actively discriminate against. However, for electron-recoil dark matter, nuclear recoil events are that background. This changes the way those experiments are carried out, as can be seen by comparing the results of a nuclear recoil search, such as [80], with an electron recoil search, such as [83]. Additionally, the differential rate for electron-recoil dark matter is significantly different from that for nuclear recoils discussed in § 1.3, as explained in Ref. [84]. Since the interaction between the electronic and nuclear system in a solid is not well understood at low energies, it is difficult to conjecture what effect defect creation processes could have on electron recoil events. On the other hand, there are many ways defect creation could help with a search for nuclear recoil dark matter, as explained later in the dissertation.

1.6 Challenges and Backgrounds

As difficult as it might be to observe dark matter particles directly because of their purported small scattering cross sections, it is even more difficult to determine whether a particle signal is from dark matter or simply looks like a signal that could be from dark matter. Additionally, with the recent paradigm shift in the dark matter community to embrace a larger region of possible parameter space, as shown in Figure 1.14, precisely measuring the energy deposited from a particle interaction is more important than ever before. SuperCDMS-style detectors satisfy both of these crucial properties because they simultaneously measure the signal from phonons, the lowest quantum of excitation in a crystal lattice, and charges, released as a by-product of the energy of the interaction. This combination of signals, coupled with the basic design principle of the detectors, makes them ideal for dark matter searches.

Since dark matter events are expected to occur very rarely, the experiment needs to minimize all possible background sources so that the background events do not interfere with the signal events that could be from dark matter. One way to do this is to shield the experiment as much as possible from known background sources. To do so, the SuperCDMS experiment is surrounded by multiple layers of shielding. From inside to outside, the experiment is enclosed in polyethylene plastic, ancient lead, low-radioactivity lead, polyethylene, and an active muon veto to minimize the effect of background radiation and muon products, as shown in Fig. 1.15. Additionally, the ratio of the energy deposited as charges to the energy released from phonons, known as the ionization yield [86], can be used to actively discriminate signals from backgrounds. Events with higher yield are from backgrounds, and those with lower yield could be from signal.

None of the methods discussed so far, however, can determine whether an event is from particles that could behave like a potential dark matter signal, such as neutrons and

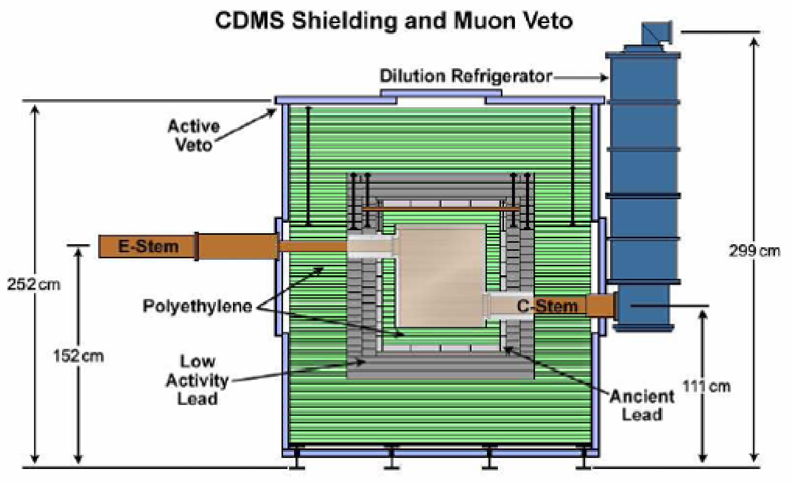

Figure 1.15: Schematic illustrating the main hardware and shielding components of the SuperCDMS-Soudan experiment. The dark matter detectors, from inside to outside, were enclosed in polyethylene plastic, ancient lead, low-radioactivity lead, polyethylene, and an active muon veto to minimize background radiation and muon products from interacting with the detector. The entire assembly was deep underground in Soudan Underground Laboratory, Minnesota, to minimize neutron interactions. Reprinted with permission from [85].

neutrinos. The experiment is located deep underground to mitigate cosmogenic muons that can produce neutrons and is surrounded by two thick polyethylene layers to further reduce the neutron background. The muon flux at several experiment locations is shown in Fig. 1.16. According to [87], "The rock overburden at the [Soudan Underground Laboratory] provides a cosmic ray flux that is equivalent to 2090 meters of water overburden, reducing the muon flux by a factor of 5×10^4 relative to the flux at the surface."

There are some backgrounds that cannot be mitigated even with extra shielding. This includes neutrinos that represent an almost irreducible background for future dark matter experiments because of their extremely high number density and low cross sections. This is best illustrated by Fig. 1.14, which shows the neutrino floor as the yellow region that dark matter experiments, given by the solid lines, are approaching. A calculation of the solar

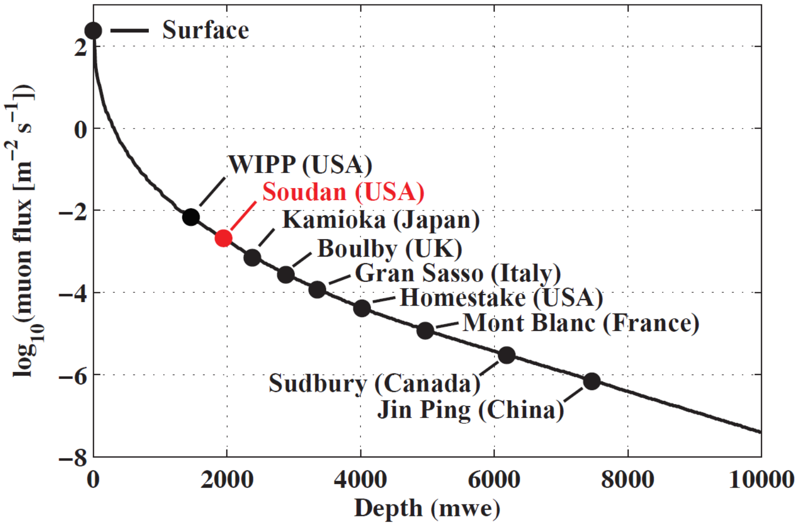

Figure 1.16: Plot showing the logarithm of the muon flux as a function of meters of water equivalent (mwe) depth. The points show where different underground laboratory sites reside on this plot. The most relevant points are Soudan and Sudbury, the old and new locations of the SuperCDMS experiment, respectively. Reprinted with permission from [87].

neutrino rate, which is a large component of the neutrino floor, is given below. On the other hand, a solid-state detector that is sensitive to defect creation, as discussed further in § 3.4.3 and § 4.3.2, could be used to mitigate the effect of even this irreducible background.

1.6.1 Solar Neutrino Rate

Similar to the calculation for dark matter, one starts by calculating the expected differential rate expected from solar neutrinos as a function of time at a particular location on the Earth's surface. Doing so requires the position of the Sun in the sky as a function of time at a given latitude and longitude. One finds the solar right ascension (RA) and declination (dec) using the formulas in Ref. [88]. Julian Day (JD), which is required to find the correct RA and dec, can be found by considering the number of days after the start of the Julian calendar, which yields equations such as those in Ref. [89]. RA and dec are

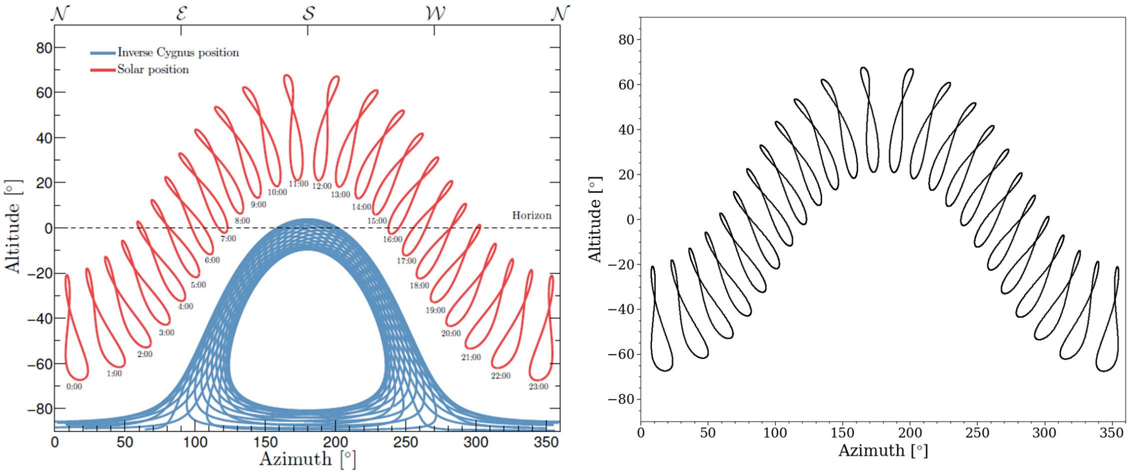

Figure 1.17: Position of the sun as a function of time at Modane Underground Laboratory from Ref. [72] (left) and using my solar position code (right). The leftmost solar position in the leftmost plot is in red, and the solar position in my plot is black. The leftmost plot also includes the direction of the dark matter flux in blue. Plot at left reprinted with permission from Ref. [72].

converted to altitude and azimuth (alt, az), which give the position of the Sun in the sky at a given location on Earth, via formulas such as those in Ref. [90]. As shown in Fig. 1.17, the solar position found this way agrees well with what is expected from Ref. [72].

Given the position of the Sun, one can find the expected solar neutrino rate. Following the procedure in Ref. [72], I show here how to calculate the expected coherent neutrino-nucleon scattering (CENNS) in a detector made of a single element with atomic number A given a solar spectrum like that shown in Fig. 1.18. According to Ref. [72], the differential cross-section is given by

$$\frac{\mathrm{d}\sigma}{\mathrm{d}E_r} = \frac{G_F^2}{4\pi} Q_W m_N \left(1 - \frac{m_N E_r}{2E_\nu^2}\right) F^2(E_r). \tag{1.55}$$

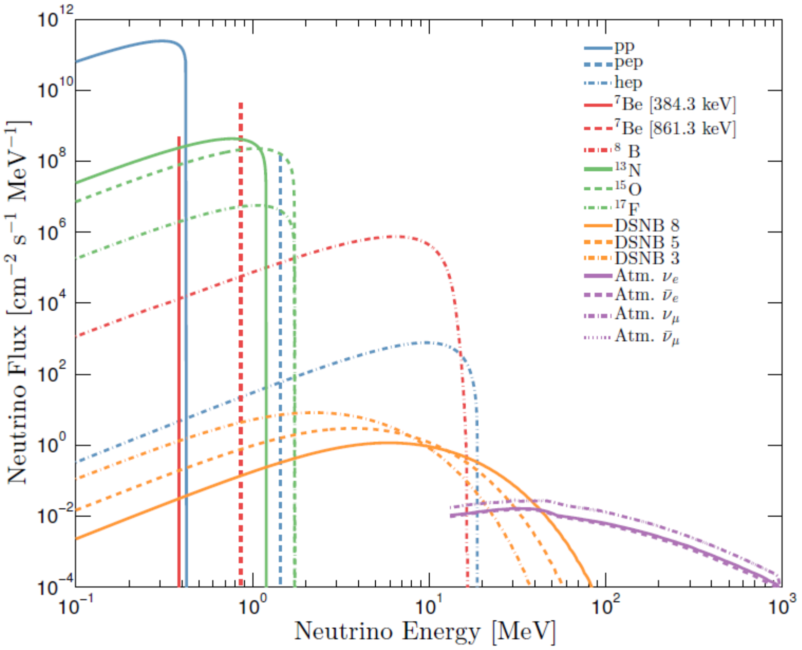

Figure 1.18: Plot showing the expected neutrino spectrum from the Sun, the diffuse supernova neutrino background (DSNB), and the atmosphere. Plot reprinted with permission from [72].

The weak nuclear hypercharge, Q_W, is

$$Q_W = \mathscr{N} - \mathscr{Z}\left(1 - 4\sin^2\theta_W\right) \tag{1.56}$$

for a nucleus with $\mathscr{N}$ neutrons and $\mathscr{Z}$ protons, G_F is the Fermi coupling constant, θ_W is the weak mixing angle, and m_N is the target nucleus mass. $F^2(E_r)$ is the Helm nuclear form factor [74] from § 1.19.

The total differential rate, assuming a source whose position changes over time, is

$$\frac{\partial^3 R}{\partial E_r \partial \Omega_r \partial t} = N \int_{E_\nu^{\min}} \frac{\partial^2 \sigma}{\partial E_r \partial \Omega_r} \times \frac{\partial^3 \Phi}{\partial E_\nu \partial \Omega_\nu \partial t} \mathrm{d}E_\nu \mathrm{d}\Omega_\nu . \tag{1.57}$$

where N is the number of target nuclei per mass, $\frac{\partial^2\sigma}{\partial E_r \partial \Omega_r}$ is the differential cross section, and $\frac{\partial^3\Phi}{\partial E_\nu \partial \Omega_\nu \partial t}$ is the differential flux per unit time.

If one assumes that the Sun is a delta-function source [†] in the sky whose direction changes over time, equations 1.55 and 1.57 can be combined to yield

$$\frac{\partial^3 R}{\partial E_r \partial \Omega_r \partial t} = \frac{N}{2\pi} \times \frac{1}{\Delta t}\left[1 + 2\epsilon\cos\left(\frac{2\pi(t - t_\nu)}{T_\nu}\right)\right] \times \frac{\mathscr{E}^2}{E_\nu^{\text{min}}}\frac{\mathrm{d}\sigma}{\mathrm{d}E_R}(E_r, \mathscr{E})\frac{\mathrm{d}\Phi}{\mathrm{d}E_\nu}\bigg|_{\mathscr{E}} \tag{1.58}$$

where

$$\frac{1}{\mathscr{E}} = \frac{\hat{\mathrm{q}}_r \cdot \hat{\mathrm{q}}_\odot}{E_\nu^{\text{min}}} - \frac{1}{m_N}. \tag{1.59}$$

Here,

$$E_\nu^{\text{min}} = \sqrt{\frac{m_N E_r}{2}}, \tag{1.60}$$

Δt is the time interval over which the measurement is taken, $\epsilon = 0.016722$ is the eccentricity of the Earth's orbit around the Sun, t is the time from January 1st, $t_\nu = 3$ days is the time at which the Earth is at its perigee in relation to the Sun, T_ν is the period of Earth's orbit around the Sun (one year), $\hat{\boldsymbol{q}}_r$ is the unit vector in the recoil direction of the nucleus, $\hat{\boldsymbol{q}}_\odot$ is the direction of the sun, and m_N is the mass of the recoiling nucleus.

1.7 Different Experiments

As can be seen in Fig. 1.14 and Fig. 1.19, there are many kinds of direct-detection dark matter experiments. Some use liquid noble gases such as XENON1T, DS50, and LZ (not shown) and others use solid-state materials such as KIMS, CRESST, and SuperCDMS. Some experiments, like DAMIC, use sophisticated charge-coupled devices (CCDs), and some experiments, such as DRIFT, even use low-pressure gases in time-projection chambers. There are also several direct-detection experiments looking for axions and axion-like

---

[†] The Sun is actually about a half-degree across, but this approximation seems to work well enough, as per Ref. [72].

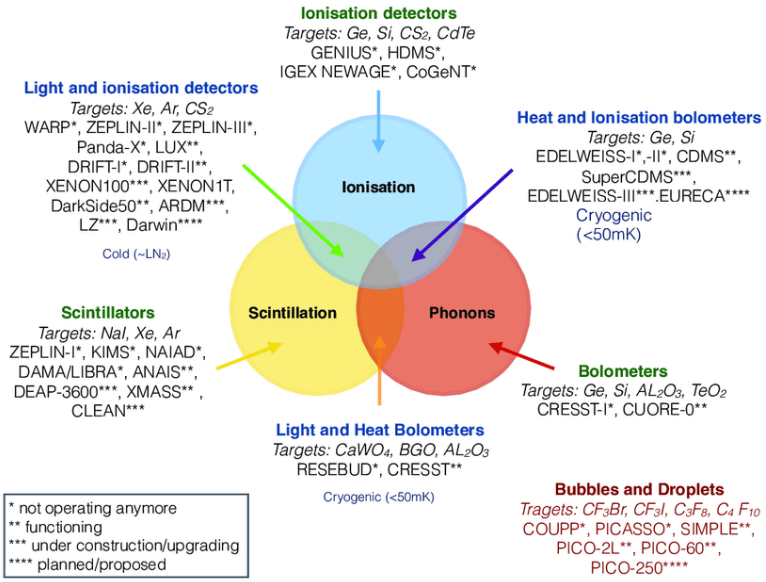

Figure 1.19: Venn diagram showing multiple direct dark matter search experiments with the general types of detector technology used by each. Figure reprinted with permission from [91].

particles [42], such as ADMX, HAYSTAC, ORGAN, CULTASK, RADES, KLASH, Orpheus, MADMAX, CASPEr, ABRACADABRA, DM-Radio Pathfinder, and QUAX. Additionally, as mentioned earlier, the SuperCDMS experiment is also sensitive to axion-like particles. Unfortunately, a full description of all of the types of dark matter direct-detection experiments is outside of the scope of this work, and the author invites the interested reader to consult references such as [42], [92], [70], and [93] for further information. I now turn my attention to one of these direct-detection dark matter experiments, the SuperCDMS experiment, improvements of which, and the possibilities therein, that are the focus of this dissertation.

1.8 Advantage of Low Temperature Detectors and Large Mass Calorimeters with Single Electron Resolution

It may be possible to circumvent the background limitations discussed earlier with a directional dark matter detector since this could discriminate signal from background based on direction. Nonetheless, directionality comes at a serious price for low rate particle detection experiments. For example, time-projection chamber experiments using low pressure gases, which can discriminate on an event-by-event basis, require enormous volumes to have exposures high enough to detect dark matter [94]. Additionally, the expected dark matter spectrum has no pronounced features, such as absorption or emission lines, which makes discriminating signal from backgrounds challenging. There has been significant progress recently on phonon-mediated detectors, especially those using Neganov-Luke phonon amplification [95, 96], which could lead to large-mass semiconductor detectors with single-electron resolution [97]. The process of defect creation in single-crystalline semiconductors, such as germanium (Ge) and silicon (Si), could address both problems since the energy threshold for defect creation that depends on crystal direction could be used for directional sensitivity and the energy loss due to defect creation could cause features in the expected recoil energy spectrum.

2. SINGLE ELECTRON RESOLUTION 100 GRAM SI DETECTOR [*]

2.1 Detector Concept

2.1.1 CDMS Detection Method

To understand the SuperCDMS experiment and similar experiments like it, one must consider what might happen when a dark matter particle interacts with a solid-state detector. On a rare occasion, a particle similar to a weakly interacting massive particle (WIMP) might interact with the nucleus of an atom in the lattice of the detector. This would deposit some energy in the lattice, some of which would propagate from the interaction site via phonons, some of which would produce a cloud of electrons and holes, and some of which might create one or several defects. For a SuperCDMS-style detector, an electric field applied across the detector causes the electrons and holes to emit Neganov-Trofimov-Luke (NTL) gain phonons as they traverse the crystal. Surface sensors independently measure the phonon and charge signals thus produced. The amount of energy deposited in each of these two main channels varies depending on the type of particle interaction, as shown in Fig. 2.2.

For example, for experimental neutron calibration event data for Ge detectors, $\sim$9/10 of the energy releases phonons, $\sim$1/10 causes ionization, and a small amount produces defects, depending on the energy [98]. Similarly, for a simulated 1 keV nuclear recoil event in Ge, 683 +/- 10 eV converts to phonons, 250 +/- 6 eV goes to electronic stopping, and 67 +/- 8 eV creates defects [99]. Electronic stopping refers to the energy transferred to the interatomic bonds in the detector bulk as opposed to the electron-hole pair production across the band gap. The electronic stopping contribution produces electron-hole pairs that

---

[*] Part of this chapter is reprinted with permission from F. Kadribasic, G. Agnolet, S. Esmaeili, A. Jastram, A. Kubik, R. Mahapatra, M. Platt, N. Mirabolfathi, "Progress in Interface Studies for NTL Phonon-Assisted Large Calorimeters," *J. Low. Temp. Phys* to appear, Copyright 2020 by Springer Nature.

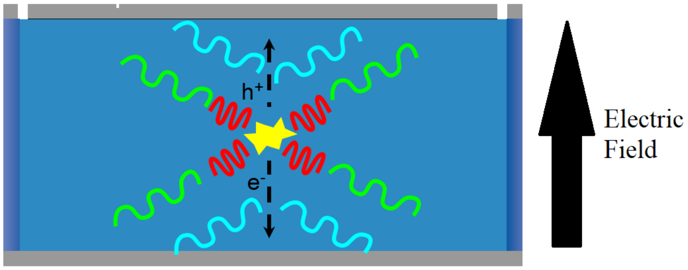

Figure 2.1: Diagram explaining how the energy from a particle interaction with a detector (yellow) transfers to phonons (red, green, and blue) and electrons and holes (black). During the initial interaction, prompt, quasi-diffusive THz phonons (red) are produced that down-convert into ballistic low-frequency phonons (green). In the presence of an electric field, the electrons and holes are accelerated across the semiconductor crystal to produce Neganov-Luke phonons (blue). Phonon sensors read out the phonon signal, and charge sensors collect the signal from the electrons and holes. This schematic is more representative of the kind of detector used for CDMS II than those for SuperCDMS; nonetheless, the main principles remain the same. Modified with permission from [85].

either recombine if there is no voltage bias, which produces more phonons, or traverse the crystal and are measured as an ionization signal if there is a voltage bias. The charge carriers then recombine at the surface of the detector if the detector is biased via metallic contacts [95], thereby further increasing the phonon signal. The electronic stopping also produces phonons while generating e-h pairs [98]. When all of these factors are included, the simulated result qualitatively agrees with experimental data.

Since these detectors use phonons produced during particle interactions in the detector bulk as a proxy for the energy deposited, they have the potential to reach the very low energy thresholds required for measuring events from dark matter below $\sim$10 GeV/c^2 mass. Phonons are the lowest quantum of excitation in a material, which means that any energy transferred to the material bulk that does not produce defects is eventually converted into phonons. In order to measure such a weak signal, the detectors are operated at $<$20 mK and thermalized to the cold stage of a dilution refrigerator via a weak thermal link.

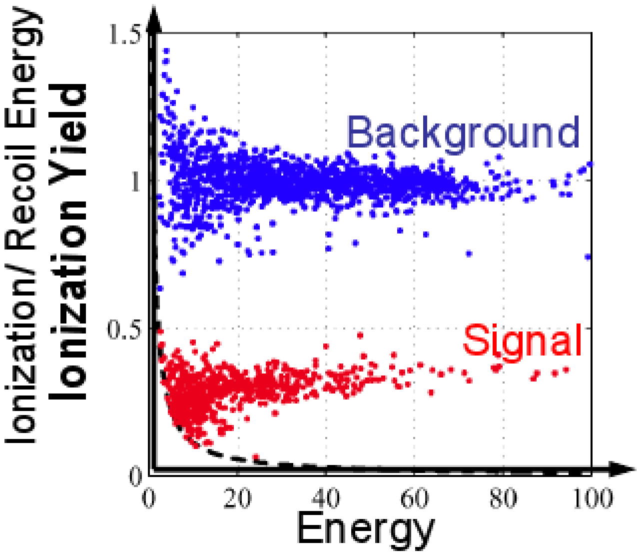

Figure 2.2: Plot illustrating how the energy yield for electron versus nuclear recoils can be used to discriminate possible dark matter signal from background events. The total energy deposited during the event is shown on the x-axis, while the ionization energy divided by the recoil energy, also known as the ionization yield, is shown on the y-axis. The background events from a gamma-ray source separate out from the potential signal events mimicked by a neutron source. This effect can be used for active background rejection when searching for dark matter. Reprinted with permission from [100].

Quasiparticle-trap-assisted electro-thermal-feedback transition edge sensors (QETs) photolithographically patterned on the detector surface can detect, and cold electronics can amplify, the phonon signals so that they can be read out by electronics at room temperature.

2.1.2 Ionization and Phonon Detectors: Active Background Rejection

Simply measuring phonons, however, is not useful for dark matter direct-detection experiments because they cannot discriminate dark matter signal from backgrounds. Except for the energy required to produce defects, which is ∼5 % of the total energy deposited for recoil energies greater than ∼100 eV, the energy deposited from any particle interactions, including from background events, is eventually converted into phonons. Most backgrounds that may mimic dark matter signal come from electromagnetic radiation emitted by the environment, which can be anything from radioactive decay to infrared photons from room temperature. Semiconductors, on the other hand, have the unique property that particle interactions with valence electrons, if the energy deposited is greater than that of the semiconductor band gap, produce measurable conduction electron-hole pairs. Since this energy threshold is very low ($\sim$1.17 eV in Si at the temperature at which the detector is operated), measuring the signal from these electrons allows an experiment to discriminate nuclear from electron recoils via QETs to measure phonons and charge rails to measure charges.

The result of doing so is shown in Fig. 2.2. A SuperCDMS-style detector can measure the charge produced and total energy of a particle interaction when biased with a low voltage. As mentioned in the previous subsection, about a tenth of the energy transferred to the detector's crystal lattice during a nuclear recoil particle interaction is transferred to the charges in SuperCDMS-style detectors. The ratio of the energy transferred to the electrons divided by the total energy is referred to as the ionization yield [86], and it is not known for nuclear recoils with energies below 1 keV [101]. The low-energy limit of this property for nuclear recoils is that, below some anisotropic energy threshold [102], nuclear interactions do not produce any electron-hole pairs.

2.1.3 Signal to Noise Difficulty due to Ionization Readout

According to Ref. [103], "dual measurement techniques fail at low energies due to second measurement fundamental noise." The limit comes from the 40 pF capacitor used in parallel with the charge readout circuit input. If not enough charges accumulate at the input quickly, the change in current will not be read out because of the high input impedance. Additionally, the ionization yield used to define the the cut between the signal and background events diverges at low energies because of the charge readout noise.

On the other hand, phonons are read out with a circuit with very low input impedance, which means that they do not suffer from the same concern as the charge measurement system. Because phonons represent the lowest quantum of excitation in the material, a lot of recent research and development has been focused on making SuperCDMS-style detectors that only measure phonons. CDMSlite represents an excellent recent example of science results these kinds of detectors are capable of, as further presented in the next subsection.

2.1.4 CDMSlite and NTL Gain

Another useful property of high-purity semiconductor detectors, mentioned briefly earlier, is that electrons and holes accelerated across a semiconductor detector produce their own phonons, which is referred to as the NTL effect [95]. These phonons add to those produced during the initial interaction. This effect is similar to the reason why conductors have a finite resistance; electrons scatter off defects in the crystal lattice producing phonons. NTL gain is linear with respect to the voltage applied modulo a constant that depends on the total event energy deposited and the energy required to form electron-hole pairs [95, 104]. Thus, the total energy produced during an interaction in a semiconductor detector with an applied electric field through the bulk is given by

$$\begin{aligned} E_{\text{tot}} &= E + E_{\text{field}} && (2.1) \\ &= E + n_{\text{e-h}} eV && (2.2) \\ &= E + \frac{E}{\epsilon}(eV) && (2.3) \\ &= E\left(1 + \frac{eV}{\epsilon}\right) && (2.4) \end{aligned}$$

Here, the particle interaction deposits energy E, causes $n_{\text{e-h}}$ electron-hole pairs to form, each of which requires ϵ net energy to form. Since the electron-hole pair excitations recombine at the surface, the energy required to produce the electron-hole pair is returned to the lattice as phonons, which is why there is no term corresponding to the energy needed to create the excitations [95].

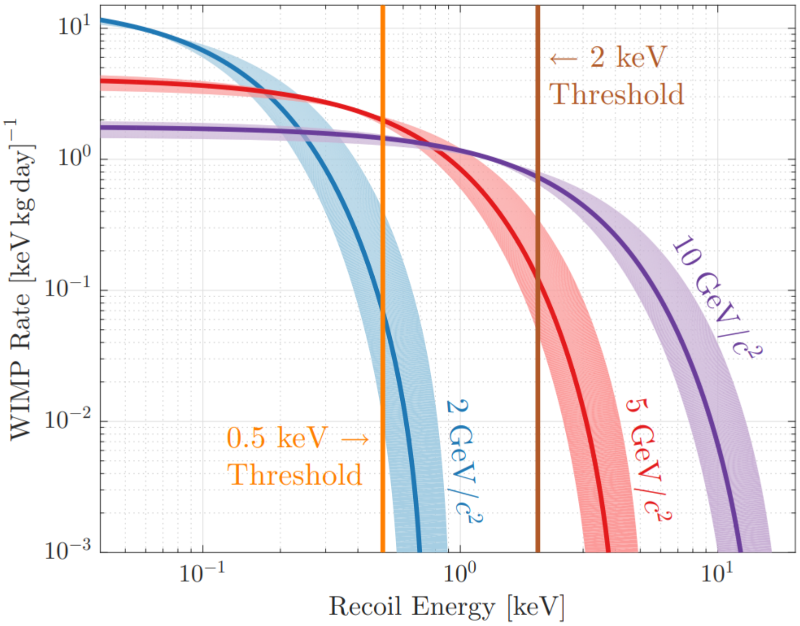

Figure 2.3: Plot showing how a dark matter experiment with germanium detectors becomes more sensitive to dark matter below about 10 GeV/c^2mass as the detector threshold is lowered. The curves show the dark matter differential rate for different datk matter masses, and the shaded regions correspond to known observational uncertainties associated with calculating the dark matter rate. Vertical lines represent two different detector thresholds. This is the main reason why many dark matter experiments, including SuperCDMS, are improving detector resolution to reach single-electron resolution. Reprinted with permission from [80].

The NTL effect implies that a detector biased by several hundred volts could have an unprecedented energy resolution. This is because particle events depositing even a few electronvolts of energy would be amplified up to several hundred electronvolts, rendering these events measurable despite noise limitations. This improvement in energy resolution is what allowed CDMSlite to set the once world-leading limits for WIMP-like dark matter with masses below $\sim$10 GeV/c^2. Low mass dark matter implies larger number density and, hence, the possibility of detection with low background. This is best illustrated in Figure 2.3, which shows how the measurable rate significantly increases for low-mass dark matter the lower the energy threshold - a direct consequence of improved energy resolution. The NTL gain allowed the CDMSlite experiment to achieve much greater sensitivity at low dark matter masses, despite only using a small fraction of all of the detectors for the SuperCDMS experiment [80].

Because the gain in phonon amplification depends on the voltage bias, the gain is, in principle, independent of the phonon noise. However, if there are leakage current events, then these appear as random fluctuations in phonon signal that reduce the signal-to-noise gain. For this reason, if the leakage current is constant above a certain voltage, then above that voltage there is no further gain in NTL amplification. On the other hand, if the leakage current scales with applied voltage, the signal-to-noise may even drop as the voltage is increased.

2.1.5 Challenges in Reaching Single Electron: Problematic Due to Leakage

According to Ref. [105], “the noise sources we care about are those which add current noise to the TES circuit.” This noise can be divided into four general categories: the Johnson noise of the passive components (PJN), the Johnson noise of the TES (TJN), the thermal fluctuation noise (TFN), and the SQUID noise (sn) [106, 44, 105]. Thus, Ref. [105] gives the total current noise as

$$I_{\text{tot}} = \sqrt{I_{\text{sq}}^2 + I_{\text{PJN}}^2 + I_{\text{TJN}}^2 + I_{\text{TFN}}^2}. \tag{2.5}$$

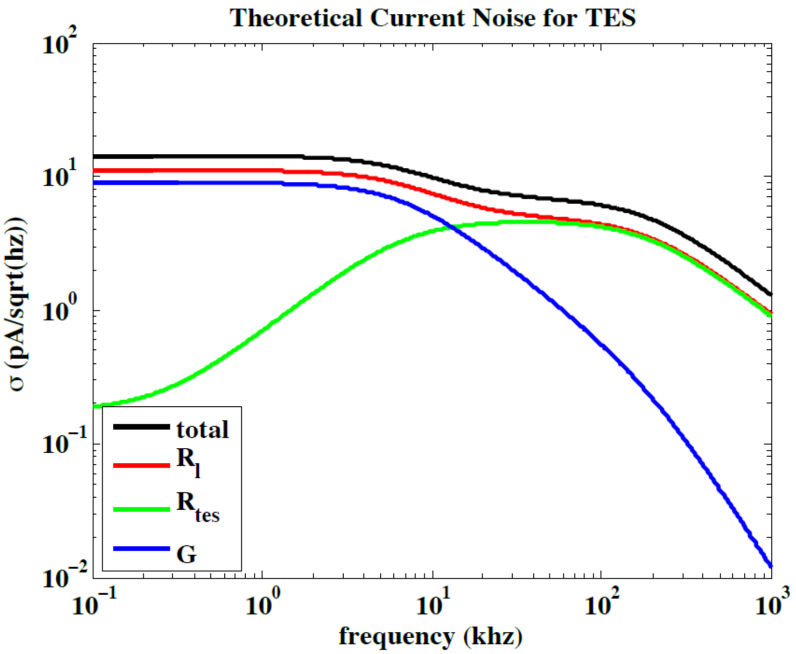

Figure 2.4: Plot showing the current power of different TES noise contributions. Reprinted with permission from [44].

The contribution from each component is shown in Fig. 2.4.

However, in addition to these well-understood noise sources, SuperCDMS-style detectors have observed a leakage current noise that significantly reduces the maximum possible detector resolution by limiting the maximum voltage at which a detector can be run before the resolution is completely degraded. Because the leakage current can be modeled as a Poisson-distributed train of single-electron pulses, it introduces significant low-frequency noise that reduces the resolution, as shown by the Fourier transform of event templates in Fig. 2.5. This plot is generated by first choosing many calibration events from the same calibration line, subtracting the linear offset in the event baselines, scaling the events with respect to their peak heights (found using a parabola fit to the peak), and averaging over all of those events to reduce the contribution from electronic noise. Taking the Fourier transform of the result yields the plot in Fig. 2.5.

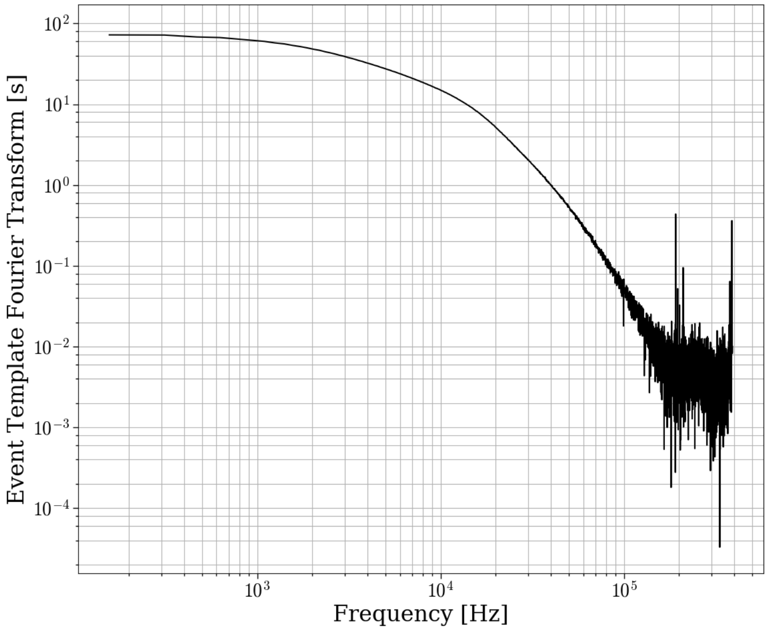

Figure 2.5: Plot showing the Fourier transform of an event template as a function of frequency.

Following the procedure in Ref. [107], the leakage current is measured by adding Poisson-distributed event templates scaled to the expected single-electron event height at a given voltage to noise traces without leakage current. A χ^2 fit is performed on the resulting noise power spectral density (PSD) to find the minimum, as shown in Fig. 2.6. The minimum value of χ^2 corresponds to the best model fit to the data, which is shown as the red point in Fig. 2.6. Following this method, the best-fit noise PSDs for each voltage are shown alongside the data in Fig. 2.7. Only the lower frequencies are shown. Detector nonlinearities due to detector heating could be responsible for the worse fit as the voltage is increased. Additionally, it seems that the leakage current increases nonlinearly as the voltage is increased, as shown in Fig. 2.8. This agrees with results from other SuperCDMS detectors [107]. Error bars are estimated by finding the relative error between two

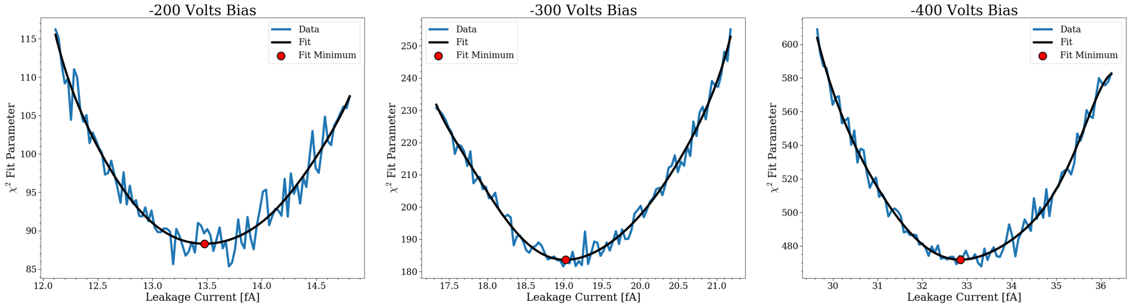

Figure 2.6: χ^2 fit parameter versus leakage current in fA. The blue curve shows the χ^2 versus leakage current data, and the black curve is a polynomial fit to the data. The red point indicates the minimum χ^2 value of the polynomial, which corresponds to the best-fit leakage current.

best-fit noise PSDs starting from two separate datasets with no measurable leakage current. Hence, the error bars include both statistical errors from the χ^2 minimization routine as well an estimate of systematic errors that could come from changes in gain when using the other dataset, for example.

2.1.6 Tunneling Process

The current density can be written as

$$J_n = q v_R n \Theta \tag{2.6}$$

where q is the charge of an electron, v_R is the Richardson velocity, n is the density of carriers, and Θ is the tunneling probability [108]. For a triangular barrier of height ϕ_B and width L of the form

$$V(x) - E = q\phi_B \left(1 - \frac{x}{L}\right), \tag{2.7}$$

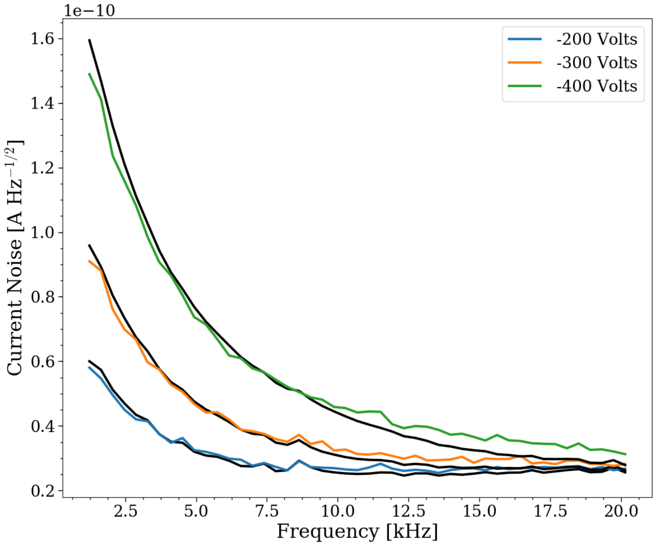

Figure 2.7: Current noise as a function of power supply bias. Colored curves show the leakage current power spectral density data. Black curves show the best-fit curves to the data.

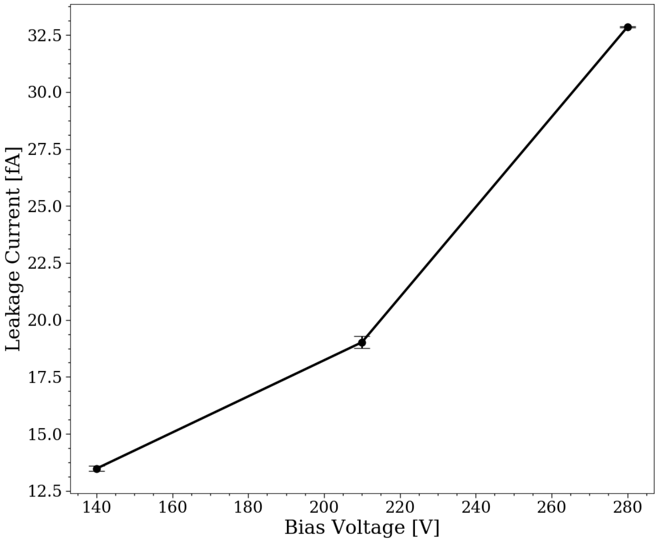

Figure 2.8: Leakage current versus reverse bias voltage across the detector. Error bars are estimated using the relative error between fits to noise PSDs from two separate datasets.

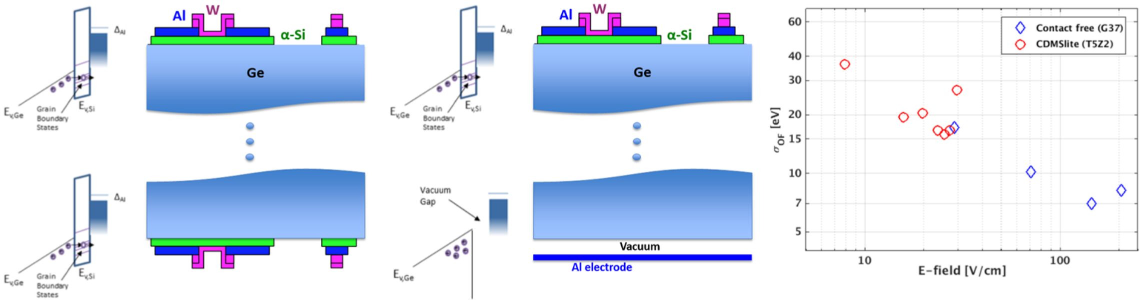

Figure 2.9: [Left] The difficulty in understanding contact physics with CDMS symmetric readout [97]. [Center] Placing an electrode with a vacuum gap on one side breaks the symmetry and by definition removes the leakage on one surface [97]. [Right] Plot showing how past-generation CDMSlite detectors at Soudan [80] compare to one with a contact-free design [97]. In one polarity, the detector can be run at much larger voltage bias, which significantly increases NTL gain caused by electron-hole pairs drifting across the detector and producing phonons along the way. Modified with permission from [97] and [109].

the tunneling probability is given by

$$\Theta = \exp\left[-\frac{4}{3}\frac{\sqrt{2qm_e}}{\hbar}\frac{\phi_B^{3/2}}{E}\right] \tag{2.8}$$

where m_e is the mass of an electron, E is the electric field $E = \phi_B/L$ in the barrier, and $\hbar$ is the reduced Planck's constant.

Depending on the location of the Fermi level of aluminum versus germanium, there is either electron or hole tunneling [101]. The interface also includes an amorphous layer with many inter-band states [101], as shown in the left panel in Fig. 2.9. Replacing the contacts on one side of the detector with a flat surface and a vacuum electrode breaks the symmetry between the two sides and allows one to study the leakage current of the interface, like in the middle panel of Fig. 2.9. In general, in reverse polarity the leakage current remains constant until a critical voltage, at which point the current quickly increases, as shown in the plot at right in Fig. 2.9.

2.1.7 G37R and S17B

The previous description becomes relevant in the context of the three thin film materials the phonon sensors are made from in a standard SuperCDMS detector. These are, in order from nearest to detector to furthest away: poly-crystalline[†] silicon (PC-Si), aluminum, and tungsten layers [85]. Unlike the aluminum and tungsten layers, which are needed for proper QET function, the PC-Si was introduced during the CDMS experiment to mitigate two major concerns with overall detector performance. These are the deficit in charge collection for events near the surface, commonly referred to as the "dead layer" [111, 112, 113] and under-cutting of the 1.2 μm-wide TES sensors photolithographically etched on the surface [110]. However, the dead layer is not a concern for the detector at the focus of this thesis because the dead layer decreases the greater the bias voltage, and this detector's performance was evaluated at high voltages [101]. Additionally, silicon detectors do not suffer from the same under-cutting process, sometimes referred to as edge-stop, observed with germanium detectors since silicon is resistant to etchants [101, 110].

It is possible that leakage current might not be due to the sensor interface since leakage is also possible from bulk discharge of shallow energy states that are charged and because there could be leakage on the fringe surfaces [101]. However, an earlier study with a germanium detector [97] seems to indicate that at least some of the leakage current comes from the contacts. The detector for that study, G37R, was a germanium detector fabricated with phonon readout only on one side. The other side was machined flat. The detector was biased from the flat side with a metal electrode with a physical gap between it and the detector, so-called contact-free-detector operation. This detector measured significantly lower leakage current, and consequently much better resolution, than previous detector

---

[†] Poly-crystalline refers to the fact that the silicon layer is composed of many small crystals with local periodicity, as opposed to being amorphous without any periodicity or single-crystal with periodicity throughout. In some older studies, the poly-crystalline silicon is called amorphous since the SuperCDMS collaboration recently discovered that the layer is poly-crystalline rather than amorphous [101, 110].

designs because replacing electrodes bonded to the detector surface with a vacuum electrode seemed to significantly mitigate the leakage current. We therefore investigate what causes the leakage current by modifying the metal-superconductor interface on the surface of a SuperCDMS-style detector.

Hence, the simplest modification for such a study is removing the poly-crystalline silicon layer directly underneath the sensors, which is what was done for the detector for this study, S17B. S17B was fabricated out of silicon for contact-free-electrode operation, similar to G37R, without a PC-Si layer to remove the interband states that may allow for band pinning [101], a process that occurs at some semiconductor-metal interfaces that "pins" the Fermi level, thereby producing a surface dipole that could increase leakage current from the contact surface [114]. This detector's data was analyzed as part of this dissertation to understand the role that the poly-crystalline silicon layer plays with respect to the leakage current.

2.1.8 Setup

Figures 2.10, 2.11, 2.12, and 2.13 illustrate how the energy transferred to a SuperCDMS-style detector during a particle event is converted into a measurable signal. As shown in Figure 2.10, athermal phonons released by the particle interaction interact with and break Cooper pairs in aluminum fins on the surface of a SuperCDMS-style detector. Quasiparticles produced during the process transport the energy to the trapping region, which produces hot electrons. These electrons heat up the TES, which is read out with cryogenic amplifiers. In this way, the energy resolution of the TES is preserved while making sure that a large fraction of the detector surface can absorb phonons, thereby improving the phonon collection efficiency of the QET assembly.

The slight increase in current through the TES causes a signal that is read out by the circuit in Fig. 2.11. The changing current through the TES, R_S, causes a changing mag-

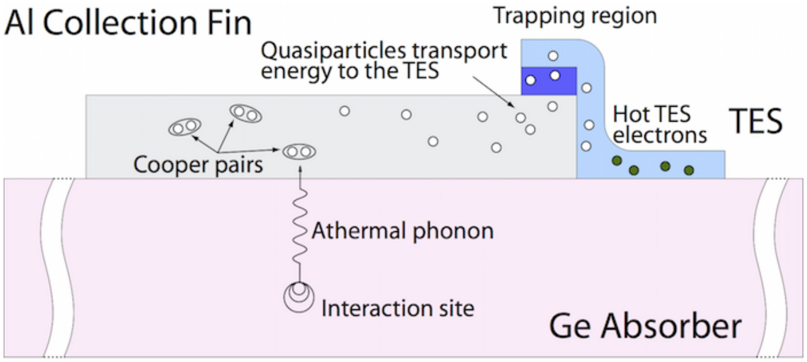

Figure 2.10: Schematic indicating how energy is transferred from the particle interaction with the detector bulk ultimately to the transition edge sensors (TES). The particle interaction releases phonons that break the Cooper pairs in the superconducting aluminum "fins" surrounding the TES. This produces quasiparticles that diffuse towards the TES and heat it up. This preserves the energy resolution of the TES while making sure that a large fraction of the detector surface can absorb phonons. Reprinted with permission from [115].

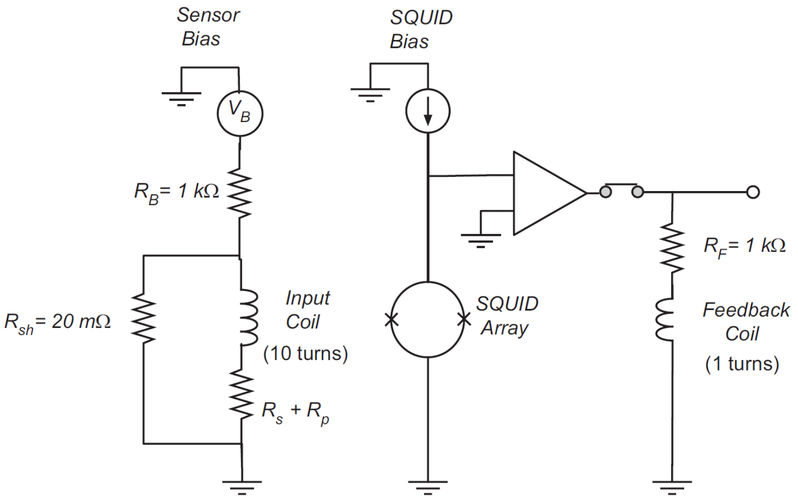

Figure 2.11: Circuit diagram showing the phonon readout on a CDMS II-style detector. Although the detector geometry has changed significantly since then, the basic detector layout and readout circuit has stayed the same. The phonon signal causes the temperature of the QET to increase, thereby changing the magnetic flux through the SQUID, which produces a measureable pulse. More electronics further amplifies and shapes the signal. Reprinted with permission from [106].

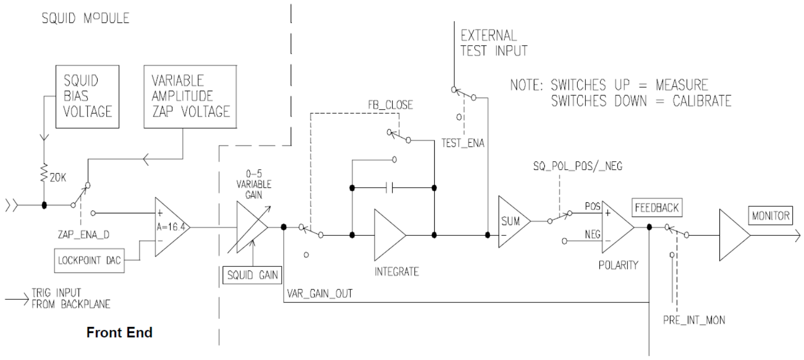

Figure 2.12: Circuit diagram illustrating how the signal from the SQUID amplifier is further amplified and reshaped. The portion of the circuit to the left of the large dotted line is cryogenic, and that to the right is at room temperature. Although current SuperCDMS readout has been significantly modified since this diagram was made, the basic principle remains the same. Reprinted with permission from [116].

netic field in the input coil. This changing magnetic field causes a voltage drop across the SQUID array, which is amplified by the amplifier in the diagram. Running the system in closed-loop mode, as was done for detector S17B, gives a gain of 10 at the cryogenic SQUID amplifier stage. The signal is then further amplified via the electronics stages shown in Fig. 2.12. The analog signal is digitized with a digitizer and saved to a computer for further analysis. For a particle event, the raw data saved to the computer is similar to that shown in Fig. 2.13.

We use S17B - a Si detector $\sim$100 grams in mass with four tungsten-based QET channels photolithographically patterned on one side of the detector, as shown in the upper left of Fig. 2.19. Using multiple channels provides positional information based on the relative amplitudes and arrival times of the event energy measured by each channel, which can be used to identify calibration source events. The other side is polished flat and is positioned $\sim$300 μm from the surface of a high-voltage charge-bias aluminum electrode to minimize leakage current that would otherwise prevent the detector from achieving its

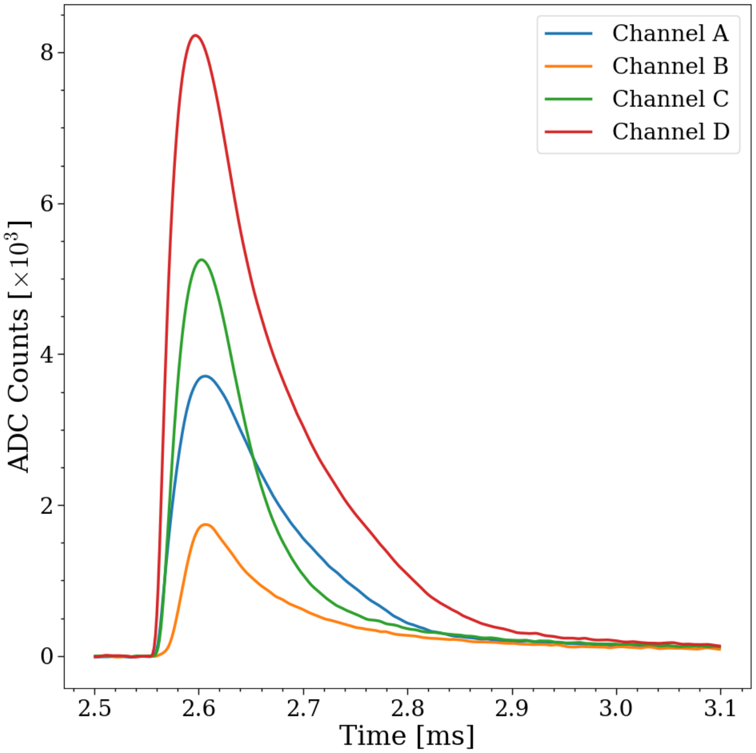

Figure 2.13: Sample phonon pulse from a particle interaction with a SuperCDMS-style detector. The fact that the signal from Channel D is both greater than that from the other channels and appears before them indicates that this event likely took place near that Channel. This kind of information can be very useful for selecting calibration events, since these are localized where the source is placed relative to the detector, and potential dark matter signal, since these are expected in the detector bulk rather than near the surface.

optimal high-voltage performance [97]. A DC power supply biases the electrode up to 400 V at the power supply, which corresponds to about 280 V across the detector. The reason for the difference is because the circuit formed from the electrode to the ground on the detector is two capacitors in series. Thus, there is less voltage across the detector because of the vacuum gap; if the gap were smaller, the voltage drop across the detector is greater. Higher voltages were not used to mitigate the risk of a short-circuit at the vacuum fitting, which may cause a leak to air at a cryogenic temperature that could incapacitate the entire

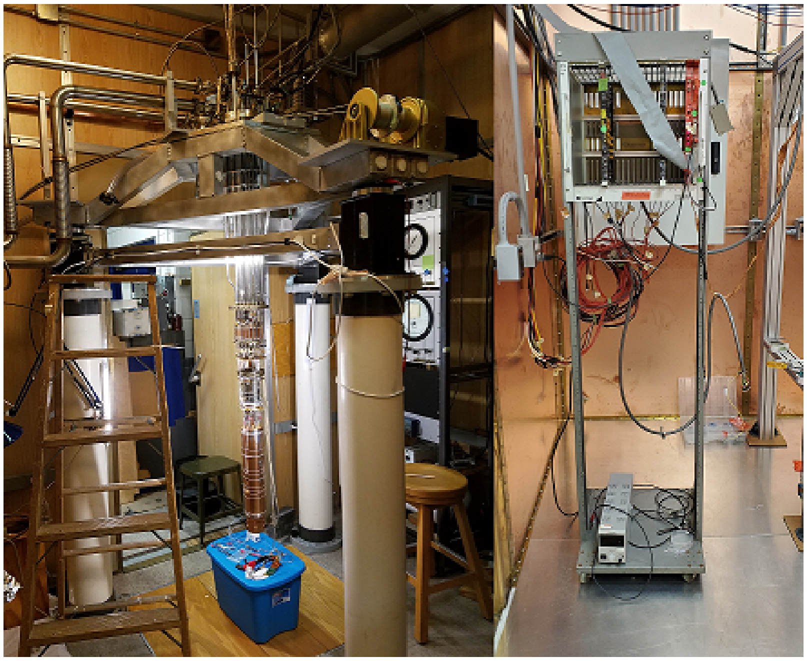

Figure 2.14: Dilution refrigerator disassembled (left) and example of front end readout electronics (right). The detector, inside a special housing and read out by cryogenic electronics, is installed in the dilution refrigerator at left. The cryogenic electronics are further read out by the electronics at room temperature, similar to those shown at right. The left photograph shows the Texas A&M University facility in 2016, and the right one is from a related Texas A&M University facility in 2020.

dilution refrigerator.

The drop can be accurately measured using Neganov-Luke amplification, the number of electron-hole pairs produced per unit deposited energy, and the calibration peak height at 0 V. 3.8 eV is needed to excite an electron-hole pair in silicon [118, 107]. Dividing the location of the 17.8 keV calibration peak in the leftmost plot in Fig. 2.22 by 3.8 eV thus yields 63.1 ± 2.3 ADC counts needed per electron-hole pair for a 17.8 keV event. On the other hand, using the 13.9 keV to minimize saturation gives 36.15 ± 0.16 ADC counts per electron-hole pair for a 13.9 keV peak, or 46.30 ± 0.20 ADC counts per electron-hole pair for a 17.8 keV event. Hence, the ratio of the voltage bias across the detector and the total

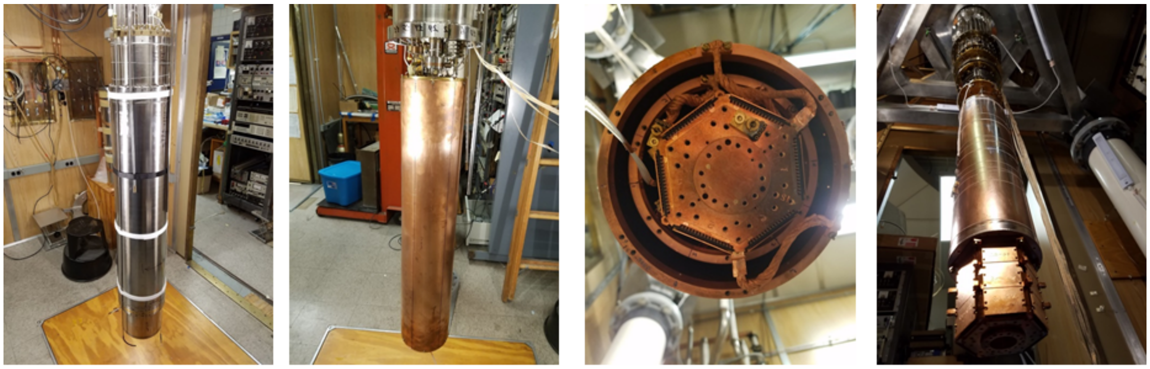

4 K can 600 mK can 100 mK can 10 mK can

Figure 2.15: Photographs showing, from left to right, the 4 K can, 600 mK can, 100 mK can, and 10 mK can. The 100 mK can is the innermost visible circular shield in the third image, and the 600 mK can surrounds it. Each of these layers shields the lower temperature stages from the thermal radiation from higher temperature components to avoid “heating” the colder stages. Hence, they allow the detector, which is coupled to the lowest-temperature stage, to reach sub-100 mK temperatures. Each can connects to separate thermal stages on the detector tower (holes at can bottom) to help thermalize the detector and its associated electronics. Each can needed to be designed and manufactured in-house to accommodate SuperCDMS-style detectors and electronics.

voltage applied is simply

$$r = \frac{46.30 \pm 0.20}{63.1 \pm 2.3} = 0.734 \pm 0.027. \tag{2.9}$$

Propagation of uncertainties assuming a ratio of two measurements and assuming no covariance is used to find the error bars.

Furthermore, the gap between the electrode and the detector can be determined using this voltage ratio and the formula for parallel-plate capacitors since the detector gap and

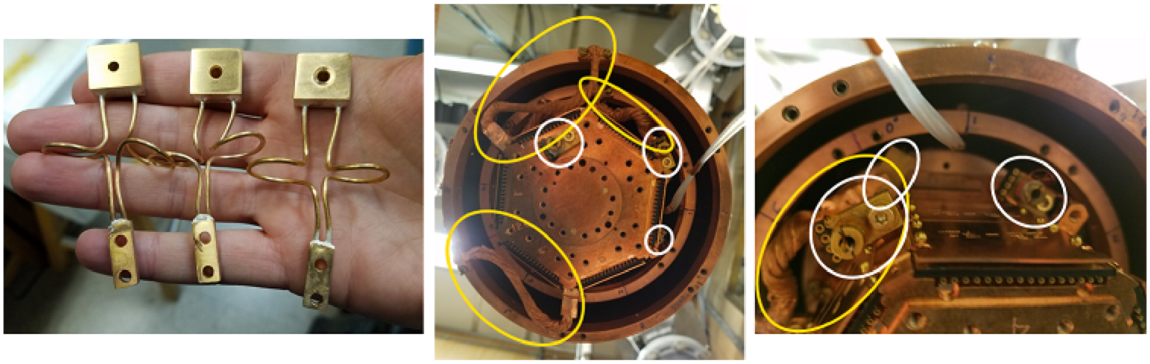

Figure 2.16: Photographs showing the 4 K heatsinks (left), 600 mK heatsinks (center, yellow ovals), and one of the 100 mK heatsinks (right, yellow oval). The heatsinks thermalize each of the electronics layers to the proper thermal stages of the dilution refrigerator via the cans. All of the heatsinks were manufactured in-house, and the 4 K heatsinks were gold-plated using Transene Bright Electroless Gold in-house. Thermometers, mounted on each of the different thermal stages, are indicated via white ovals. The melting-curve thermometer, mounted on the 10 mK stage and indicated with the smallest white oval, was recalibrated each detector run, including that of S17B.

electrode are a pair of capacitors in series biased by a DC voltage. Hence,

$$\begin{aligned} r &= \frac{V_{\text{det}}}{V_{\text{tot}}} \\ &= \frac{V_{\text{det}}}{V_{\text{gap}} + V_{\text{det}}} \\ &= \frac{Q/C_{\text{det}}}{Q/C_{\text{gap}} + Q/C_{\text{det}}} \\ &= \frac{\frac{Qd_{\text{det}}}{\epsilon_0 k_{\text{det}} A}}{\frac{Qd_{\text{gap}}}{\epsilon_0 k_{\text{gap}} A} + \frac{Qd_{\text{det}}}{\epsilon_0 k_{\text{det}} A}} \\ &= \frac{d_{\text{det}}/k_{\text{det}}}{d_{\text{gap}}/k_{\text{gap}} + d_{\text{det}}/k_{\text{det}}} \end{aligned} \tag{2.10}$$

where Q is the biasing charge, ϵ_0 is the permittivity of free space, A is the area, d_{gap} and d_{det} are the width of the gap and detector, respectively, and k_{gap} and k_{det} are the relative permittivity of the gap and detector, respectively. Using the fact that $k_{\text{gap}} = 1$ since it is a

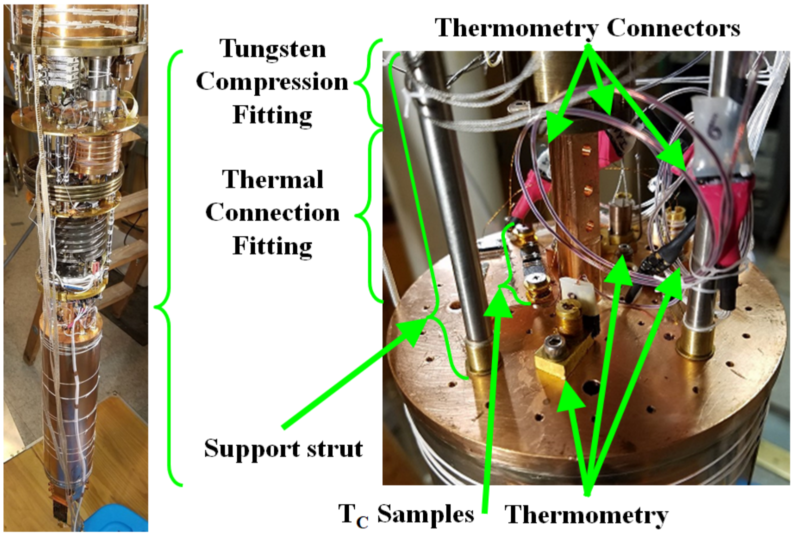

Figure 2.17: Two photographs showing the upper portion of the 10 mK stage with thermometers, wiring connections, and stages for mounting small experiments separate from the SuperCDMS-style detectors mounted at the bottom. Also shown are the struts that help support the 10 mK stage alongside the tungsten compressional fitting that provides the thermal contact. All of the parts shown in the picture on the right were designed and assembled in-house.

vacuum gap and simplifying Eq. 2.10 yields the width of the gap

$$d_{\text{gap}} = \frac{d_{\text{det}}}{k_{\text{det}}} \frac{1-r}{r}. \tag{2.11}$$

Plugging in the voltage ratio 2.9, the 1 cm thickness of the detector, and the relative permittivity of silicon at cryogenic temperature, which is about 11.45 [119], into Eq. 2.11 gives 317 ± 44 μm for the gap width, and the error bars are found via propagation of uncertainty.

The electrode contains an Am-241 calibration source with a lead collimator. On the side nearest the detector, the aluminum is thick enough to stop high-energy alpha particles but thin enough to allow some of the $\sim$20 keV x-rays to pass through. The thin aluminum layer also inadvertently reduces events with energies below $\sim$20 keV from the source.

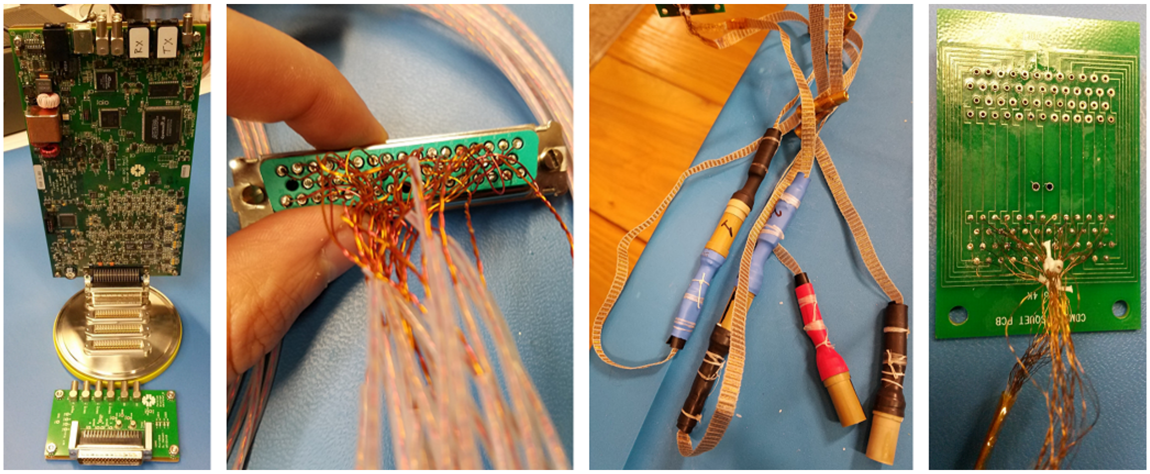

Figure 2.18: Photographs showing the electronics pipeline that includes, from left to right, legacy CDMS electronics (shown is the more recent detector control and readout card [DCRC], which serves the same purpose), room-temperature to cryogenic-temperature twisted pairs adapter, heatsinks for thermalizing the wiring to the 4 K stage, and the adapter that mates to the SQUET (SQUID-FET) board that is used to read out the detector. Note that all of the wires are in twisted pairs, with signal wires twisted with returns, to minimize the noise measured on the signal wires. That wiring scheme reduces cross-talk between neighboring wire pairs and reduces external electromagnetic interference on the signal lines. All of these parts, aside from the CDMS electronics, were designed and manufactured in-house.

We use a calibrated He-3 melting curve thermometer to measure the temperature of the mixing-chamber-anchored thermal stage to which the detector and high-voltage electrode are weakly thermally anchored. We use a Kelvinox-400 dilution refrigerator to cool the mixing chamber down to a temperature of $\sim$50-60 mK, and the QETs are tuned and kept at the bias point of the transition edge sensors via legacy CDMS II LabView software. Pulsing a light-emitting diode (LED) for several hours overnight while grounding the detector, a process referred to as LED "baking," neutralizes ionized impurities that may have accumulated while taking data during the day [76]. These ionized impurities can trap charges that can significantly degrade the detector performance, especially at low voltage bias [76, 120]. Therefore, by pulsing the LED, one can neutralize the impurities to reduce

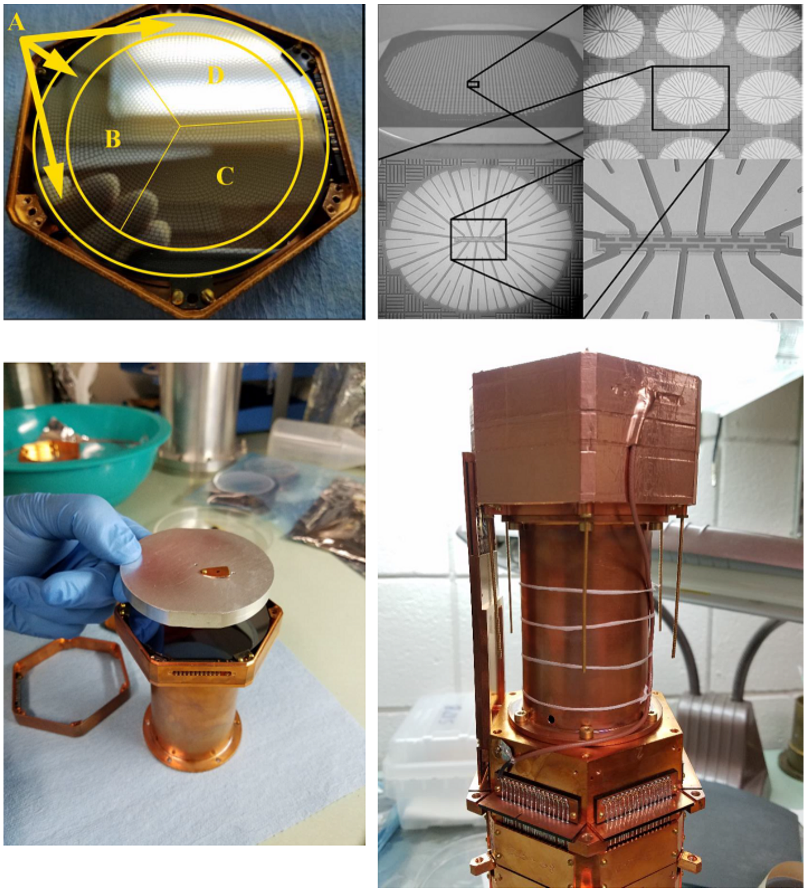

Figure 2.19: Photographs showing the geometry of detector S17B, with letters indicating the locations of the four detector channels, (upper left), a zoom-in of QETs (upper right), the aluminum electrode prior to installation above the detector (lower left), and the assembled detector housings with readout electronics stage referred to as the tower (lower right). Modified with permission from [117].

their risk of trapping charges by orders of magnitude [76, 120]. The LED was pulsed for 3 hours with a pulse every 2.5 milliseconds.

Legacy CDMS II hardware reads out the detector, which includes a Front-End Board (FEB), Receive Trigger Filter (RTF) board, a GPIB interface device to control the boards via computer, and power supplies for each board. The RTF board and power supplies are installed outside of the shielded room that houses the dilution refrigerator to minimize the

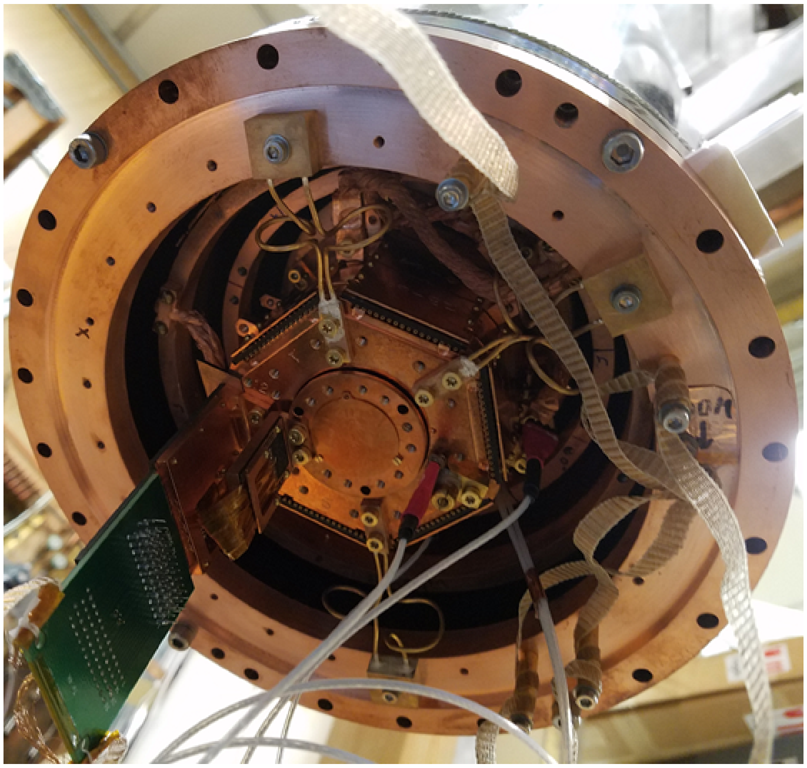

Figure 2.20: Detector tower with the SQUET, thermometry, and all heatsinks installed prior to closing up the dilution refrigerator.

electronics noise on the detector. A CAEN Mod. V1724 digitizer reads out the raw analog data directly from the RTF board. Although this is not standard SuperCDMS readout, it does mitigate the digitizer noise that was observed in data taken during Run 6 in late January 2018.

Figures 2.14, 2.15, 2.16, 2.17, 2.18, 2.19, and 2.20 further illustrate the detector characterization facility developed. Figure 2.21 shows how parts similar to these fit together for the CDMS experiment, which the Texas A&M setup imitates. The 400 μW dilution refrigerator was commissioned in 1988 for measuring crystallization waves at the liquid-solid interface of ^{4}He [121, 122]. It needed major modifications to accommodate SuperCDMS-style detectors, and the entire process took over two years to complete. The dilution re-

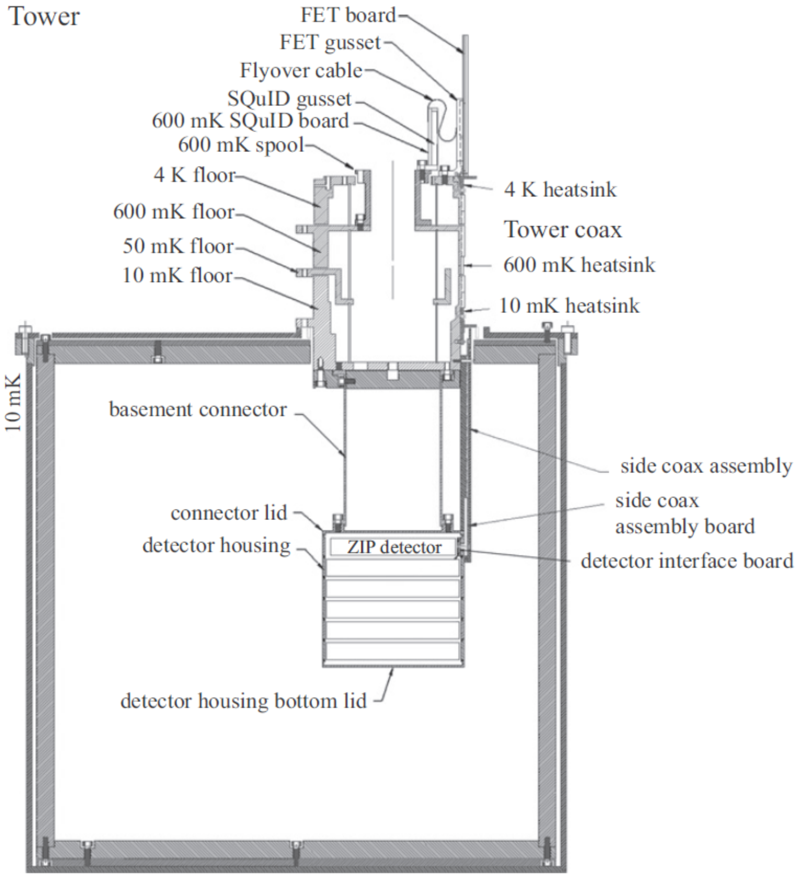

Figure 2.21: Diagram of a detector tower showing all of the relevant components as they might be installed for the CDMS experiment. The dilution refrigerator setup at Texas A&M was meant to replicate this general design as closely as possible due to the electronics amplifiers at different temperature stages as well as to mitigate the wiring and infrared radiation from higher-temperature layers from heating the detector. Reprinted with permission from [106].

frigerator heat shields, also referred to as cans, needed to be enlarged, so new 4 K, 600 mK, 100 mK, and 10 mK cans were designed and fabricated. Pictures of the new cans are shown in Fig. 2.15. SuperCDMS-style detectors need to be installed from the bottom of a dilution refrigerator with the cans already installed so that the detector housings and electronics can be properly thermalized to the cans. This is unlike most cryogenic experiments that can only be installed once all the cans are removed. Hence, a set of cryogenic

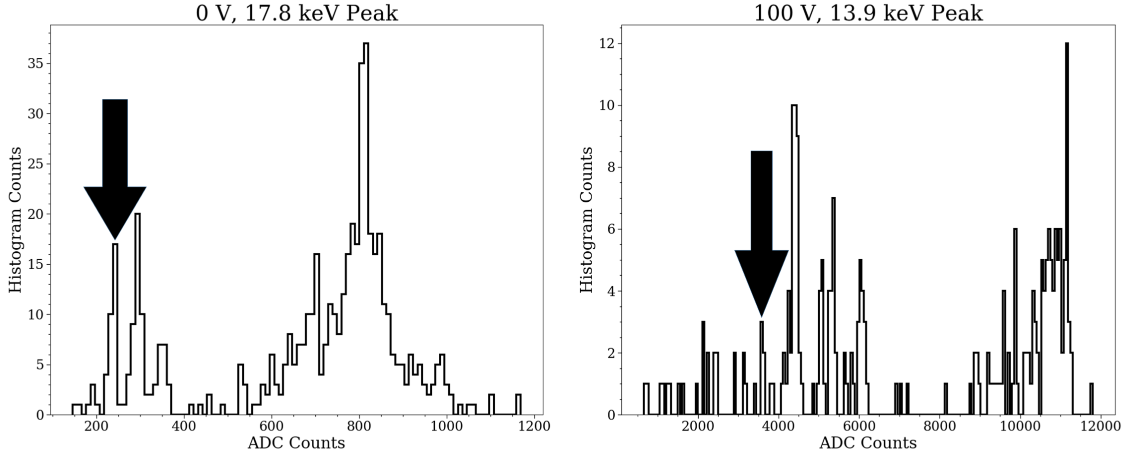

Figure 2.22: [Left] Am-241 spectrum at 0 V power supply bias with the 17.8 keV calibration peak indicated. [Right] Am-241 spectrum at 100 V power supply bias with the 13.9 keV calibration peak indicated.

flanges at the bottom of the 4 K can was required for thermalization and for holding vacuum. A cryogenic leak due to a mismatch of thermal expansion coefficient between the new flanges was diagnosed and fixed in the process.

Each detector requires 38 wires in a twisted-pair configuration for readout, which are connected to the detector housing via a cryogenic CDMS ribbon cable, commonly referred to as a stripline. However, since the existing piping inside the dilution refrigerator could not accommodate striplines, separate detector readout wiring needed to be made. Striplines use copper wiring to minimize parasitic resistance for the SQUID readout. However, copper wires also have a high thermal conductivity, which means that they transfer a large amount of heat from the connection at room temperature to the 4 K stage where they connect to the cold electronics. Consequently, beryllium-copper twisted pairs from CMR-Direct [123] were used to minimize the heat conductivity concern while minimizing the parasitic resistance [124]. This extra resistance may also have helped mitigate some of the electronic noise during detector operation. These wires are soldered to a custom adapter that mates to the CDMS SQUET, which is a combination of a FET amplifier for charge readout and the SQUID for phonon readout. The top of 2.21 shows a schematic of the SQUET assembly as well as the flyover cable connecting the SQUID to the FET board. The SQUET adapter is shown in the rightmost photograph in Fig. 2.18. The wiring pinout, which has signals twisted together with returns to minimize electronic noise, is shown in Table 2.23. Enough wiring was made to read out two detectors simultaneously.

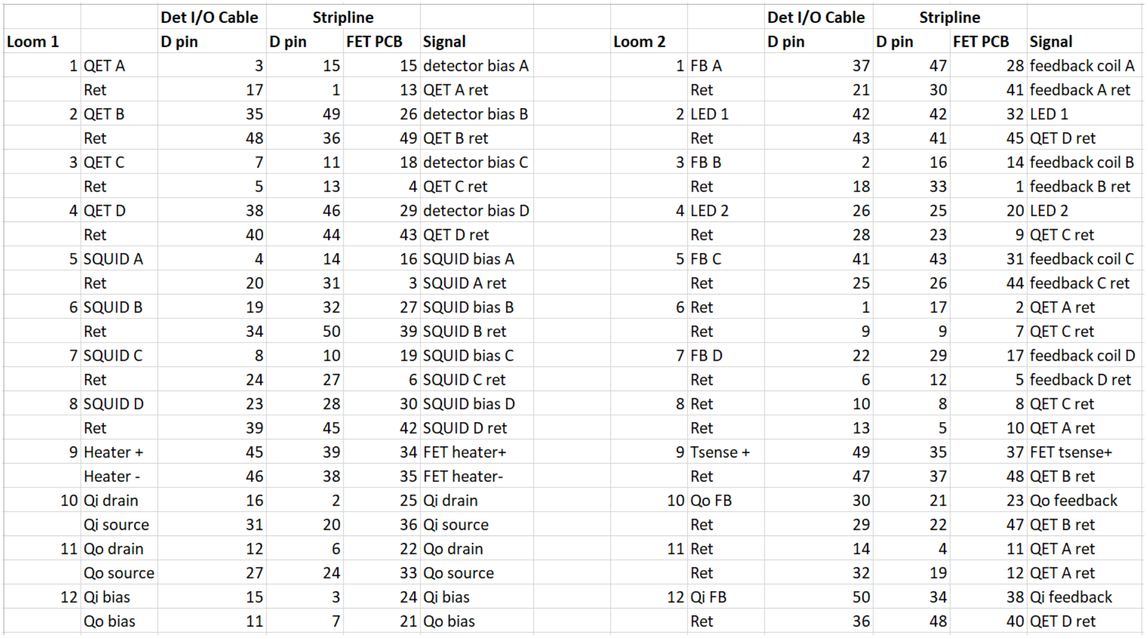

		Det I/O Cable	Stripline					Det I/O Cable	Stripline		
Loom 1		D pin	D pin	FET PCB	Signal	Loom 2		D pin	D pin	FET PCB	Signal
1	QET A	3	15	15	detector bias A	1	FB A	37	47	28	feedback coil A
	Ret	17	1	13	QET A ret		Ret	21	30	41	feedback A ret
2	QET B	35	49	26	detector bias B	2	LED 1	42	42	32	LED 1
	Ret	48	36	49	QET B ret		Ret	43	41	45	QET D ret
3	QET C	7	11	18	detector bias C	3	FB B	2	16	14	feedback coil B
	Ret	5	13	4	QET C ret		Ret	18	33	1	feedback B ret
4	QET D	38	46	29	detector bias D	4	LED 2	26	25	20	LED 2
	Ret	40	44	43	QET D ret		Ret	28	23	9	QET C ret
5	SQUID A	4	14	16	SQUID bias A	5	FB C	41	43	31	feedback coil C
	Ret	20	31	3	SQUID A ret		Ret	25	26	44	feedback C ret
6	SQUID B	19	32	27	SQUID bias B	6	Ret	1	17	2	QET A ret
	Ret	34	50	39	SQUID B ret		Ret	9	9	7	QET C ret
7	SQUID C	8	10	19	SQUID bias C	7	FB D	22	29	17	feedback coil D
	Ret	24	27	6	SQUID C ret		Ret	6	12	5	feedback D ret
8	SQUID D	23	28	30	SQUID bias D	8	Ret	10	8	8	QET C ret
	Ret	39	45	42	SQUID D ret		Ret	13	5	10	QET A ret
9	Heater +	45	39	34	FET heater+	9	Tsense +	49	35	37	FET tsense+
	Heater -	46	38	35	FET heater-		Ret	47	37	48	QET B ret
10	Qi drain	16	2	25	Qi drain	10	Qo FB	30	21	23	Qo feedback
	Qi source	31	20	36	Qi source		Ret	29	22	47	QET B ret
11	Qo drain	12	6	22	Qo drain	11	Ret	14	4	11	QET A ret
	Qo source	27	24	33	Qo source		Ret	32	19	12	QET A ret
12	Qi bias	15	3	24	Qi bias	12	Qi FB	50	34	38	Qi feedback
	Qo bias	11	7	21	Qo bias		Ret	36	48	40	QET D ret

Figure 2.23: Wiring pinout from room temperature cabling ("Det I/O Cable") to D connector inside vacuum fitting ("Stripline - D pin") to cryogenic temperature SQUET adapater ("Stripline - FET PCB") with the names of each signal and number on the connector indicated. The loom labels (1 or 2) correspond to the numbers written at the cryogenic end of the Cryoloom ® (odd Cryoloom ® labels to 1, even Cryoloom ® labels to 2).

The detector readout wiring is thermalized to the 4 K stage at two locations prior to connecting to the SQUET adapter, one near the upper vacuum chamber connection and another at a copper flange where the CDMS detector housing and wiring assembly, also called the tower, is installed. Different portions of the tower are thermalized to the 4 K, 600 mK, and 100 mK stages using heatsinks extending out from the lower ends of the cans, as shown in Fig. 2.20. These heatsinks were all made in-house using oxygen-free high-conductivity copper annealed in an argon atmosphere following Appendix A3.1 in Ref. [125]. Annealing the heatsinks increases the thermal conductivity by enlarging the grains that make up the copper in the heatsink.

The detectors are thermalized to the mixing chamber of the dilution refrigerator via its CDMS housing. The CDMS housing is made of OFHC copper, and it is mounted on the 10 mK stage of the tower, which is mounted on the bottom of the 10 mK can, as shown at the bottom of the left photograph in Fig. 2.17. The 10 mK can was also annealed to maximize thermal conductivity. The top of the 10 mK can has a column that connects to a tungsten compression collar on the dilution refrigerator mixing chamber, as shown near the top of the right photograph in Fig. 2.17. The plate at the top of the 10 mK can was used for mounting thermometers as well as for small experiments prior to commissioning the dilution refrigerator for SuperCDMS-style detector research and development. These experiments included measuring transition temperatures of superconducting tungsten samples as well as measuring leakage currents of interface materials in late 2015.

2.2 Detector Analysis

2.2.1 Progress in Interface Studies

Prior to the experimental run with the SuperCDMS-style detector S17B, a reference spectrum using the same collimator and source, except a slightly smaller lead collimator hole opening, was taken using a commercial detector at liquid nitrogen temperature. It was taken at the Texas A&M University Nuclear Science Center. Fig. 2.24 shows the spectrum of the Am-241 calibration source measured by an XR-100SDD silicon drift detector (SDD). The 13.9 keV, 17.8 keV, and 59.5 keV Am-241 lines [126] were used to calibrate

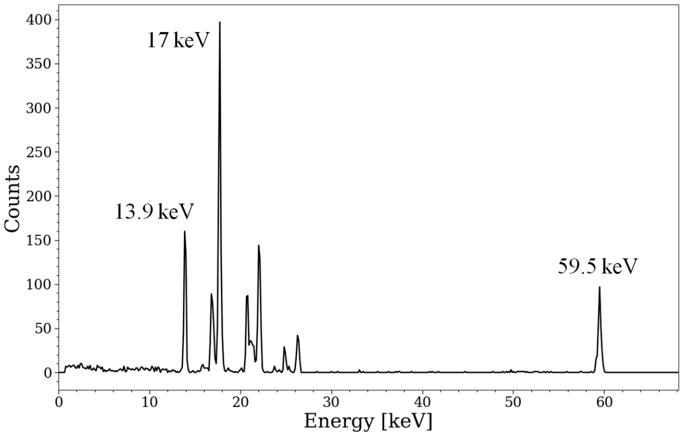

Figure 2.24: Spectrum of the calibration source inside the collimator and high-voltage vacuum electrode taken at the Texas A&M University Nuclear Science Center. The data were taken with an XR-100SDD silicon drift detector. The 13.9 keV, 17.8 keV, and 59.5 keV lines were used for the calibration since those could be easily identified.

the spectrum since they could be most easily identified. Comparison with the spectrum in [126] shows good agreement for the highest-energy lines. Because the XR-100SDD detector is physically much smaller than the SuperCDMS-style detector analyzed, it has a much lower efficiency at higher x-ray energies. That is the reason why the 60 keV line is much shorter in this spectrum than those shown later in this dissertation.

As discussed previously, a power supply applies a bias voltage across the detector. The amount of signal amplification increases with the bias voltage applied, as shown in Fig. 2.25. In the main plot, the total measured phonon energy is plotted as a function of applied voltage, which indicates the expected increase in energy measured as a function of voltage. The inset plot shows how the NTL effect causes the pulse heights to increase as a function of applied voltage. By increasing the measured signal via NTL gain, it is possible to significantly increase the signal-to-noise of SuperCDMS-style detectors since, in principle, NTL gain does not affect the noise level. This plot has been modified with

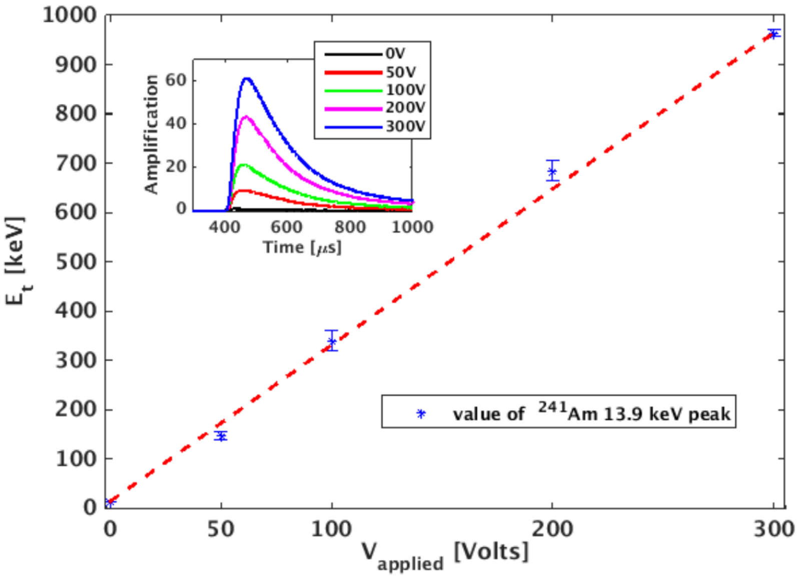

Figure 2.25: Nuclear recoil energy as a function of applied voltage. The Luke-Neganov effect is clearly seen as an increase in the pulse amplitude, whereas the noise remains constant [97]. Plot has been enlarged, reformated, and two sub-plots have been removed compared to the original version. Modified with permission from [97].

permission from [97] and [127].

The above amplification ceases to improve signal-to-noise for voltages greater than a threshold where leakage current dominates the electronics noise [80]. The resulting resolution degradation is shown by the red points in the rightmost plot in Fig. 2.9, which shows the resolution as a function of applied electric field across two different detectors. However, this leakage current can be somewhat mitigated using contact-free SuperCDMS-style detectors, such as G37R in the past [97] and S17B for this study. As the first in a series of tests with large-mass detectors, S17B uses a contact-free design with the polycrystalline silicon metal-semiconductor interface layer removed. This detector is 3 inches across, 1 cm thick, and uses the phonon layout presented in Fig. 2.19 [81]. The high-voltage aluminum electrode contains a collimated Am-241 source that is covered with a thin aluminum layer

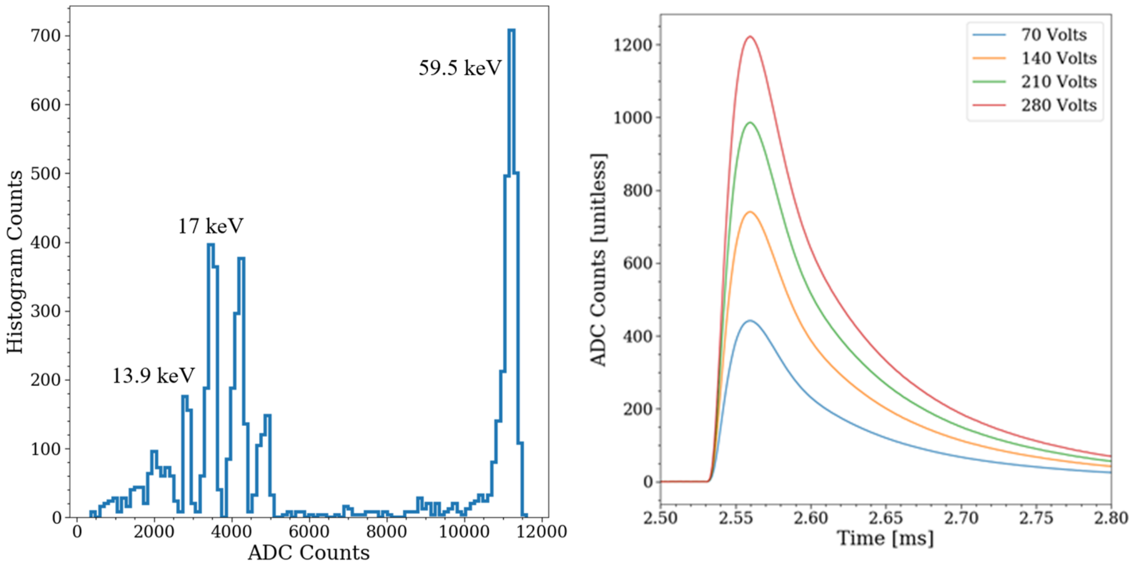

Figure 2.26: [Left] Am-241 events generated via an optimal filter template fit. These data are at 200 V bias at the power supply in reverse bias mode. Of the Am-241 peaks shown, the two peaks with the highest number of counts, in addition to the 13.9 keV peak used to generate the template, are indicated. [Right] Plot showing how NTL gain increases the signal traces as the voltage increases. Plot generated using a template from 13.9 keV traces scaled with respect to the detector voltages given. The factor of ∼0.7 scaling between the voltages comes from the fact that ∼70% of the voltage drop is across the detector due to the vacuum gap. Reproduced with permission from [117].

to prevent high-energy alpha particles from interacting with the detector. SuperCDMS Soudan electronics read out the detector via vacuum coaxial cables, a SQUID amplifier, and twisted pairs, in that order from coldest to warmest, all thermalized prior to the cold stage.

The results of this experiment are shown in Fig. 2.26 and 2.27. NTL amplification was observed up to 280 V bias across the detector, which includes the vacuum gap correction. This is shown in Fig. 2.26 at right, which allowed the main features of the Am-241 source to be resolved, as shown in Fig. 2.26 at left. Additionally, the noise remained relatively constant in positive polarity relative to the electrode, as shown in the leftmost plot in Fig.

2.27, which could be a significant improvement compared to the results in [97]. With the reverse voltage applied, as shown in the plot in Fig. 2.27 at right, significant leakage current as a function of voltage was observed, consistent with previous results [80, 97] with a similar setup with germanium detectors. Preliminary measurements of the leakage current in reverse detector bias seem consistent with values for other SuperCDMS detectors, such as those in Ref. [107], as further explained below.

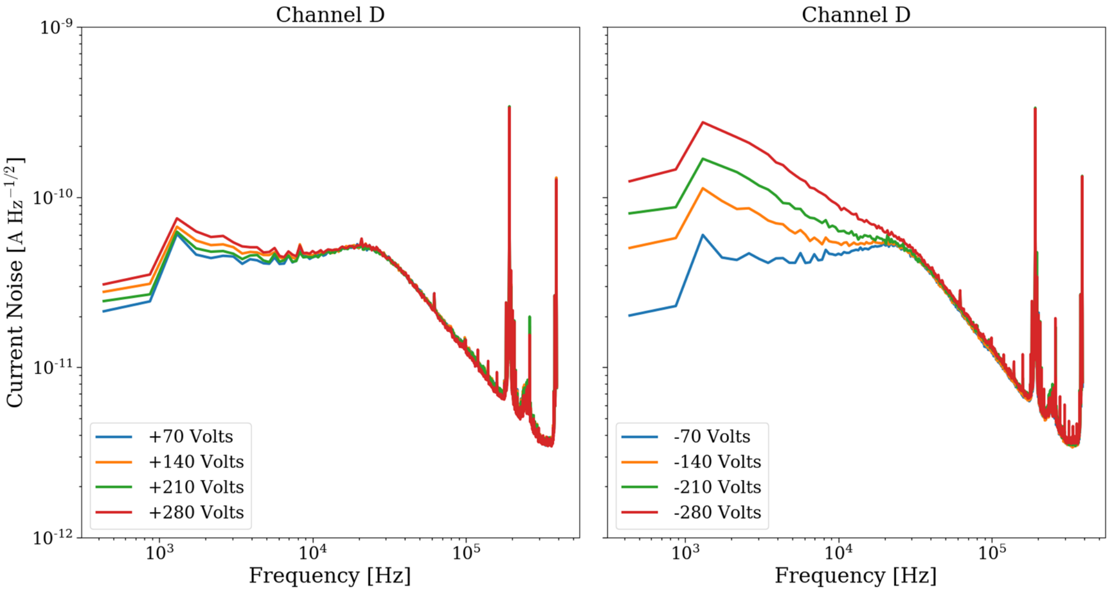

Figure 2.27: [Left] Noise power spectral density (PSD) for positive voltages for Channel D, the channel with the Am-241 source. Due to the asymmetric nature of the contact-free design, there is very little voltage-dependent leakage current at high voltages in this polarity. Compare to the results from [97], shown earlier in this work. The peak near 20 kHz is from the transition edge sensor Johnson noise. [Right] Noise PSD for negative voltages for Channel D. Due to the asymmetric nature of the contact-free design, negative polarity has much higher leakage current than positive polarity shown at left.

According to [76], an event pulse has two main components: the noise and the event pulse signal. Mathematically, this relation can be expressed as

$$v(t) = As(t) + n(t) \tag{2.12}$$

where $v(t)$ is a raw trace with the baseline subtracted, $As(t)$ is the pulse component, and $n(t)$ is a realization of the noise, which is assumed to be time-independent for this analysis. This form also assumes no nonlinearities, such as those due to transition edge sensor (TES) performance as a function of energy and event position on the detector. Thus, A represents the amplitude of the measured event, which is proportional to the event energy, and $s(t)$ is the normalized shape of an event.

One desires to optimally estimate the signal given the noise added to it. The usual procedure is to define a value of χ^2 whose minimum as a function of the parameter of interest corresponds to the best estimate of that parameter. In the case of particle interaction events, this means finding the best fit for A given the data that has the general form of 2.12. Following [76], the appropriate χ^2 is given by

$$\chi^2 = \int_{-\infty}^{\infty} \frac{|\tilde{v}(f) - A\tilde{s}(f)|^2}{J(f)}. \tag{2.13}$$

$\tilde{v}(f)$ and $\tilde{s}(f)$ represent the Fourier transform of $\tilde{v}(t)$ and $\tilde{s}(t)$, respectively. $J(f)$ is the power spectral density of the noise, which is given by the squared magnitude of the Fourier transform of the noise, as per [76]. Finding the minimum χ^2 as a function of the peak amplitude A gives the best fit to the peak.

According to [76], it can be shown that, following this minimization procedure, the best estimate of the amplitude given the χ^2 in 2.13 is

$$\widehat{A} = \frac{\int_{-\infty}^{\infty} \frac{\tilde{s}^*(f)\,\tilde{v}(f)}{J(f)} \mathrm{d}f}{\int_{-\infty}^{\infty} \frac{|\tilde{s}(f)|^2}{J(f)} \mathrm{d}f} \tag{2.14}$$

where $\tilde{s}^*(f)$ is the complex conjugate of $\tilde{s}(f)$. Thus, one can find the resolution of a detector by measuring the amplitudes of events from a monoenergetic source using Eq. 2.14. The width of this event distribution gives the resolution of the detector at a particular energy, as is commonly reported in the detector literature.

This general prescription runs into some problems in the case of SuperCDMS-style detectors because these detectors measure the phonon energy released from a particle interaction. When a voltage is applied across the detector to increase the signal-to-noise via Neganov-Trofimov-Luke (NTL) gain, the variation in the number of electrons produced during different particle interactions artificially worsens the detector resolution. For this reason, among others, one cannot use a distribution of events with voltage applied across a SuperCDMS-style detector to measure the detector resolution. At the same time, it is next to impossible to select only the events from a source when a SuperCDMS-style detector is run at zero volts bias.

Nonetheless, one can use the template generated from the average of many actual events to simulate the expected signal from a truly monoenergetic source. The signal read out by each channel for the Am-241 event can be used to scale each of the four channels in the template to resemble events coming from the Am-241 source. These templates are scaled by the approximate position of the 13.9 keV line and as many noise realizations as possible are added to those templates to simulate many such events. A Gaussian fit to the distribution gives a measurement of the detector resolution, as shown in Fig. 2.28 for one of the datasets at zero volts bias.

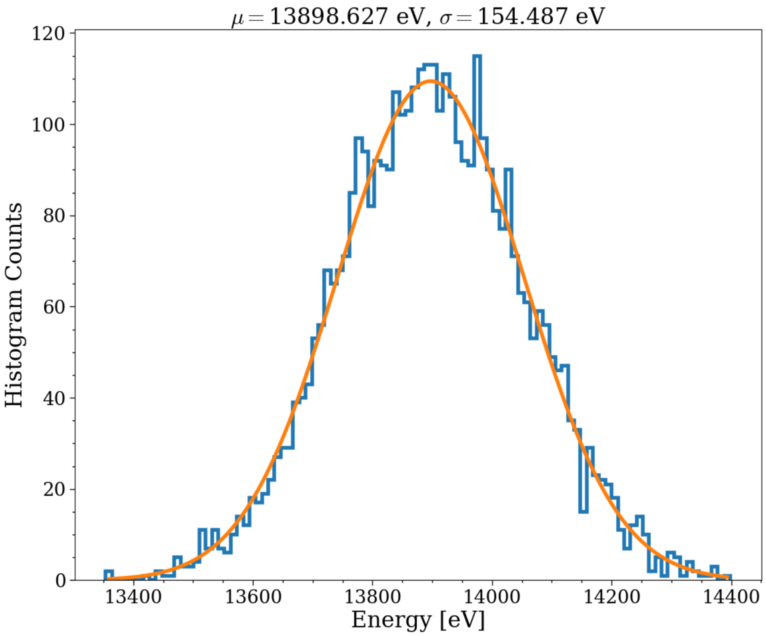

Figure 2.28: Histogram of artificial 13.9 keV Am-241 events at zero volts bias. The blue curve is the data, and the orange curve is a Gaussian fit to the data.

Since about 3.8 eV of energy deposited by a radioactive source corresponds to one electron-hole pair drifted across the detector, the energy resolution at zero volts can be used to estimate the expected resolution at high voltages. According to Fig. 2.28, the resolution at 0 V is about 154 eV. Thus, one expects about 4.2 eV resolution for the same detector and same noise performance at a voltage bias of 200 V since that voltage corresponds to about 140 V across the detector.

The detector, however, does not behave perfectly linearly at high total phonon energies, as shown in Fig. 2.29. This plot shows the ADC counts as a function of bias voltage for 13.9 keV events for several bias voltages. The bias voltage is measured from the power supply to the ground on the side of the detector with the sensors, and positive bias is defined so that the positive voltage is at the vacuum electrode. The energy is measured by summing the contribution from all four channels after linearly correcting for the falling pre-pulse baseline. A relative channel calibration of 1 is used between the four channels. Although the nonlinearity is not large, it does increase the higher the voltage bias.

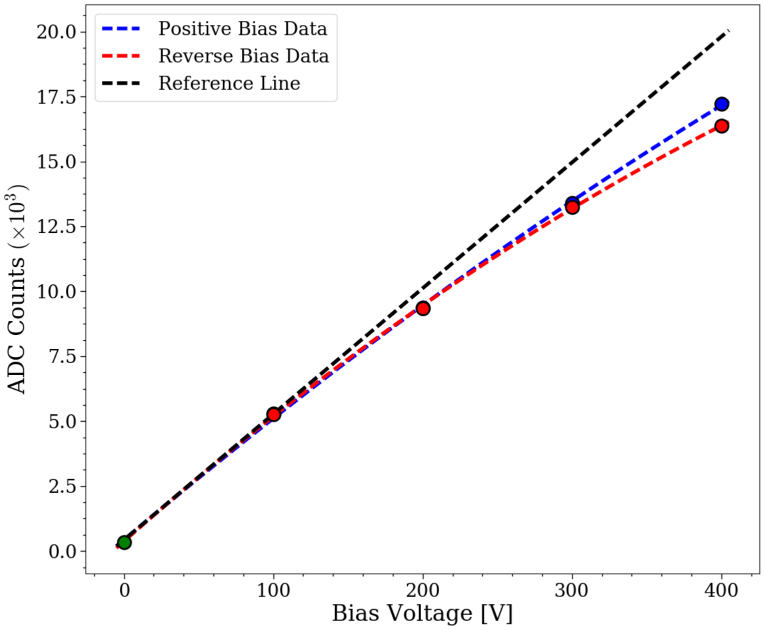

Figure 2.29: 13.9 keV Am-241 peak heights as a function of power supply bias voltage. Blue points and curves correspond to the detector operated in positive polarity, and red points and curves correspond to the detector operated in reverse polarity. The blue and red curves correspond to parabola fits to the blue and red points, respectively. The green point is data at zero volts bias, and the black curve is the linear component of the blue curve, which approximately shows the expected scaling were it not for detector nonlinearities as a function of total phonon energy.

The peak values thus calculated can be used to measure resolution as described earlier. The resolution as a function of voltage is shown in Fig. 2.30 for positive and reverse voltage bias. In agreement with previous results [97], the resolution continues to improve as the voltage is increased up to a certain voltage. In this case, this maximum is 400 V at the power supply, which corresponds to about 280 V across the detector. In reverse bias, on the other hand, the resolution degrades as a function of applied voltage because of an increasing leakage event rate as a function of voltage bias. These results could prove useful for designing large-mass dark matter detectors in the future, as well as for other applications discussed below.

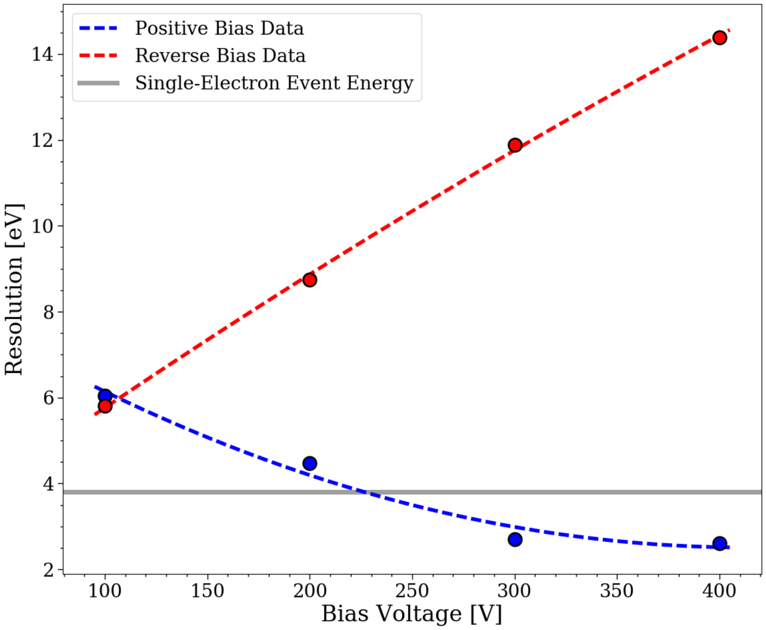

Figure 2.30: Detector resolution as a function of voltage for several voltages in both positive and reverse polarity. The curves show parabola fits to the data. Resolution is calculated by adding templates scaled to the height of a 13.9 keV event at that voltage bias to the noise data. The gray line shows the 3.8 eV expected energy for a single-electron event for comparison.

2.2.2 Future Directions

Given these preliminary results, such detector research could be taken in several future directions. These include setting limits on low-mass dark matter, similar to the work in

[83] as well as improving signal-to-noise via a higher phonon collection efficiency mask. Another possibility is to assess other candidate electrode interfaces, such as SiO_2, α-Si, and other dielectrics as well as to identify and mitigate infrared background, as observed in Ref. [96]. Once signal-to-noise is high enough, it may be possible to see single electron-hole pair events as in Ref. [96] using a low-intensity laser light source.

Detectors with an energy resolution, and hence energy threshold, as low as those possibly achieved in this work have many potential applications. I will describe one of the most important advantages of single electron resolution in the following chapters. If the process of defect creation is related to electron-hole pair production in semiconductor detectors, it could lead to directional solid-state detectors, as described in Ref. [102]. Such high-mass detectors with excellent resolution could pave the way for similar directional detectors in the near future. Similarly, these detectors could be directionally-sensitive to neutrinos from the sun via the same technique. Finally, these detector advancements could lead to high-resolution neutron detectors, with possible directional sensitivity, for commercial, government, or military applications.

3. DIRECTIONAL SIGNAL USING SINGLE ELECTRON RESOLUTION SEMICONDUCTOR DETECTORS

3.1 Introduction

As was mentioned earlier in this thesis, any type of dark matter experiment benefits significantly if it can discriminate particle interaction events that could be from dark matter from those that are definitely not from dark matter. However, most dark matter experiments have no direct way to tell whether a signal actually is from dark matter particles or simply resembles what one expects of dark matter particles, some examples of which are shown in Fig. 1.9 in the introductory chapter. As shown in Fig. 3.1, there are many different backgrounds that contribute to a dark matter search such as SuperCDMS [128] that can mimic the dark matter signal. Hence, even a detector with nuclear recoil versus electron recoil discrimination can be affected by background events such as those from the fringes of the detector volume, neutrons, and neutrinos.

A directional detector, on the other hand, could resolve this problem. That is because directionality would allow the detector to differentiate between the mostly isotropic backgrounds and dark matter that changes direction as a function of time, mostly due to Earth's rotation. Fig. 3.2 shows how this is possible. Even though detectors cannot track the dark matter particle directly, the recoiling detector nucleus can approximate the direction of the incoming particle. A fine-tuned analysis using this method could even allow the experiment to discriminate between dark matter and solar neutrinos, which are both time-dependent, anisotrpic signals and are discussed in greater detail later in this thesis.

Because of how useful directional detectors could be for dark matter searches, there has been a lot of research and development recently to make those detectors specifically for dark matter searches. Some of these detector technologies include those used for time-

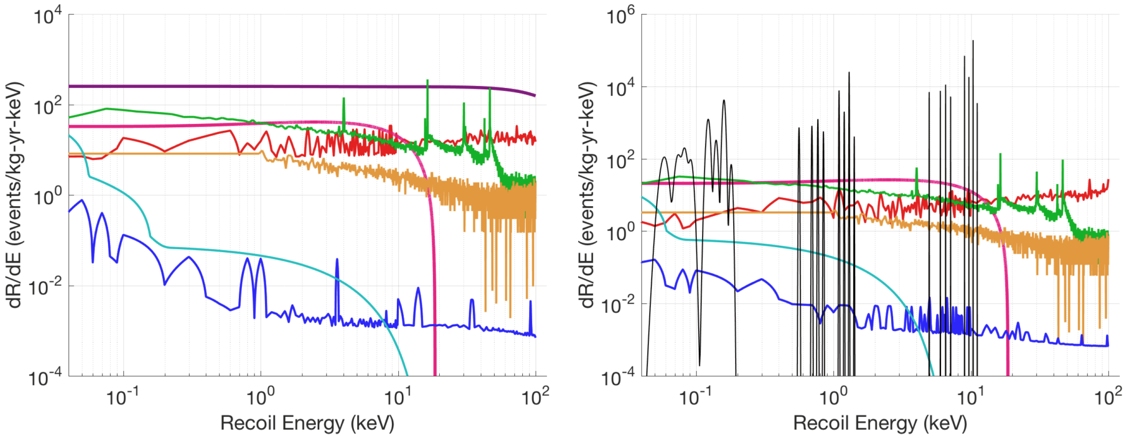

Figure 3.1: Background contributions to the SuperCDMS experiment calculated by Monte Carlo simulation for an Si (left) and Ge (right) detector. Each color represents a different component as follows: ^{3}H decays (pink), ^{32}Si decays (purple), Ge activation lines (black), with a 10 eV r.m.s. resolution expected for the Ge detector, Compton scatters from gamma-rays (red), detector surface beta decays from ^{210}Pb (green), detector surface ^{206}Pb recoils (orange), neutrons (blue), and coherent elastic neutrino-nucleus scattering (cyan). Figure reprinted with permission from [128].

projection chamber (TPC) experiments [94] and three-dimensional Charge-Coupled Devices (CCDs) used by DAMIC [129]. However, many of these technologies are very difficult to scale to large masses because they either require extremely large volumes (in the case of TPC detectors) or many small detectors (in the case of DAMIC CCD detectors), which limits their applicability for low cross-section dark matter searches.

Additionally, many experiments are searching for dark matter at masses below ∼10 GeV/c^2 due to recent signal claims, compelling theoretical models, and the lack of a convincing signal at higher masses [81]. This means that semiconductor detector experiments, such as SuperCDMS, need detectors with ever-lower energy thresholds to probe low-mass dark matter parameter space, as illustrated in Fig. 1.14. Additionally, SuperCDMS-style detectors discriminate nuclear recoils (potential signal) from electron recoils (likely background) progressively worse the lower the recoil energy. This is due to charge measure-

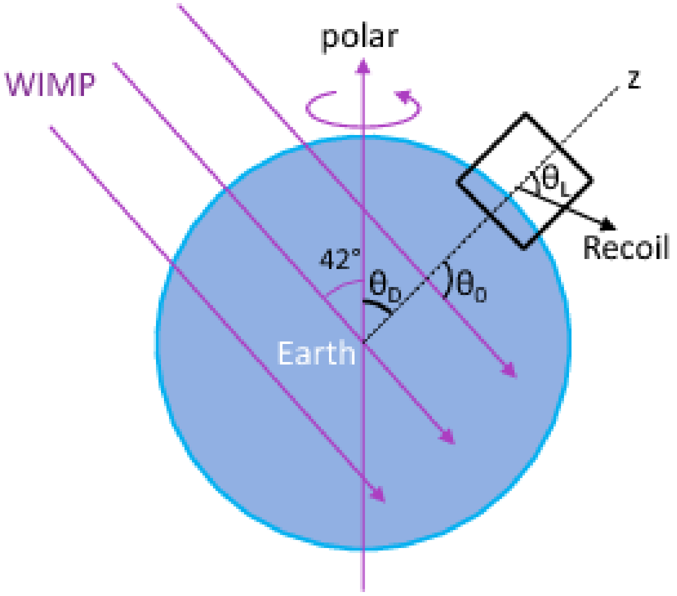

Figure 3.2: Schematic showing how a directional dark matter detector at a particular location on the Earth's surface could experience a diurnal signal modulation. The model detector is the black square, the dark matter wind is given by the purple arrows, and a nuclear recoil is indicated by the black arrow. Schematic reprinted with permission from [130].

ment fundamental noise limitations [102], among other reasons. On top of this, all dark matter experiments eventually need to contend with the so-called neutrino floor caused by coherent elastic neutrino-nucleus scattering from the Sun and other sources [131] that, realistically, can only be overcome with a directional dark matter detector [132, 72]. SuperCDMS-style detectors could also be sensitive to a directional signal, and understanding how that is possible requires an explanation of the physics behind SuperCDMS-style detectors.

3.2 Nuclear Recoil Ionization Process

Penetrating radiation of all forms, which mimics the behavior of certain dark matter models, produces long-lived defects in materials [133, 134]. This includes high-energy electromagnetic radiation, such as x-rays and gamma rays, that interact with the electrons in solid-state detectors, and other particles such as neutrons, which interact with the nuclei in solid-state detectors [86, 135, 136]. However, the amount of energy absorbed by the electronic structure of the material, and measured as electron-hole pairs in SuperCDMS-style detectors, relative to the energy dissipated as phonons varies depending on whether the particle initially recoils off an electron or a nucleus [137]. The ratio between the ionization and nuclear energy deposition is called the "Lindhard Factor" [85], and similar quantities often referred to in the literature are the ionization yield [107], quenching factor [138, 139], and stopping power [140].

The term "Lindhard Factor" refers to Lindhard theory, a theoretical framework for estimating the energy transferred to the electronic system versus the nuclear system during a particle interaction with the nucleus in a crystal lattice [140]. Lindhard theory makes several basic assumptions concerning the dynamics of the particle interaction:

1. Electron interactions with lattice atoms do not produce recoil atoms with large energies.
2. The energy due to atomic binding, on the order of a few eV, is small compared to the scale of the nuclear recoil energy so that the atomic binding energy can be ignored.
3. The overall energy transferred to the electronic system is much smaller than the difference between the initial energy of the particle and the energy transferred to the nucleus.
4. Nuclear and electronic collisions can be treated as independent processes.

5. The initial energy of the particle is large compared to the energy of the recoiling nucleus.

The resulting integral equation of Lindhard theory, equation 5.1 in Ref. [140], can only be solved computationally, except in a few simple cases. However, in the asympotic limit of large recoil energies, Ref. [140, 107, 141] give the average energy transferred to the nuclear structure according to Lindhard theory as

$$\bar{E}_{\mathrm{nr}} = \frac{\epsilon}{1 + kg(\epsilon)} \tag{3.1}$$

where

$$k = 0.133\frac{Z^{2/3}}{\sqrt{A}}, \tag{3.2}$$

which is the electronic stopping constant,

$$g(\epsilon) = 3\epsilon^{0.15} + 0.7\epsilon^{0.6} + \epsilon, \tag{3.3}$$

$$\epsilon = 11.5\ E_{\mathrm{nr}}\ (\mathrm{keV})Z^{-7/3}, \tag{3.4}$$

Z is the atomic number, and A is the mass number of the nuclei in the lattice. Hence, the ionization yield, given as

$$Y(E_{\mathrm{r}}) \equiv \frac{E_{\mathrm{elec}}}{E_{\mathrm{r}}} = \frac{E_{\mathrm{r}} - E_{\mathrm{nr}}}{E_{\mathrm{r}}}, \tag{3.5}$$

can be rewritten as

$$\bar{Y}(\bar{E}_{\mathrm{r}}) = \frac{kg(\epsilon)}{1 + kg(\epsilon)} \tag{3.6}$$

since, in this limit,

$$E_{\mathrm{r}} = \bar{E}_{\mathrm{nr}} + \bar{E}_{\mathrm{elec}}. \tag{3.7}$$

The results of these equations are shown in Fig. 3.3. This Figure shows several quenching factor measurements in germanium (Ge), alongside two Lindhard theory approximations using different values for the electronic stopping constant k.

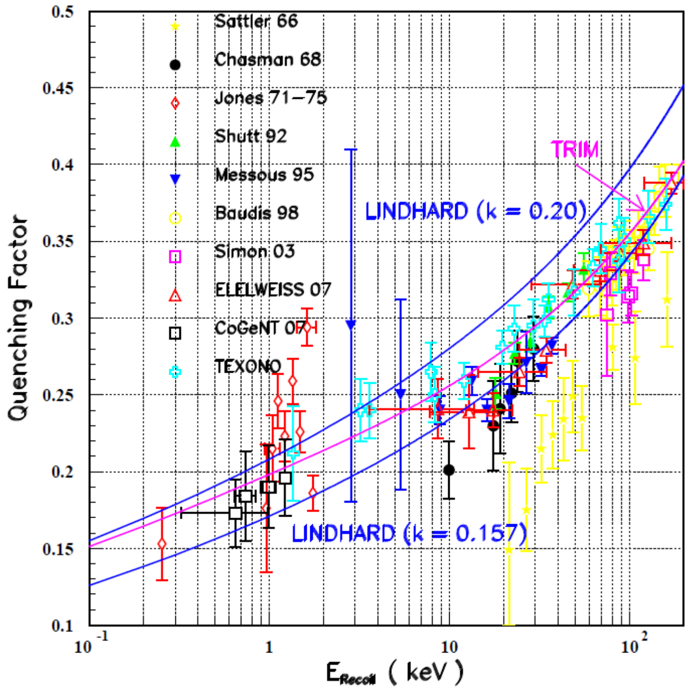

Figure 3.3: Plot showing the measured quenching factor as a function of recoil energy in a Ge detector. Reprinted with permission from Ref. [139].

Nonetheless, recent experimental and computational results [142, 143, 144, 145] indicate that Lindhard theory breaks down at nuclear recoil energies that approach the defect creation energy scale [146, 147]. This fact corroborates experiments that have measured the ionization threshold [148, 149] and computations that have simulated it [150, 151]. At low energies, the nuclear recoil energy becomes comparable to the energy of the bonds between atoms in the lattice, which violates assumption 2.

Currently, no computer models or experimental data can precisely predict the minimum energy required for electron-hole pair production due to nuclear recoils, especially as a function of recoil direction. On the other hand, a finite amount of energy is required to produce a defect since the recoiling atom ends up at a higher potential energy than it had to begin with [143]. This energy needed varies from material to material and even varies with the direction of the recoiling atom [134, 136, 152]. Additionally, computational and experimental data indicates that the threshold displacement energy is comparable to that of defect creation in semiconductors [153, 143, 146, 147] and that the ionization yield for materials is highest in directions with lower threshold [151, 154]. Calculations carried out by Dr. Andrea Sand in the Professor Kai Nordlund group, to be published soon, analogous to the time-dependent density functional theory calculations carried out in Ref. [153] further corroborate these observations.

Taken together, the threshold displacement energy, efficiently approximated using classical potentials, can be used as a proxy for the ionization threshold, which requires more computationally-intensive calculations to find. Hence, the anisotropic variation in threshold displacement energy can be used to look for the expected diurnal modulation of a dark matter signal [102]. The directional effect is mostly relevant for nuclear recoil interaction energies at the scale of $\sim$1 electron excitation. One loses directional information for large-mass WIMPs without recoil energy binning. Nonetheless, the effect benefits directional low mass dark matter searches. Additionally, the fact that low-energy nuclear recoils produce defects whereas low-energy electron recoils do not means that, in principle, the energy not measured because a defect is created can be used to discriminate nuclear recoils from electron recoils. In this chapter, I explore how the first of these processes, the anisotropic threshold for defect creation, could affect the dark matter rate. The energy loss due to defect creation is further discussed in the next chapter.

3.3 Anisotropic Threshold for Defect Creation and Its Effect on Dark Matter Rate*

Many astrophysical observations indicate that standard model particles compose only 15% of the matter in the universe [1]. Understanding the nature of dark matter, the remaining 85%, is of fundamental importance to cosmology, astrophysics, and high energy particle physics. Although Weakly Interacting Massive Particles (WIMPs) of mass 10-100 GeV/c^2 have been the main interest of the majority of direct dark matter detection experiments, recent signal claims, compelling theoretical models, and the lack of a convincing signal at those masses have shifted the old paradigm to include broader regions in the dark matter parameter space well below 10 GeV/c^2 [81].

Direct detection experiments attempt to detect WIMPs via their elastic interaction with detector nuclei [155]. Since very low energy nuclear recoils and small interaction rates from these low-mass WIMPs are expected, large-mass detectors with very low threshold are desirable. Solid state detectors, especially those utilizing phonon-mediated readout technology, have already reached the sensitivities required to detect these very-low-mass WIMPs or are braced to do so [156].

Both reducible (environmental) and irreducible (solar neutrino) backgrounds that may mimic WIMPs affect WIMP direct search experiment sensitivity. A potential tool to circumvent these backgrounds is the directionality of the WIMPs' signal due to Earth's motion through their isothermal halo distribution in our galaxy. The WIMP velocity distribution in the lab frame, and hence the expected direction of the WIMP-induced recoils, varies daily depending on the angular orientation of the detectors with respect to the galactic WIMP flux.

Although many experiments propose to track WIMP-induced recoils using low-pressure

---

*Reprinted with permission from F. Kadribasic, N. Mirabolfathi, K. Nordlund, A. E. Sand, E. Holmström, and F. Djurabekova, "Directional Sensitivity In Light-Mass Dark Matter Searches With Single-Electron Resolution Ionization Detectors," *Phys. Rev. Lett.*, vol. 120, no. 11, p. 111301, Copyright 2018 by American Physical Society. [Online]. Available: https://doi.org/10.1103/PhysRevLett.120.111301.

gas or even liquid scintillators, they do not offer low enough energy thresholds to detect recoils from low-mass WIMP interactions ($<$1 GeV/c^2) [94]. Furthermore, low-pressure-gas detectors require prohibitively large volumes to detect any WIMP signal. We argue that single-electron resolution phonon-mediated semiconductor detectors, such as those in development for SuperCDMS and future generation-3 dark matter experiments, are sensitive to the nuclear recoil direction and can be used for a directional dark matter search. Our method uses the fundamental processes involved in nuclear recoil ionization excitation, whose threshold exhibits a strong recoil direction dependence. Recent progress on phonon-mediated detectors, especially Neganov-Luke phonon amplification detectors [95], promises future large-mass semiconductor detectors with single-electron resolution [97].

Neither a computational framework nor experimental data exists to estimate the minimum energy required to create single electron-hole pair excitations via nuclear recoil interactions. We assume that this ionization threshold is correlated to the minimum energy required to eject the recoiling nucleus permanently to a crystal defect position (threshold displacement energy). Three recent observations motivate this. First, strong recent experimental and theoretical evidence indicates that a threshold in the ionization (electronic stopping) exists at low projectile energies [157, 144, 149, 145, 153]. Second, the threshold displacement energy is generally lowest in crystal directions where the recoil immediately hits a neighboring atom in a strong collision [146, 147]. Third, time-dependent density functional theory calculations show that the ionization is highest in such strong collisions [154, 151, 153]. Taken together, these three observations provide strong evidence that the ionization has a threshold which is firmly correlated to the displacement energy. To provide a framework for the subsequent calculations, we propose the simplest form of this correlation, *i.e.* proportionality, and we compute the expected WIMP rate interaction with the proportionality coefficient equal to 1 and 0.5 respectively. Below, we demonstrate that the threshold for the lattice defect creation process, and thus the ionization excitation via nuclear recoil, strongly depends on recoil angle.

We consider the threshold variation for two common detector materials, Ge and Si. For both, density-functional theory (DFT) molecular dynamics (MD) simulations previously have obtained the average threshold displacement energy and the direction-specific values in the $\langle 100\rangle$ and $\langle 111\rangle$ crystal directions [146, 147]. Due to the high computational cost of DFT, we calculate the full threshold displacement energy surface using a less-expensive method - MD simulations [158] with classical interatomic potentials, following the procedure described in Ref. [159].

Put succinctly, a 4096 atom Ge or Si simulation cell was equilibrated at 0.04 K (an upper limit for the experimental detector temperature), giving all atoms random thermal displacements. After this, an atom was randomly chosen within the central eight unit cells of the simulation cell and given a recoil of energy E in a randomly selected direction (θ, ϕ) in three dimensions, where θ is defined as the polar angle off the [001] crystal direction and ϕ as the azimuthal angle from the [100] direction towards [010]. The evolution of the collision sequence thus generated was simulated for 10 ps, and we analyze possible defect creation automatically using Wigner-Seitz and potential energy criteria [159]. For each atom and direction, the energy E was increased from 2 eV in steps of 1 eV until a stable defect was created.

The outcome of MD simulations depends crucially on the interatomic potential used [158, 159]. Hence, for the purpose of this study, we compared several different Ge and Si interatomic potentials with the DFT results. Among the three tested interatomic potentials for Ge [160, 161, 162], the modified Stillinger-Weber (SW) potential from Ref. [161] reproduced all of the reported DFT threshold displacement energies [147] within the error bars, giving us high confidence of a reliable description of the entire data range. Hence, this potential was used for all Ge simulations. We have previously shown that, out of three commonly used Si potentials, SW [163] reproduces the DFT and experimental results the best. Consequently, we use this potential to calculate the rates in Si.

In total, we simulate about 85,000 directions for Ge and about 24,000 for Si a total of eight times. Fig. 3.4 illustrates the average over the resulting threshold displacement energy surfaces for Ge and Si. The symmetry of the diamond crystal structure causes the periodicity with respect to $\phi = 45^\circ$, and the zero-point quantum motion of atoms in the lattice causes the graininess in the plots. Fig. 3.4 shows that the energy threshold to create a defect strongly depends on the nuclear recoil direction. The Ge threshold ranges from 12.5 eV to 63.5 eV whereas that for Si ranges from 17.5 eV to 77.5 eV.

The expected total WIMP signal rate above the detection threshold can be calculated by integrating the differential rate over the recoil angle and recoil energy. In the case of a charge detector (assuming that defect and electronic excitation thresholds are equal), the energy thresholds, henceforth referred to as $E_{th}(\theta, \phi)$ and shown in Fig. 3.4, simply provide the lower limit to the integral

$$R(t) = \oint_{4\pi} \int_{E_{th}(\theta,\phi)}^{E_r^{max}} \frac{\partial^2 R}{\partial E_r \partial \Omega_r} \mathrm{d}E_r \mathrm{d}\Omega_r. \tag{3.8}$$

This rate, measured by a fixed detector on the surface of Earth, which is moving and rotating relative to the WIMP halo, should, therefore, exhibit a diurnal modulation since E_{th} is a function of θ and ϕ.

We calculate signal rates assuming a detector with 1 eV resolution, 100% detection efficiency, and no backgrounds. We perform the integral in Eq. A.19 over the recoil energy E_r and recoil angle Ω_r using 48 time steps on September 6, 2015. The date was chosen to cross-check our differential rate calculations with those in Ref. [72]. An equidistant coordinate partition interpolation of the data shown in Fig. 3.4 is performed on a grid with 2400 elements in the θ direction and 4800 in the ϕ direction. For faster computation, the

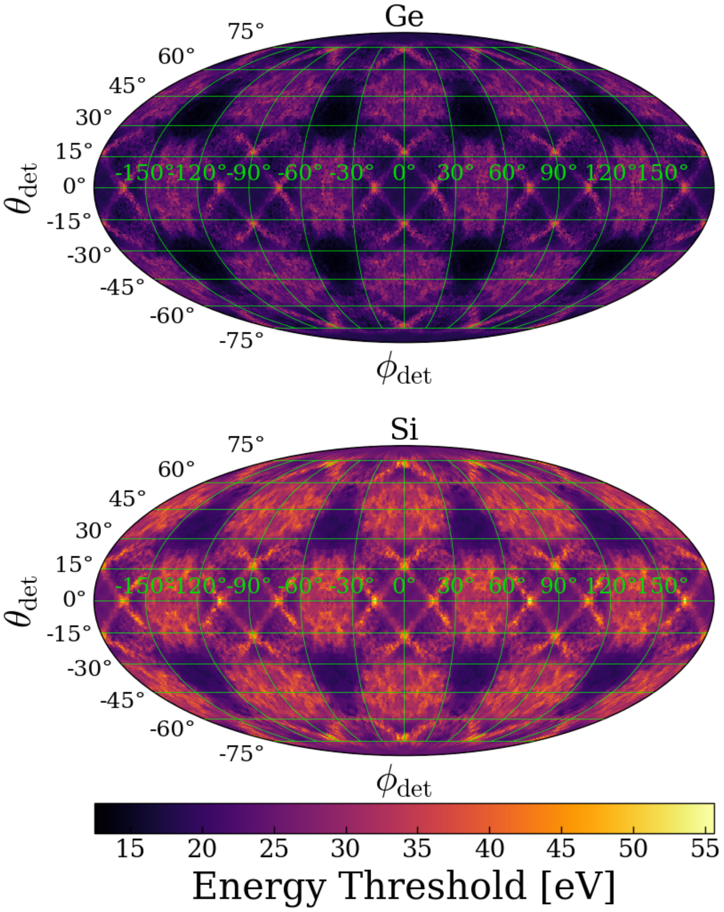

Figure 3.4: Threshold displacement energy surface in different crystal directions in Ge (top) and Si (bottom) determined from classical molecular dynamics simulations assuming the Stillinger-Weber potential and illustrated with a Mollweide projection. These plots represent the averages over the eight threshold surface datasets. Darker regions correspond to a lower energy threshold and, hence, a higher differential rate (see Fig. 3.5).

grid is resampled to a size of 196,608 pixels using the HEALPix algorithm [164]. We compute a multidimensional Riemann sum over each dimension with 200 sample points for E_r and 196,608 for Ω_r.

Fig. 3.5 shows the integrated event rate for a WIMP of mass 300 MeV/$c^2$and cross section $\sigma_{\text{WIMP-nucleon}}$=$10^{-39}$cm^2 over the course of one day (Sept 6 2015). The mass and cross

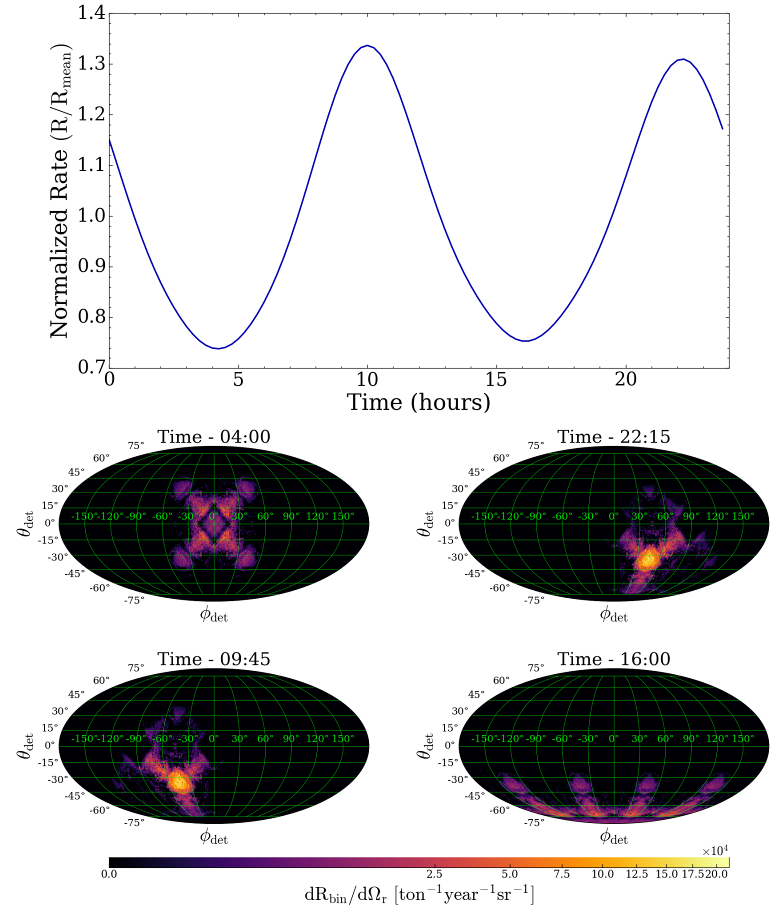

Figure 3.5: (Top) Normalized integrated rate with respect to mean over one day for a 300 MeV/c^2 WIMP at the SNOLAB site. (Bottom) Angular distribution of differential rate per steradian for a nucleon cross section of 10^{-39}cm^2 over one day for a 300 MeV/c^2 WIMP at the SNOLAB site. Each angle plot corresponds to a local extremum of the integrated rate.

section were arbitrarily chosen within the unexplored region in the halo WIMP parameter space. Also shown in this figure are the angular distributions of the rates at four different times illustrating recoil orientation change with respect to the crystal over the course of the day. As Earth rotates, more events are detected at the energy minima than the maxima, which leads to an integrated rate modulation (in this case $\sim$60%) with a phase imposed by the threshold data in Fig. 3.4.

We repeated this study for WIMPs covering a mass range between 230 MeV/$c^2$and 10 GeV/c^2in Ge and between 165 MeV/$c^2$and 10 GeV/c^2in Si. Lighter-mass WIMPs do not produce stable defects or electron-hole pair excitation even when traveling at the escape velocity $v_{\text{esc}} = 544$ km s^{-1}. Fig. 3.6 shows the recoil angular distribution in Ge at a given time (4:00 on September 6, 2015) for a sample of WIMP masses in this range. As shown in this figure, larger mass WIMPs produce a broader recoil angle distribution. Hence, the integrated signal rate associated with larger mass WIMPs is less sensitive to the crystallographic orientation of the detector. We expect smaller event rate modulation for larger mass WIMPs due to this effect.

To assess the strength of the signal rate modulation with respect to the signal mean rate, we perform a normalized root-mean squared (RMS) modulation integral over one day

$$R_{\text{RMS, norm}} = \sqrt{\frac{1}{\langle R\rangle^2 \Delta t} \oint_{\Delta t} (R(t) - \langle R\rangle)^2 dt} \tag{3.9}$$

where $\langle R\rangle$ is the average value over Δt, which is one solar day (24 hours). The results of these studies are shown in Fig. 3.7. We find a clear rate modulation for WIMPs of mass below 1 GeV/c^2. As expected, while the signal mean rate (thicker graph) decreases at lower WIMP masses, the modulation gains strength, which enables the experiments to maintain their signal to background ratio by only looking at the time intervals when the signal rate is maximized. Furthermore, since the Si nucleus is less massive than that of Ge, the energy transfer from a WIMP is more efficient; hence, a lower WIMP mass is required to transfer recoil energy sufficient to overcome the threshold displacement energy. Consequently, the peak of the modulation appears at lower WIMP masses for Si than for Ge.

The SW potential used in this report to produce Si threshold data in Fig. 3.4 overestimates the minimum threshold energy in the $\langle 111\rangle$ direction [165]. We expect the modulation to peak at lower WIMP masses for Si than those found in this paper when this

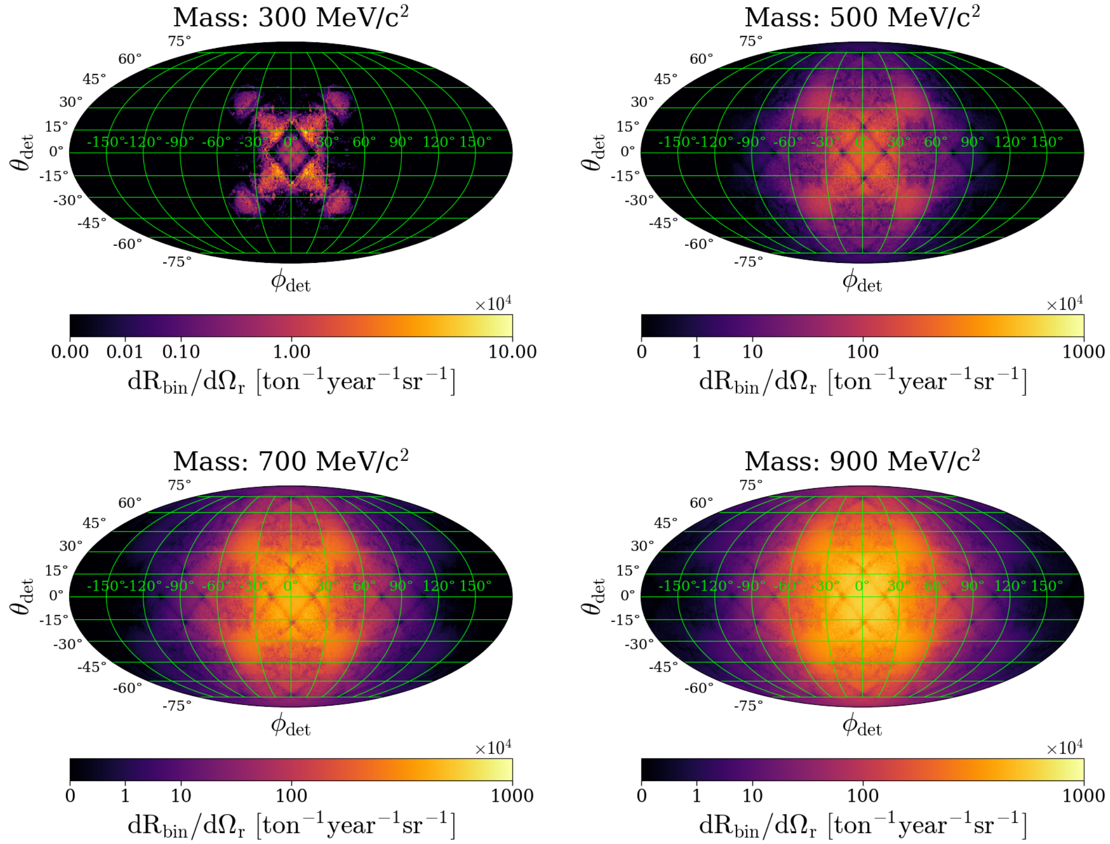
Mass: 300 MeV/c^2

Mass: 500 MeV/c^2

Mass: 700 MeV/c^2

Mass: 900 MeV/c^2

Figure 3.6: Angular distribution of differential rate per steradian for a Ge detector assuming a nucleon cross section of 10^{-39}cm^2 for several WIMP masses at 4:00 on September 6, 2015. As the WIMP mass increases, the differential rate angular spread increases due to the Maxwell-Boltzmann velocity distribution and hard-sphere scattering acting in conjunction with the energy thresholds (see Fig. 3.4).

experiment is carried out, which could also result in a higher overall modulation for Si.

The stochastic threshold displacement caused by the zero-point quantum motion of atoms was included based on the Debye model, which allows calculating the one-dimensional RMS displacement amplitude [166, 167].We calculate eight separate threshold datasets for Ge and Si using MD simulations. In Fig. 3.7, the RMS curves and shaded regions show the mean and standard deviation of the normalized RMS modulation values over all eight datasets. The kinks in the normalized RMS modulation curves correspond to the various

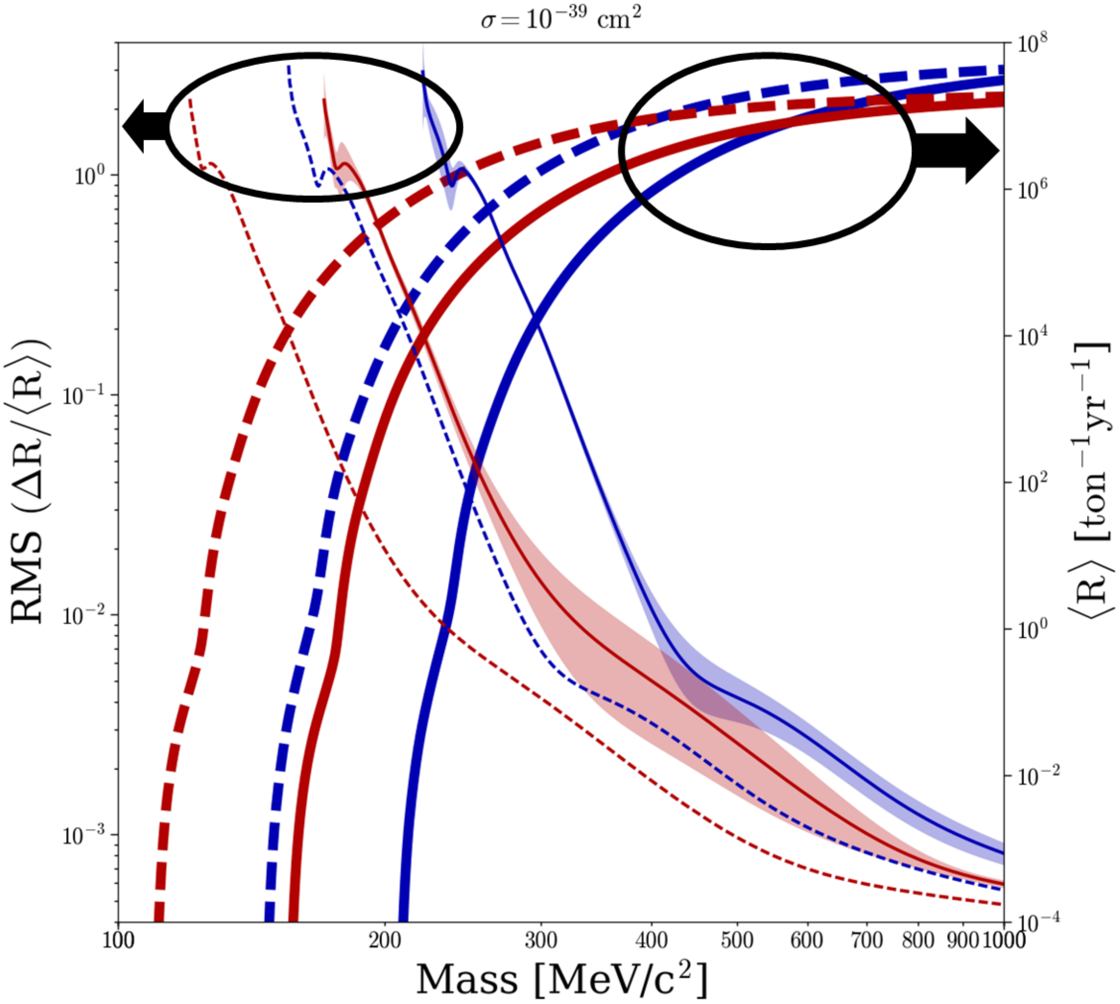

Figure 3.7: Normalized RMS of the rate modulation (left axis, thin lines) and mean rate (right axis, thick lines) as a function of dark matter mass for Ge (blue) and Si (red). Ovals and black arrows indicate which curves correspond to which axis. A WIMP-nucleon cross section of 10^{-39}cm^2 is assumed. Normalized RMS modulation error is given by the shaded regions. Mean rate error is negligible and consequently not included. The thick and thin dashed curves show the normalized RMS modulation and mean rate given thresholds half of those used for the solid curves. Modified with permission from [102].

length-scale transitions in the energy threshold shown in Fig. 3.4, which reveal themselves due to the larger solid angle coverage at higher dark matter masses.

We reproduce the normalized RMS modulation and mean rate using energy thresholds 50% of those in Fig. 3.4 as dashed curves. As expected, there is a clear diurnal modulation, albeit at lower masses. This work provides strong motivation for experimental validation of the energy thresholds for ionization excitations via nuclear elastic scattering in Ge or Si.

Based on the substantiated evidences for the threshold dependence on the nuclear recoil direction, we project a strong diurnal modulation in the expected detection rate of galactic halo WIMPs. This modulation strongly depends on the target detector material and WIMP mass, and, together with the overall mean rate, it provides an extra handle to determine WIMP mass and cross section independently. This effect can be used to discriminate WIMPs from solar neutrino backgrounds that will become the irreducible background for all dark matter search experiments. Even if future experiments find different ionization thresholds, the anisotropy predicted for electron-hole pair creation could still cause modulation in dark matter signal, albeit over a different mass range. The significance of these results motivates thorough semiconductor detector calibration at low recoil energies.

3.4 Other Defect Creation Energy Threshold Applications

3.4.1 Solar Neutrino CENNS

The presence of the modulation effect could have a widespread impact on the field of dark matter direct detection experiments, the most straightforward of which is the daily modulation that can be used as a signature of dark matter. Additionally, because the strength of the integrated rate modulation is a function of the dark matter mass, this effect could provide another handle to set limits on dark matter mass. Similarly, defect creation anisotropy could be used to discriminate dark matter from the otherwise indistin-

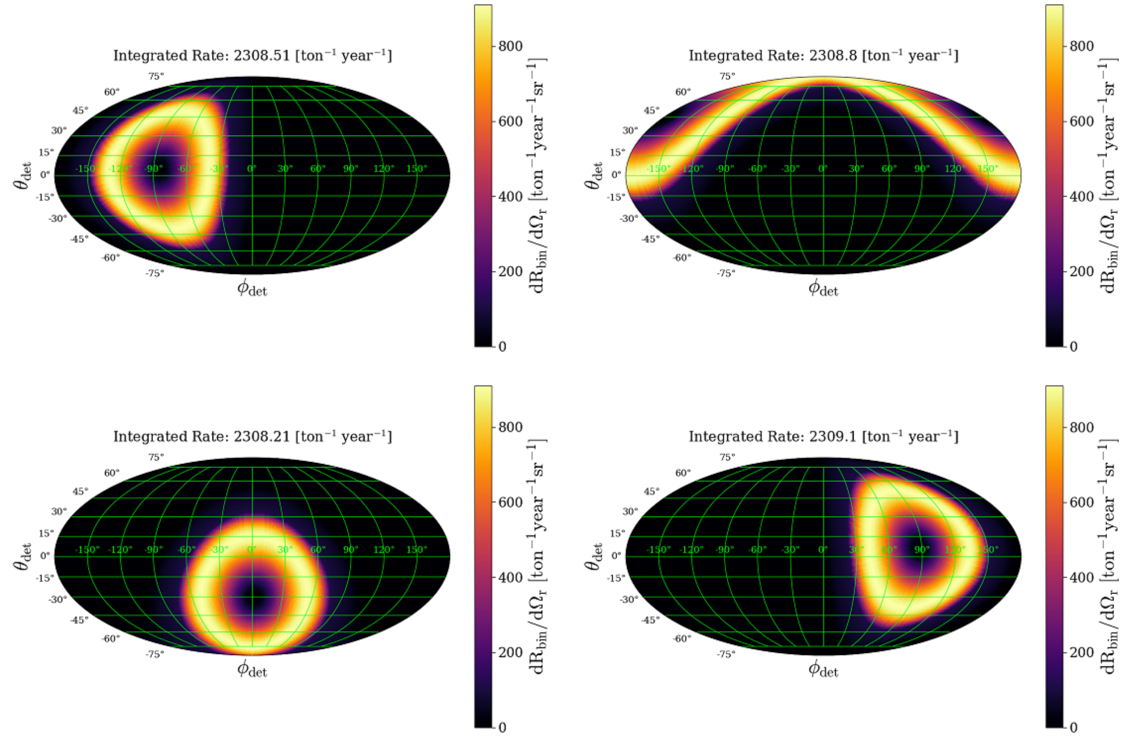
Integrated Rate: 2308.51 [ton^{-1} year^{-1}]

Integrated Rate: 2308.8 [ton^{-1} year^{-1}]

Integrated Rate: 2308.21 [ton^{-1} year^{-1}]

Integrated Rate: 2309.1 [ton^{-1} year^{-1}]

Figure 3.8: The differential rate per unit steradian for all solar neutrinos at several times over the course of a day for a germanium (Ge) detector assuming a constant energy threshold for nuclear recoils of 1 eV. The upper left is 6 a.m., upper right is midnight, lower right is 6 p.m., and lower left is noon on September 6, 2015 at Modane Undergound Laboratory (45.1966°N, 6.6668°W) for easier comparison with Ref. [72]. All rates are integrated up to 100 eV nuclear recoil energy.

guishable solar neutrino signal, which should also have a diurnal variation, except with a different phase. All of this could be investigated by finding the signal modulation expected from solar neutrinos and running a likelihood analysis to see how well the directionality due to defect formation can actually be used to discriminate a potential dark matter signal from solar neutrinos.

Given the fact that the solar neutrino rate changes direction over any given day, because the Sun's position in the sky changes, the defect creation effect discussed in § 3.3 should

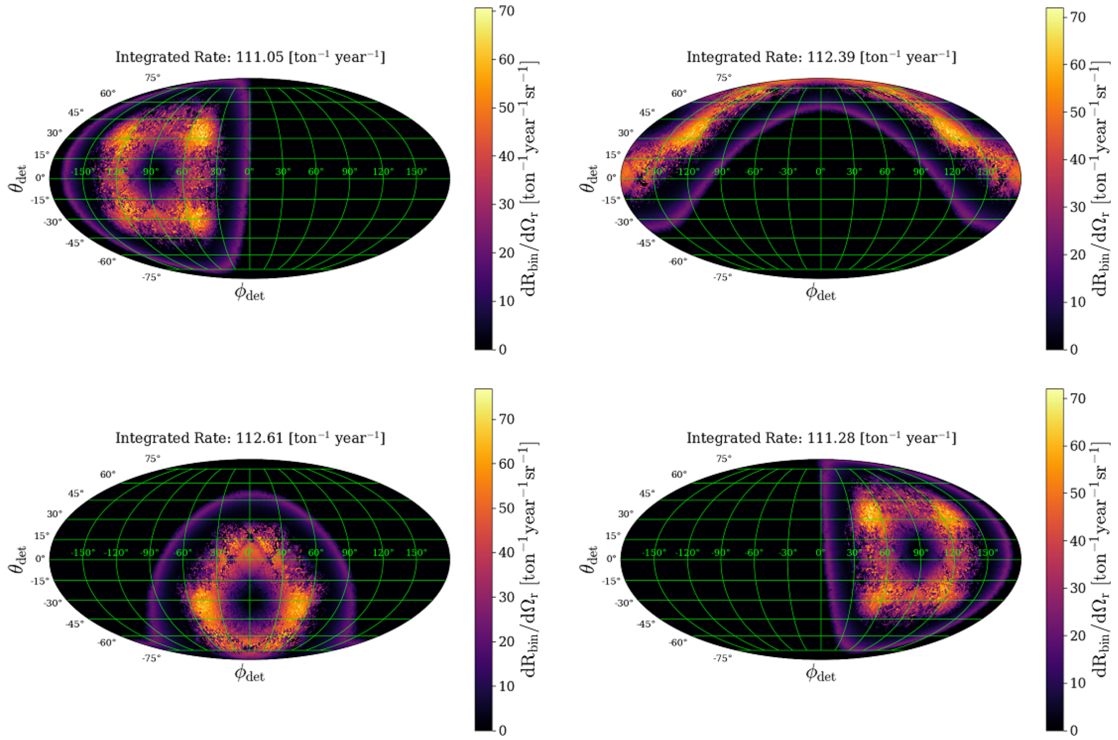

Figure 3.9: The differential rate per unit steradian for all solar neutrinos at several times over the course of a day for a germanium (Ge) detector assuming the energy thresholds discussed in § 3.3. The upper left is 6 a.m., upper right is midnight, lower right is 6 p.m., and lower left is noon on September 6, 2015 at Modane Undergound Laboratory (45.1966°N, 6.6668°W) for easier comparison with Ref. [72]. All rates are integrated up to 100 eV nuclear recoil energy.

apply to the solar neutrino rate as well. This is best illustrated in Figures 3.8 and 3.10, which show how the differential solar neutrino rate per unit steradian changes over the course of a day assuming a Ge and Si detector, respectively. In these plots, lighter regions correspond to a higher rate and darker ones to a lower one. Aside from the difference in position in the sky, the biggest difference between the solar neutrino signal and that of a potential dark matter signal is that the neutrino differential rate appears as a ring whereas the potential dark matter signal would appear as a more gaussian-like distribution. This is

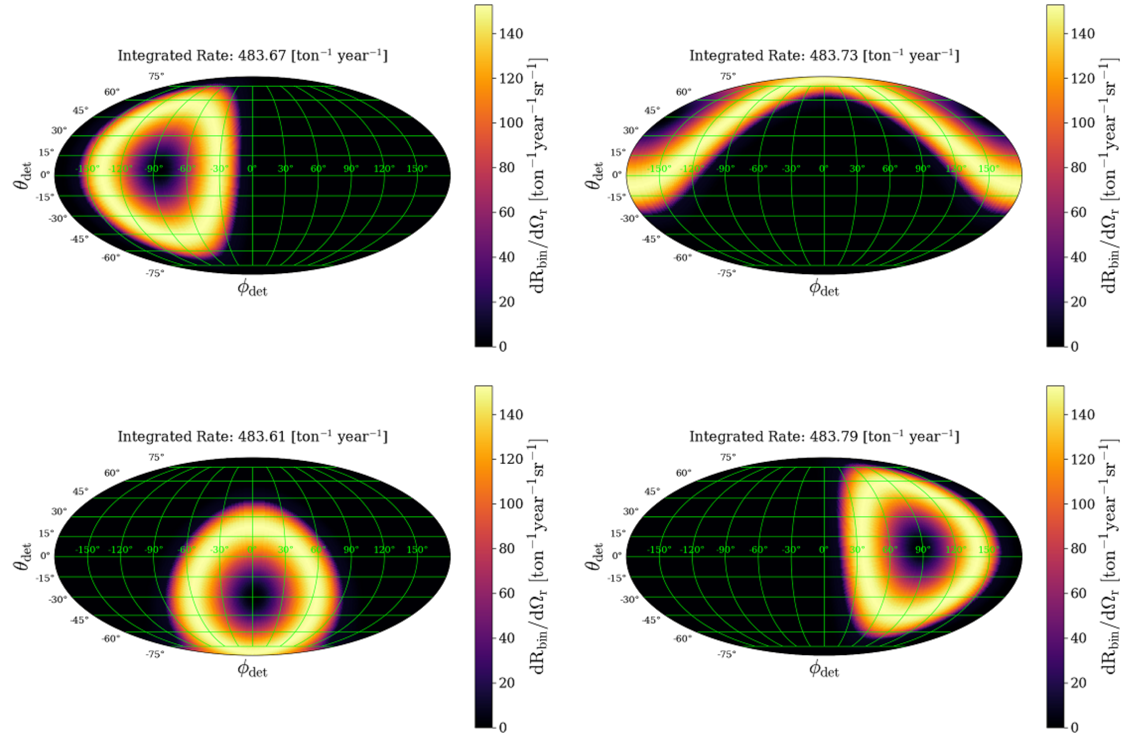

Figure 3.10: The differential rate per unit steradian for all solar neutrinos at several times over the course of a day for a silicon (Si) detector assuming a constant energy threshold for nuclear recoils of 1 eV. The upper left is 6 a.m., upper right is midnight, lower right is 6 p.m., and lower left is noon on September 6, 2015 at Modane Undergound Laboratory (45.1966°N, 6.6668°W) for easier comparison with Ref. [72]. All rates are integrated up to 100 eV nuclear recoil energy.

because the solar neutrino signal arrives from a point source, whereas dark matter arrives from all directions but is more localized to a particular direction in the sky at a given time. All of the figures in this section are generated assuming a detector at Modane Undergound Laboratory (45.1966°N, 6.6668°W) on September 6, 2015 for easier comparison with Ref. [72].

Applying the energy thresholds yields the differential rate per unit steradian for solar neutrinos shown in Figures 3.9 and 3.12 for Ge and 3.11 and 3.13 for Si, respectively.

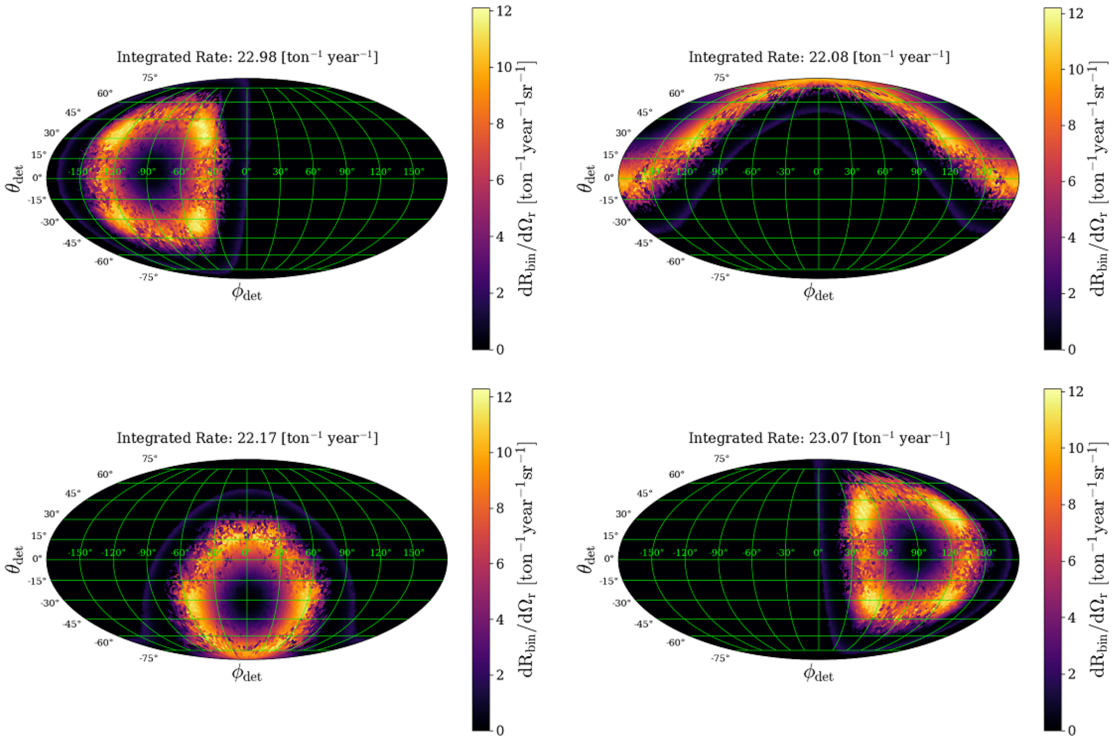

Figure 3.11: The differential rate per unit steradian for all solar neutrinos at several times over the course of a day for a silicon (Si) detector given the energy thresholds discussed in § 3.3. The upper left is 6 a.m., upper right is midnight, lower right is 6 p.m., and lower left is noon on September 6, 2015 at Modane Undergound Laboratory (45.1966°N, 6.6668°W) for easier comparison with Ref. [72]. All rates are integrated up to 100 eV nuclear recoil energy.

Similar to the effect defect creation has on the dark matter differential rate shown in Figures 3.5 and 3.6. these plots show the four symmetric light inner regions corresponding to displacement energy threshold minima. However, there are also marked differences in the signal, such as the ring that circles the inner four light regions in Figures 3.9 and 3.11. This ring occurs because of a complex interplay between neutrino cross section, which tends to favor interactions with low recoil energy and high neutrino energy, the form factor, which approaches zero as the recoil energy approaches infinity, the thresholds, which

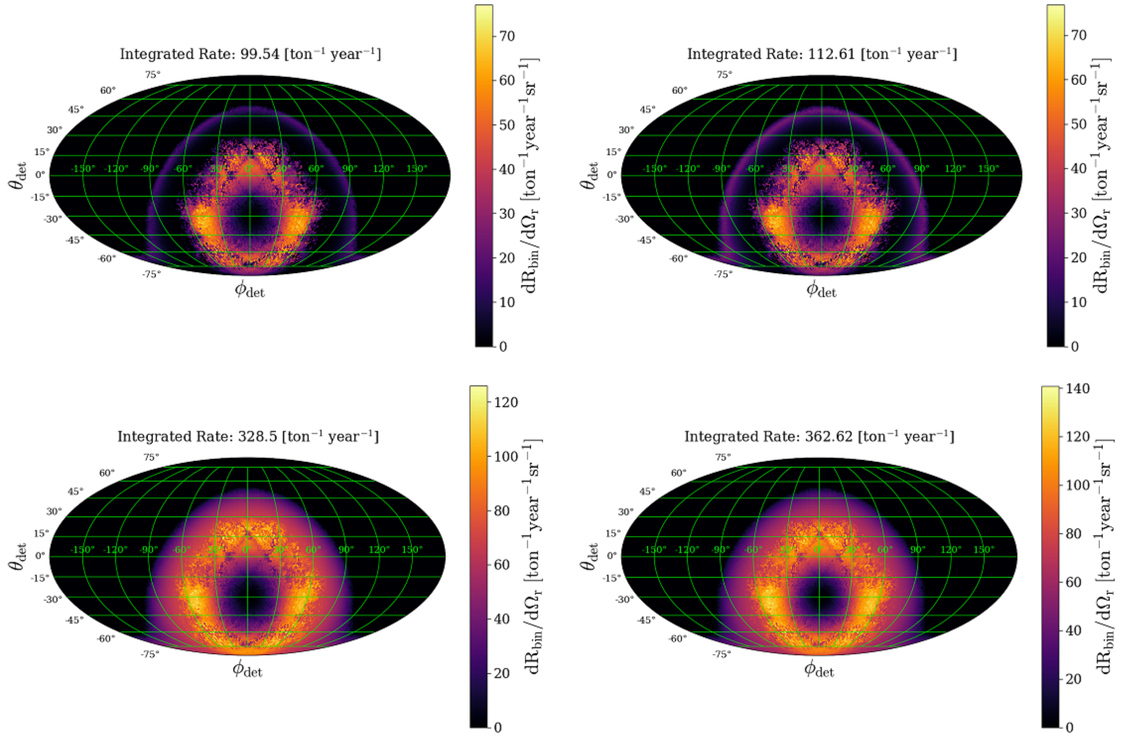

Figure 3.12: The differential rate per unit steradian for all solar neutrinos for a germanium (Ge) detector assuming the detector energy thresholds discussed in § 3.3 for several recoil energy upper bounds. The maxima for calculating the rate are: 63.5 eV, the maximum for the Ge energy thresholds (upper left), 100 eV (upper right), 1666.7 eV (lower left) for comparison with Ref. [72], and the maximum recoil energy (lower right). All plots are calculated on September 6, 2015 at midnight at Modane Undergound Laboratory (45.1966°N, 6.6668°W) for easier comparison with Ref. [72].

prevent recoils smaller than about 10 eV from contributing to the differential rate, and the 100 eV upper recoil energy bound. The result is two populations of events - those that have very low initial energies and are just above the energy thresholds (center population), and those that have higher initial energies, but not too high so that the form factor significantly lowers the rate, that are scattered far off-axis to lower the recoil energy, and hence increase the differential rate (ring around the center).

All of these factors contribute to the neutrino interaction having a very unique modu-

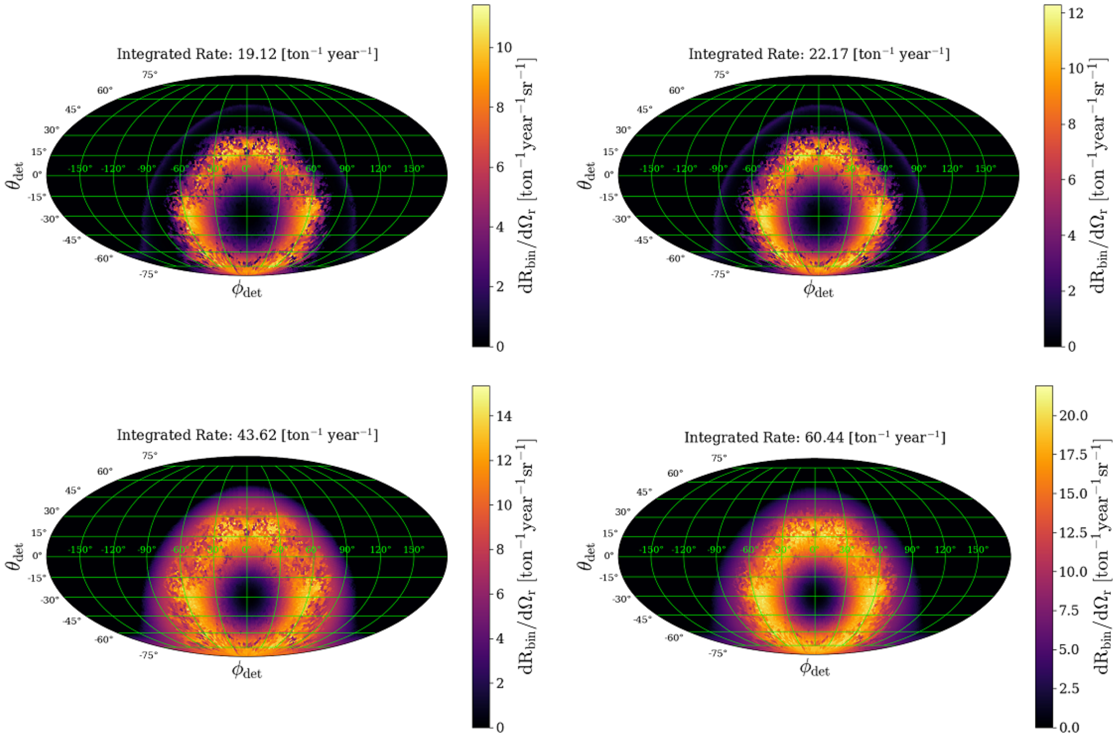

Figure 3.13: The differential rate per unit steradian for all solar neutrinos for a silicon (Si) detector assuming the detector energy thresholds discussed in § 3.3 for several recoil energy upper bounds. The maxima for calculating the rate are: 77.5 eV, the maximum for the Si energy thresholds (upper left), 100 eV (upper right), 1666.7 eV (lower left) for comparison with Ref. [72], and the maximum recoil energy (lower right). All plots are calculated on September 6, 2015 at midnight at Modane Undergound Laboratory (45.1966°N, 6.6668°W) for easier comparison with Ref. [72].

lation signal, given the thresholds shown in 3.4. A preliminary plot of this modulation, for ^{13}N solar neutrinos over one day for a germanium detector at the Modane Underground Laboratory, is shown in Fig. 3.14. Including all of the terms produces the integrated rates shown in Figures 3.15 and 3.16 for Ge and Si detectors, respectively. These plots show the integrated rate given the thresholds in § 3.3 and varying maximum recoil energy bounds. The upper recoil energy is the maximum for the given threshold (63.5 eV for Ge, 77.5 eV for Si) for the plots at upper left, 100 eV for those at the upper right, 1666.7 eV for compar-

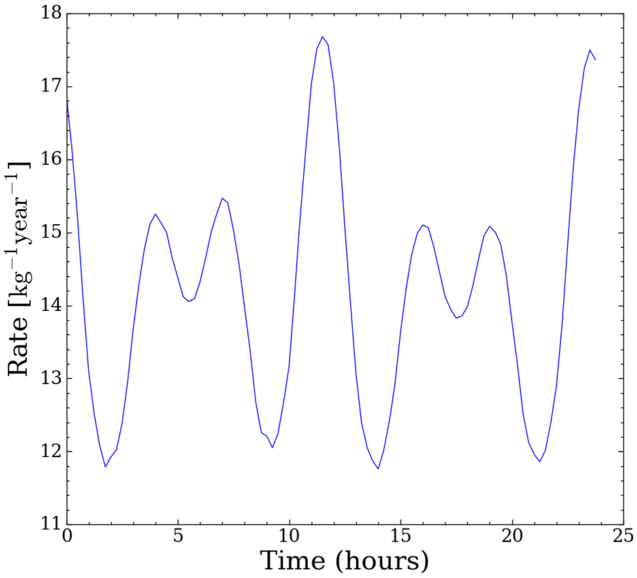

Figure 3.14: The integrated rate for 13-N neutrinos from the sun over one day for a germanium detector. This assumes the same detector energy thresholds discussed in § 3.3.

ison with Ref. [72] at lower left, and the maximum recoil energy for those at lower right. Given the differences between the expected modulation due to solar neutrinos and dark matter, future studies could explore how the modulation due to energy threshold could help future dark matter experiments reach lower cross sections given the solar neutrino background.

3.4.2 Reactor Antineutrino CENNS

Since many experiments, such as MINER at Texas A&M University, are investigating CENNS, it is useful to see whether defect creation effects can be observed with reactor neutrinos. This calculation, which was started in October 2017, may not be as relevant anymore since the COHERENT collaboration announced observing CENNS [168]. However, it may still be relevant as dark matter experiments get closer to the solar neutrino

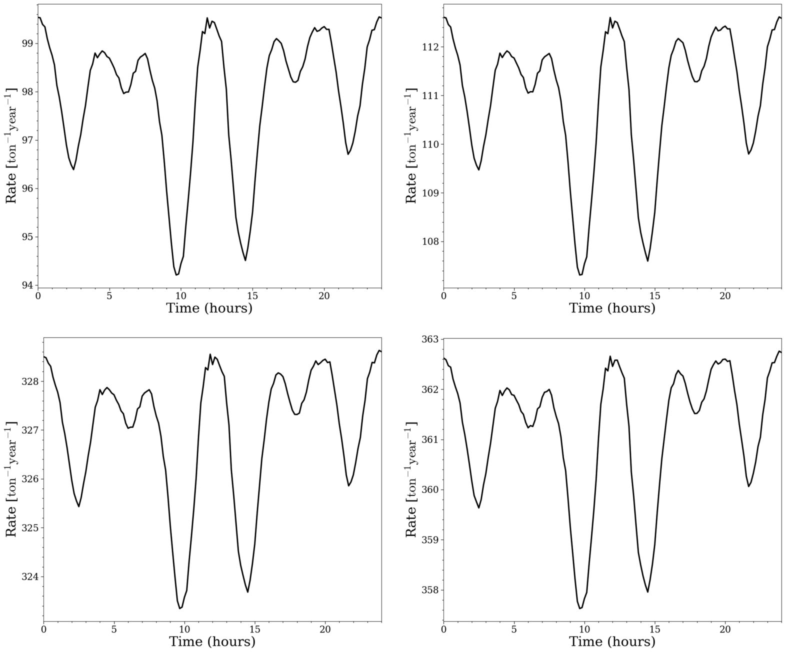

Figure 3.15: The integrated rate for all solar neutrinos over one day for a germanium (Ge) detector assuming the detector energy thresholds discussed in § 3.3 for several recoil energy upper bounds. The maxima for calculating the rate are: 63.5 eV, the maximum for the Ge energy thresholds (upper left), 100 eV (upper right), 1666.7 eV (lower left) for comparison with Ref. [72], and the maximum recoil energy (lower right). All plots are calculated on September 6, 2015 at Modane Undergound Laboratory (45.1966°N, 6.6668°W) for easier comparison with Ref. [72].

floor and, hence, require the means to discriminate possible dark matter signal from neutrino backgrounds. Thus, in this portion of the thesis, I explore how defect creation could produce observable effects in the reactor antineutrino spectrum.

Given the solar neutrino calculations in § 3.4.1, it is relatively straightforward to calculate the result of including the defect creation threshold and energy loss effects. The former are discussed below and the latter in § 4. The only significant parts of Eq. 1.58 that change are the neutrino spectrum $\frac{\mathrm{d}\Phi}{\mathrm{d}E_\nu}$, excluding the time-dependent distance corrections, and the position of the source relative to the laboratory. Since the source is not the Sun but rather a

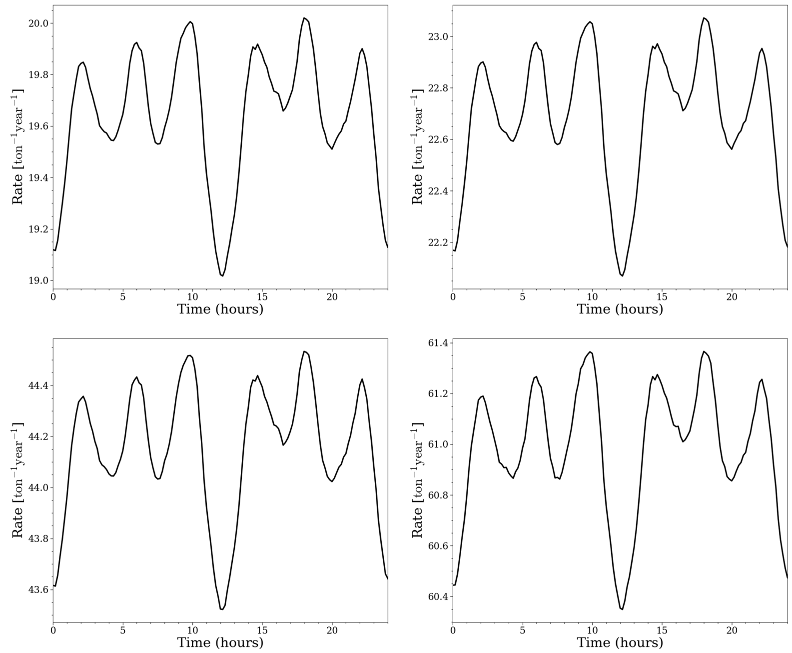

Figure 3.16: The integrated rate for all solar neutrinos over one day for a silicon (Si) detector assuming the detector energy thresholds discussed in § 3.3 for several recoil energy upper bounds. The maxima for calculating the rate are: 77.5 eV, the maximum for the Si energy thresholds (upper left), 100 eV (upper right), 1666.7 eV (lower left) for comparison with Ref. [72], and the maximum recoil energy (lower right). All plots are calculated on September 6, 2015 at Modane Undergound Laboratory (45.1966°N, 6.6668°W) for easier comparison with Ref. [72].

stationary reactor, the source direction can be selected to be from whichever direction the actual experiment is, or, in the case of these calculations, whichever direction can be experimentally implemented straightforwardly and produce a measurable signal. Hence, this calculation assumes that the stationary detector is rotated around the (111) axis, with the integrated rate measured every degree of rotation, and that the reactor direction is orthogonal to the rotation direction. $0°$ rotation is defined with the reactor in the (100) direction with respect to the crystal lattice structure of the detector. For the input spectrum data, the calculations use the spectrum in Ref. [169], which is digitized using [170]. Preliminary

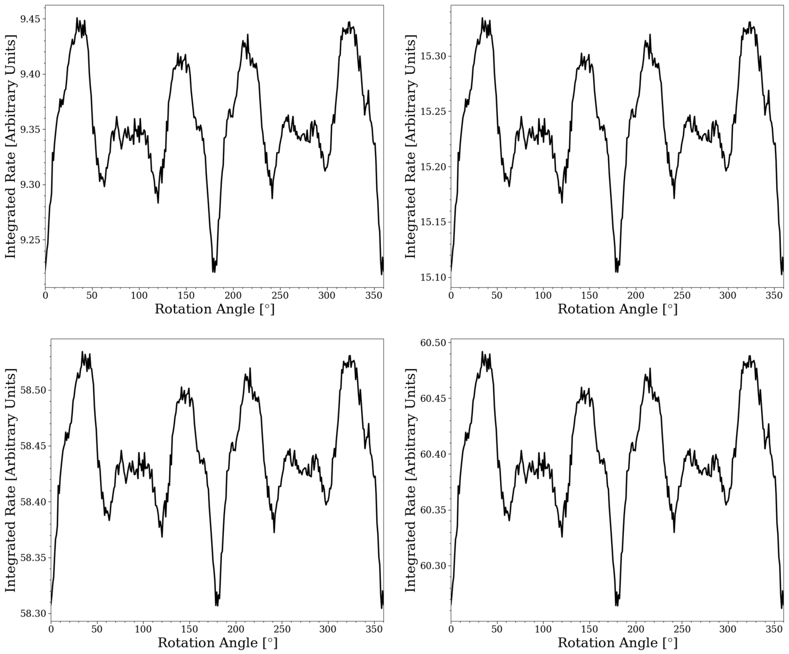

Figure 3.17: Total integrated rate for a typical reactor given a germanium (Ge) detector and the defect creation thresholds discussed in § 3.3 as a function of angle relative to a reactor antineutrino source. The rotation axis is aligned with the (111) crystal lattice direction. Each plot assumes a different maximum recoil energy for calculating the integrated rate: the maximum of the defect creation threshold for Ge, which is 63.5 eV (upper left), 100 eV (upper right), 1.6667 keV for consistency with [72] (lower left), and the recoil energy maximum given the neutrino spectrum and a Ge detector (lower right).

plots of the integrated rate as a function of rotation angle are shown in Figures 3.17 and 3.18.

As is the case with the solar neutrino signal, a difference in the integrated signal rate is expected depending on the direction of the source. However, because the expected reactor antineutrino signal has fewer sharp features, the change in the total rate is also smaller. As shown in Figures 3.17 and 3.18, the effect is essentially unobservable unless one uses a very small upper bound for the recoil energy to calculate it, which significantly reduces the total number of measured events. Nonetheless, the effect is there regardless of energy

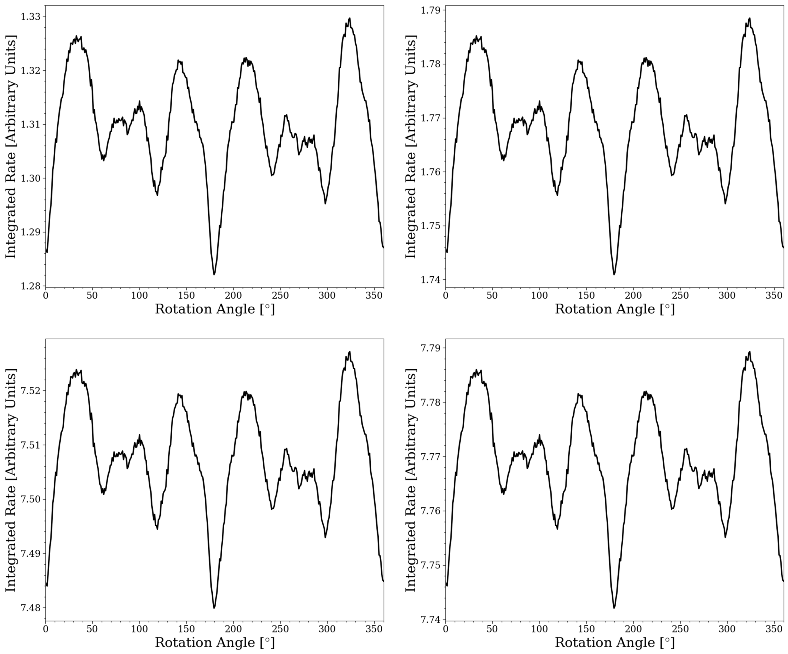

Figure 3.18: Total integrated rate for a typical reactor given a silicon (Si) detector and the defect creation thresholds discussed in § 3.3 as a function of angle relative to a reactor antineutrino source. The rotation axis is aligned with the (111) crystal lattice direction. Each plot assumes a different maximum recoil energy for calculating the integrated rate: the maximum of the defect creation threshold for Si, which is 77.5 eV (upper left), 100 eV (upper right), 1.6667 keV for consistency with [72] (lower left), and the recoil energy maximum given the neutrino spectrum and a Ge detector (lower right).

binning, which means that it could be observable with a large enough number of events in the future.

3.4.3 Low-Energy Neutron Source Calibration

One way to investigate whether the defect creation used for many of the calculations in this work, especially the assumption that defect creation implies electron-hole pair creation, is using a low-energy neutron source. At the moment, an experiment is being set up at the Triangle Universities National Laboratory (TUNL) facility to utilize the neutron source there to calibrate nuclear recoil events in SuperCDMS-style detectors at low energies. By comparing the event rate in a semiconductor detector with that in neutron scintillator veto detectors, it is possible to determine whether there is a directionality to electron-hole pair production, which would strongly imply its association with defect creation energy thresholds.

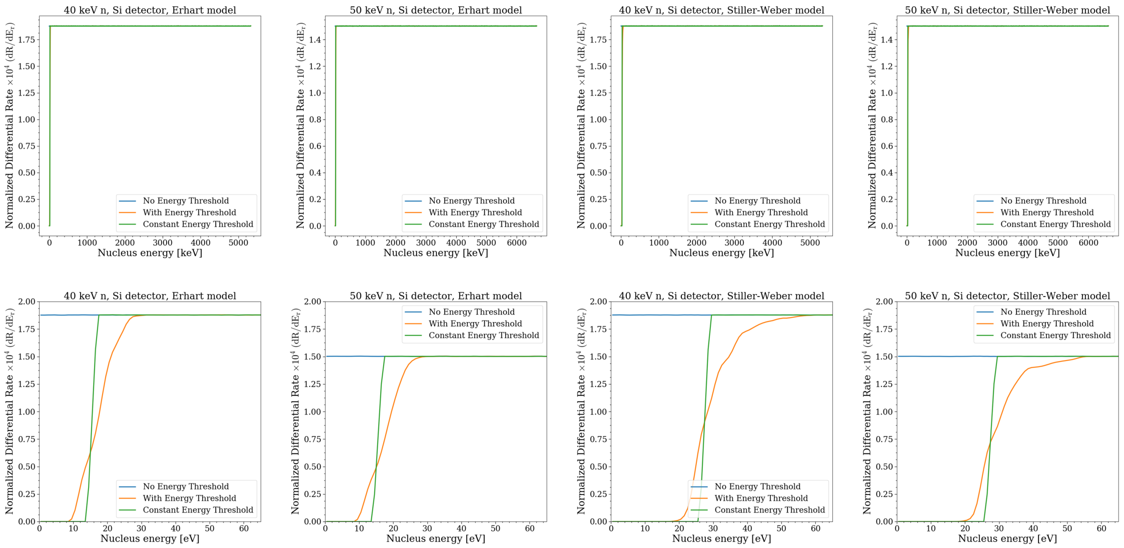

Figure 3.19: Differential rate per unit nucleus recoil energy normalized to 1 assuming either the Erhart or Stiller-Weber defect creation models, a 40 keV or 50 keV neutron beam, and a silicon detector. The lower images show the closeup for each plot above at the energy scale where the defect creation models are relevant. The blue curves represent the differential rate assuming no energy thresholds, the orange curves show the differential rate assuming either the Erhart or Stiller-Weber models, and the green curves assume a constant energy threshold equal to the median for either the Erhart or Stiller-Weber models.

To estimate the feasibility of the above claim, Monte Carlo simulations were performed using the defect creation data from Professor Kai Nordlund's group. Fig. 3.19 and Fig. 3.20 illustrate the results of these simulations. Fig. 3.19 shows the differential rate per unit nuclear recoil energy normalized to 1, and Fig. 3.20 shows the differential rate per

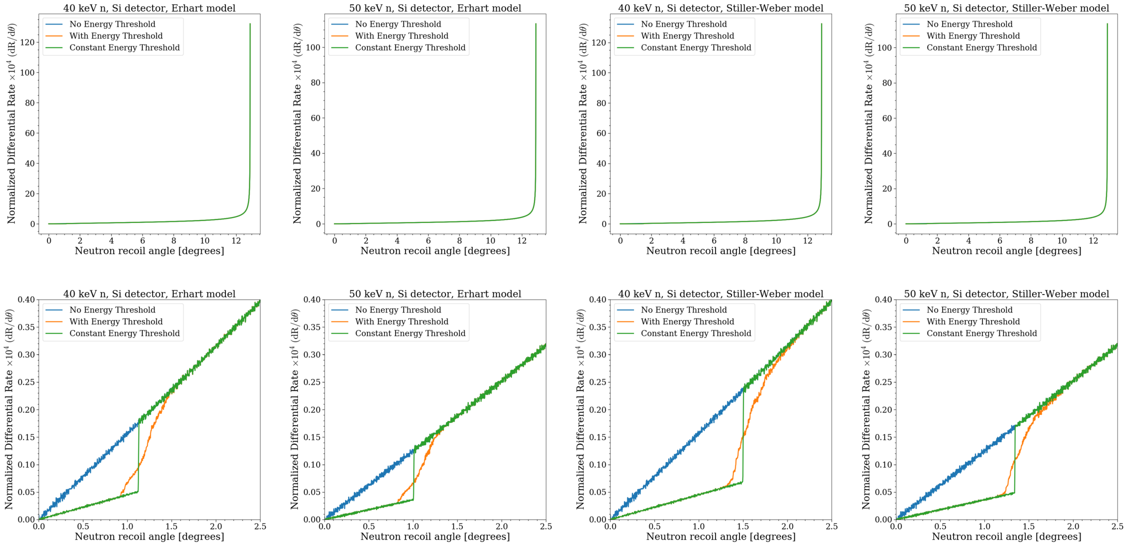

Figure 3.20: Differential rate per unit neutron recoil angle normalized to 1 assuming either the Erhart or Stiller-Weber defect creation models, a 40 keV or 50 keV neutron beam, and a silicon detector. The lower images show the closeup for each plot above at the energy scale where the defect creation models are relevant. The blue curves represent the differential rate assuming no energy thresholds, the orange curves show the differential rate assuming either the Erhart or Stiller-Weber models, and the green curves assume a constant energy threshold equal to the median for either the Erhart or Stiller-Weber models.

unit neutron recoil angle normalized to 1. The plots in both figures are generated using 20 billion events for each type of plot, which use either 40 keV or 50 keV neutrons and the Erhart or the Stiller-Weber defect creation models. The neutron beam travels in the positive z-direction, and the coordinate system is aligned with the coordinate system for Miller indices for the Si unit cell. Both the neutrons from the monoenergetic beam and the nuclei are assumed to be point-like, which is why there are no back-scattered neutrons. The final plots are smoothed out using a moving average of window size 3 to mitigate some of the noise caused by the randomness inherent to the simulation.

These preliminary plots seem to indicate that testing the directional defect creation and associated electron-hole-pair production may require a very long exposure and very high neutron scintillator directional resolution. It may be possible to improve the resolving power of the experiment by carefully positioning the detector relative to the neutron beam to maximize the neutron signal in one set of detectors relative to another, but further tests are needed.

Other future directions include running the same simulation with a more precise expected or measured neutron spectrum from the beam. This spectrum could also be input into a more accurate neutron interaction code, such as GEANT4 [171, 172, 173]. The nuclear energies could then be reconstructed from the neutron direction and energy. They can then be combined with the defect creation models to see whether any particular neutron interaction event could have produced an electron-hole pair, which would yield plots similar to those in Fig. 3.19 and Fig. 3.20. Such precise computations can be compared with experimental results to verify electron-hole-pair production via defect creation.

Altogether, these preliminary results and possible future directions demonstrate how the detector setup at the TUNL facility could pave the way for precisely comparing the defect creation results of simulations with experiments. Doing so could allow future dark matter direct-detection experiments to use defect creation in materials to facilitate identifying the signature of dark matter. In the next chapter, I explore how related defect creation effects could be used to discriminate nuclear recoils, the possible dark matter signal, from electron recoils without needing to measure the electron-hole pairs produced during the interaction.

4. DEFECT CREATION IN VERY LOW THRESHOLD DETECTORS AND THE POSSIBILITY OF NUCLEAR RECOIL VERSUS ELECTRON RECOIL DISCRIMINATION DOWN TO EV SCALE

4.1 Particle Interaction Energy Partition

It is useful to discuss how energy is partitioned during a particle interaction with a SuperCDMS-style detector given the computational work that follows. Further details about this process can be found in Ref. [174] and Ref. [107].

A particle interacting with a solid-state detector will either interact with an electron or an atomic nucleus in the detector. During an electron recoil, the energy is transferred from the primary knock-on electron to other nearby electrons in a collision cascade. If the energy that a particular electron receives is high enough (3.0 eV for Ge and 3.8 eV for Si), an electron-hole pair is created. This electron-hole pair relaxes down to the band gap (0.74 eV for Ge and 1.12 eV for Si), and the energy is released as phonons to the crystal lattice. For nuclear recoils, the energy is transmitted between other nuclei and the electronic structure so that much less of the energy gets transferred to the electrons than in the electron recoil case. Other excitations, like excitons, a bound system consisting of an electron and hole pair, can also form. When a voltage bias is applied across the detector, the electrons and holes in the conduction band transfer their kinetic energy from the electric field to the lattice as phonons. If there is no voltage bias, all of these excitations relax to phonons that propagate throughout the lattice.

Because the energy of a nuclear recoil is transferred to other nuclei as well, the nuclei sometimes form stable defects that decrease the total phonon signal measured. This changes the shape of the nuclear recoil event spectrum, which provides a way of differentiating nuclear recoil events from electron recoil events even without measuring the charge collected using a voltage bias. I explore this defect creation energy loss and its possible applications in this chapter.

4.2 Defect Creation Energy Loss [*]

Low energy threshold detectors are desirable since low-mass dark matter signal cannot be measured otherwise, as discussed in § 3.1. However, dual measurement techniques fail at low energies due to charge measurement fundamental noise, which motivates research into alternative methods to discriminate nuclear (signal) recoils from electron (noise) ones. One possibility is to use the energy required to produce a defect, which is referred to as the defect creation energy "loss" since it cannot be measured by a detector. At low recoil energies, the energy loss takes on discrete values that, at higher energies, get smoothed out into a linear ∼5% energy loss. The energy loss steps correspond to peaks in the expected measured recoil energy spectrum, as discussed later. In this subsection, I show how the features that occur in the spectrum can help discriminate dark matter signal from backgrounds by producing a signature for a potential dark matter signal.

We use numerical simulations of classical potentials backed by density functional theory (DFT) calculations to find the energy loss as a function of recoil energy and nuclear recoil angle. We simulate defect creation with the PARCAS code [161, 175, 176] for elemental carbon (C), silicon (Si), and germanium (Ge) atoms in a diamond cubic lattice structure. Each element is initialized as a unit cell of 4096 atoms that is thermalized to 40 mK, and the potential energy of the entire system is measured afterwards. A random atom from the central 64 atoms is selected and displaced in a random direction with an energy from 1 to 200 eV. Contrary to Ref. [102] and the previous chapter where the energy scan

---

[*] Part of this section is reprinted with permission from F. Kadribasic, N. Mirabolfathi, K. Nordlund, E. Holmström, and F. Djurabekova, "Defect Creation in Crystals: A Portal to Directional Dark Matter Searches," *J. Low. Temp. Phys.*, vol. 193, no. 5-6, pp. 1146-1150, Copyright 2018 by Springer Nature. [Online]. Available: https://doi.org/10.1007/s10909-018-2062-5 and F. Kadribasic, N. Mirabolfathi, K. Nordlund, and F. Djurabekova "Crystal Defects: A Portal To Dark Matter Detection," *Phys. Rev. Lett.* to appear, Copyright 2020 by American Physical Society. [Online]. Available: https://arxiv.org/abs/2002.03525.

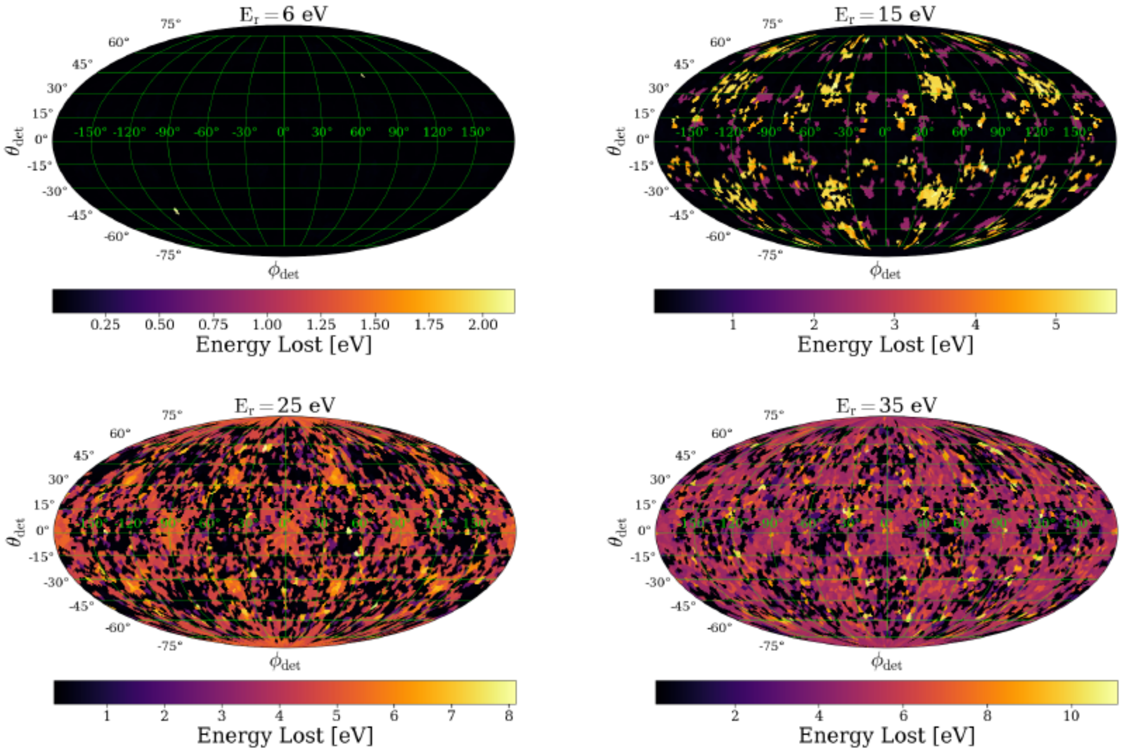

Figure 4.1: Four Mollweide-projection plots showing the defect creation energy loss in germanium at recoil energies of 6 eV (upper left), 15 eV (upper right), 25 eV (lower left), and 35 eV (lower right). The color of the region on each plot indicates the amount of energy that went into creating a defect in a particular direction at a particular energy. Below about 6 eV in germanium, the recoil is not strong enough to create a defect, hence why most of the 6 eV recoil energy plot is dark. The two sharpest jumps in energy loss occur at ∼6 eV and ∼15 eV, which are energies at which the two dominant defect energy loss scenarios begin to occur. As the recoil energy increases, the defect creation energy loss is smeared out and approaches a linear regime at energies greater than about 100 eV in germanium.

was stopped when the threshold in a given direction was reached, defects are simulated up to 200 eV to get the stored energy for above-threshold recoils as well. After waiting for 10 ps, the amount of time necessary for a defect to stabilize [146, 147], the energy of the system is calculated. The difference between the final energy of the system and the initial energy gives the energy loss to defect creation since that is the energy that is not converted into phonons. Therefore, this energy cannot be measured with a phonon-sensitive direct-

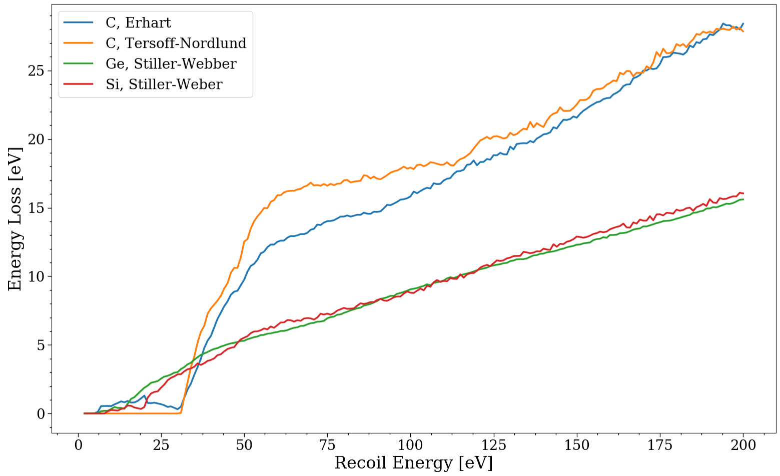

Figure 4.2: Defect creation energy loss over all recoil directions for several materials. We employ two models for carbon - Erhart (blue) and Tersoff-Nordlund (orange). Since it is difficult to display all of the data used in this study, this plot summarizes the functional form of the energy loss as a function of recoil energy.

detection dark matter detector, such as those used by the SuperCDMS experiment. We use the Stillinger-Weber potential [163, 160] for Si and Ge, and we use the Tersoff potential extended by Nordlund [177, 178] and Erhart [179] potentials for C. These potentials were chosen because they give good agreement with experimental [180, 181] or quantum mechanical density functional theory threshold energies [146, 147]. 347 recoil directions are simulated for the C-Erhart data, 343 for C-Tersoff-Nordlund, 6591 for Ge, and 1003 for Si.

A summary of the energy loss results thus obtained is shown in Fig. 4.1 and Fig. 4.2. Fig. 4.1 shows the energy loss as a function of recoil energy and recoil angle for several representative recoil energies. The fact that there is a periodic variation in energy loss as a function of recoil angle indicates that the energy loss is anisotropic, as expected from the crystal lattice structure. Additionally, the dark regions demonstrate that this is a stochastic process that does not always produce defects; however, when a defect is produced, the

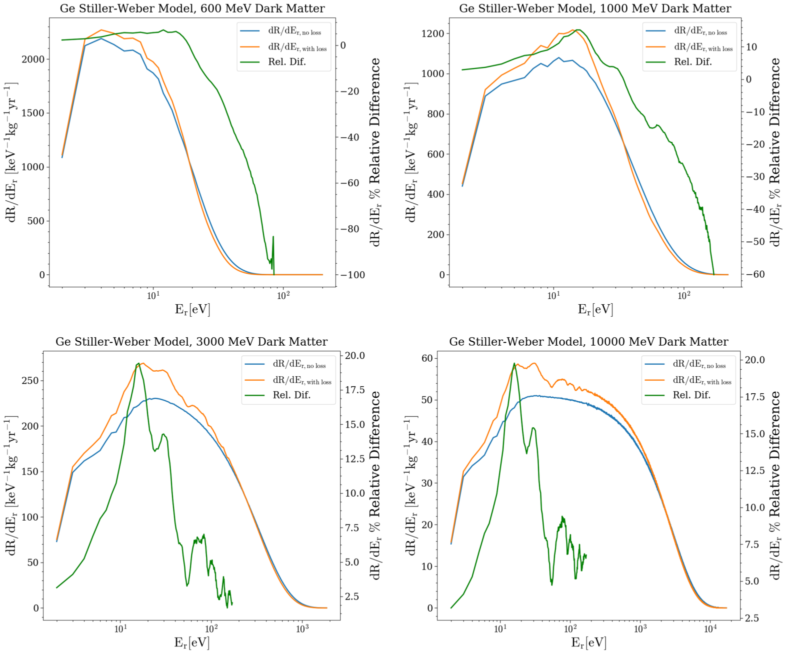

Figure 4.3: Differential rate per unit recoil energy as a function of nuclear recoil energy for several dark matter masses measured by a Ge detector. Blue curves show the differential rate for a detector with 3 eV resolution and no energy loss effect, orange curves show the differential rate with the energy loss effect included, and green curves show the energy difference. The effect of the energy loss is such that, at a given energy, a detector measures both the events that have a particular recoil energy and no energy loss and those with a higher recoil energy that have lost energy to defect formation.

effect can be very pronounced, especially at recoil energies of a few tens of eV. Fig. 4.2 shows the mean energy loss calculated over all recoil energies for all three elements. The energy loss has the strongest effect at energies of a few tens of eV when the energy loss can be comparable to the energy of the recoiling nucleus, and the variation in energy loss is also consistently larger at these low energies than it is past about 100 eV.

We calculate $\dfrac{\partial^2 R}{\partial E_r \partial \Omega_r}$ at the SNOLAB site (46.4719°N, 81.1868°W) on September 6, 2015 (to match [72]) via integral A.19 to get the differential rate per unit recoil energy, which gives the differential rate one assumes for a perfect detector. We choose 2×10^8 sample events from the distribution given by $\dfrac{\partial^2 R}{\partial E_r \partial \Omega_r}$ and add energies sampled from a

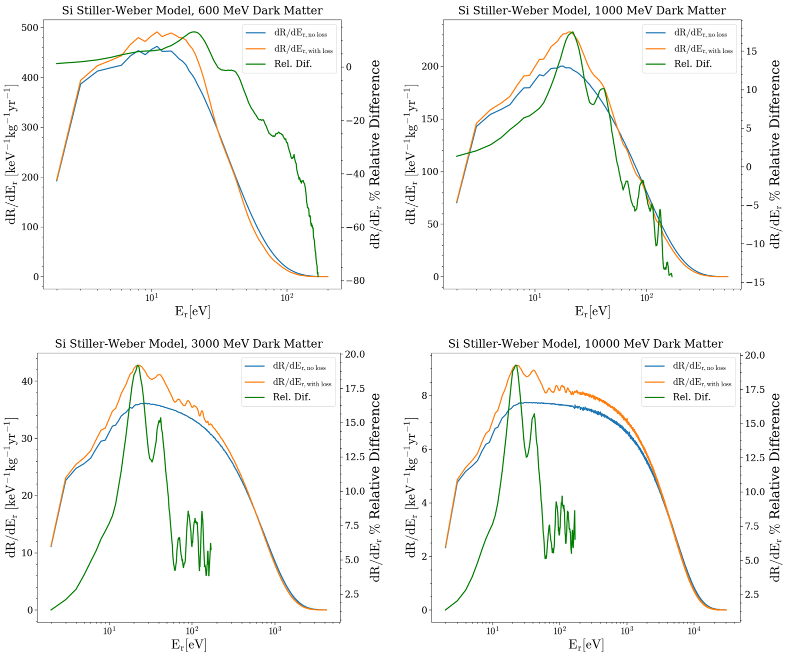

Figure 4.4: Differential rate per unit recoil energy as a function of nuclear recoil energy for several dark matter masses measured by a Si detector. Blue curves show the differential rate for a detector with 3 eV resolution and no energy loss effect, orange curves show the differential rate with the energy loss effect included, and green curves show the energy difference. The effect of the energy loss is such that, at a given energy, a detector measures both the events that have a particular recoil energy and no energy loss and those with a higher recoil energy that have lost energy to defect formation.

Gaussian distribution centered at 0 eV to simulate a detector with 3 eV resolution and 10 eV threshold. This is shown as the blue curve in Figures 4.3, 4.4, 4.6, and 4.5. To find the effect of the energy losses, we use the sampled events from the previous step and subtract the numerically calculated energy losses for recoil energies 2-170 eV. For recoil energies greater than 170 eV, we calculate a linear functional fit for the energy loss using the mean of the angle-dependent energy loss data from 100 to 200 eV. The resulting distribution is integrated over all recoil angles to yield the orange curve in Figures 4.3, 4.4, 4.6, and 4.5. Green curves show the relative difference between differential rate with and without the energy loss effect included up to 170 eV recoils.

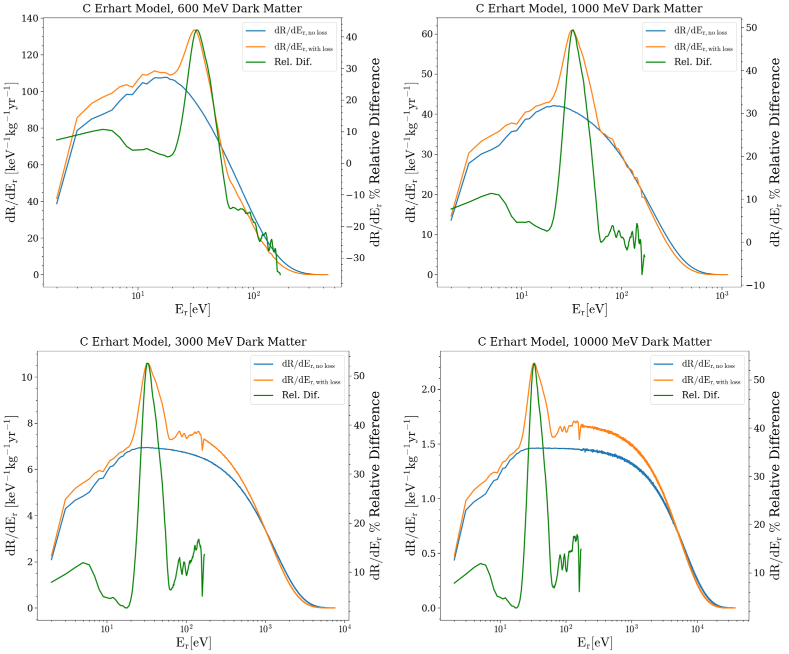

Figure 4.5: Differential rate per unit recoil energy as a function of nuclear recoil energy for several dark matter masses measured by a C detector and assuming the Erhart potential for the calculation. Blue curves show the differential rate for a detector with 3 eV resolution and no energy loss effect, orange curves show the differential rate with the energy loss effect included, and green curves show the energy difference. The effect of the energy loss is such that, at a given energy, a detector measures both the events that have a particular recoil energy and no energy loss and those with a higher recoil energy that have lost energy to defect formation.

Thus, Figures 4.3, 4.4, 4.5, and 4.6 show the effect that the phonon energy loss can have on the dark matter spectrum at low recoil energies. Applying the energy losses transforms the featureless spectrum to one with a peak that corresponds to the energy at which higher potential energy defects start to occur, as shown in the plots in Fig. 4.1. The kind of material used for the detector, as well as the model for the potential function in the lattice, has a significant effect on the size and location of the features that appear due to defect creation energy loss. Although the ultimate resolution of the detector has an effect on whether fine features due to the energy loss are resolved, the large features in the spectrum for car-

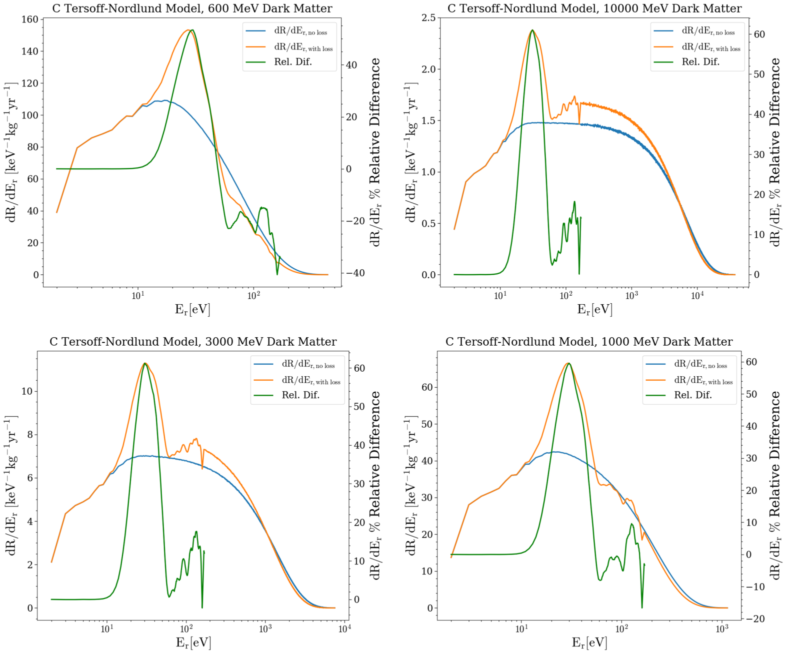
C Tersoff-Nordlund Model, 600 MeV Dark Matter

C Tersoff-Nordlund Model, 10000 MeV Dark Matter

C Tersoff-Nordlund Model, 3000 MeV Dark Matter

C Tersoff-Nordlund Model, 1000 MeV Dark Matter

Figure 4.6: Differential rate per unit recoil energy as a function of nuclear recoil energy for several dark matter masses measured by a C detector and assuming the Tersoff-Nordlund potential for the calculation. Blue curves show the differential rate for a detector with 3 eV resolution and no energy loss effect, orange curves show the differential rate with the energy loss effect included, and green curves show the energy difference. The effect of the energy loss is such that, at a given energy, a detector measures both the events that have a particular recoil energy and no energy loss and those with a higher recoil energy that have lost energy to defect formation.

bon, irrespective of model, can still be resolved. Additionally, the location of the energy loss peaks relative to the high-energy recoil energy tail can, given a large enough signal, be used to determine the mass of the dark matter particle. The change in the differential rate spectrum further emphasizes the importance of developing detectors that can probe ever lower energy thresholds since doing so not only probes large regions of dark matter parameter space but also accentuates the features shown in Figures 4.3, 4.4, 4.5, and 4.6.

We further quantify the discrimination power as a function of dark matter mass by calculating a normalized root-mean-squared (normalized RMS) statistic as a function of dark matter mass. The procedure for doing so is the same as in Ref. [102] with the exception that the fluctuations in the spectrum due to energy loss are compared to the case of a perfect detector with 3 eV resolution and 10 eV threshold. Mathematically, this is given by

$$\mathrm{RMS}_{\mathrm{norm}} = \sqrt{\frac{\oint_{\Delta E} \left(R_{\mathrm{Eloss}} - R_{\mathrm{no\ loss}}\right)^2 dE}{\oint_{\Delta E} R_{\mathrm{no\ loss}}^2 dE}} \tag{4.1}$$

In other words, the normalized RMS is found by looking at the squared difference between the orange and blue curves divided by the squared integral of the blue curves in Figures 4.3, 4.4, 4.5, and 4.6.

Fig. 4.7 shows the result of doing so for all four models over a range of dark matter masses for a detector with 3 eV resolution and 10 eV detector threshold. The left y-axis indicates the normalized RMS statistic, whereas the right y-axis indicates the total rate found by integrating the differential rate, like that in in Figures 4.3, 4.4, 4.5, and 4.6, over all recoil energies given the defect creation energy loss effect. Although this analysis cannot determine exactly how effective this method is in resolving a dark matter signal from a given noise, it does give an idea of what range of dark matter masses it is most useful for and what detector materials show the strongest effect. Of the three materials investigated in this study, the signal strength would be by far the strongest in carbon, independent of model used, as long as the bulk of the events are not near the detector threshold. For this reason, in addition to the other useful properties of diamond detectors described in Ref. [105], diamond detectors need to be developed to verify their theoretical capabilities for finding dark matter.

Nonetheless, despite the potential impact this method could have on the field of direct dark matter detection, the change in spectra can most likely only be observed once many events have been measured. This limits the applicability of this method to future dark matter experiments that will, hopefully, have enough statistics to see this effect. How-

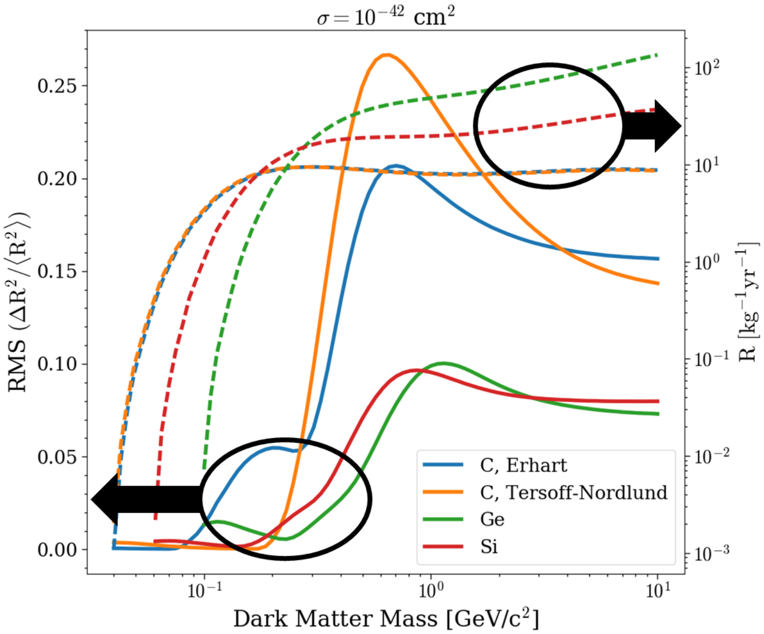

Figure 4.7: Signal strength due to defect creation energy loss, as normalized RMS, on the left y-axis and total integrated rate on the right y-axis, both as a function of dark matter mass. Solid curves correspond to the RMS, and dashed curves correspond to the integrated rate, as indicated by the black ovals and arrows. The normalized RMS quantity gives a qualitative measure of the ability of a potential dark matter spectrum, with the features present due to defect creation energy loss, to be differentiated from the noise floor. In this case, we assume that the dark matter spectrum without energy loss approximates the noise floor and to show that, given a detector with sufficient resolution and a high enough dark matter signal, measurable features can be observed in an, otherwise, featureless spectrum. The integrated rate is found by integrating the differential rate over all recoil energies given the energy loss effect. 2×10^8 events are used for these simulations, and a detector with 3 eV resolution and 10 eV threshold is assumed. Modified with permission from [182].

ever, it could still be extremely useful for other kinds of experiments, such as those attempting to detect coherent elastic neutrino-nucleus scattering like the MINER experiment [183]. These results, in conjunction with other recent studies such as [105], corroborate the necessity to investigate novel detector materials. With many experiments coming online that could be sensitive to the energy loss effect described in this work, such as the

IMPACT@TUNL measurement, the way is paved not only for novel dark matter detection methods but also for understanding defect creation on an experimental rather than purely computational level. Only time will tell the full extent of this method as experiments strive for ever-higher energy resolutions and even more intriguing materials are investigated.

4.3 Defect Creation Energy Loss Applications

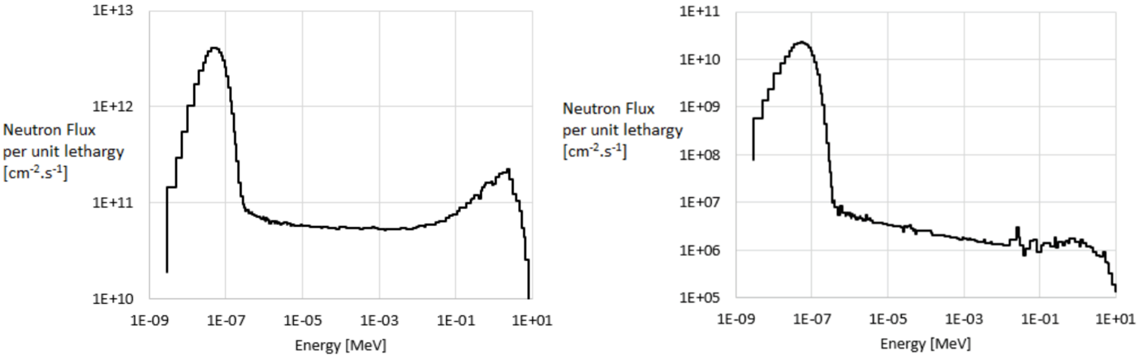

Figure 4.8: Reactor neutron spectrum per unit lethargy at the Texas A&M University Nuclear Science Center Reactor. The plot at left shows the neutron spectrum before shielding and the plot at right shows the neutron spectrum inside the experimental cavity, as calculated using MCNP. Results using both spectra as inputs are calculated in this subsection. Plot reprinted with permission from [183].

4.3.1 Reactor Neutrons

Just like an experiment looking for dark matter, an experiment looking for CENNS needs to contend with backgrounds that resemble the neutrino signal one wants to measure. For example, if the experiment looks for CENNS from antineutrinos produced in a nuclear reactor, it needs a way to discriminate the neutron background from the expected neutrino signal. This is in addition to discriminating the signal from electromagnetic backgrounds, which are outside the scope of this portion of the thesis.

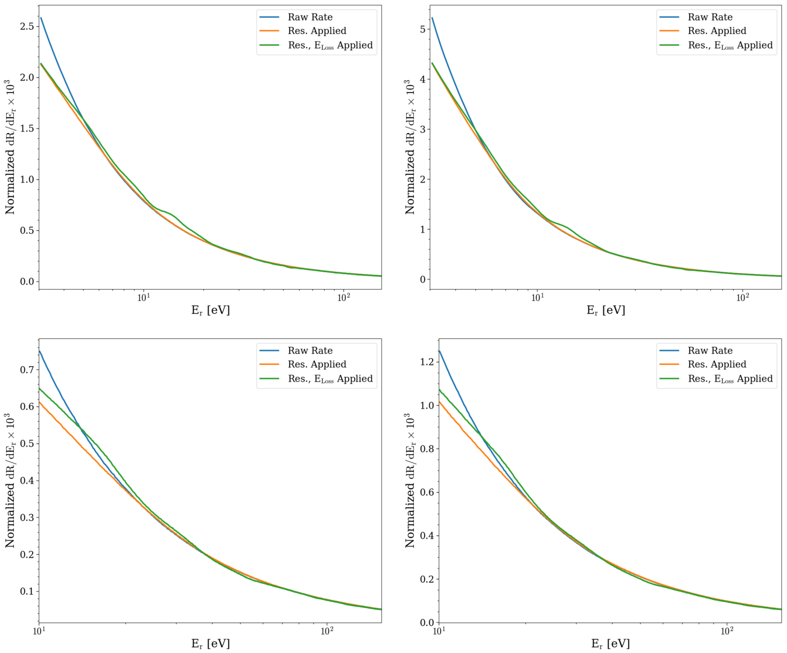

Figure 4.9: Calculated differential rate as a function of nuclear recoil energy for a phonon detector made of germanium given the neutron spectra without shielding (left two plots) and inside the experimental cavity (right two plots) for the nuclear reactor at the Texas A&M Nuclear Science Center. All of the curves are normalized with respect to 10^9 total events simulated for each calculation, and each plot includes energies up to 150 eV to more easily show the main energy loss features. The blue curves show the differential rate for a perfect detector, the orange curves for a detector with a given resolution and threshold, and the green curves for a detector given defect creation energy loss. The Stiller-Weber potential is used for finding the defect creation energy loss, which is further discussed in § 4.2. The upper two plots are for 1 eV resolution and 3 eV energy threshold, and the bottom two plots are for 3 eV resolution and 10 eV energy threshold. All plots are calculated given a neutron coming from a point source in the (001) direction for simplicity.

In the case of the MINER experiment, the neutron background might look like one of the two spectra shown in Fig. 4.8, as per Ref. [183]. Both plots show the neutron flux per unit lethargy as a function of neutron energy in MeV, as calculated by the Monte Carlo N-Particle Transport Code (MCNP). The plot at left is without any shielding, and the plot at right shows the spectrum inside the experimental chamber. Both spectra are used for the

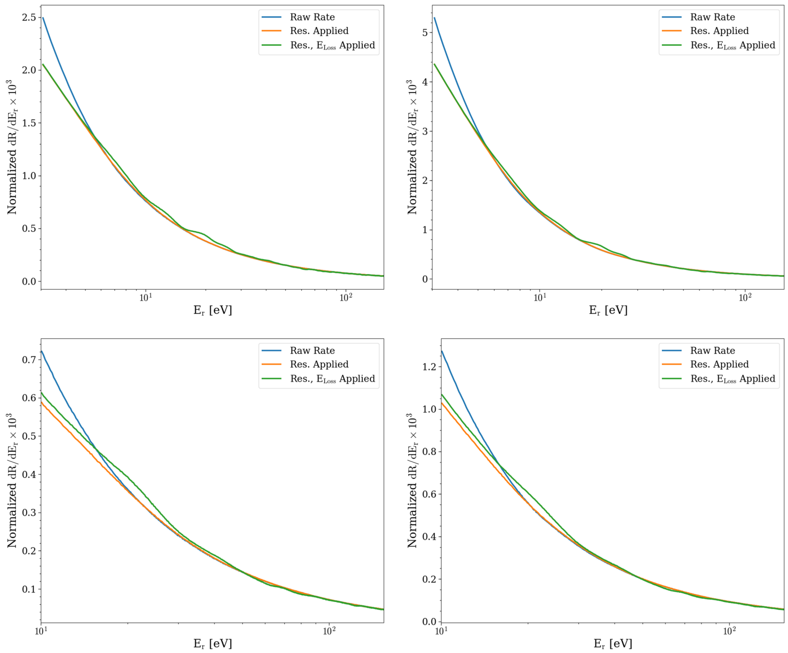

Figure 4.10: Calculated differential rate as a function of nuclear recoil energy for a phonon detector made of silicon given the neutron spectra without shielding (left two plots) and inside the experimental cavity (right two plots) for the nuclear reactor at the Texas A&M Nuclear Science Center. All of the curves are normalized with respect to 10^9 total events simulated for each calculation, and each plot includes energies up to 150 eV to more easily show the main energy loss features. The blue curves show the differential rate for a perfect detector, the orange curves for a detector with a given resolution and threshold, and the green curves for a detector given defect creation energy loss. The Stiller-Weber potential is used for finding the defect creation energy loss, which is further discussed in § 4.2. The upper two plots are for 1 eV resolution and 3 eV energy threshold, and the bottom two plots are for 3 eV resolution and 10 eV energy threshold. All plots are calculated given a neutron coming from a point source in the (001) direction for simplicity.

calculations in this part of the thesis.

As pointed out in § 4.2, a detector with resolution approaching the eV scale could show features in the spectrum caused by the energy required to produce a defect - energy that cannot be measured by a phonon detector. Because neutrons interact with atomic nuclei rather than electrons, a similar effect to that seen with dark matter in § 4.2 is expected

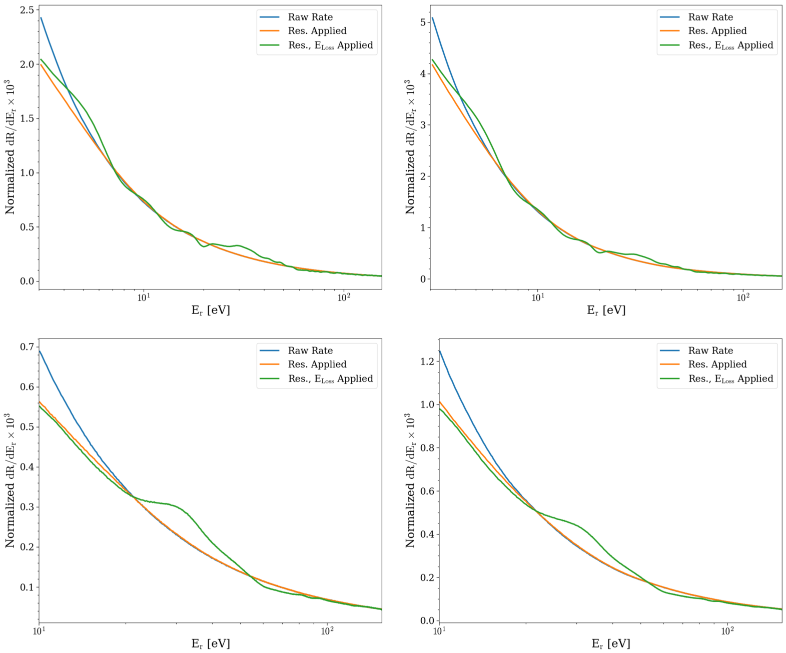

Figure 4.11: Calculated differential rate as a function of nuclear recoil energy for a phonon detector made of diamond given the neutron spectra without shielding (left two plots) and inside the experimental cavity (right two plots) for the nuclear reactor at the Texas A&M Nuclear Science Center. All of the curves are normalized with respect to 10^9 total events simulated for each calculation, and each plot includes energies up to 150 eV to more easily show the main energy loss features. The blue curves show the differential rate for a perfect detector, the orange curves for a detector with a given resolution and threshold, and the green curves for a detector given defect creation energy loss. The Erhart potential is used for finding the defect creation energy loss, which is further discussed in § 4.2. The upper two plots are for 1 eV resolution and 3 eV energy threshold, and the bottom two plots are for 3 eV resolution and 10 eV energy threshold. All plots are calculated given a neutron coming from a point source in the (001) direction for simplicity.

to occur with reactor neutrons. The difference in the shape of the spectrum between the reactor neutrons and reactor antineutrinos could then, in principle, be used to differentiate between reactor neutrons and reactor antineutrinos given a high enough number of events.

To calculate the energy loss effect for reactor neutrons, a full Monte Carlo simulation is carried out to find the differential rate per unit recoil energy before the energy loss is ap-

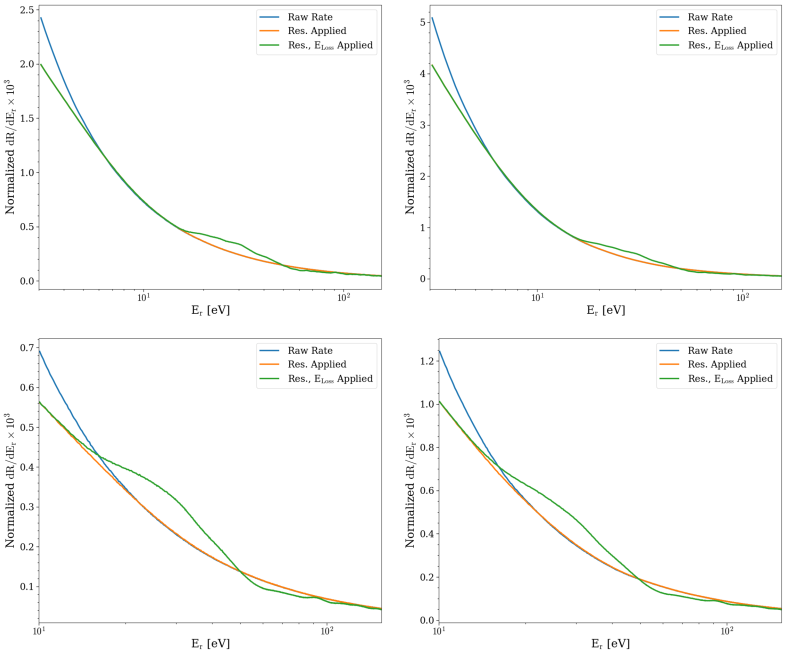

Figure 4.12: Calculated differential rate as a function of nuclear recoil energy for a phonon detector made of diamond given the neutron spectra without shielding (left two plots) and inside the experimental cavity (right two plots) for the nuclear reactor at the Texas A&M Nuclear Science Center. All of the curves are normalized with respect to 10^9 total events simulated for each calculation, and each plot includes energies up to 150 eV to more easily show the main energy loss features. The blue curves show the differential rate for a perfect detector, the orange curves for a detector with a given resolution and threshold, and the green curves for a detector given defect creation energy loss. The Tersoff-Nordlund potential is used for finding the defect creation energy loss, which is further discussed in § 4.2. The upper two plots are for 1 eV resolution and 3 eV energy threshold, and the bottom two plots are for 3 eV resolution and 10 eV energy threshold. All plots are calculated given a neutron coming from a point source in the (001) direction for simplicity.

plied and afterwards. In other words, neutron energies are sampled from the distributions in Fig. 4.8, which are digitized using the program in Ref. [170], the nuclear recoil direction is simulated assuming isotropic scattering, and the recoil energy is calculated using relation 1.5 given that m_χ is the mass of a neutron and m_A is the mass of the nucleus for a particular detector material. The energy loss models in § 4.2 are applied to each simulated

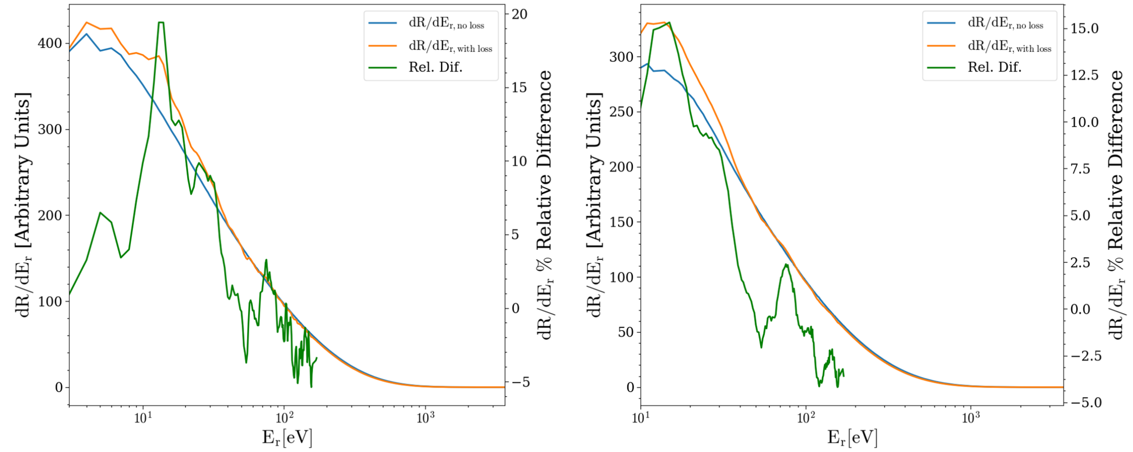

Figure 4.13: Differential rate per unit recoil energy as a function of recoil energy for a germanium detector and a reactor antineutrino source given the defect creation energy loss discussed in § 4.2. The Stiller-Weber potential energy model is used for calculating the energy loss. The blue curves show the differential rate without the energy loss, the orange curves show the differential rate with the energy loss included, and the green curves show the relative difference between the orange and blue curves as a function of recoil energy. The plots are for a detector with [left] 1 eV energy resolution and 3 eV energy threshold and [right] 3 eV energy resolution and 10 eV energy threshold. The relative difference is computed up to 170 eV.

nuclear reaction depending on the direction and recoil energy of the particle. For simulated energies greater than 200 eV, since that is the maximum of the defect creation energy loss data, a linear extrapolation of the mean energy loss from 170 eV to 200 eV, inclusive, is used for each defect creation model and detector material. Since any phonon detector does not have a perfect energy resolution, an energy selected from a Gaussian distribution with a given standard deviation to simulate the true detector resolution is added to the energy of each simulated events. The simulated event energies measured with a perfect detector, a detector with a given resolution and threshold, and the energy loss from § 4.2 are used to calculate the differential rate per unit recoil energy, integrated over all recoil angles.

The differential rates thus calculated are shown in Figures 4.9, 4.10, 4.11, and 4.12. The

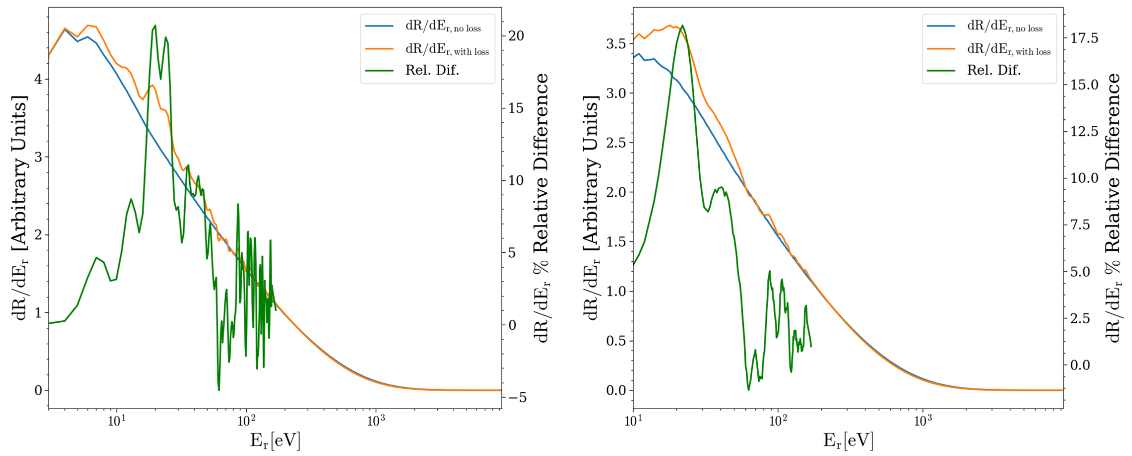

Figure 4.14: Differential rate per unit recoil energy as a function of recoil energy for a silicon detector and a reactor antineutrino source given the defect creation energy loss discussed in § 4.2. The Stiller-Weber potential energy model is used for calculating the energy loss. The blue curves show the differential rate without the energy loss, the orange curves show the differential rate with the energy loss included, and the green curves show the relative difference between the orange and blue curves as a function of recoil energy. The plots are for a detector with [left] 1 eV energy resolution and 3 eV energy threshold and [right] 3 eV energy resolution and 10 eV energy threshold. The relative difference is computed up to 170 eV.

differential rate spectra are found using 10^9 events total for each curve, and the spectra are normalized with respect to this quantity. 1 eV bins are used for the histograms for each curve. For the simulations, the neutron source is assumed to be in the (001) crystal direction. The plots at left use the leftmost spectrum in Fig. 4.8 as the input, and the plots at right use the rightmost spectrum. Additionally, the upper plots assume a detector with 1 eV resolution and 3 eV energy threshold, and the bottom plots assume a detector with 3 eV resolution and 10 eV threshold, as indicated by the difference in the range for the x-axes. All plots assume a maximum recoil energy of 155 eV to best show the main energy loss features.

These plots show how the defect creation energy loss can change the expected re-

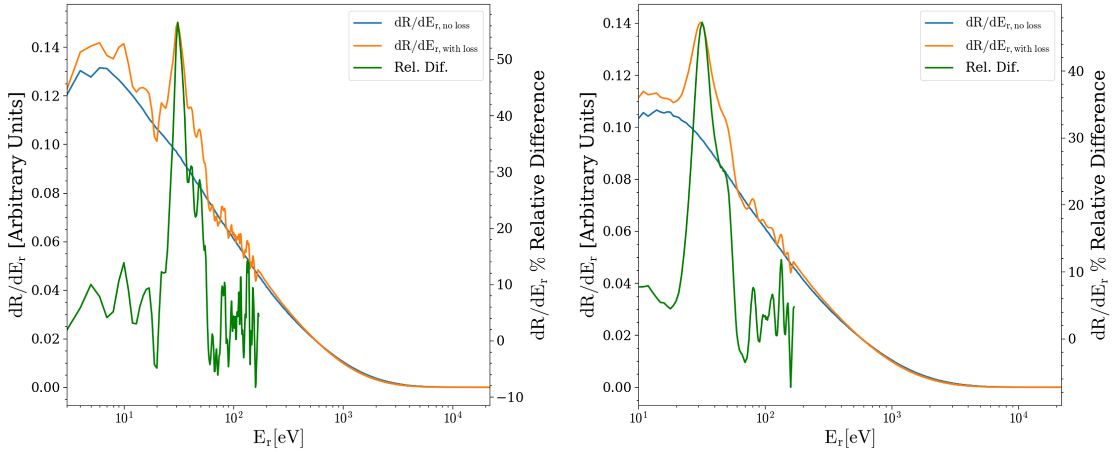

Figure 4.15: Differential rate per unit recoil energy as a function of recoil energy for a diamond detector and a reactor antineutrino source given the defect creation energy loss discussed in § 4.2. The Erhart potential energy model is used for calculating the energy loss. The blue curves show the differential rate without the energy loss, the orange curves show the differential rate with the energy loss included, and the green curves show the relative difference between the orange and blue curves as a function of recoil energy. The plots are for a detector with [left] 1 eV energy resolution and 3 eV energy threshold and [right] 3 eV energy resolution and 10 eV energy threshold. The relative difference is computed up to 170 eV.

actor neutron spectrum. Additionally, they show that the strength of the effect changes depending on the material used and that the features are largest for both diamond models compared to silicon or germanium. In the next portion of the dissertation, I discuss how the same defect creation energy loss models can affect the reactor neutrino spectrum.

4.3.2 Reactor Antineutrino CENNS

This analysis follows the same reasoning used for the results in § 3.4.2. However, in this case, one applies the energy loss values calculated in § 4.2 to the antineutrino spectrum rather than the energy thresholds. Similar to the dark matter calculation, the energy loss introduces peaks in an otherwise featureless spectrum that may help discriminate antineutrino signal from backgrounds.

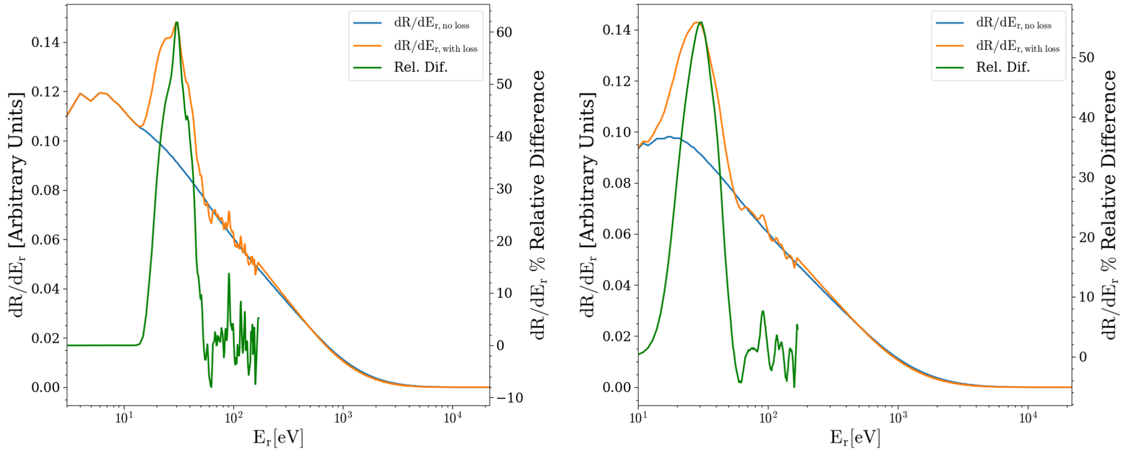

Figure 4.16: Differential rate per unit recoil energy as a function of recoil energy for a diamond detector and a reactor antineutrino source given the defect creation energy loss discussed in § 4.2. The Tersoff-Nordlund potential energy model is used for calculating the energy loss. The blue curves show the differential rate without the energy loss, the orange curves show the differential rate with the energy loss included, and the green curves show the relative difference between the orange and blue curves as a function of recoil energy. The plots are for a detector with [left] 1 eV energy resolution and 3 eV energy threshold and [right] 3 eV energy resolution and 10 eV energy threshold. The relative difference is computed up to 170 eV.

The expected change in the differential rate given the energy loss effect for different detector materials are shown in Figures 4.13, 4.14, 4.15, and 4.16. The blue curve is the differential rate given a certain detector resolution and threshold, the orange curve shows the effect of the energy loss, and the green curve is the relative difference between the orange and blue curves. The differential rate spectra are found using 2×10^8 events total for each curve, and 1 eV bins are used for the histograms for each. For each Figure, the plot at left assumes a detector with 1 eV resolution and 3 eV energy threshold, and the plot at right assumes a detector with 3 eV resolution and 10 eV threshold, as indicated by the difference in the range for the x-axes. 1 eV bins are used for the histograms. The energy loss data are used as given to calculate the energy loss effect on the spectrum for energies less than 200 eV. As discussed in § 4.3.1, a linear extrapolation using the energy loss data from 170 eV recoil energy and higher is used to model the defect creation energy loss effect for recoil energies greater than 200 eV.

Consistent with the results shown elsewhere in this dissertation, the change in differential energy per unit recoil energy is greatest for diamond, regardless of model, and the effect seems to be preserved as long as the detector has energy resolution close to the eV-scale. Hence, the energy loss could be observed with reactor CENNS given a high enough event rate and good enough detector resolution.

5. CONCLUSION AND PERSPECTIVE

There are many research areas where the effects of defect creation in solid-state detectors can be applied that range far beyond simply dark matter signal-background discrimination. For example, since this effect is independent of the charge signal, this method opens up many kinds of detector materials to use for detecting dark matter via athermal particle-interaction phonons, such as sapphire. Additionally, if materials exist that have an even larger range of energy losses depending on direction, it might be possible to have directional detectors utilizing this method via energy binning. This idea would then synergize with many current CENNS experiments that expect much larger event rates than dark matter, such as the MINER experiment at Texas A&M University, which is poised to use the semiconductor detectors considered in this work. This method could even act as a cross-disciplinary probe of DFT calculations since, at the moment, there is no strong experimental evidence at the atomic level to support their results, which are crucial for developing materials resistant to high radiation levels.

In the more distant future, it may even be possible, via sophisticated simulations and very high resolution detectors, to investigate the origin of the leakage current directly by using a potential anisotropy in the band gap for semiconductors, which has already been demonstrated in other materials [184]. Since all SuperCDMS-style detectors have readout circuitry printed on faces in the [100] crystal direction, there may be a measureable difference in the energy from leakage current events if the leakage current is coming from the contacts compared to if it is coming from the bulk. The results addressed in this dissertation could set the stage for such future detectors and simulations, thereby increasing our understanding of defect creation in materials and possibly even paving the way for next-generation dark matter detectors.

REFERENCES

[1] P. A. R. Ade *et al.*, “Planck 2013 results. XVI. Cosmological parameters,” *Astron. Astrophys.*, vol. 571, p. A16, 2014. [Online]. Available: https://doi.org/10.1051/0004-6361/201321591

[2] M. D. Leo, “File:Rotation curve of spiral galaxy Messier 33 (Triangulum).png,” https://upload.wikimedia.org/wikipedia/commons/c/cd/Rotation_curve_of_spiral_galaxy_Messier_33_%28Triangulum%29.png, Nov 2018.

[3] E. Corbelli and P. Salucci, “The Extended Rotation Curve and the Dark Matter Halo of M33,” *Mon. Not. Roy. Astron. Soc.*, vol. 311, pp. 441–447, 2000. [Online]. Available: https://doi.org/10.1046/j.1365-8711.2000.03075.x

[4] Y. Sofue and V. Rubin, “Rotation curves of spiral galaxies,” *Ann. Rev. Astron. Astrophys.*, vol. 39, pp. 137–174, 2001. [Online]. Available: https://doi.org/10.1146/annurev.astro.39.1.137

[5] H. Baumgardt and M. Hilker, “A catalogue of masses, structural parameters, and velocity dispersion profiles of 112 Milky Way globular clusters,” *Monthly Notices of the Royal Astronomical Society*, vol. 478, no. 2, pp. 1520–1557, 05 2018. [Online]. Available: https://doi.org/10.1093/mnras/sty1057

[6] P. van Dokkum, R. Abraham, J. Brodie, C. Conroy, S. Danieli, A. Merritt, L. Mowla, A. Romanowsky, and J. Zhang, “A High Stellar Velocity Dispersion and $\sim$100 Globular Clusters for the Ultra-diffuse Galaxy Dragonfly 44,” *Astrophys. J.*, vol. 828, no. 1, p. L6, 2016. [Online]. Available: https://doi.org/10.3847/2041-8205/828/1/L6

[7] G. Battaglia, A. Helmi, H. Morrison, P. Harding, E. W. Olszewski, M. Mateo, K. C. Freeman, J. Norris, and S. A. Shectman, “The Radial velocity dispersion

profile of the Galactic Halo: Constraining the density profile of the dark halo of the Milky Way," *Mon. Not. Roy. Astron. Soc.*, vol. 364, pp. 433–442, 2005, [Erratum: Mon. Not. Roy. Astron. Soc. 370, 1055 (2006)]. [Online]. Available: https://doi.org/10.1111/j.1365-2966.2005.09367.x

[8] E. K. McNeil-Moylan, K. C. Freeman, M. Arnaboldi, and O. E. Gerhard, "Planetary nebula kinematics in NGC 1316: a young Sombrero," *Astron. Astrophys.*, vol. 539, p. A11, 2012. [Online]. Available: https://doi.org/10.1051/0004-6361/201117875

[9] G. W. Pratt, M. Arnaud, A. Biviano, D. Eckert, S. Ettori, D. Nagai, N. Okabe, and T. H. Reiprich, "The galaxy cluster mass scale and its impact on cosmological constraints from the cluster population," *Space Sci. Rev.*, vol. 215, no. 2, p. 25, 2019. [Online]. Available: https://doi.org/10.1007/s11214-019-0591-0

[10] G. W. Pratt, J. H. Croston, M. Arnaud, and H. Boehringer, "Galaxy cluster X-ray luminosity scaling relations from a representative local sample (REXCESS)," *Astron. Astrophys.*, vol. 498, p. 361, 2009. [Online]. Available: https://doi.org/10.1051/0004-6361/200810994

[11] D. Clowe, M. Bradac, A. H. Gonzalez, M. Markevitch, S. W. Randall, C. Jones, and D. Zaritsky, "A direct empirical proof of the existence of dark matter," *Astrophys. J.*, vol. 648, pp. L109–L113, 2006. [Online]. Available: https://doi.org/10.1086/508162

[12] W. Tucker, P. Blanco, S. Rappoport, L. David, D. Fabricant, E. E. Falco, W. Forman, A. Dressler, and M. Ramella, "1e0657-56: a contender for the hottest known cluster of galaxies," *Astrophys. J.*, vol. 496, p. L5, 1998. [Online]. Available: https://doi.org/10.1086/311234

[13] D. Clowe, A. Gonzalez, and M. Markevitch, "Weak lensing mass reconstruction of the interacting cluster 1E0657-558: Direct evidence for the existence of dark matter," *Astrophys. J.*, vol. 604, pp. 596–603, 2004. [Online]. Available:

https://doi.org/10.1086/381970

[14] D. Harvey, R. Massey, T. Kitching, A. Taylor, and E. Tittley, “The non-gravitational interactions of dark matter in colliding galaxy clusters,” *Science*, vol. 347, pp. 1462–1465, 2015. [Online]. Available: https://doi.org/10.1126/science.1261381

[15] M. B. Pandge, R. Monteiro-Oliveira, J. Bagchi, A. Simionescu, M. Limousin, and S. Raychaudhury, “A combined X-ray, optical, and radio view of the merging galaxy cluster MACS J0417.5-1154,” *Mon. Not. Roy. Astron. Soc.*, vol. 482, no. 4, pp. 5093–5105, 2019. [Online]. Available: https://doi.org/10.1093/mnras/sty2937

[16] A. Del Popolo, “Dark matter, density perturbations, and structure formation,” *Astron. Rep.*, vol. 51, pp. 169–196, 2007. [Online]. Available: https://doi.org/10.1134/S1063772907030018

[17] C. S. Frenk and S. D. M. White, “Dark matter and cosmic structure,” *Annalen Phys.*, vol. 524, pp. 507–534, 2012. [Online]. Available: https://doi.org/10.1002/andp.201200212

[18] NASA / WMAP Science Team, “1e0657 scale.jpg,” https://upload.wikimedia.org/wikipedia/commons/3/3c/Ilc_9yr_moll4096.png, Apr 2017.

[19] NASA/WMAP Science Team, “WMAP TT power spectrum.png,” https://upload.wikimedia.org/wikipedia/commons/6/6a/WMAP_TT_power_spectrum.png, Dec 2005.

[20] K. Naidoo, A. Benoit-Lévy, and O. Lahav, “The cosmic microwave background Cold Spot anomaly: the impact of sky masking and the expected contribution from the integrated Sachs-Wolfe effect,” *Mon. Not. Roy. Astron. Soc.*, vol. 472, no. 1, pp. L65–L69, 2017. [Online]. Available: https://doi.org/10.1093/mnrasl/slx140

[21] R. Mackenzie, T. Shanks, M. N. Bremer, Y.-C. Cai, M. L. P. Gunawardhana, A. Kovács, P. Norberg, and I. Szapudi, “Evidence against a supervoid causing the CMB Cold Spot,” *Mon. Not. Roy. Astron. Soc.*, vol. 470, no. 2, pp. 2328–2338,

2017. [Online]. Available: https://doi.org/10.1093/mnras/stx931

[22] A. Kovács and J. García-Bellido, “Cosmic troublemakers: the Cold Spot, the Eridanus Supervoid, and the Great Walls,” *Mon. Not. Roy. Astron. Soc.*, vol. 462, no. 2, pp. 1882–1893, 2016. [Online]. Available: https://doi.org/10.1093/mnras/stw1752

[23] N. Aghanim *et al.*, “Planck 2018 results. VI. Cosmological parameters,” 2018. [Online]. Available: https://arxiv.org/abs/1807.06209

[24] G. Hinshaw *et al.*, “Nine-Year Wilkinson Microwave Anisotropy Probe (WMAP) Observations: Cosmological Parameter Results,” *Astrophys. J. Suppl.*, vol. 208, p. 19, 2013. [Online]. Available: https://doi.org/10.1088/0067-0049/208/2/19

[25] C. L. Bennett *et al.*, “Nine-Year Wilkinson Microwave Anisotropy Probe (WMAP) Observations: Final Maps and Results,” *Astrophys. J. Suppl.*, vol. 208, p. 20, 2013. [Online]. Available: https://doi.org/10.1088/0067-0049/208/2/20

[26] X. Dupac and M. Giard, “Map-making methods for cosmic microwave background experiments,” *Monthly Notices of the Royal Astronomical Society*, vol. 330, no. 3, pp. 497–505, 03 2002. [Online]. Available: https://doi.org/10.1046/j.1365-8711.2002.05057.x

[27] Edward L. Wright, “Cosmic Microwave Background Anisotropy,” http://www.astro.ucla.edu/~wright/CMB-DT.html, Jan 2013.

[28] Sloan Digital Sky Survey, “Science Results,” https://www.sdss.org/science/, 2018.

[29] P. van Dokkum *et al.*, “A galaxy lacking dark matter,” *Nature*, vol. 555, no. 7698, pp. 629–632, 2018. [Online]. Available: https://doi.org/10.1038/nature25767

[30] P. van Dokkum, S. Danieli, R. Abraham, C. Conroy, and A. J. Romanowsky, “A Second Galaxy Missing Dark Matter in the NGC 1052 Group,” *The Astrophysical Journal*, vol. 874, no. 1, p. L5, mar 2019. [Online]. Available: https://doi.org/10.3847%2F2041-8213%2Fab0d92

[31] S. Danieli, P. van Dokkum, C. Conroy, R. Abraham, and A. J. Romanowsky, "Still Missing Dark Matter: KCWI High-resolution Stellar Kinematics of NGC1052-DF2," *The Astrophysical Journal*, vol. 874, no. 2, p. L12, Mar 2019. [Online]. Available: https://doi.org/10.3847%2F2041-8213%2Fab0e8c

[32] Q. Guo *et al.*, "Further evidence for a population of dark-matter-deficient dwarf galaxies," *Nature*, 2019. [Online]. Available: https://doi.org/10.1038/s41550-019-0930-9

[33] K.-Y. Choi, J. E. Kim, and L. Roszkowski, "Review of axino dark matter," *J. Korean Phys. Soc.*, vol. 63, pp. 1685–1695, 2013. [Online]. Available: https://doi.org/10.3938/jkps.63.1685

[34] J. L. Feng *et al.*, "Planning the Future of U.S. Particle Physics (Snowmass 2013): Chapter 4: Cosmic Frontier," in *Proceedings, 2013 Community Summer Study on the Future of U.S. Particle Physics: Snowmass on the Mississippi (CSS2013): Minneapolis, MN, USA, July 29-August 6, 2013*, 2014. [Online]. Available: https://www.slac.stanford.edu/econf/C1307292/docs/CosmicFrontier.html

[35] L. Wyrzykowski *et al.*, "The OGLE View of Microlensing towards the Magellanic Clouds. IV. OGLE-III SMC Data and Final Conclusions on MACHOs," *Mon. Not. Roy. Astron. Soc.*, vol. 416, p. 2949, 2011. [Online]. Available: https://doi.org/10.1111/j.1365-2966.2011.19243.x

[36] P. Tisserand *et al.*, "Limits on the Macho Content of the Galactic Halo from the EROS-2 Survey of the Magellanic Clouds," *Astron. Astrophys.*, vol. 469, pp. 387–404, 2007. [Online]. Available: https://doi.org/10.1051/0004-6361:20066017

[37] T. D. Brandt, "Constraints on MACHO Dark Matter from Compact Stellar Systems in Ultra-Faint Dwarf Galaxies," *Astrophys. J.*, vol. 824, no. 2, p. L31, 2016. [Online]. Available: https://doi.org/10.3847/2041-8205/824/2/L31

[38] C. Alcock *et al.*, "The MACHO project: limits on planetary mass dark matter in

the galactic halo from gravitational microlensing," *Astrophys. J.*, vol. 471, p. 774, 1996. [Online]. Available: https://doi.org/10.1086/178005

[39] A. G. Riess *et al.*, "Observational evidence from supernovae for an accelerating universe and a cosmological constant," *Astron. J.*, vol. 116, pp. 1009–1038, 1998. [Online]. Available: https://doi.org/10.1086/300499

[40] R. Amanullah *et al.*, "Spectra and Light Curves of Six Type Ia Supernovae at 0.511 < z < 1.12 and the Union2 Compilation," *Astrophys. J.*, vol. 716, pp. 712–738, 2010. [Online]. Available: https://doi.org/10.1088/0004-637X/716/1/712

[41] R. H. Cyburt, B. D. Fields, and K. A. Olive, "Primordial nucleosynthesis in light of WMAP," *Phys. Lett.*, vol. B567, pp. 227–234, 2003. [Online]. Available: https://doi.org/10.1016/j.physletb.2003.06.026

[42] M. Tanabashi *et al.*, "Review of Particle Physics," *Phys. Rev.*, vol. D98, no. 3, p. 030001, 2018. [Online]. Available: https://doi.org/10.1103/PhysRevD.98.030001

[43] R. I. Epstein, J. M. Lattimer, and D. N. Schramm, "The origin of deuterium," *Nature*, vol. 263, pp. 198–202, 1976. [Online]. Available: https://doi.org/10.1038/263198a0

[44] M. C. Pyle, "Optimizing the design and analysis of cryogenic semiconductor dark matter detectors for maximum sensitivity," Ph.D. dissertation, Stanford U., 2012. [Online]. Available: http://purl.stanford.edu/bj167zz6539

[45] R. Essig, J. Mardon, and T. Volansky, "Direct detection of sub-GeV dark matter," *Phys. Rev.*, vol. D85, p. 076007, 2012. [Online]. Available: https://doi.org/10.1103/PhysRevD.85.076007

[46] J. L. Feng and J. Kumar, "The WIMPless Miracle: Dark-Matter Particles without Weak-Scale Masses or Weak Interactions," *Phys. Rev. Lett.*, vol. 101, p. 231301, 2008. [Online]. Available: https://doi.org/10.1103/PhysRevLett.101.231301

[47] C. Boehm and P. Fayet, "Scalar dark matter candidates," *Nucl. Phys.*, vol. B683,

pp. 219–263, 2004. [Online]. Available: https://doi.org/10.1016/j.nuclphysb.2004.01.015

[48] C. Boehm, P. Fayet, and J. Silk, "Light and heavy dark matter particles," *Phys. Rev.*, vol. D69, p. 101302, 2004. [Online]. Available: https://doi.org/10.1103/PhysRevD.69.101302

[49] N. Borodatchenkova, D. Choudhury, and M. Drees, "Probing MeV dark matter at low-energy e+e- colliders," *Phys. Rev. Lett.*, vol. 96, p. 141802, 2006. [Online]. Available: https://doi.org/10.1103/PhysRevLett.96.141802

[50] M. Pospelov, A. Ritz, and M. B. Voloshin, "Secluded WIMP Dark Matter," *Phys. Lett.*, vol. B662, pp. 53–61, 2008. [Online]. Available: https://doi.org/10.1016/j.physletb.2008.02.052

[51] P. Fayet, "U-boson production in e+ e- annihilations, psi and Upsilon decays, and Light Dark Matter," *Phys. Rev.*, vol. D75, p. 115017, 2007. [Online]. Available: https://doi.org/10.1103/PhysRevD.75.115017

[52] D. Hooper and K. M. Zurek, "Natural Supersymmetric Model with MeV Dark Matter," *Phys. Rev.*, vol. D77, p. 087302, 2008. [Online]. Available: https://doi.org/10.1103/PhysRevD.77.087302

[53] S. Nussinov, "Technocosmology - could a technibaryon excess provide a "natural" missing mass candidate?" *Phys. Lett.*, vol. 165B, pp. 55–58, 1985. [Online]. Available: https://doi.org/10.1016/0370-2693(85)90689-6

[54] D. B. Kaplan, "Single explanation for both the baryon and dark matter densities," *Phys. Rev. Lett.*, vol. 68, pp. 741–743, 1992. [Online]. Available: https://doi.org/10.1103/PhysRevLett.68.741

[55] D. E. Kaplan, M. A. Luty, and K. M. Zurek, "Asymmetric dark matter," *Phys. Rev.*, vol. D79, p. 115016, 2009. [Online]. Available: https://doi.org/10.1103/PhysRevD.79.115016

[56] A. Falkowski, J. T. Ruderman, and T. Volansky, "Asymmetric dark matter from leptogenesis," *JHEP*, vol. 05, p. 106, 2011. [Online]. Available: https://doi.org/10.1007/JHEP05(2011)106

[57] M. Pospelov, A. Ritz, and M. B. Voloshin, "Bosonic super-WIMPs as keV-scale dark matter," *Phys. Rev.*, vol. D78, p. 115012, 2008. [Online]. Available: https://doi.org/10.1103/PhysRevD.78.115012

[58] K. Rajagopal, M. S. Turner, and F. Wilczek, "Cosmological implications of axinos," *Nucl. Phys.*, vol. B358, pp. 447–470, 1991. [Online]. Available: https://doi.org/10.1016/0550-3213(91)90355-2

[59] L. Covi, J. E. Kim, and L. Roszkowski, "Axinos as cold dark matter," *Phys. Rev. Lett.*, vol. 82, pp. 4180–4183, 1999. [Online]. Available: https://doi.org/10.1103/PhysRevLett.82.4180

[60] K.-Y. Choi, L. Covi, J. E. Kim, and L. Roszkowski, "Axino cold dark matter revisited," *JHEP*, vol. 04, p. 106, 2012. [Online]. Available: https://doi.org/10.1007/JHEP04(2012)106

[61] J. R. Ellis, J. E. Kim, and D. V. Nanopoulos, "Cosmological gravitino regeneration and decay," *Phys. Lett.*, vol. 145B, pp. 181–186, 1984. [Online]. Available: https://doi.org/10.1016/0370-2693(84)90334-4

[62] A. Kusenko, "Sterile neutrinos: The dark side of the light fermions," *Phys. Rept.*, vol. 481, pp. 1–28, 2009. [Online]. Available: https://doi.org/10.1016/j.physrep.2009.07.004

[63] R. D. Peccei and H. R. Quinn, "CP Conservation in the Presence of Pseudoparticles," *Phys. Rev. Lett.*, vol. 38, pp. 1440–1443, 1977, [,328(1977)]. [Online]. Available: https://doi.org/10.1103/PhysRevLett.38.1440

[64] R. D. Peccei, "The Strong CP Problem and Axions," *Lect. Notes Phys.*, vol. 741, pp. 3–17, 2008, [,3(2006)]. [Online]. Available: https://doi.org/10.1007/

978-3-540-73518-2_1

[65] T. Aralis *et al.*, “Constraints on dark photons and axion-like particles from SuperCDMS Soudan,” 2019. [Online]. Available: https://arxiv.org/pdf/1911.11905.pdf

[66] P. Svrcek and E. Witten, “Axions in string theory,” *JHEP*, vol. 06, p. 051, 2006. [Online]. Available: https://doi.org/10.1088/1126-6708/2006/06/051

[67] D. J. E. Marsh, “Axions and ALPs: a very short introduction,” in *Proceedings, 13th Patras Workshop on Axions, WIMPs and WISPs, (PATRAS 2017): Thessaloniki, Greece, 15 May 2017 - 19, 2017*, 2018, pp. 59–74. [Online]. Available: https://doi.org/10.3204/DESY-PROC-2017-02/marsh_david

[68] G. Grilli di Cortona, E. Hardy, J. Pardo Vega, and G. Villadoro, “The QCD axion, precisely,” *JHEP*, vol. 01, p. 034, 2016. [Online]. Available: https://doi.org/10.1007/JHEP01(2016)034

[69] A. Derevianko, V. A. Dzuba, V. V. Flambaum, and M. Pospelov, “Axio-electric effect,” *Phys. Rev.*, vol. D82, p. 065006, 2010. [Online]. Available: https://doi.org/10.1103/PhysRevD.82.065006

[70] R. W. Schnee, “Introduction to dark matter experiments,” in *Physics of the large and the small, TASI 09, proceedings of the Theoretical Advanced Study Institute in Elementary Particle Physics, Boulder, Colorado, USA, 1-26 June 2009*, 2011, pp. 775–829. [Online]. Available: http://inspirehep.net/record/885795/files/arXiv:1101.5205.pdf

[71] N. Bozorgnia, G. B. Gelmini, and P. Gondolo, “Daily modulation due to channeling in direct dark matter crystalline detectors,” *Phys. Rev.*, vol. D84, p. 023516, 2011. [Online]. Available: https://doi.org/10.1103/PhysRevD.84.023516

[72] C. A. J. O’Hare, A. M. Green, J. Billard, E. Figueroa-Feliciano, and L. E. Strigari, “Readout strategies for directional dark matter detection beyond the neutrino

background," *Phys. Rev.*, vol. D92, no. 6, p. 063518, 2015. [Online]. Available: https://doi.org/10.1103/PhysRevD.92.063518

[73] G. Duda, A. Kemper, and P. Gondolo, "Model-independent form factors for spin independent neutralino-nucleon scattering from elastic electron scattering data," *JCAP*, vol. 0704, p. 012, 2007. [Online]. Available: https://doi.org/10.1088/1475-7516/2007/04/012

[74] J. D. Lewin and P. F. Smith, "Review of mathematics, numerical factors, and corrections for dark matter experiments based on elastic nuclear recoil," *Astropart. Phys.*, vol. 6, pp. 87–112, 1996. [Online]. Available: https://doi.org/10.1016/S0927-6505(96)00047-3

[75] P. Gondolo, "Recoil momentum spectrum in directional dark matter detectors," *Phys. Rev.*, vol. D66, p. 103513, 2002. [Online]. Available: https://doi.org/10.1103/PhysRevD.66.103513

[76] S. R. Golwala, "Exclusion limits on the WIMP nucleon elastic scattering cross-section from the Cryogenic Dark Matter Search," Ph.D. dissertation, UC, Berkeley, 2000. [Online]. Available: http://lss.fnal.gov/cgi-bin/find_paper.pl?thesis-2000-59

[77] N. Trevisani, "Collider Searches for Dark Matter (ATLAS + CMS)," *Universe*, vol. 4, no. 11, p. 131, 2018. [Online]. Available: https://doi.org/10.3390/universe4110131

[78] M. Wood, J. Buckley, S. Digel, S. Funk, D. Nieto, and M. A. Sanchez-Conde, "Prospects for Indirect Detection of Dark Matter with CTA," in *Proceedings, 2013 Community Summer Study on the Future of U.S. Particle Physics: Snowmass on the Mississippi (CSS2013): Minneapolis, MN, USA, July 29-August 6, 2013*, 2013. [Online]. Available: http://www.slac.stanford.edu/econf/C1307292/docs/submittedArxivFiles/1305.0302.pdf

[79] T. Saab and E. Figueroa, "Dark Matter Limit Plotter," https://supercdms.slac.

stanford.edu/dark-matter-limit-plotter, Dec 2019.

[80] R. Agnese *et al.*, “Low-mass dark matter search with CDMSlite,” *Phys. Rev.*, vol. D97, no. 2, p. 022002, 2018. [Online]. Available: https://doi.org/10.1103/PhysRevD.97.022002

[81] P. Cushman *et al.*, “Working Group Report: WIMP Dark Matter Direct Detection,” in *Proceedings, 2013 Community Summer Study on the Future of U.S. Particle Physics: Snowmass on the Mississippi (CSS2013): Minneapolis, MN, USA, July 29-August 6, 2013*, 2013. [Online]. Available: http://www.slac.stanford.edu/econf/C1307292/docs/CosmicFrontier/WIMPDirect-24.pdf

[82] S. Knapen, T. Lin, and K. M. Zurek, “Light dark matter: Models and constraints,” *Phys. Rev.*, vol. D96, no. 11, p. 115021, 2017. [Online]. Available: https://doi.org/10.1103/PhysRevD.96.115021

[83] R. Agnese *et al.*, “First Dark Matter Constraints from a SuperCDMS Single-Charge Sensitive Detector,” *Phys. Rev. Lett.*, vol. 121, no. 5, p. 051301, 2018, [erratum: Phys. Rev. Lett. 122, no. 6, 069901 (2019)]. [Online]. Available: https://doi.org/10.1103/PhysRevLett.121.051301

[84] R. Essig, M. Fernandez-Serra, J. Mardon, A. Soto, T. Volansky, and T.-T. Yu, “Direct detection of sub-GeV dark matter with semiconductor targets,” *JHEP*, vol. 05, p. 046, 2016. [Online]. Available: https://doi.org/10.1007/JHEP05(2016)046

[85] A. K. Jastram, “CDMS Detector Fabrication Improvements and Low Energy Nuclear Recoil Measurements in Germanium,” Ph.D. dissertation, Texas A&M University, 2015. [Online]. Available: https://doi.org/10.2172/1352051

[86] D. Speller for the SuperCDMS Collaboration, “Dark matter direct detection with SuperCDMS Soudan,” *Journal of Physics: Conference Series*, vol. 606, p. 012003, may 2015. [Online]. Available: https://doi.org/10.1088/1742-6596/606/1/012003

[87] D. C. Moore, "A search for low-mass dark matter with the cryogenic dark matter search and the development of highly multiplexed phonon-mediated particle detectors," Ph.D. dissertation, Caltech, 2012. [Online]. Available: http://thesis.library.caltech.edu/7043/

[88] Astronomical Applications Department, U.S. Naval Observatory, "Approximate Solar Coordinates," https://aa.usno.navy.mil/faq/docs/SunApprox.php, Nov 2012.

[89] Claus Tøndering, "The Julian Period," https://www.tondering.dk/claus/cal/julperiod.php, Sep 2011.

[90] Keith Burnett, "Converting RA and DEC to ALT and AZ," http://www.stargazing.net/kepler/altaz.html, May 1998.

[91] L. Manenti, "Liquid Argon Time Projection Chambers for Dark Matter and Neutrino Experiments," Ph.D. dissertation, U. Coll. London, 2016. [Online]. Available: http://discovery.ucl.ac.uk/1517934/

[92] P. F. Smith and J. D. Lewin, "Dark matter detection," *Phys. Rept.*, vol. 187, p. 203, 1990. [Online]. Available: https://doi.org/10.1016/0370-1573(90)90081-C

[93] T. Marrodán Undagoitia and L. Rauch, "Dark matter direct-detection experiments," *J. Phys.*, vol. G43, no. 1, p. 013001, 2016. [Online]. Available: https://doi.org/10.1088/0954-3899/43/1/013001

[94] F. Mayet *et al.*, "A review of the discovery reach of directional Dark Matter detection," *Phys. Rept.*, vol. 627, pp. 1–49, 2016. [Online]. Available: https://doi.org/10.1016/j.physrep.2016.02.007

[95] P. N. Luke, J. Beeman, F. S. Goulding, S. E. Labov, and E. H. Silver, "Calorimetric ionization detector," *Nucl. Instrum. Meth.*, vol. A289, pp. 406–409, 1990. [Online]. Available: https://doi.org/10.1016/0168-9002(90)91510-I

[96] R. K. Romani *et al.*, "Thermal detection of single e-h pairs in a biased silicon crystal detector," *Appl. Phys. Lett.*, vol. 112, p. 043501, 2018. [Online]. Available:

https://doi.org/10.1063/1.5010699

[97] N. Mirabolfathi, H. R. Harris, R. Mahapatra, K. Sundqvist, A. Jastram, B. Serfass, D. Faiez, and B. Sadoulet, "Toward Single Electron Resolution Phonon Mediated Ionization Detectors," *Nucl. Instrum. Meth.*, vol. A855, pp. 88–91, 2017. [Online]. Available: https://doi.org/10.1016/j.nima.2017.02.032

[98] N. Mirabolfathi, Email communication, Mar 2020.

[99] K. Nordlund, Email communication, Sep 2020.

[100] R. Moffatt, "Two-Dimensional Spatial Imaging of Charge Transport in Germanium Crystals at Cryogenic Temperatures," Ph.D. dissertation, Stanford University, 2016. [Online]. Available: https://doi.org/10.2172/1350526

[101] N. Mirabolfathi, Email communication, Jan 2020.

[102] F. Kadribasic, N. Mirabolfathi, K. Nordlund, A. E. Sand, E. Holmström, and F. Djurabekova, "Directional Sensitivity In Light-Mass Dark Matter Searches With Single-Electron Resolution Ionization Detectors," *Phys. Rev. Lett.*, vol. 120, no. 11, p. 111301, 2018. [Online]. Available: https://doi.org/10.1103/PhysRevLett.120.111301

[103] F. Kadribasic, K. Nordlund, F. Djurabekova, and N. Mirabolfathi, "Using Defect Creation in Materials as a Potential Signature of Dark Matter," Poster presented at 2019 TSAPS Meeting, Stephen F. Austin State University, Nacogdoches, Texas, USA.

[104] M. Biassoni *et al.*, "Large area Si low-temperature light detectors with Neganov-Luke effect," *Eur. Phys. J.*, vol. C75, no. 10, p. 480, 2015. [Online]. Available: https://doi.org/10.1140/epjc/s10052-015-3712-2

[105] N. A. Kurinsky, T. C. Yu, Y. Hochberg, and B. Cabrera, "Diamond detectors for direct detection of sub-GeV dark matter," *Phys. Rev.*, vol. D99, no. 12, p. 123005, 2019. [Online]. Available: https://doi.org/10.1103/PhysRevD.99.123005

[106] D. S. Akerib *et al.*, "Design and performance of a modular low-radioactivity readout system for cryogenic detectors in the CDMS experiment," *Nucl. Instrum. Meth.*, vol. A591, pp. 476–489, 2008. [Online]. Available: https://doi.org/10.1016/j.nima.2008.03.103

[107] W. A. Page, "Searching for Low-Mass Dark Matter with SuperCDMS Soudan Detectors," Ph.D. dissertation, University of British Columbia, 2019. [Online]. Available: https://open.library.ubc.ca/collections/24/items/1.0376351

[108] B. V. Zeghbroeck, *Principles of Semiconductor Devices*. Online, 2011. [Online]. Available: https://ecee.colorado.edu/~bart/book/book/title.htm

[109] N. Mirabolfathi, "Toward Single Electron Resolution Large Mass Detectors: Dark Matter, Neutrino physics," Lecture presented at 2016 Condensed Matter Seminar, Texas A&M University, College Station, USA.

[110] M. Platt, Email communication, Feb 2019.

[111] Z. Ahmed, "A Dark-Matter Search Using the Final CDMS II Dataset and a Novel Detector of Surface Radiocontamination," Ph.D. dissertation, Caltech, 2012. [Online]. Available: http://thesis.library.caltech.edu/6542/

[112] V. Mandic *et al.*, "Study of the dead layer in germanium for the CDMS detectors," *Nucl. Instrum. Meth.*, vol. A520, pp. 171–174, 2004. [Online]. Available: https://doi.org/10.1016/j.nima.2003.11.285

[113] T. Shutt, J. Emes, E. E. Haller, J. Hellmig, B. Sadoulet, D. Seitz, S. White, and B. A. Young, "A solution to the dead-layer problem in ionization and phonon-based dark matter detectors," *Nucl. Instrum. Meth.*, vol. A444, pp. 340–344, 2000. [Online]. Available: https://doi.org/10.1016/S0168-9002(99)01379-0

[114] Raymond T. Tung, "Free Surfaces of Semiconductors," http://academic.brooklyn.cuny.edu/physics/tung/Schottky/surface.htm, Jul 2019.

[115] Figueroa Group, "ATHERMAL DETECTORS." [Online]. Available: http:

//faculty.wcas.northwestern.edu/enectali-figueroa-feliciano/research/athermal.html

[116] Wayne Johnson, on behalf of the CDMS Collaboration, “ZIP Module V2 Users Manual,” 2001.

[117] F. Kadribasic, G. Agnolet, S. Esmaeili, A. Jastram, A. Kubik, R. Mahapatra, M. Platt, and N. Mirabolfathi, “Progress in Interface Studies for NTL Phonon-Assisted Large Calorimeters,” *J. Low. Temp. Phys. [pending publication]*, 2020.

[118] R. C. Alig and S. Bloom, “Electron-Hole-Pair Creation Energies in Semiconductors,” *Phys. Rev. Lett.*, vol. 35, pp. 1522–1525, Dec 1975. [Online]. Available: https://link.aps.org/doi/10.1103/PhysRevLett.35.1522

[119] J. Krupka, J. Breeze, A. Centeno, N. Alford, T. Claussen, and L. Jensen, “Measurements of Permittivity, Dielectric Loss Tangent, and Resistivity of Float-Zone Silicon at Microwave Frequencies,” *IEEE Transactions on Microwave Theory and Techniques*, vol. 54, no. 11, pp. 3995–4001, Nov 2006. [Online]. Available: https://doi.org/10.1109/TMTT.2006.883655

[120] T. A. Shutt, “A Dark Matter Detector Based on the Simultaneous Measurement of Phonons and Ionization at 20 mK,” Ph.D. dissertation, UC, Berkeley, 1993. [Online]. Available: http://lss.fnal.gov/cgi-bin/find_paper.pl?thesis-1993-28

[121] C. L. Wang and G. Agnolet, “Damping of crystallization waves at the solid-liquid interface of helium,” *Phys. Rev. Lett.*, vol. 69, pp. 2102–2105, Oct 1992. [Online]. Available: https://link.aps.org/doi/10.1103/PhysRevLett.69.2102

[122] C.-L. Wang, “Crystallization waves of solid-liquid interface of helium-4,” Ph.D. dissertation, 1994, copyright - Database copyright ProQuest LLC; ProQuest does not claim copyright in the individual underlying works; Last updated - 2020-02-20. [Online]. Available: http://proxy.library.tamu.edu/login?url=https://search.proquest.com/docview/304154931?accountid=7082

[123] CMR-Direct, “Cryoloom ® - Cryogenic Woven Loom,” http://www.cmr-direct.

com/en/woven-loom, 2020.

[124] E. Marquardt, J. Le, and R. Radebaugh, *Cryogenic Material Properties Database*, 01 2002, pp. 681–687. [Online]. Available: https://doi.org/10.1007/0-306-47112-4_84

[125] J. W. Ekin, *Experimental Techniques for Low-Temperature Measurements: Cryostat Design, Material Properties, and Superconductor Critical-Current Testing*. Oxford: Oxford Univ. Press, 2006. [Online]. Available: https://cds.cern.ch/record/1016440

[126] M. C. Veale, J. Kalliopuska, H. Pohjonen, H. Andersson, S. Nenonen, P. Seller, and M. D. Wilson, "Characterization of M-pi-n CdTe pixel detectors coupled to HEXITEC readout chip," *JINST*, vol. 7, p. C01035, 2012. [Online]. Available: https://doi.org/10.1088/1748-0221/7/01/C01035

[127] F. Kadribasic and S. Esmaeili, "Recent Progress Towards Understanding SuperCDMS High-Voltage Detector Contacts," Poster presented at 2018 April APS Meeting, Columbus, Ohio, USA.

[128] R. Agnese *et al.*, "Projected Sensitivity of the SuperCDMS SNOLAB experiment," *Phys. Rev.*, vol. D95, no. 8, p. 082002, 2017. [Online]. Available: https://doi.org/10.1103/PhysRevD.95.082002

[129] J. R. T. de Mello Neto *et al.*, "The DAMIC dark matter experiment," *PoS*, vol. ICRC2015, p. 1221, 2016. [Online]. Available: https://doi.org/10.22323/1.236.1221

[130] J. Li, "Directional dark matter by polar angle direct detection and application of columnar recombination," *Phys. Rev.*, vol. D92, no. 4, p. 043523, 2015. [Online]. Available: https://doi.org/10.1103/PhysRevD.92.043523

[131] C. Bœhm, D. G. Cerdeño, P. A. N. Machado, A. Olivares-Del Campo, and E. Reid, "How high is the neutrino floor?" *JCAP*, vol. 1901, p. 043, 2019. [Online].

Available: https://doi.org/10.1088/1475-7516/2019/01/043

[132] P. Grothaus, M. Fairbairn, and J. Monroe, “Directional dark matter detection beyond the neutrino bound,” *Phys. Rev.*, vol. D90, no. 5, p. 055018, 2014. [Online]. Available: https://doi.org/10.1103/PhysRevD.90.055018

[133] R. Averback and T. de la Rubia, “Displacement Damage in Irradiated Metals and Semiconductors,” *Solid State Physics: Advances in Research and Applications*, vol. 51, no. C, pp. 281–402, 12 1997. [Online]. Available: https://doi.org/10.1016/S0081-1947(08)60193-9

[134] K. Nordlund, S. J. Zinkle, A. E. Sand, F. Granberg, R. S. Averback, R. Stoller, T. Suzudo, L. Malerba, F. Banhart, W. J. Weber, F. Willaime, S. Dudarev, and D. Simeone, “Primary radiation damage: A review of current understanding and models,” *J. Nucl. Mater.*, vol. 512, pp. 450–479, 2018. [Online]. Available: https://doi.org/10.1016/j.jnucmat.2018.10.027

[135] J.-F. Mercure, R. Karmouch, Y. Anahory, S. Roorda, and F. Schiettekatte, “Radiation damage in silicon studied in situ by nanocalorimetry,” *Physica B Condensed Matter*, vol. 342, 12 2003. [Online]. Available: https://doi.org/10.1016/j.physb.2003.09.243

[136] K. Nordlund, “Historical review of computer simulation of radiation effects in materials,” *J. Nucl. Mater.*, vol. 520, p. 273, 2019. [Online]. Available: https://doi.org/10.1016/j.jnucmat.2019.04.028

[137] D. H. Speller, “Systematics of Low Threshold Modulation Searches in DMS II,” *Phys. Procedia*, vol. 61, pp. 774–781, 2015. [Online]. Available: https://doi.org/10.1016/j.phpro.2014.12.098

[138] B. J. Scholz, A. E. Chavarria, J. I. Collar, P. Privitera, and A. E. Robinson, “Measurement of the low-energy quenching factor in germanium using an ^{88}Y/Be photoneutron source,” *Phys. Rev.*, vol. D94, no. 12, p. 122003, 2016. [Online].

Available: https://doi.org/10.1103/PhysRevD.94.122003

[139] S. T. Lin *et al.*, “New limits on spin-independent and spin-dependent couplings of low-mass WIMP dark matter with a germanium detector at a threshold of 220 eV,” *Phys. Rev.*, vol. D79, p. 061101, 2009. [Online]. Available: https://doi.org/10.1103/PhysRevD.79.061101

[140] J. Lindhard, V. Nielsen, M. Scharff, and P. Thomsen, “INTEGRAL EQUATIONS GOVERNING RADIATION EFFECTS. (NOTES ON ATOMIC COLLISIONS, III),” *Kgl. Danske Videnskab., Selskab. Mat. Fys. Medd.*, vol. Vol: 33: No. 10, Jan 1963.

[141] M. D. Pepin, “Low-Mass Dark Matter Search Results and Radiogenic Backgrounds for the Cryogenic Dark Matter Search,” Ph.D. dissertation, Minnesota U., 2016. [Online]. Available: http://lss.fnal.gov/archive/thesis/2000/fermilab-thesis-2016-31.pdf

[142] D. Barker and D. M. Mei, “Germanium detector response to nuclear recoils in searching for dark matter,” *Astropart. Phys.*, vol. 38, pp. 1–6, 2012. [Online]. Available: https://doi.org/10.1016/j.astropartphys.2012.08.006

[143] R. Agnese *et al.*, “Energy loss due to defect formation from ^{206}Pb recoils in SuperCDMS germanium detectors,” *Appl. Phys. Lett.*, vol. 113, no. 9, p. 092101, 2018. [Online]. Available: https://doi.org/10.1063/1.5041457

[144] J. E. Valdes, C. Parra, J. Diaz-Valdes, C. D. Denton, C. Agurto, F. Ortega, N. R. Arista, and P. Vargas, “Experimental energy loss of slow H^+ and H_2^+ in channeling conditions,” *Phys. Rev. A*, vol. 68, p. 064901, Dec 2003. [Online]. Available: http://link.aps.org/doi/10.1103/PhysRevA.68.064901

[145] D. Primetzhofer, “Inelastic energy loss of medium energy H and He ions in Au and Pt: Deviations from velocity proportionality,” *Phys. Rev. B*, vol. 86, p. 094102, 2012. [Online]. Available: https://doi.org/10.1103/PhysRevB.86.094102

[146] E. Holmström, A. Kuronen, and K. Nordlund, “Threshold defect production in silicon determined by density functional theory molecular dynamics simulations,” *Phys. Rev. B*, vol. 78, no. 4, p. 045202, 2008. [Online]. Available: https://doi.org/10.1103/PhysRevB.78.045202

[147] E. Holmström, K. Nordlund, and A. Kuronen, “Threshold defect production in germanium determined by density functional theory molecular dynamics simulations,” *Physica Scripta*, vol. 81, p. 035601, 2010. [Online]. Available: https://doi.org/10.1088/0031-8949/81/03/035601

[148] C. Auth, A. Mertens, H. Winter, and A. Borisov, “Threshold in the Stopping of Slow Protons Scattered from the Surface of a Wide-Band-Gap Insulator,” *Phys. Rev. Lett.*, vol. 81, pp. 4831–4834, Nov 1998. [Online]. Available: https://link.aps.org/doi/10.1103/PhysRevLett.81.4831

[149] S. N. Markin, D. Primetzhofer, and P. Bauer, “Vanishing Electronic Energy Loss of Very Slow Light Ions in Insulators with Large Band Gaps,” *Physical Review Letters*, vol. 103, no. 11, p. 113201, 2009. [Online]. Available: https://doi.org/10.1103/PhysRevLett.103.113201

[150] J. M. Pruneda, D. Sánchez-Portal, A. Arnau, J. I. Juaristi, and E. Artacho, “Electronic Stopping Power in LiF from First Principles,” *Phys. Rev. Lett.*, vol. 99, p. 235501, Dec 2007. [Online]. Available: https://link.aps.org/doi/10.1103/PhysRevLett.99.235501

[151] A. Ojanperä, A. V. Krasheninnikov, and M. Puska, “Electronic stopping power from first-principles calculations with account for core electron excitations and projectile ionization,” *Phys. Rev. B*, vol. 89, p. 035120, Jan 2014. [Online]. Available: https://link.aps.org/doi/10.1103/PhysRevB.89.035120

[152] P. Vajda, “Anisotropy of electron radiation damage in metal crystals,” *Rev. Mod. Phys.*, vol. 49, p. 481, 1977. [Online]. Available: https:

//doi.org/10.1103/RevModPhys.49.481

[153] A. Lim, W. M. C. Foulkes, A. P. Horsfield, D. R. Mason, A. Schleife, E. W. Draeger, and A. A. Correa, "Electron Elevator: Excitations across the Band Gap via a Dynamical Gap State," *Phys. Rev. Lett.*, vol. 116, p. 043201, 2016. [Online]. Available: https://doi.org/10.1103/PhysRevLett.116.043201

[154] A. V. Krasheninnikov, Y. Miyamoto, and D. Tománek, "Role of Electronic Excitations in Ion Collisions with Carbon Nanostructures," *Phys. Rev. Lett.*, vol. 99, p. 016104, Jul 2007. [Online]. Available: https://link.aps.org/doi/10.1103/PhysRevLett.99.016104

[155] R. J. Gaitskell, "Direct Detection of Dark Matter," *Ann. Rev. Nucl. Part. Sci.*, vol. 54, pp. 315–359, 2004. [Online]. Available: https://doi.org/10.1146/annurev.nucl.54.070103.181244

[156] R. Agnese *et al.*, "Search for Low-Mass Weakly Interacting Massive Particles Using Voltage-Assisted Calorimetric Ionization Detection in the SuperCDMS Experiment," *Phys. Rev. Lett.*, vol. 112, no. 4, p. 041302, 2014. [Online]. Available: https://doi.org/10.1103/PhysRevLett.112.041302

[157] D. Barker, W. Z. Wei, D. M. Mei, and C. Zhang, "Ionization efficiency study for low energy nuclear recoils in germanium," *Astropart. Phys.*, vol. 48, p. 8, 2013. [Online]. Available: https://doi.org/10.1016/j.astropartphys.2013.06.010

[158] M. P. Allen and D. J. Tildesley, *Computer Simulation of Liquids*. Oxford, England: Oxford University Press, 1989.

[159] K. Nordlund, J. Wallenius, and L. Malerba, "Molecular dynamics simulations of threshold energies in Fe," *Nucl. Instr. Meth. Phys. Res. B*, vol. 246, no. 2, pp. 322–332, 2005. [Online]. Available: https://doi.org/10.1016/j.nimb.2006.01.003

[160] K. Ding and H. C. Andersen, "Molecular-dynamics simulation of amorphous germanium," *Phys. Rev. B*, vol. 34, no. 10, p. 6987, 1986. [Online]. Available:

https://doi.org/10.1103/physrevb.34.6987

[161] K. Nordlund, M. Ghaly, R. S. Averback, M. Caturla, T. Diaz de la Rubia, and J. Tarus, “Defect production in collision cascades in elemental semiconductors and fcc metals,” *Phys. Rev. B*, vol. 57, pp. 7556–7570, Apr 1998. [Online]. Available: https://link.aps.org/doi/10.1103/PhysRevB.57.7556

[162] M. Posselt and A. Gabriel, “Atomistic simulation of amorphous germanium and its solid phase epitaxial recrystallization,” *Phys. Rev. B*, vol. 80, p. 045202, 2009. [Online]. Available: https://doi.org/10.1103/PhysRevB.80.045202

[163] F. H. Stillinger and T. A. Weber, “Computer simulation of local order in condensed phases of silicon,” *Phys. Rev. B*, vol. 31, p. 5262, 1985. [Online]. Available: https://doi.org/10.1103/physrevb.31.5262

[164] K. M. Górski, E. Hivon, A. J. Banday, B. D. Wandelt, F. K. Hansen, M. Reinecke, and M. Bartelman, “HEALPix: A Framework for High-Resolution Discretization and Fast Analysis of Data Distributed on the Sphere,” *Astrophys. J.*, vol. 622, pp. 759–771, 2005. [Online]. Available: https://doi.org/10.1086/427976

[165] E. Holmström, A. V. Krasheninnikov, and K. Nordlund, “Quantum and Classical Molecular Dynamics Studies of the Threshold Displacement Energy in Si Bulk and Nanowire,” in *Ion Beams and Nano-Engineering*, ser. MRS Symposium Proceedings, D. Ila, J. K. N. Lindner, P. K. Chu, J. Baglin, and N. Kishimoto, Eds. Warrendale, PA, USA: MRS, 2010, vol. 1181, pp. 111–122. [Online]. Available: https://doi.org/10.1557/PROC-1181-DD05-02

[166] D. S. Gemmell, “Channeling and related effects in the motion of charged particles through crystals,” *Rev. Mod. Phys.*, vol. 46, pp. 129–227, 1974. [Online]. Available: https://doi.org/10.1103/RevModPhys.46.129

[167] M. Blackman, *Handbuch der Physik*. Berlin: Springer-Verlag, 1955, vol. VII.

[168] D. Akimov *et al.*, “Observation of coherent elastic neutrino-nucleus scattering,”

Science, vol. 357, no. 6356, pp. 1123–1126, 2017. [Online]. Available: https://doi.org/10.1126/science.aao0990

[169] V. Sharma, V. Singh, V. S. Subrahmanyam, and H. T. Wong, “Status of the search of coherent neutrino nucleus elastic scattering at KSNL,” *Indian J. Phys.*, vol. 92, no. 9, pp. 1145–1152, 2018. [Online]. Available: https://doi.org/10.1007/s12648-018-1202-8

[170] Ankit Rohatgi, “WebPlotDigitizer,” https://automeris.io/WebPlotDigitizer, Apr 2019.

[171] S. Agostinelli *et al.*, “GEANT4: A Simulation toolkit,” *Nucl. Instrum. Meth.*, vol. A506, pp. 250–303, 2003. [Online]. Available: https://doi.org/10.1016/S0168-9002(03)01368-8

[172] J. Allison *et al.*, “Geant4 developments and applications,” *IEEE Trans. Nucl. Sci.*, vol. 53, p. 270, 2006. [Online]. Available: https://doi.org/10.1109/TNS.2006.869826

[173] Allison, J. and others, “Recent developments in Geant4,” *Nucl. Instrum. Meth.*, vol. A835, pp. 186–225, 2016. [Online]. Available: https://doi.org/10.1016/j.nima.2016.06.125

[174] S. A. Hertel, “Advancing the Search for Dark Matter: from CDMS II to SuperCDMS,” Ph.D. dissertation, MIT, 2012. [Online]. Available: http://lss.fnal.gov/cgi-bin/find_paper.pl?thesis-2012-19

[175] M. Ghaly, K. Nordlund, and R. S. Averback, “Molecular dynamics investigations of surface damage produced by kiloelectronvolt self-bombardment of solids,” *Philosophical Magazine A*, vol. 79, no. 4, pp. 795–820, 1999. [Online]. Available: https://doi.org/10.1080/01418619908210332

[176] K. Nordlund, “Molecular dynamics simulation of ion ranges in the 1-100 keV energy range,” *Computational Materials Science*, vol. 3, no. 4, pp. 448 –

456, 1995. [Online]. Available: http://www.sciencedirect.com/science/article/pii/092702569400085Q

[177] J. Tersoff, “Modeling solid-state chemistry: Interatomic potentials for multicomponent systems,” *Phys. Rev. B*, vol. 39, no. 8, p. 5566, 1989. [Online]. Available: https://doi.org/10.1103/physrevb.39.5566

[178] K. Nordlund, J. Keinonen, and T. Mattila, “Formation of Ion Irradiation Induced Small-Scale Defects on Graphite Surfaces,” *Phys. Rev. Lett.*, vol. 77, no. 4, p. 699, 1996. [Online]. Available: https://doi.org/10.1103/PhysRevLett.77.699

[179] P. Erhart and K. Albe, “Analytical potential for atomistic simulations of silicon, carbon, and silicon carbide,” *Phys. Rev. B*, vol. 71, p. 035211, 2005. [Online]. Available: https://doi.org/10.1103/PhysRevB.71.035211

[180] J. Koike and D. M. Parkin and T. E. Mitchell, “Displacement threshold energy for type IIa diamond,” *Appl. Phys. Lett.*, vol. 60, no. 12, p. 1450, 1992. [Online]. Available: https://doi.org/10.1063/1.107267

[181] J. C. Bourgoin and B. Massarani, “Threshold energy for atomic displacement in diamond,” *Phys. Rev. B*, vol. 14, no. 8, p. 3690, 1976. [Online]. Available: https://doi.org/10.1103/PhysRevB.14.3690

[182] F. Kadribasic, N. Mirabolfathi, K. Nordlund, and F. Djurabekova, “Crystal Defects: A Portal To Dark Matter Detection,” 2020. [Online]. Available: https://arxiv.org/abs/2002.03525

[183] G. Agnolet *et al.*, “Background Studies for the MINER Coherent Neutrino Scattering Reactor Experiment,” *Nucl. Instrum. Meth.*, vol. A853, pp. 53–60, 2017. [Online]. Available: https://doi.org/10.1016/j.nima.2017.02.024

[184] A. J. Bennett, “Theory of the Anisotropic Energy Gap in Superconducting Lead,” *Phys. Rev.*, vol. 140, pp. A1902–A1920, Dec 1965. [Online]. Available: https://link.aps.org/doi/10.1103/PhysRev.140.A1902

[185] N. Mirabolfathi, Email communication, Jan 2020.

[186] Samuel Watkins, “Derivation of Energy Absorbed,” 2020. [Online]. Available: https://confluence.slac.stanford.edu/download/attachments/248421666/energy_absorbed_deriv.pdf?version=1&modificationDate=1571253583000&api=v2

[187] Samuel Watkins for the SuperCDMS Collaboration, “Internal Documentation: PD2 DM Search,” 2020. [Online]. Available: https://confluence.slac.stanford.edu/display/CDMS/Internal+Documentation%3A+PD2+DM+Search

[188] K. Irwin and G. Hilton, *Transition-Edge Sensors*. Berlin, Heidelberg: Springer Berlin Heidelberg, 2005, pp. 63–150. [Online]. Available: https://link.springer.com/chapter/10.1007%2F10933596_3

[189] D. Freedman and P. Diaconis, “On the histogram as a density estimator: L2 theory,” *Probability Theory and Related Fields*, vol. 57, no. 4, pp. 453–476, Dec. 1981. [Online]. Available: http://dx.doi.org/10.1007/BF01025868

APPENDIX A

4 K HEATSINK HEAT TRANSFER CALCULATIONS

A.1 Synopsis

I present calculations to find the optimal material for constructing the heat contact on the new 4 K can for the Kelvinox-400 Dilution Refrigerator in the B09 Lab at the ENPH building at Texas A&M University.

A.2 Heat Conduction Theory

In the realm of cryogenics, all three forms of heat transfer (conduction, convection, and radiation) are relevant in different contexts. In the case of constructing the new 4 K can, the most important is heat transfer via conduction. This is governed by Fourier's Law, which is most conveniently written in its differential form as

$$\boldsymbol{q} = -k\boldsymbol{\nabla}T \tag{A.1}$$

where $\boldsymbol{q}$ is the local heat flux density, k is the thermal conductivity, and T is the temperature. The negative sign comes from the fact that heat flow is from a higher to a lower temperature.

This result can be integrated to yield

$$\frac{dQ}{dt} = -k \oint_S \boldsymbol{\nabla}T \cdot \mathrm{d}\boldsymbol{S}. \tag{A.2}$$

In the case of 1-D geometry and a single, continuous material, Eq. A.2 can be rewritten as

$$\frac{\Delta Q}{\Delta t} = -kA\frac{\Delta T}{\Delta x} \tag{A.3}$$

where $\frac{\Delta Q}{\Delta t} = P$ is the rate of heat flow (or cooling power in this context), k is the thermal conductivity, A is the cross-sectional area, ΔT is the temperature difference between the two sides of the material, and Δx is the distance between the two sides.

One can rearrange Equation A.3 to give

$$\Delta T = \frac{P\Delta x}{kA} \tag{A.4}$$

In this form, one can see that to minimize the temperature gradient across some material, one can either decrease the heat load provided by the device under test (DUT), decrease the distance between the cold and hot end, increase the thermal conductivity, or increase the area. Since this dilution refrigerator will be running FET cards that have a relatively constant heat load and the shape of the final can remains constant, I will group all such constant terms into a factor σ defined as

$$\sigma \equiv \frac{P\Delta x}{A} \tag{A.5}$$

so that A.4 can be rewritten as

$$\Delta T = \frac{\sigma}{k} \tag{A.6}$$

Due to symmetry considerations, there is a large class of problems that can be solved using the simplified form A.4. It turns out that some more complicated problems, even though they cannot be written simply as A.4, can be turned into a form resembling A.6. Thus, in the next section I proceed to solve for σ for three geometries relevant to this refrigerator - a cylinder of constant cross-sectional area, a cube heated from the bottom and heatsunk on the side, and a quarter-disk heated on one flat side and heatsunk on the other. The cube and quarter-disk are meant to approximate a toroid heated unevenly from the bottom. I finish with the experimental data used to derive the temperature gradients.

A.3 σ for Relevant Geometries

A.3.1 Cylindrical Rod

Table A.1: Calculated thermal gradient across a 2 mm diameter wire that is 2 inches long

Material	**Thermal Conductivity (W/m K)**	**Temperature Gradient (K)**
Copper (RRR = 100)	400	0.404
Copper (RRR = 20)	100	1.62
Aluminum (6063-T5)	30	5.39
Brass	4	40.4
Stainless Steel	0.272	594

For the case of a cylindrical rod with radius r and length L, it is most prudent to solve for σ using A.5. The cross-sectional area A is given by

$$A = \pi r^2 \tag{A.7}$$

and Δx is just given by

$$\Delta x = L. \tag{A.8}$$

Putting this into A.5 yields

$$\sigma = \frac{PL}{\pi r^2}, \tag{A.9}$$

and the thermal gradient for a 2 mm diameter wire that is 2 inches (5 cm) long are shown in Table A.1.

A.3.2 Rectangular Prism Heated at Bottom Face and Heatsunk on Side Face

The rectangular prism is the simplest approximation to the toroid geometry that will be implemented in the new fridge design. In this case, one can again employ A.5 if one is careful about selecting the distance Δx.

The problem can be solved most straightforwardly if one assumes that the prism has two dimensions of length s and a third of length L with the condition that the edge connecting the heated and cooled face has dimension L. Thus, the area for heat transfer is given approximately by

$$A = Ls. \tag{A.10}$$

We note that far away from the edge where the heatsunk and heated face meet Δx is much greater than closer to that edge. Thus, we approximate Δx by taking the average between the two sides. Since each side has length s and this is an isosceles right triangle, Δx is given by

$$\Delta x = \sqrt{2}\frac{s}{2} = \frac{x}{\sqrt{2}} \tag{A.11}$$

Combining A.10 with A.11 in Equation A.5 yields

$$\sigma = \frac{P\Delta x}{A} = P\frac{s}{\sqrt{2}}\frac{1}{Ls} = \frac{P}{\sqrt{2}L} \tag{A.12}$$

This result shows that, at least in this simple approximation, the thermal gradient across the toroid is independent of its thickness.

Table A.2: Temperature gradient from the bottom to the side face of a 2 mm thick prism.

Material	**Thermal Conductivity (W/m K)**	**Temperature Gradient (mK)**
Copper (RRR = 100)	400	0.696
Copper (RRR = 20)	100	2.784
Aluminum (6063-T5)	30	9.28
Brass	4	69.6
Stainless Steel	0.272	1023

A.3.3 Thin Quarter-Disk

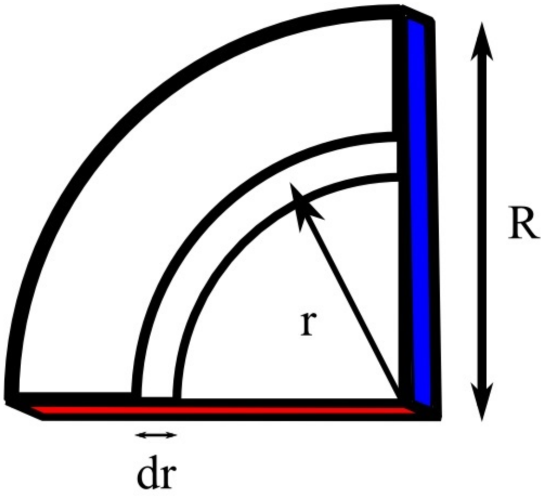

Figure A.1: Schematic showing the geometry for the quarter-disc approximation. The lower side has 10 mW of heat applied, and the right side is heatsunk to the 4 K bath.

The cube result, however, is only a first-order approximation because the heat conduction surface area is not constant from the heated to the cooled face. This can be problematic considering that the thermal connection between the TES and toroid is via relatively thin wires (see § A.3.1). In this subsection we consider a quarter-disk with a specified small thickness since this should give a much better approximation to the highest temperature gradient possible with heatsinking thin wires. A schematic is shown in Figure A.1.

Since this is a more complex geometry than that considered in previous sections, we will need to invoke the full one-dimensional result A.3 with some careful caveats. Rearranging the terms and considering differentials gives

$$\mathrm{d}P(r) = -kA(r)\frac{\mathrm{d}T(r)}{\mathrm{d}x} \tag{A.13}$$

We now consider a differential volume element on the disk and calculate the relevant quantities in A.13. The orthogonal area element for heat transfer, assuming the disc has a uniform thickness L, is given by

$$A(r) = L\mathrm{d}r. \tag{A.14}$$

The differential length element in the angular direction parallel to the heat propagation is given by

$$\mathrm{d}x = \frac{\pi}{2}r \tag{A.15}$$

where azimuthal symmetry has been assumed since the heat is only added to one side of the quarter-disc. Plugging A.14 and A.15 into A.13 yields

$$\mathrm{d}P(r) = -\frac{2kL}{\pi r}\Delta T(r)\mathrm{d}r \tag{A.16}$$

where, again, azimuthal symmetry has been assumed. $\Delta T(r)$ represents thus the difference in temperature between the heated face at $\theta = 0$ and the cooled one at $\theta = \frac{\pi}{2}$. Since we are attempting to solve for the temperature gradient ΔT, we can rewrite A.16 to yield

$$\Delta T = -\frac{\pi}{2kL}r\frac{\mathrm{d}P}{\mathrm{d}r}. \tag{A.17}$$

One might naïvely assume that since we have derived Equation A.17 that we are now done since we can just integrate this result over the radius of the quarter-circle. However, this is not the case since it could lead to asymptotic behavior at $r = 0$ where the two heatsunk planes meet. To avoid this, we will instead integrate A.17 from R' to R and take the limit as R' goes to 0. By being careful about $P(r)$ at the origin, this asymptotic behavior can be avoided.

Thus, integrating A.17 yields

$$\int_{R'}^{R} \Delta T(r) \mathrm{d}r = -\frac{\pi}{2kL} \int_{R'}^{R} r \frac{\mathrm{d}P}{\mathrm{d}r} \, \mathrm{d}r \tag{A.18}$$

Using integration by parts, the integral on the right-hand side can be rewritten as

$$\int_{R'}^{R} r \frac{\mathrm{d}P}{\mathrm{d}r} \, \mathrm{d}r = \left[rP - \int P \, dr \right]_{R'}^{R} = R'P(R') - RP(R) - \int_{R'}^{R} P \, \mathrm{d}r. \tag{A.19}$$

Plugging A.19 into A.18 yields

$$\int_{R'}^{R} \Delta T(r) \, \mathrm{d}r = \frac{\pi}{2kL} \left[RP(R) - R'P(R') + \int_{R'}^{R} P \, \mathrm{d}r \right] \tag{A.20}$$

The result A.20 is very difficult to interpret in the context of the refrigerator setup because it is difficult to measure the temperature and power precisely as a function of position, both because of time and the physical size of standard cryogenic thermometers. Average temperatures and powers over some surface are thus more relevant properties, which can be obtained by dividing A.20 by $R - R'$. This yields

$$\overline{\Delta T} = \frac{\pi}{2kL} \left[\frac{RP(R) - R'P(R')}{R - R'} + \overline{P} \right] \tag{A.21}$$

where $\overline{P}$ is the average input power over the heated surface.

We complete this derivation by taking the limit of A.21 as R' goes to 0. The averaged temperature and pressure terms remained unchanged. The fractional term becomes, assuming the power is bounded over its domain,

$$\lim_{R' \to 0} \frac{RP(R) - R'P(R')}{R - R'} = \frac{RP(R)}{R} = P(R) \tag{A.22}$$

and plugging A.22 into A.21 gives

$$\overline{\Delta T} = \frac{\pi}{2kL}\left[\overline{P} + P(R)\right] \tag{A.23}$$

Since the power source will be concentrated at the center of the toroidal piece because of the heatsinking wires, one can argue that $P(R)$ is negligible compared to $\overline{P}$ since R marks the outer edge of the quarter-disk. This simplifies A.23 to give

$$\overline{\Delta T} = \frac{\pi}{2kL}\overline{P} \tag{A.24}$$

so that σ is given by

$$\sigma = \frac{\pi}{2L}\overline{P}. \tag{A.25}$$

The temperature gradient for a 2 mm thick quarter disc is shown for different materials in Table A.3.

Table A.3: Temperature gradient from the one flat face to the other of a 2 mm thick quarter-disk of arbitrary radius

Material	**Thermal Conductivity (W/m K)**	**Temperature Gradient (K)**
Copper (RRR = 100)	400	0.0196
Copper (RRR = 20)	100	0.0785
Aluminum (6063-T5)	30	0.262
Brass	4	1.96
Stainless Steel	0.272	28.9

A.4 Interfacial Thermal Conductivity of Thermometer Heatsinks

In addition to the shape of the heatsinks, the interfacial heat conduction between the heatsink and the experimental apparatus is relevant when designing heatsinks for cryogenic environments. This calculation, and all of the source material used, is directly from Jack Ekin's Experimental Techniques for Low Temperature Measurements [125].

Due to the availability of a relatively cheap, electroless gold-plating solution, I assume that every type of heatsink used will be completely electroplated. However, due to the physical size of the piece to which it is meant to attach to, I assume that the surface to which it makes contact is copper. Thus, the interfacial thermal conductivity is

$$\frac{2 \times 10^{-1} + 1 \times 10^{-2}}{2}\text{W/K} = 0.105\ \text{W/K} \tag{A.26}$$

Based on the drawings provided by Joel Larakers, one can calculate the surface area of the surface on the heatsink making contact with the copper substrate. The heatsink is in the shape of a rectangular prism that has two through holes. The larger of the two is to press the other half of the heatsink into. The smaller is for a screw to hold the heatsink securely fastened. Since both of these holes have circular cross sections, their areas are given by

$$A = \pi r^2 \tag{A.27}$$

so that, using diameters of 0.125 inch and 0.082 inch,

$$A_{\text{press hole}} = 0.07917\text{cm}^2, A_{\text{screw hole}} = 0.0.03407\text{cm}^2. \tag{A.28}$$

The area of the rectangular piece that makes is given by

$$A_{rect} = lw = 0.340'' \times 0.600'' = 1.32\text{cm}^2 \tag{A.29}$$

so that the total area making contact is given by

$$A_T = A_{rect} - A_{\text{press hole}} - A_{\text{screw hole}} = 1.207\text{cm}^2 \tag{A.30}$$

Following the calculation in Ref. [125], using Apiezon grease, the interfacial thermal conductivity is given by

$$\frac{\dot{q}}{T} = (0.1 \text{ W/K}) \frac{1.207\text{cm}^2}{1\text{cm}^2} = 0.1207 \text{ W/K}. \tag{A.31}$$

On the other hand, using an M2 stainless steel screw, for which one can apply a maximum of 157 lb of force, and with a gold on copper interface,

$$\frac{\dot{q}}{T} = (0.105 \text{ W/K}) \left(\frac{157 \text{ lb}}{100 \text{ lb}}\right) = 0.165 \text{ W/K}. \tag{A.32}$$

Using a safety factor of 2 (a half-tight screw), the interfacial thermal conductivity becomes 0.0824 W/K.

A similar calculation for an M3 screw yields

$$\frac{\dot{q}}{T} = (0.105 \text{ W/K}) \left(\frac{362 \text{ lb}}{100 \text{ lb}}\right) = 0.380 \text{ W/K}, \tag{A.33}$$

which, with a safety factor of 2, yields 0.190 W/K. Thus, it can be concluded that an M3 screw provides the best thermal conductivity by far. However, an M2 screw will do almost as well (depending on whether the the gold-on-copper interfacial thermal conductivity is performed correctly), and, if that is not sufficient, the application of Apiezon grease will help get the thermal conductivity closer to that for M3 screws.

A.5 Conclusions and Future Directions

From these calculations, one can conclude that the type of approximation used to calculate the thermal gradient across a material has a significant effect on the resulting thermal gradient, as seen by the large differences in temperature gradients between the results in Table A.3.3 and Table A.3. With this in mind, thermal conduction calculations should be verified computationally by a partial differential equation solving utility, like that used by Matlab, or with similar simulation software. This type of program could also be made in-house using free-to-use software like Python in case of licensing concerns.

Regardless of the approximation used, the fact remains that one side of the heat-sinking flange is heat-sunk to a large thermal bath, whereas the other is connected to comparatively thin wires. This means that the biggest potential thermal bottleneck will be with the heatsinking wires, so these wires need to be made of a high-thermal-conductivity material like copper. However, because of the much larger surface area associated with the heatsinking flange, it could even be made out of brass.

Nonetheless, due to the difference in thermal expansion coefficients between the heatsinking brass flange and the stainless steel 4 K can, a leak formed whenever the 4 K can was cooled to cryogenic temperature. Additionally, the screws on one of the two bolt circles was stretched relative to the other, which was observed after a cryogenic test of the can. Replacing the two bolt circles in the original design with one bolt circle and replacing the brass flange with a copper one fortunately resolved these two concerns, which allowed the detector research and development facility to be used for testing SuperCDMS-style detectors for future dark matter and similar experiments.

APPENDIX B

INFRARED NOISE IN SUPERCDMS GERMANIUM DETECTORS

B.1 Introduction

It has recently been proposed that room temperature infrared (IR) radiation could be a significant noise source for SuperCDMS germanium (Ge) detectors. In this document we explain how large that effect could be by calculating the power spectrum of the infrared radiation shot noise. To better estimate the effect, we calculate equations describing the noise in the general, temperature-dependent case and when we assume the contribution is only coming from a 300 K source.

B.2 Infrared Photon Power Absorbed

B.2.1 Area Term

The problem comes from the fact that, if there is an opening that allows room-temperature photons into a dilution refrigerator, there is no surface inside that can absorb the photons before they make their way to the Ge detectors. Additionally, because light moves so quickly relative to the size of the refrigerator, the light cannot equilibrate itself with the outer layers of the refrigerator. Thus, the only "protection" that the detectors have from the room-temperature light comes from the innermost can.

Mathematically, what we are concerned with is the solid angle from which the IR photons enter multiplied by the surface area of the detectors. This so-called area term, which we will denote with Γ, is given by

$$\Gamma = \frac{A_{IR}}{A_{tot} - A_{IR}} A_{Ge} \tag{B.1}$$

where A_{IR} is the area of the opening in the innermost can that allows room-temperature photons to enter, A_{tot} is the total area of all surfaces within the inner can, and A_{Ge} is the surface area of the Ge detectors. This simple result assumes that each Ge detector absorbs 100% of the radiation that strikes it. In reality, each detector only absorbs $\alpha(\nu)$ of the radiation that strikes it, which can have a large frequency dependence. The combined result for the Γ term is thus

$$\Gamma(\nu) = \frac{A_{IR}A_{Ge}}{A_{tot} - A_{IR}}\alpha(\nu) \tag{B.2}$$

B.2.2 Simple Calculation

If we assume that the IR photons are produced by a blackbody distribution all of whose photons are absorbed by the Ge, then we can use the result

$$j = \sigma T^4 \tag{B.3}$$

where j is the power emitted per unit area, T is the temperature of the blackbody, and σ is the Stefan-Boltzmann constant. For this blackbody, the peak wavelength is given by

$$\lambda = \frac{b}{T} \tag{B.4}$$

where T is the temperature and b is Wien's displacement constant. If we also assume that all of the photons have comparable energy, then

$$E = h\nu = \frac{hc}{\lambda}, \tag{B.5}$$

which, when combined with B.4, yields

$$E = \frac{hcT}{b}. \tag{B.6}$$

Combining this result with B.3 yields the flux of photons per unit time per unit area f given by

$$f = \frac{j}{E} = \frac{\sigma b T^4}{hcT} = \frac{\sigma b}{hc} T^3 \tag{B.7}$$

Taking into the area term Γ given by B.1 gives the average photon number incident per unit time n given by

$$n = \Gamma f = \frac{\sigma b}{hc} \frac{A_{IR} A_{Ge}}{A_{tot} - A_{IR}} T^3 \tag{B.8}$$

If we assume that the area of the opening is about 1 mm^2, the area of a Ge detector is about 100 cm^2, and the total area inside the inner can is about 1 m^2, we find that n is about equal to

$$n = 8.272 \times 10^6 \approx 10^7 \tag{B.9}$$

photons per second.

B.3 Power Spectrum

The noise due to the IR photons will be given by a Poisson distribution, for which the mean and variance are equal. Mathematically,

$$\mu = \sigma^2 \tag{B.10}$$

Additionally, since we know that a very large number of photons are hitting the detector over a given time interval of interest, we can assume that the Poisson distribution approaches a Gaussian distribution, which is given by

$$f(t \mid \mu, \sigma) = \frac{1}{\sigma\sqrt{2\pi}} e^{-\dfrac{(t-\mu)^2}{2\sigma^2}} . \tag{B.11}$$

Combining this result with B.10 and using the result B.8 as the mean, we get

$$f(t) = \frac{1}{\sqrt{2\pi n}} e^{-\frac{(x-n)^2}{2\sigma^2}} \tag{B.12}$$

B.4 Noise Spectral Density

The noise spectral density for shot noise is flat and equal to the average rate. In other words, the noise spectral density is just given by

$$S_{nn}(\omega) = nh\nu_{300K} \tag{B.13}$$

where n is given by B.8 and ν_{300K} is the frequency of a 300 K photon.

APPENDIX C

KELVINOX 400 FRIDGE WIRING LEAKAGE CURRENT MEASUREMENT

C.1 Synopsis

In this document, I present the results of leakage current measurements on the wiring coming to and from the Kelvinox 400 dilution refrigerator in the B09 laboratory of the Texas A&M Engineering and Physics Building. For self-consistency, the results are presented in the order they were acquired and/or analyzed from August 18, 2015 to October 2, 2015. I conclude that the wiring is sufficient for leakage current measurements on DUT's down to the 10 pA/V level and that the devices used can measure the leakage, with averaging, down to hundreds of fA.

C.2 Introduction

In recent years, there has been much interest from the SuperCDMS collaboration to explore the low-threshold region of parameter space in search of the particle responsible for dark matter. Using detectors that are biased at hundreds of volts to take advantage of Luke-Neganov gain, CDMS High-Purity Germanium (HPGe) detectors can measure down to eV-level thresholds. One of the main hurdles facing this design is the high leakage current associated with current SuperCDMS detectors run even at a few tens of volts. Using point-contact and vacuum-gap detectors, it has recently been demonstrated that such detectors are practically realizable and yield the predicted low-threshold results [97].

To further push the boundaries of this detector design, it is necessary to run them at ever-higher voltages approaching the kV range for future designs. Additionally, neither the point-contact nor vacuum-gap detectors can have both sides utilized for phonon readout because of either the very large electric field near the point contact or because of the physical gap in the vacuum-gap detector. An alternative is to use some other low-leakage material as the interface over which the voltage is applied.

Any test for low currents cannot be limited by the leakage current of the wiring utilized for the measurement. In the case of the cryogenic setup at the Kelvinox 400, this is especially important, not just for these particular samples but also for future detectors that could reach the eV threshold. Additionally, the AC noise on the lines determines the noise limit on any leakage current measurement that is made. Thus, it is pertinent to properly characterize the leakage current and noise on the refrigerator wiring to determine the leakage current on future high-voltage detector designs.

C.3 Instrumentation

During initial measurements, the HP 3457A Digital Multimeter (DMM) was used for taking voltage and resistance (V and R) measurements in conjunction with the HP 34401A DMM for less critical data. Upon finding a large DC offset with the 3457A, all subsequent V and R measurements were taken with the HP 34401A. To supply power to the circuits being measured with the above instruments, an HP 6236B Triple Output Power Supply was used. Late in the experimental process, following Professor Agnolet's suggestion, the EG&G Princeton Applied Research Model 124A Lock-In Amplifier with an EG&G Princeton Applied Research Model 184 Current Sensitive Preamplifier was used for precision measurements. The Agilent / HP 3325A Synthesizer/Function Generator was used to supply the low-frequency AC voltage for later leakage current measurements.

C.4 Experimental Setup

For most of the data-taking, the experimental setup is shown in C.1. In this case, the power supply or battery was used to supply a constant DC voltage to the wiring "resistor" and a voltage is measured across the 1 GΩ resistor. For very low leakages, batteries are recommended since, even without data averaging, a leakage current of $\sim$100 fA can be recorded using them.

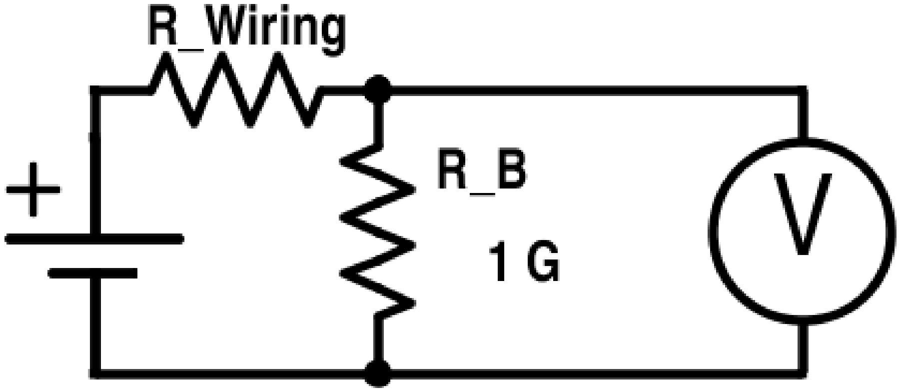

Figure C.1: Circuit used for data-taking using a battery or DC power supply source and a DMM.

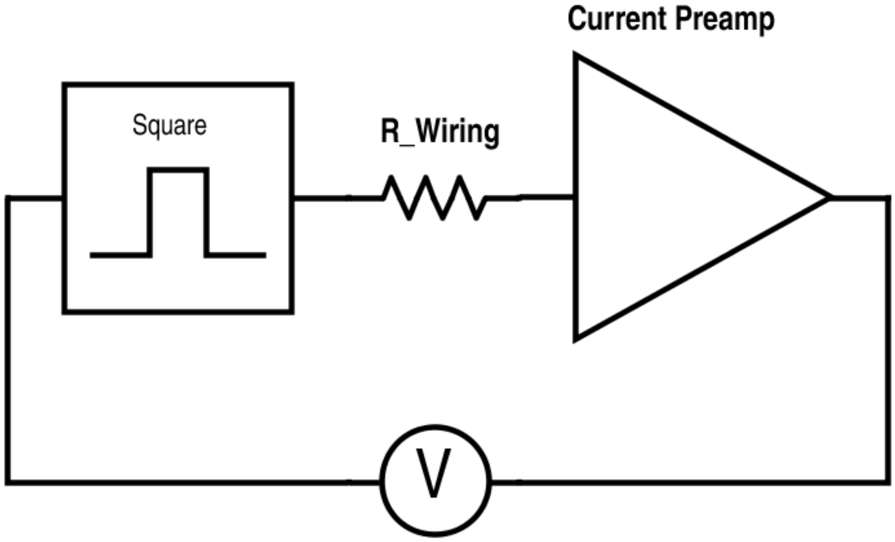

Figure C.2: Recommended circuit for future measurements using function generator source and current preamp to make measurements.

For future experimentation, however, it is recommended that the scientist use the circuit C.2. Using the large frequency range of the function generator (down to 10^{-6} Hz), one can generate AC square waves that are very close to the pure DC signal desired to measure leakage current while maintaining precise control of the signal amplitude. Additionally, preliminary measurements indicate that the AC noise from the current preamp is smaller than with a standard power supply but larger than when using batteries. However, these results need to be confirmed with more precise future measurements.

C.5 Results

C.5.1 Twisted Pairs Versus Coaxial Cables

There are two sets of wires in this refrigerator that can be used for cryogenic measurements. One is a large collection (16 4-wire sets) of twisted pairs, and the other is $\sim$20 coaxial cables. The twisted pairs are useful when the device under test (DUT) needs to have a large number of leads going into it and if one desires to quickly switch between measuring different sets since the wires are connected to a logic box. The coaxes are most useful when one needs to minimize AC noise when making the measurement.

Figure C.3 shows the leakage current versus applied voltage for the coaxial cables and twisted wire pairs. As expected, there is a significantly higher leakage when using the twisted pairs compared to the coaxial cables. Although only one set of wires is shown in this comparison, this behavior is consistent for all of the "useful" (not shorted) twisted pairs and coaxes in the fridge. Additionally, both wire sets show a linear response even at the moderately high 30 V maximum, which is useful to know for testing devices for which a linear response is not expected such as the HPGe samples discussed in § C.2. The linear fit to the coax cable data gives a leakage current of 1.7 pA/V, so that one can make leakage current measurements on a DUT down to the level of $\sim$10 pA/V with a signal-to-noise ratio of $\sim$5. Thus, assuming no additions to the fridge wiring, the coax cables are the most useful for making low-current measurements.

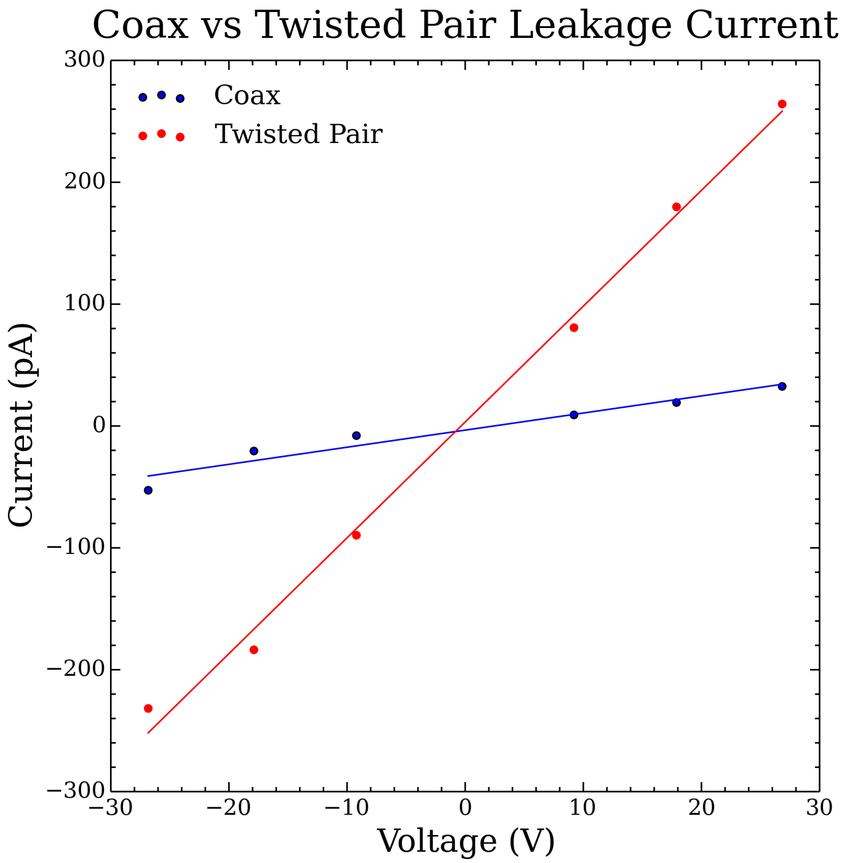

Figure C.3: Comparison between leakage current measurements for the refrigerator twisted pair wiring and the coaxial cables.

C.5.2 Leakage Current at Multiple Connection Points

Because of the physical distance between the refrigerator and the electronics rack connected to it, there isn't one coax that connects from the rack input to the top of the fridge. Additionally, since room-temperature coaxes do not operate well at cryogenic temperatures, there is a microdot connector at the top of the fridge that connects the room temperature coaxes to the cryogenic ones that go to the cold stage. The leakage current at each of these locations was measured separately to determine where the majority of the leakage occurs.

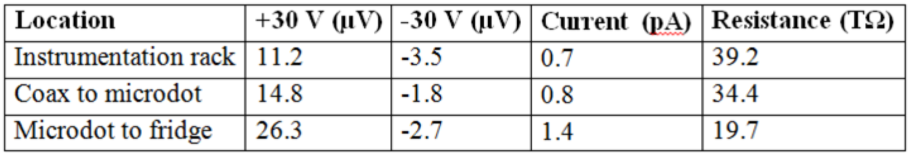

Location	+30 V (μV)	-30 V (μV)	Current (pA)	Resistance (TΩ)
Instrumentation rack	11.2	-3.5	0.7	39.2
Coax to microdot	14.8	-1.8	0.8	34.4
Microdot to fridge	26.3	-2.7	1.4	19.7

Figure C.4: Leakage current at multiple connections for the coax cables. The largest contribution is from the wiring within the fridge itself.

Figure C.4 shows the result of measuring the leakage current between two pairs of coax cables. As can be seen, the leakage current is very small (or, alternatively, the resistance is very large) regardless across which point it is measured, but it gets significantly higher when the wiring within the fridge is connected. This indicates that the largest contribution to the leakage current is from the cold wiring itself. A possible explanation for this phenomenon is that to heatsink the cryogenic coaxes there is a place inside the fridge where significant pressure is applied to them. The leakage current contribution could then be the small amount of current flowing in the compressing brass block between the wires.

C.5.3 Time Dependence

A complication in measuring the wire leakage current comes from the very long $1/RC$ time constant associated with the $\sim$1 TΩ wiring resistance. Figure C.5 shows the leakage current of one of the wires that has been biased at the highest voltage possible with the batteries ($\sim$27 V). Using the fit for the exponential, one finds that the capacitance between the two ends of the cable is $\sim$2 nF. Although this result is somewhat expected, it is important to note that for any measurements in the future approaching leakages as small as the

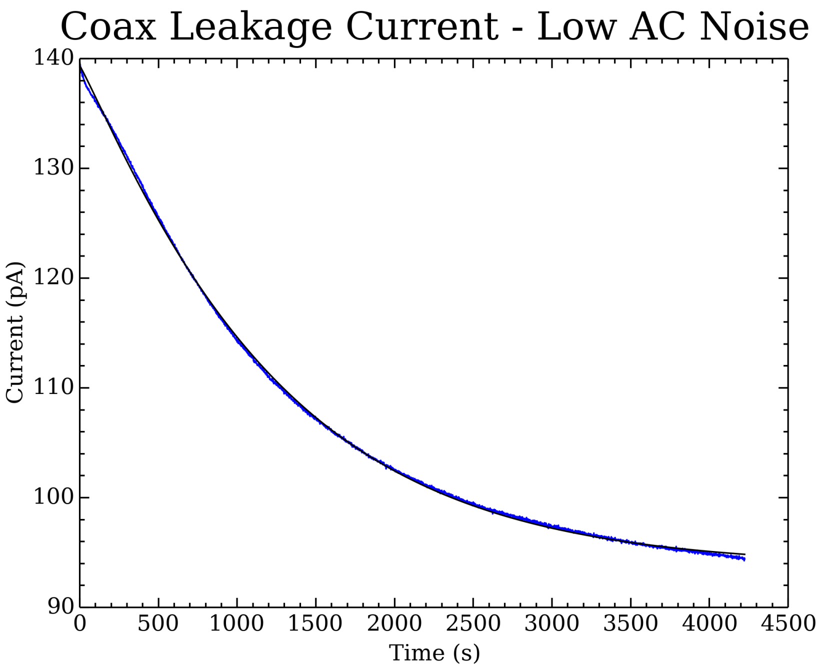

Figure C.5: Current versus time for one of the coax cables biased at 27 V. The fit is an exponential decay that agrees with the RC circuit expected of the cable.

ones measured in this study a large time-limiting factor will be the amount of time needed for the system to equilibrate.

C.5.4 Liquid Nitrogen and Vacuum Environments

Due to time limitations, it was difficult to collect copious amounts of quantitative data as was done at room temperature. However, initial measurements indicate that the wiring does at least as well, if not better, when submerged in liquid nitrogen and when it is in an evacuated environment.

Since previous measurements indicate that the largest source of leakage is within the refrigerator itself, the liquid nitrogen test was performed on a section of wire, an example of which is shown in Figure C.6. The test procedure was performed by simply inserting the wire section connected to the measuring circuit into a liquid nitrogen bath and measuring leakage before and after. Qualitative measurements indicate what could be a twofold drop in leakage when submerged in nitrogen. However, inconsistencies in the data taken most likely due to noise mean that more data needs to be taken to confirm this.

The fact that the liquid nitrogen tests were carried out on a wire independent of the refrigerator means that it was also a useful test for the AC noise inside the fridge room. Even though this is a radio-shielded copper-clad room, there is still a gradient in the AC noise measured on the wire as a function of position in the room. Since this alternating current noise could not have come from outside, it must be either produced by one of the instruments or be somehow present on the shielding itself (ground loops). These two suppositions are corroborated by the fact that the noise seemed to be 60 Hz modulating higher frequencies. Since no change was noticed when turning on and off instruments within the room and the least noisy part of the room was as far away as possible from the room walls, steel instrument rack, and refrigerator, the reason for the AC noise could be from ground loops most likely due to bad noise filtering on the AC line. Although not exactly in line with the leakage current this work attempts to address, this is still a relevant result that needs to be considered for future fridge upgrades.

The vacuum measurement was carried out by pumping on the vacuum can surrounding the cold plate and redoing the leakage current measurements for some of the coaxes. There seems to be a slight decrease in leakage current when the wires are in a vacuum environment, but more data needs to be taken to corroborate this.

C.6 Conclusions and Future Directions

I have shown that the coax cables the fridge is already equipped with in their current configuration can be used to measure leakage currents down to the 10 pA/V level, or resistances up to 100 GΩ. Additionally, most of the leakage current in the wires comes from the wiring within the fridge itself, which means that any electronics system that might be implemented in the future to measure lower leakages would first require an upgrade to the fridge wiring. One possibility for doing so would be cryogenic coax cables.

Another possibility for future measurements would be using a parametric analyzer since this device has the low-noise capabilities of batteries coupled with the precise voltage control of the function generator discussed earlier. Additionally, the fact that it can automatically save the data it collects means that the large time constant described earlier could be less of a problem if the system is set to take data for the first part of the exponential curve. One can then fit an exponential function to this raw data, thereby computing the final current at which the system would settle.

Future directions for continuing this study include more measurements at vacuum and cryogenic environments since, due to time limitations, these measurements could only qualitatively confirm an improvement in the wiring in these environments. Additionally, more data could be taken on all of the wiring not only to qualitatively confirm the similar behavior of each but also to determine which individual sets of wires are best-suited for high-precision measurements.

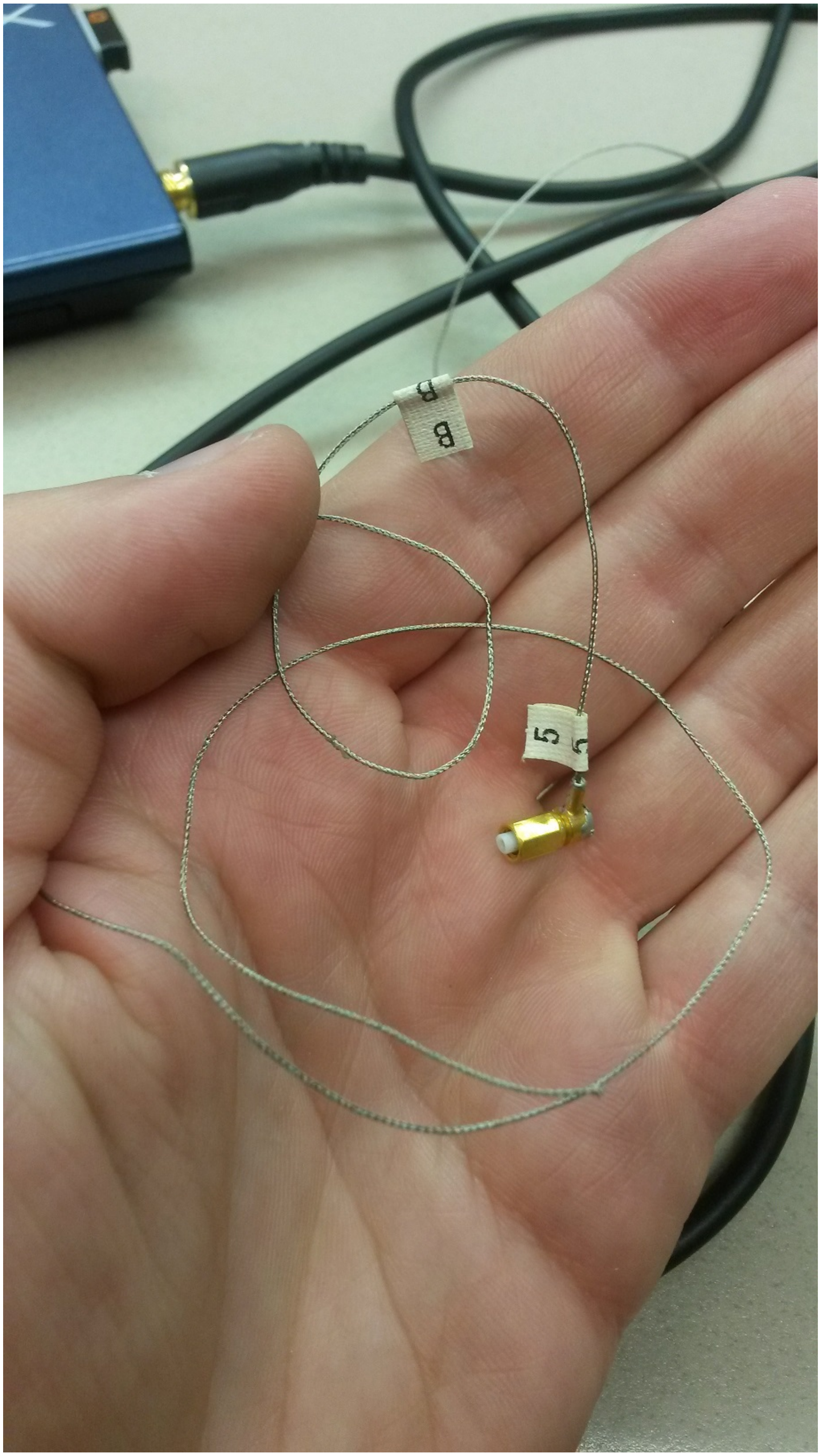

Figure C.6: Example of cryogenic coaxial cable with microdot connector attached as used inside the refrigerator.

APPENDIX D

MICRODOT CONNECTOR CONSTRUCTION INSTRUCTIONS

Microdot connectors were used for the thermometry wiring readout for the detector research and development facility. The instructions below outline the process used.

1. Removing steel braid. Microdot connectors are made using a special wire that has three layers: an outer braided steel wire, a central Teflon insulator, and an inner superconducting wire.
   (a) Remove the steel braiding carefully by pulling the wires back with tweezers and clipping the excess with small scissors.
   (b) Repeat this process until about a centimeter of insulation has been completely exposed.
   (c) Cut off the excess to minimize the steel wires catching wire bonds on experiment. It is useful to make the steel wire region as rounded as possible.
2. Removing insulation.
   (a) Tape the end with removed insulation to some hard surface.
   (b) With a razor remove the Teflon insulation leaving $\sim$1-2 mm left in front of the steel.
3. Crimping wire tube onto superconductor. One needs to remove a small section of CuNi capillary tubing ($\sim$0.030 inch OD with $\sim$0.005 inch ID) and crimp it onto the superconducting layer on the microdot wire.

   (a) Select a wire whose outer sheath is just wide enough for the microdot superconducting wire to slide into. A microscope is useful for making the distinction.
   (b) Using a small file, saw a section $\sim$5-7 mm long. Make sure the section is as straight as possible.
   (c) Using needle-nose pliers, grab metal piece and bend back and forth until it breaks.
   (d) Use pliers to remove piece.
   (e) Inspect the cut section. If it is not a clean cut (small hole partially covered over), repeat process for another section.
   (f) Carefully slide metal sheath onto exposed superconducting wire
      i. Be careful not to break superconducting wire.
      ii. If wire breaks inside metal sheath, make new sheath and remove more insulation and/or braided steel if necessary.
   (g) Using large pliers that have a, preferably, grooved tip, crimp metal sheath onto wire.

4. Tinning the steel braid. This can be accomplished using Stay-Clean Acid Flux (contains hydrochloric acid [HCl]), the specially marked “Acid only” soldering iron, and the specially-marked silver solder. CAUTION: THIS STEP MUST BE DONE UNDER FUME HOOD TO AVOID BREATHING IN TOXIC HCL AND CL_2 VAPORS.
   (a) Pour a few mL of acid flux into small glass vial.
   (b) Using a small piece of wood (or similar instrument that is not soluble in HCl), place a small drop of the solution onto steel braid.

    (c) Tin section with drop on it.

        i. Important: Hold solder just long enough for solder to bond, not longer. Otherwise the Teflon insulation will melt. This shows up later as an electrical short to ground.

        ii. Do not worry if wire is not completely covered. Even partial covering is good enough. Electrical shorts are more serious than not enough solder because they require a complete wire remake.

        iii. Inspect under microscope or strong magnifying lens to see if wire is tinned. Solder is more silver in color and shinier than steel.

5. Clean the wires

    (a) Submerge wires in large container in a water-detergent mixture and clean in ultrasonic cleaner for 15 minutes.

    (b) Wash off wires and container in tap water.

    (c) Submerge wires in large container in isopropanol and clean in ultrasonic cleaner for 15 minutes.

6. Air drying the wires.

    (a) Leave to air dry for several hours or overnight.

        i. After the wires have air-dried for a few minutes so that they are not damp, if one is making more than one wire, it is useful to tape all the wires to a piece of cardboard. The next step becomes easier.

    (b) Using a multimeter, check for continuity between central signal wires and for shorts between central conductor and steel braid.

7. Heat-drying the wires. If there are shorts to ground, it may be necessary to evaporate any leftover alcohol from the wires.
    (a) Place the large incandescent lamp onto flat surface or table.
    (b) Make small container (referred to as dish) out of aluminum foil and place wires needing drying into dish.
    (c) Place thermocouple wire with microdot wires.
    (d) By controlling the height of the lamp above the wires, one can control the temperature of the wires. Keep the temperature at ∼90 °C. Do not allow it to go over 100 °C.
    (e) Dry for several hours or overnight.
    (f) Redo continuity and shorts check.
8. Making connector. A vertically-oriented vice is necessary, and a binocular microscope is helpful.
    (a) Remove connector pieces from bag.
    (b) Separate out cylindrical piece since it is most likely not needed.
    (c) Assemble pieces and place in vice.
    (d) Cut crimped wire until it is the same size as fork-shaped piece at center of connector.
    (e) Slide wire through side hole until crimped section rests completely inside fork.
    (f) Place a small solder blob at center and add solder until the fork is completely filled and the solder bulges up slightly.
    (g) Important: do not get solder onto the sides during this process. If you accidentally do, the excess can be removed with a sharp steel pick.

(h) Check for shorts and continuity.

    i. If there is a short, desolder and remove wire from fork. Recheck for shorts.

    ii. If there is still a short in the connector, remove excess. If this does not fix it, get a new connector.

    iii. If the short is on the wire, get a new wire. This was most likely due to over-tinning in step 4.c.

(i) Solder steel braid to outside of side-tube.

(j) Although not as important as for 4.c., it is still advisable not to overheat the steel braid to avoid melting the insulation.

(k) Check for shorts and continuity.

(l) Most likely cause for short is melting of Teflon insulation.

(m) Place cap on top of connector. Solder cap to top of connector. Once enough solder has been applied (slightly convex solder), remove iron by sliding to side.

9. Final check for continuity and shorts.

    (a) Connect microdot-coax adapter to multimeter.

    (b) Connect completed microdot connector to adapter.

    (c) Check for shorts by measuring resistance between center conductor and ground.

        i. Values over tens of GΩ are acceptable.

    (d) Check for continuity by holding other end of microdot wire between two fingers such that your fingers make contact with the central conductor and steel braid simultaneously. Continue measuring the resistance.

        i. Depending on the person making the wires, resistances of $\sim$1-10 MΩ are acceptable.

    (e) By this point, assuming there were no other problems in previous parts, the only short that could occur is if the bottom of the cap is touching the top of the fork solder. To fix this, one needs to remove the cap, remove the excess solder, and repeat adding the cap.

10. Notes for future

    (a) The bit about the IPA not drying may not be 100% true. After I tinned a wire and dried it with the dry nitrogen gas, I noticed the $\sim$100 MΩ from the inner conductor to the shield characteristic of it "needing more drying." I put the wire back into the IPA for another $\sim$30 minutes, thinking that maybe not all of the soapy water came off. Sure enough, after removing the coax cable and redrying, the conductance was at the level of $\sim$0.1 nS.

APPENDIX E

DERIVATIVE ANALYSIS: POSSIBLE NOVEL ANALYSIS TECHNIQUE

Among the first steps in performing detector event analysis is removing the contribution of the nonzero baseline. Since some of the traces have changing baselines, an example of which is shown in the upper left plot of Fig. E.1, the author needed to implement a linear baseline subtraction, which may not be useful for very short subtraces. For comparison, all of the subtrace analysis codes included separate calculations with and without filtering. With this many variables, the code had become extremely time-intensive since analyzing the entire data once could take several weeks. Even optimizations of the built-in Numerical Python (numpy) library commands to perform the analysis only improved performance by about a factor of two.

Despite all of these parameters, however, there is an electronics noise source in the data that cannot be addressed easily with this kind of analysis. The upper right plot in Fig. E.1 shows an example of box-shaped electronics noise present in a large percentage, if not all, of the data. A very small size of the subtraces introduces significant noise, whereas subtraces too large start to include one or both of the edges of the box distribution. The only way to correct for this kind of effect is via a nonlinear baseline fit, which would significantly increase the already long computation time for the code. Even with this kind of correction, it would take a long time to tune the parameters so that the code subtracts the box distributions rather than, say, low-energy peaks or the noise fluctuations themselves.

For these reasons, the author devised a novel data analysis technique that addresses these concerns and could also help calibrate the energy measured by the detector down to the level of the baseline noise. An illustration of how this method addresses the concerns raised in the previous two paragraphs is shown in Fig. E.1. In this Figure, the upper plots

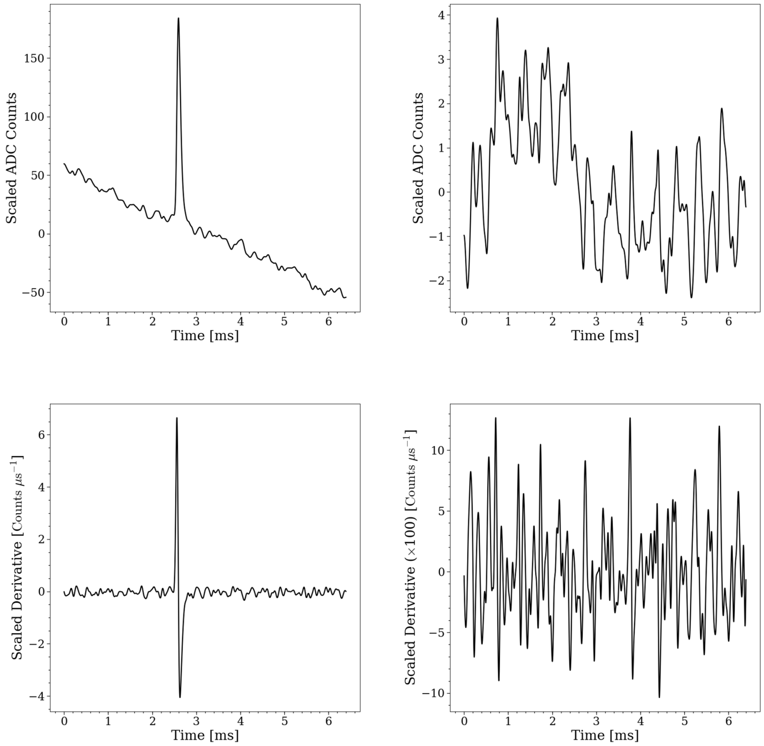

Figure E.1: Plots showing the sum of the four channels in scaled ADC counts for a trace with an event pulse on a falling baseline (upper left), untriggered trace with a box-shaped electronic noise present in a large fraction of the data (upper right), the time derivative of the event pulse (lower left), and time derivative of the noise trace (lower right). These plots illustrate the two main advantages of using the trace time derivative rather than the original values themselves for analyzing noise, namely that changing baselines become constant offsets (to first order) that do not affect the time-dependent noise analysis appreciably and that box-shaped baseline fluctuations produce a pair of peaks whose contribution is small compared to that of the rest of the noise. All traces are filtered using a running-average filter of window size 9 time bins and order 50.

show representative traces and the lower plots show the time derivatives of these traces. Both traces are filtered using a running-average filter of window size 9 time bins and order 50. The time derivative causes the slope in the baseline for the trace with the event to appear as a small constant offset, and the box-shaped noise now appears as two new peaks out of about one hundred, which means its effect is diminished to the point that it should not significantly affect the time-dependent calculations any more.

Notwithstanding these positive results, there is still the question of whether the peak slope is a good indicator of energy. According to Ref. [96], the peak values for each event are very close to linear indicators of the energy deposited in a channel, down to energy depositions of a few electron-hole pairs. Nonetheless, the author hypothesized that it still might be useful since event pulses have a characteristic shape - for the first few microseconds there is an almost exponential rise, a linear rise for the next few tens of microseconds, an approximately parabolic, but asymmetric top, and a slow, approximately exponential decay with a characteristic fall time of a few hundred microseconds. Additionally, preliminary tests indicated that the peak slope seemed to scale with the peak height of the event. Consequently, the author calculated the time derivative using the scheme in the previous paragraph for the entire dataset to test the linearity since it could prove very useful for future noise analyses.

A sample of the results of the time derivative analysis are shown in Fig. E.2. The left column shows Am-241 spectra of the SuperCDMS-style analysis peak heights, whereas the right plots show the results of the time derivative peak analysis using the same events as those used to generate the plots on the left. These plots make it clear that both methods not only show the expected Am-241 spectra but also that both the peak height and peak slope scale with voltage in accordance with Luke-Neganov gain.

These results indicate that the time derivative is effective at mitigating the effects of baseline fluctuations and that it has a very linear response as a function of input energy, at least for the energies of the Am-241 peaks. This means that a combination of the peak height, which has been shown to have a very close to linear response with respect to energy, and derivative peak height, which has been shown to be immune to baseline fluctuations, could be used to calibrate the baseline noise resolution to high accuracy. The derivative

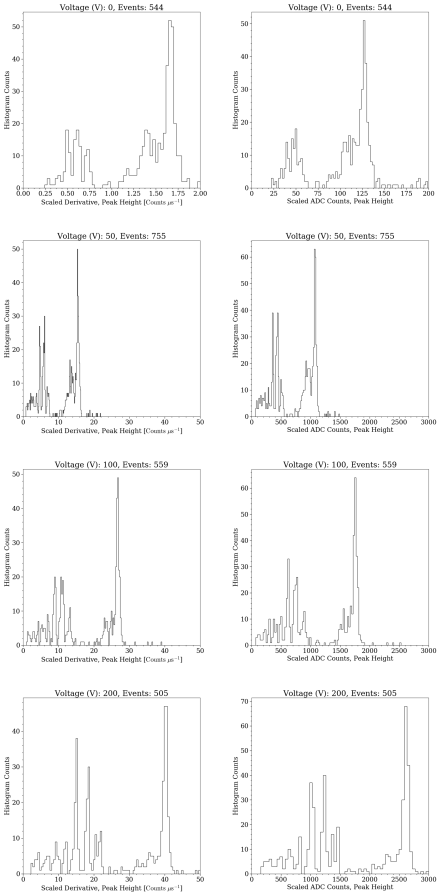
Voltage (V): 0, Events: 544

Voltage (V): 0, Events: 544

Voltage (V): 50, Events: 755

Voltage (V): 50, Events: 755

Voltage (V): 100, Events: 559

Voltage (V): 100, Events: 559

Voltage (V): 200, Events: 505

Voltage (V): 200, Events: 505

Figure E.2: Plots showing the Am-241 event spectra at several voltages for the data with dilution refrigerator cold stage thermometry recorded. Histograms with the peak heights are in the left column and the heights of the positive time derivative peaks are in the right column. Both methods show the expected Am-241 spectrum and both show peak positions that scale close to linearly as a function of voltage, as expected of Luke-Neganov gain. Both plots are generated using the sum of the peak heights from all four channels.

could also serve as an alternative method for selecting real events from the "glitch" events [44] since there could be a strong relation between these two parameters. Other directions in which such an analysis could go is to determine how the derivative minimum (downward facing peak after the maximum in the lower-left plot in Fig. E.1), the time delay between the maximum and minimum, and the slope of the line between the maximum and minimum relate to the event energy.

All of these possibilities offer potentially strong alternate handles to analyze the data measured by phonon-mediated charge detectors that could be very relevant for experiments employing them, such as the SuperCDMS experiment and MINER. Such analyses could also pave the way for understanding defect creation in phonon detectors, which could be very relevant for not only dark matter searches [102] but also for developing materials resistant to radiation since it is difficult to verify the computations that simulate defect creation without detectors sensitive to electron-hole pair creation.

APPENDIX F

TIME-DEPENDENCE CORRECTION

The following algorithm is used to take into account the time dependence in the energy measured for the Am-241 calibration peaks. This represents a portion of the data analyses performed with the data from detector S17B taken late March 2018. Since this is a multi-step process, the algorithm not only represents the analysis steps taken but also the order that they should be performed to get the final result, which is a time-dependent calibration of the energy peaks. In this section, an ntuple refers to a data structure that contains the relevant information for each trace. The main components of the process are illustrated in Fig. F.1.

F.1 Correction Process

One starts with an ntuple containing relevant information about the entire dataset and removes all of the traces from the ntuple for which the voltage changes during data taking. The ntuple data from the previous cut is combined into one ntuple and is sorted based on the arrival time of each trace. A text file is generated that contains the start and end times of the traces within each directory with raw data stored. This step is critical as a preliminary time cut for defining the end of one dataset and the beginning of the next, which is crucial for correctly implementing the time-dependent correction.

The data, which are now divided roughly based on the directory they were saved under, are then further divided based on the fluctuations within the data in each directory. This is a manual process that results in about a hundred separate ntuple arrays, one for each time the data changes. This final list of ntuples is used to generate start and end times for each dataset that can then be used for a timing cut for a single ntuple with all of the data.

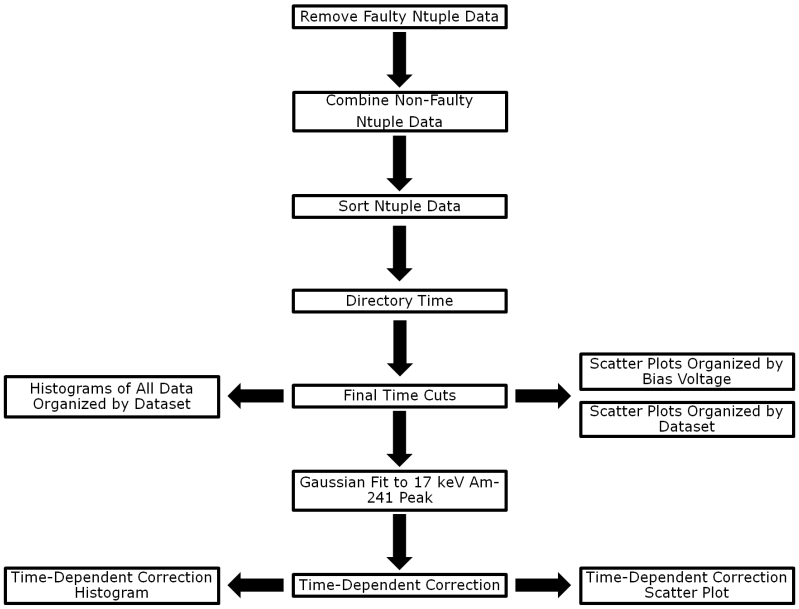

Figure F.1: Flow chart illustrating the steps used to calibrate all of the data taken with S17B as a function of time.

At this point, several sets of plots to check the results of the previous steps are generated. Scatter plots of all of the data solely organized by bias voltage show how strong the time dependence is in the data. All of the scatter plots show the sum of the peak values for all four channels for each Am-241 event on the y-axis and the time-sorted event index on the x-axis for each portion of the entire dataset. This is prior to applying any time-dependent corrections. Scatter plots of all of the data divided by the dataset are generated to check whether the dataset divisions were correctly applied. Since the scatter plots confirm how strong the effect of detector channel saturation on Channel D is, the analysis following this point is performed on the sum of Channels A, B, and C, excluding Channel D. Finally, one generates histograms of all of the data divided by the dataset to show the locations of the peaks from one dataset to the next. This result is used to manually select only the data with a high enough number of statistics to clearly resolve the 17 keV peak.

It is also used to save the data in the histograms for use in the next step, which is the main part of the time-dependence correction.

The peak position of the 17 keV peak are determined empirically from the $\sim$100 histograms in the previous step. A start and end position for each peak for each dataset are recorded as well since a Gaussian distribution needs to be fit to the location of each peak to accurately determine its position. This information along with the histogram counts from the histogram plots are used to select only those counts representative of the 17 keV events for each dataset. A Gaussian fit is performed for the selected distribution, and the dataset index, fit parameters, and a χ^2 parameter are saved. Plots showing the peaks with the Gaussian fit are saved to empirically verify that the Gaussian fit is performing well. This is crucial since different initial parameters for the Gaussian fit may not fit all of the data correctly.

Finally, one uses the peak position of the Gaussian fits in the previous step to scale the 17 keV events to correct for their positions as a function of time. All of the positive voltage data are scaled to the events for a dataset taken while maintaining as close to a constant cold plate temperature as possible. Since no negative voltage bias data were taken during this time, these data were normalized to the location of the 17 keV peak.

Similar to the previous scatter plots, one checks the result by generating a scatter plot of all of the events at a particular voltage after applying the time-dependent scaling factor. This shows how well the time-dependent correction worked. It also indicates that the time-dependent correction, although helpful, was not perfect since some of the other non-60-keV peaks do still fluctuate with time. Similar to the previous histograms, one also generates histograms of all of the data at a particular voltage after the time-dependent correction has been applied. This is useful for illustrating that, even solely using a multiplicative constant for rescaling the data, the data can be combined to make histograms of the entire dataset.

F.2 Analysis Results and Discussion

The data for this experimental run were taken over several days. This includes data for which the data-collection software only captured a trace if a pulse is present as well as traces taken at specified times. These are referred to as triggered and untriggered data, respectively. Voltages ranging from -400 to 400 V were applied to the electrode. Higher voltages were not used to mitigate the risk of a short-circuit at the vacuum fitting, which may cause a leak to air at a cryogenic temperature that could incapacitate the entire dilution refrigerator.

Dilution refrigerators, like the one used to cool down the detector for this run, employ a pump on the still, a portion of the dilution refrigerator at a temperature of $\sim$600 mK, to cool down the mixing chamber, which can in principle be cooled to $\sim$10 mK. A powerful mechanical pump should be sufficient to cool the mixing chamber, via the still, down to a sufficiently low temperature to run small-scale experiments. However, the mechanical pump did not provide enough pumping speed when the detector for this cooling run was tested. Thus, a turbopump was needed in series with the mechanical pump to decrease the pressure on the still to lower the still temperature. This allowed the dilution refrigerator to achieve a lower base temperature, which may make it possible to cool lower T_C samples for better signal to noise since signal to noise improves as T_C^{-3} [185]. Running the turbopump also helps pre-cool the mix at the same circulation rate. Running the turbopump, on the other hand, introduced so much electronic noise that triggering on the pulses was difficult while the turbopump was on. For this reason, triggered data with the turbopump off, untriggered data with the turbopump on, and untriggered data with the turbopump off were taken.

Because there are close to a million events taken over the entire experimental run, the data were recalibrated over time using the peak closest to 50,000 scaled ADC counts in the lower-left plot in Fig. F.3, which is most likely the 17.8 keV x-ray peak from the Am-241 source. From this point forward, this peak is referred to as the “calibration peak”. Despite having the largest number of counts, the 59.5 keV peak is not used for this analysis to mitigate the effects of saturation, among other potential concerns. Saturation is any effect that causes the peaks in the data acquisition to have flattened tops. It can be caused by either the digitizer saturating, which means the event is such a high energy the digitizer cannot read out its peak height, or by the event causing a large number of TESs to enter the nonlinear performance regime. The latter effect happens when the TESs are driven past their nominal operating range near their transition temperatures to the region where the change in resistance versus temperature is much smaller than nearer the transition. Hence, the peak appears to have a flat top once a large fraction of the TESs measuring it reach that region in their performance curves.

To improve the signal-to-noise of each trace, the sum of the peak maxima in channels A, B, and C were used to measure the energy of each event. Channel D was not used because high-energy calibration events saturate it (peak has a flat top) and because the positions of the calibration peaks in the Channel D data change significantly more than those of the other channels as a function of time. The positions on the detector corresponding to each of those channels are shown in the photograph of the detector at the upper left of Fig. 2.19. Channel A wraps around the outside edge of the detector, and channels B, C, and D are in the middle. The relative signal strengths between the four channels, combined with the arrival time of the event at each channel, can be used to determine the location of an event in two dimensions.

The saturation effect mentioned earlier is illustrated in Fig. F.2, which shows the Am-241 event spectrum at 100 V DC power supply bias generated from the peak maxima values for each event measured on each channel. The data for this plot was taken when the temperature of the dilution refrigerator was carefully monitored and kept as close to

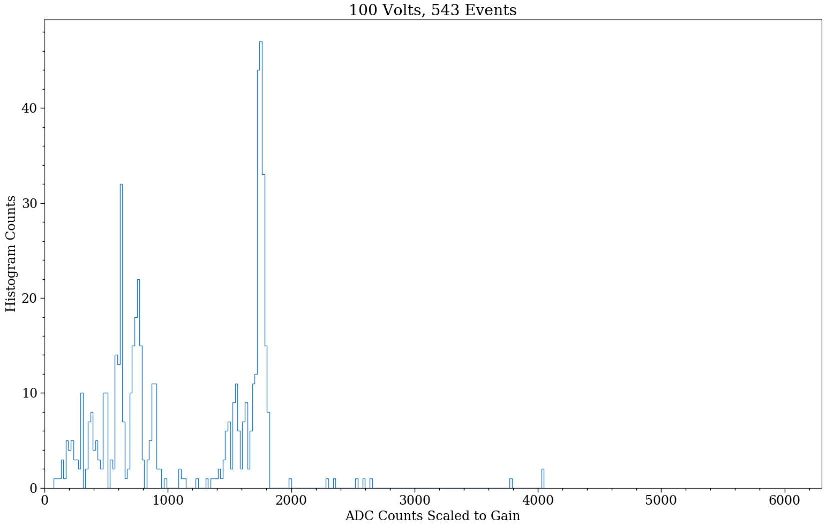

Figure F.2: Histogram showing the sum of the signal from each channel for the dataset from the evening of March 28, 2018. The spectra includes only the events from the Am-241 source, selected via energy and timing cuts. The temperature of the dilution refrigerator was carefully monitored and kept as close to constant as possible for these data.

constant as possible. Nonetheless, the 59.5 keV peak appears shifted towards the peaks near 20 keV compared to the data taken with a silicon drift detector shown in Fig. 2.24, which demonstrates the saturation effect since the sum of all the channels includes Channel D, the channel closest to the Am-241 source. In other words, because of the location of the source, the largest energy for each event from the Am-241 source is deposited on Channel D compared to the other channels, which makes Channel D the most susceptible of the four to saturation when measuring events from the Am-241 source.

Comparing Fig. F.2 to the plots in Fig. F.3 also shows how integrating over the pulse, rather than measuring the peak value as a proxy for energy, seems to be unaffected by saturation. This is also the reason for the significant difference in the x-axes of the plots in the two figures. The reason why the pulse integral is a better energy estimator than simply taking the peak has to do with the electrothermal feedback that permits negative feedback

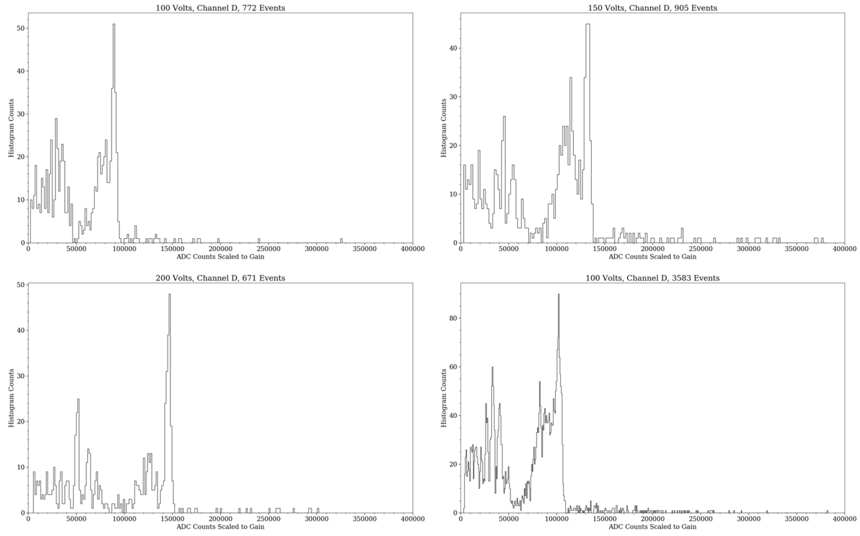

Figure F.3: Spectra showing events from the calibration source only for channel D for different voltages and datasets. All spectra, except that at the lower right, are from the data during which the turbopump was off and the temperature of the dilution refrigerator was carefully monitored. The spectrum at the lower right is from a different dataset with many triggered events at 100 V.

TES operation. Following Ref. [186] in Ref. [187] and Ref. [188], the power-to-current transfer function for a TES is given as

$$\frac{\partial P}{\partial I}(\omega) = \left[I_0\left(1-\frac{1}{\mathscr{L}}\right)\left(1+\frac{i\omega\tau_0}{1-\mathscr{L}}\right)\right] \left[R_\ell + R_0\left(1+\beta\right) + i\omega L + \frac{R_0\mathscr{L}\left(2+\beta\right)}{\left(1-\mathscr{L}\right)\left(1+\dfrac{i\omega\tau_0}{1-\mathscr{L}}\right)}\right], \tag{F.1}$$

which can be rewritten as

$$\frac{\partial P}{\partial I}(\omega) = \frac{I_0}{\mathscr{L}}\left(\mathscr{L}-1-i\omega\tau_0\right)\left[R_\ell + R_0\left(1+\beta\right) + i\omega L + \frac{R_0\mathscr{L}\left(2+\beta\right)}{1-\mathscr{L}+i\omega\tau_0}\right] \tag{F.2}$$

where i is the imaginary unit, ω is the angular frequency, $\mathscr{L}$ is the loop gain, L is the inductance of the TES input coil, $R_\ell = R_{\text{SH}} + R_{\text{PAR}}$, the sum of the shunt and parasitic resistances, R_0 is the steady-state resistance of the TES, I_0 is the steady-state current of the TES, τ_0 is a time constant, and

$$\beta \equiv \frac{I_0}{R_0}\frac{\partial R}{\partial I}\bigg|_{T_0}. \tag{F.3}$$

When $\mathscr{L}$ tends to infinity, which is a good approximation when the TES is low in the transition, the zero-frequency component of $\partial P/\partial I$ becomes

$$\frac{\partial P}{\partial I}(0) = I_0\left(R_\ell - R_0\right), \tag{F.4}$$

or

$$\mathrm{d}P_0 = I_0\left(R_\ell - R_0\right). \tag{F.5}$$

Substituting $R_0 = V_b/I_0 - R_\ell$ gives

$$\mathrm{d}P_0 = I_0\left(2I_0R_\ell - V_b\right). \tag{F.6}$$

By energy conservation, $\mathrm{d}P_{\text{abs}} = -\mathrm{d}P_0$, which implies

$$\Delta P_{\text{abs}} = -\Delta P_0 = -\int_{P_0'}^{P_0'+\Delta P_0} \mathrm{d}P_0 \tag{F.7}$$

$$= \int_{I_0'}^{I_0'+\Delta I} \left(V_b - 2I_0R_\ell\right)\mathrm{d}I_0, \tag{F.8}$$

or

$$\Delta P_{\text{abs}} = \left(V_b - 2I_0R_\ell\right)\Delta I - \Delta I^2 R_\ell. \tag{F.9}$$

Hence, the total energy absorbed is the total time integral of Eq. F.9 given by

$$E_{\text{abs}} = \int_0^{\infty} \left[\left(V_b - 2 I_0 R_\ell \right) \Delta I - \Delta I^2 R_\ell \right] \mathrm{d}t. \tag{F.10}$$

For this reason, the pulse integral is a better energy estimator than the pulse height, and, because of Eq. F.10 derived from electrothermal feedback, the pulse integral should also be independent of saturation [185].

Hence, to elaborate, the plots in Fig. F.3 are generated by integrating the entire peak for Channel D for datasets biased at different voltages by the high-voltage DC power supply. Only traces that had maximal energy on channel D and were within the regions on the timing parameter cuts similar to those in Fig. F.6 were included since these cuts include events from the Am-241 source and exclude events from the background. For these plots, data traces were filtered via a moving average with a window of 9 time steps, each of which is 1.28 μs long, with order 100. On the other hand, Fig. F.2 was made by summing the peak values of all four channels. The raw data traces were filtered with the same moving average algorithm as those used to generate Fig. F.3, except with window size 5 and order 5. The same cuts, defined using the timing parameter and energy deposited on each channel, were utilized. However, the energy cut was made using the peak maxima, not the integrated values for each channel.

Since it is more difficult to identify the location of the 17.8 keV calibration peak in the plots used for illustrating the time dependence, such as Fig. F.4, the integrated value of pulses is used rather than the peak maxima. Thus, the sum of the peak maxima for Channels A, B, and C is used to simultaneously mitigate saturation effects while allowing one to correct for the time dependence in the data from the calibration source.

The 758,851 events in the entire run were sorted and divided based on the time the event happened, as recorded by the digitizer. In other words, continuous data were treated

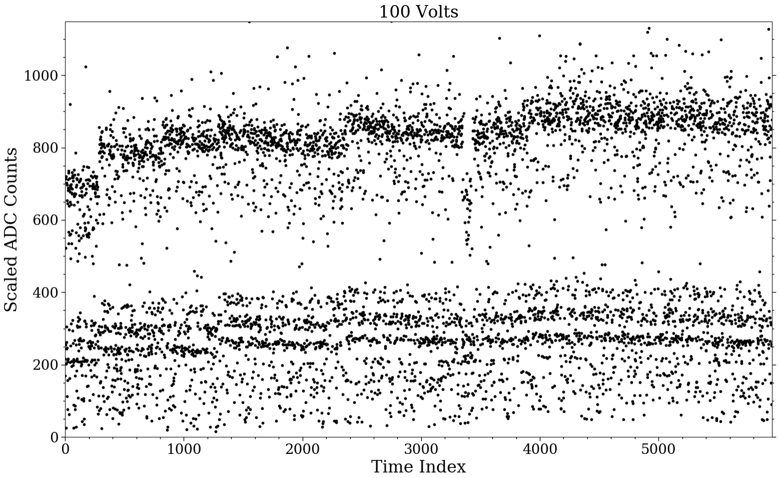

Figure F.4: Scatter plot showing all of the events passing the calibration cut prior to the time-dependent correction. Every event is a single point, and the amplitude for each point is found using the sum of channels A, B, and C. The plot shows the scaled ADC counts as a function of time index, which contracts the data taken over several days into a scatter plot that displays all of the data. The peak used for calibration is the most prominent line near 250 ADC counts. The voltage is that supplied by the DC power supply.

as one "dataset." Time gaps larger than a few seconds were counted as separate datasets. Any changes in amplifier gain or voltage were also counted as dataset divisions. Since datasets with less than a hundred or so events have too few events to easily discern the calibration peaks, the data were divided by hand based on the time each data file was taken, the folders into which the data were divided during acquisition, the ADC gain information recorded with each trace, and the DC power supply voltage bias applied. For example, if there is a jump of several minutes or a change in the ADC gain from one set of data files to another, then the next set of files is considered a new dataset.

Once each dataset was defined using the procedure in the previous paragraph, the raw traces were filtered using a moving average filter with a window size of 5 time bins, or 6.4 μs, and an order of 5. The peak value is found by evaluating the global maximum for each trace and channel. The baseline is found by calculating the median of the first 30% of the

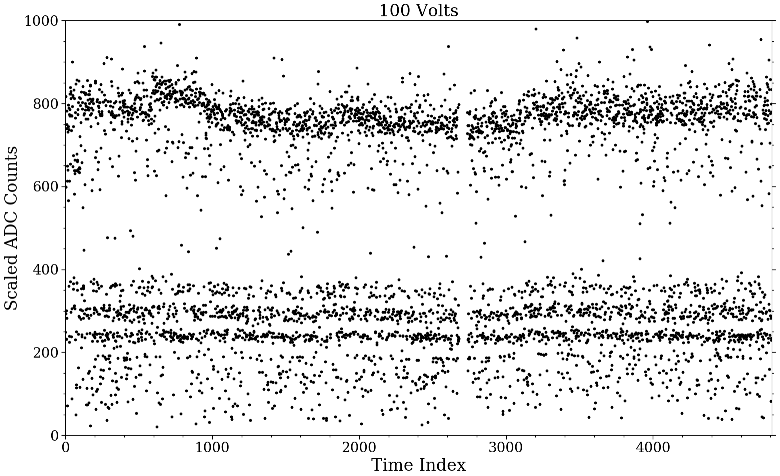

Figure F.5: Scatter plot showing all of the events from datasets with enough events for time-dependent calibration. Every event is a single point, and the amplitude for each point is found using the sum of channels A, B, and C. All of the lines close to the main calibration line are now much more aligned than prior to calibration. The position of the highest-energy line, although much improved compared to prior to this calibration, still fluctuates significantly with time. Additionally, there are small time-dependent fluctuations in the low-energy peaks, especially near time indices of 1800, 2800, 3200, and 4200. The voltage is that supplied by the DC power supply.

trace for each channel and is subtracted from the global maximum to find the maximum height of the peak for each channel. The start time of the pulse, necessary for the timing cut, is found by fitting a line to values from 20% to 60% of the peak height for each channel and finding the point where the line intersects the baseline. The x-coordinate of this point gives the start time of the pulse. After the raw data is processed, the timing cut selects the population of events localized on Channel D and the energy cut selects events with maximal energy deposition on channel D. Example plots showing the timing parameter and the timing parameter cut are shown in Fig. F.6. $\sim$100 histograms were generated via bin sizes calculated using a modified Freedman-Diaconis relation [189]. The modification used a larger scaling factor than 2, which is the standard Freedman-Diaconis rule, due to

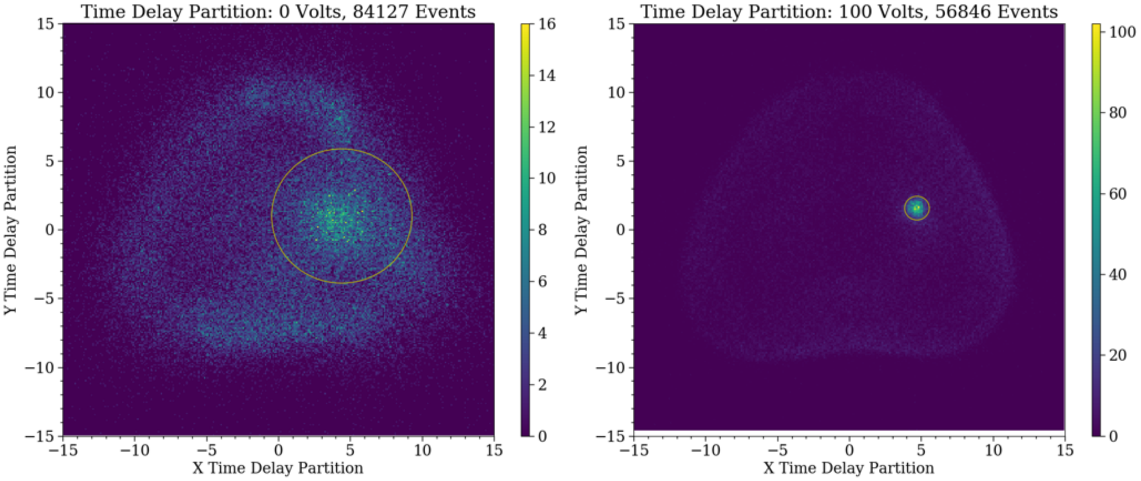

Figure F.6: Time delay partition plots showing the large discrepancy in time delay between data at 0 V bias (left) and that with voltage applied (right, 100 V DC power supply bias). The Am-241 source events are circled.

the multi-valued nature of the data distributions. For the data at 0 volts the factor was 4, for that at ±10 volts it was 10, and it was 24 for that at the other voltages. For each histogram a window for the calibration peak was selected by hand, and a Gaussian fit was applied to the points within the window. A χ^2 statistic was calculated for each fit, and each fit was manually inspected for quality.

The positions of the calibration peak in each dataset was used as a multiplicative scaling factor for all of the data as a function of time. Since the dilution refrigerator temperature was kept as close to constant as possible for this dataset, the data with zero or positive bias voltage applied was rescaled to those data. Data taken with negative voltage bias, since there is no clear reference dataset, were kept unscaled. In other words, dividing by the time-dependent calibration factor from the calibration peak preserves the Luke-Neganov gain effect at positive voltages after the correction but does not for negative voltage bias data.

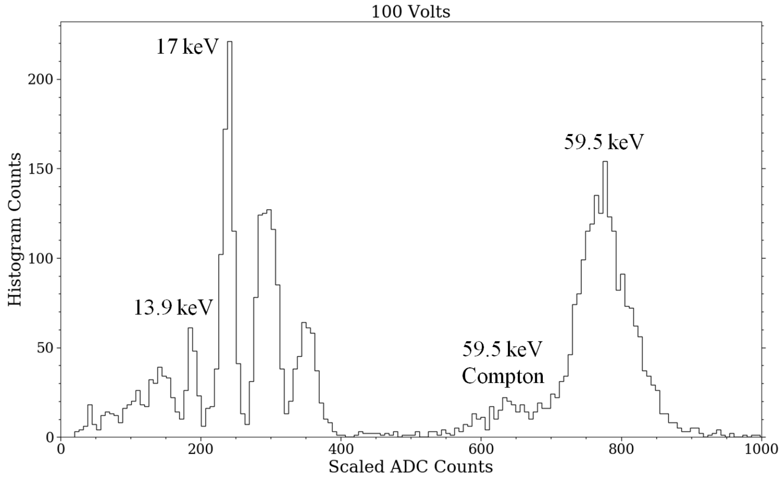

Figure F.7: Spectrum of all data taken during Run 7 at 100 V. The amplitude for each point is found using the sum of channels A, B, and C. The data were combined by calibrating for any time-dependent detector performance using the location of the peak between 200 and 250 ADC counts. Any datasets with too few events to distinguish that peak are excluded. The locations of three of the more prominent peaks are indicated (13.9 keV, 17 keV and 59.5 keV). The secondary peak next to the 59.5 keV peak is from events that have Compton-scattered with materials outside the detector and were then measured by the detector. The voltage is that supplied by the DC power supply.

The results of the calibrations are best illustrated by the scatter plots in Fig. F.4 and Fig. F.5, which represent data before and after the time-dependent calibration, respectively. These scatter plots show the Channels A, B, and C summed peak values for each event as a function of time index, which is the index position of each event sorted with respect to time, within the set of data at 100 volts bias. This representation shows how variations in detector performance can have an effect even on events at energies too small to saturate the channel. The time-dependent calibration significantly reduces the variation in peak position due to the variation in detector performance with time. However, the benefit is much less pronounced for the 59.5 keV peak than it is for the peaks near 20 keV. Additionally, even the low-energy calibration is not perfect since there are nontrivial variations within each dataset, especially near time indices of 1800, 2800, 3200, and 4200 in Fig. F.5. These variations could be caused by subtle changes in electronics amplifier gain during a data-taking session, which would shift the line but make it difficult to correct for, charge accumulation on the detector that would slowly drift the calibration lines because of the changing electric field inside the detector, or detector heating the higher the applied voltage, which would affect TES performance, and hence shift the location of the lines over time, among other possible reasons. For this reason, a future time-dependent calibration based on each channel separately rather than the sum that takes into account the sub-dataset variation should significantly improve the quality of this data.

With the time-dependent correction applied, histograms of the calibration source data, selected via energy and timing parameter cuts, at each voltage over the entire run time were generated. These cuts are implemented so that particle interaction event analyses select a particular population of events, in this case the x-rays originating from the Am-241 source. The energy cut is such that the energy of the event measured by channel D must be greater than the energy measured in any other channel. The timing parameter cut uses the relative start time of the pulse on each channel to localize where in the detector the event takes place. The cut using the timing parameter selects events from the population on Channel D, as shown in Fig. F.6. A representative histogram for 100 volts bias, for which there is by far the most data, is shown in Fig. F.7.

In the future, an analysis such as this could be used for calibrating contact-free high-voltage detectors over long time periods. Doing so could improve detector resolution at the high voltages needed to reach single-electron resolution.